# Molecular Line Emission from Planet-Forming Disks with ALMA


Alice S. Booth

School of Physics and Astronomy

University of Leeds

Submitted in accordance with

*Doctor of Philosophy*

February 2020

The candidate confirms that the work submitted is her own, except where work which has formed part of jointly authored publications has been included. The contribution of the candidate and the other authors to this work has been explicitly indicated. The candidate confirms that appropriate credit has been given within the thesis where reference has been made to the work of others.

For Bill, Mardie and Isobel. Thank you for everything.

*" For small creatures such as we the vastness is bearable only through love." - Carl Sagan*

# Preface

The chapters in this thesis are based on work presented in the following jointly authored publications:

I. **Booth, A. S.**, Walsh, C., Kama, M., Loomis, R. A., Maud, L. T. and Juhàsz, A., Sulphur monoxide exposes a potential molecular disk wind from the planet-hosting disk around HD 100546 (A&A, 611:A16, 2018)

II. **Booth, A. S.**, Walsh, C., and Ilee J. D., First detections of $H^{13}CO^+$ and $HC^{15}N$ in the HD 97048 protoplanetary disk: evidence for a cold gas reservoir in the outer disk (A&A, 629:A75, 2019)

III. **Booth, A. S.**, Notsu, S., Nomura, H., Walsh, C., Ilee, J. D., et al., The first detection of $^{13}C^{17}O$ in a protoplanetary disk: a robust tracer of disk gas mass (ApJL 882:L31, 2019)

IV. **Booth, A. S.** and Ilee, J. D., $^{13}C^{17}O$ suggests gravitational instability in the HL Tau disk (MNRAS, 493:L108, 2020)

Papers III and IV form the basis of Chapter 3, paper II forms the basis of Chapter 4 and Paper I forms the basis of Chapter 5. For I and II C. Walsh is the data PI and for III it is S. Notsu (supervised by H. Nomura). For I and II ALMA data were self-calibrated by C. Walsh with L. Maud and A. Juhàsz, and for III by E. Akiyama. Archival data used in II and IV was self-calibated by A. S. Booth. A. S. Booth detected and imaged the SO, $H^{13}CO^+$, $HC^{15}N$ and $^{13}C^{17}O$ lines and performed all of the data analysis. R. Loomis developed the Matched

Filter package used in I and III. The disk model used in I was provided by M. Kama, in II a public model from the DIANA project was used with guidance from J. D. Ilee and in III C. Qi provided a model. These persons provided guidance on the use and origin of the models. A. S. Booth performed all of the line radiative transfer modelling in each paper. A. S. Booth wrote the first drafts of all manuscripts. A second draft was iterated with C. Walsh and then further drafts with the rest of the co-authors in the case of I, II, and III. For IV second and subsequent drafts were iterated with J. D. Ilee.

# Acknowledgements

I would first like to thank my supervisor Catherine Walsh for always being there to answer my questions, even if I was asking the same thing for the second or third time. You are everything a student needs in a mentor and more. Secondly, a big thank you goes to John Ilee for being such a helpful chap over the last few years both in science and in refilling my pint glass. Then to my office mates, I am overwhelmingly grateful for the scientific discussions, camaraderie and adventures we have shared over the past few years. You have all made me feel at home in Leeds and I have made some wonderful friends. I am thankful for the "Girls Nights" featuring copious amounts of wine and cheese, trips to the cinema and long evenings in the Fenton. I'd like to thank my drum teachers Dave Jones and Nestor Matthews for indulging me in my rockstar dreams with equal parts Taylor Swift and Sleater-Kinney. Thank you to my disk partner in crime James for being an excellent travelling companion. To Abi, you have made my time in Leeds incredibly special. Thank you for always having a shoulder for me to to lean on. For my friends in other places thank you, and specifically, Amber - for the continuous encouragement; and Jennifer - for always finding time to laugh with me. For my family in Aberdeen, thank you for supporting me in pursuing this PhD no matter how frustrating I can be. We have had a difficult few years and I could not have done this without you all. A special mention has to go to Uncle Brian who at times has had more enthusiasm about astronomy than I do. Finally, I cannot forget about Ollie our dog who is a lighting bolt of love in the darkest of times.

# Abstract

The physical and chemical conditions in the protoplanetary disk set the initial conditions for planet formation. Constraining the properties of disks is of key importance for understanding how planets assemble. Observations of molecular lines in disks provide valuable information on disk properties. This thesis presents ALMA observations, analysis and modelling of molecular line emission from four disks that all exhibit evidence for forming planets. Using the first-ever observations of $^{13}C^{17}O$ in protoplanetary disks, the CO gas mass of the HD 163296 and HL Tau disks are robustly constrained. The new masses are a factor of 2-10 times higher than existing estimates using $C^{18}O$, and highlight the potential gravitational instability of the HL Tau disk. Analysis of the radial distribution of $HCO^+$ and $H^{13}CO^+$ in the HD 97048 disk reveals a low ratio that can be explained via chemical fractionation. This indicates that the gas temperature in the outer disk is low ($\approx$ 10 K) despite this disk being hosted by an A-type star. Both silicon and sulphur bearing volatiles are observed to be significantly depleted in disks, similar to dark clouds. Multiple lines of SO and SiO are targeted towards HD 100546 and HD 97048. The detection of the shock tracer SO in the HD 100546 disk is attributed to either a disk wind or a circumplanetary disk. Complementary chemical modelling reveals the molecular carriers of S and Si in the two sources, and predicts SiS as tracer of S and Si in disks. This thesis shows that $^{13}C^{17}O$ is a robust tracer of disk gas mass, $HCO^+$ isotopologue emission may trace reservoirs of cold gas in typically warm disks, and Si and S bearing molecules are useful probes of shock induced structures such as circumplanetary disks.

# Contents

# List of Figures

## LIST OF FIGURES

# List of Tables

# Chapter 1

# Introduction

Over the past two decades, extreme advances have been made in the field of exoplanet science and there are now more than 4000 planets detected around stars in the Milky Way [1]. Most of these detections ($> 75\%$) are due to the incredibly successful Kepler mission (Borucki, 2017). The diversity of these exoplanet systems now brings their formation history, in the disks of gas and dust around young stars, to the forefront of research. Over the last six years, observations of these protoplanetary disks with the Atacama Large Millimeter/submillimeter Array (ALMA) are driving forward our understanding of planet formation. Observing at millimetre wavelengths, ALMA allows us to map the physical and chemical conditions of the disk: the initial conditions of planet formation. This Chapter summarises the relevant background material for observing and modelling molecular line emission from disks on which this thesis is focused. This includes an overview of star formation, disk evolution, disk structure, and the different disk properties probed with ALMA.

[1] NASA Exoplanet Archive: https://exoplanetarchive.ipac.caltech.edu/

## 1.1 Star formation

The formation and evolution of protoplanetary disks in inherently linked to the formation of stars. The general paradigm of isolated low mass star formation has been understood now for a number of decades (Larson, 2003; Shu *et al.*, 1987). Star formation is associated with giant molecular clouds (GMCs; Bergin & Tafalla, 2007). These clouds are $2-10$ pc across with $H_2$ densities of order $10^2-10^3$ cm$^{-3}$ and temperatures of $\approx 10$ K. Observations show that these clouds are made up of complexes of higher density filaments and even more compact cores. These cores have typical $H_2$ densities of order $10^4-10^5$ cm$^{-3}$, temperatures of $\approx 10$ K and are $\leq 0.5$pc across.

The internal gas pressure of the core is the primary support mechanism against gravitational collapse. The maximum density a cloud can have to be stable to collapse can be estimated by the Jeans criterion which is determined from the balance between internal cloud pressure and self-gravity (Jeans, 1902). An extension of this estimation is the Bonnor-Ebert critical density which considers an isothermal cloud in hydrostatic equilibrium within a medium with some external pressure (Shu, 1977). If the gas in molecular clouds was all unstable and undergoing a free-fall collapse then the galactic star formation rate would be $\approx 100\times$ greater than has been measured. This, coupled with the long cloud lifetimes ($\approx 10$ Myr), means that there have to be other support mechanisms in clouds (Evans, 1999). Molecular clouds are observed to be undergoing rotation, but the rotational energy is only a few percent of the gravitational energy; therefore, they cannot be rotationally supported (Goodman *et al.*, 1993). Magnetic fields and turbulence; therefore, are thought to provide significant cloud support (McKee *et al.*, 1993).

At some point these cores become unstable to gravitational collapse due to the loss of turbulent, thermal and magnetic support via cooling and ambipolar

diffusion. The slow rotation of the cloud is amplified upon collapse due to the conservation of angular momentum. A centrifugal force arises due to this increase in rotational velocity that opposes a spherical collapse. This force is strongest perpendicular to the rotation axis resulting in the formation of a circumstellar disk (Terebey *et al.*, 1984). The initial radial extent of this disk is determined by the centrifugal radius. This is where the gas and dust are no longer in-falling but are now rotating, and the radius at which this happens depends on the initial specific angular momentum of the cloud and the sound speed. The angular momentum of a typical cloud core is generally a few orders of magnitude higher than that of an individual star, meaning that this angular momentum needs to be removed from the system in order for a star to form. Disks play a key role in this as they mediate both the accretion of material onto the forming star and the transport of angular momentum outwards. This will be discussed further in Section 1.2.

As the cores located in molecular clouds are the precursors to stars they are called pre-stellar cores. Their evolution to main-sequence star can be traced observationally via spectral energy distributions (see Figure 1.1). An SED shows the energy emitted by a source as a function of wavelength and young stellar objects (YSOs) can be classified according to this. This was first formalised by Adams *et al.* (1987) and was subsequently added to by Andre *et al.* (1993) and Greene & Lada (1996). YSOs are categorised as Class 0, I, II or III with the additional flat spectrum (FS) classification between Classes I and II. This observational criteria matches with predictions from theoretical calculations of the flux from a rotating and collapsing core as described above (Adams *et al.*, 1987). In the Class I stage the SED excess is dominated by the hot dust in the envelope while in the latter stages of evolution it is due to the dust disk. As the envelope disperses and the disk settles the magnitude of this excess decreases (see Figure 1.1). A parallel classification of T Tauri stars developed alongside this

where YSOs are classified by the width of their H$\alpha$ emission line. Classical T-Tauri Stars (CTTS) are actively accreting and Weak-lined T-Tauri Stars (WTTS) are passive (Wood *et al.*, 1996). These are broadly equivalent to Class II and III respectively.

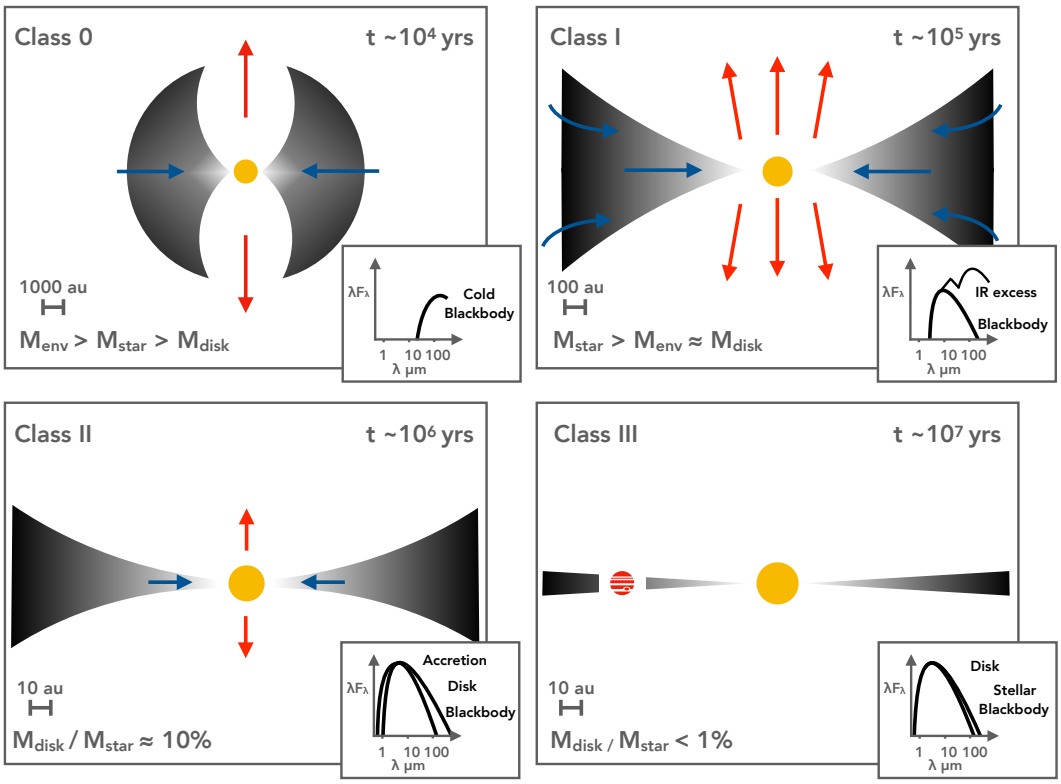


Figure 1.1: The stages of YSO evolution in low mass star formation with characteristic SEDs shown in the bottom right corners of each panel.

The protostar accretes material from the disk via magnetospheric accretion (see Hartmann *et al.*, 2016, for a review). The mass will flow onto the star along the stellar magnetic field lines and will produce a shock as it hits the stellar surface which is observable at UV and X-ray wavelengths. To conserve angular momentum this process also launches accretion powered jets and disk winds from within $\approx$ 1 au in the Class 0 to I sources. The typical accretion

rate is of order $10^{-8}$ to $10^{-7}$ $M_\odot$ $yr^{-1}$ (e.g., Calvet *et al.*, 2004) but this can be variable. EXor objects show increases in accretion rate by 1 to 2 orders of magnitude on timescales of months to years and FU Ori objects show much higher accetion rates, $10^{-5}$ to $10^{-4}$ $M_\odot$ $yr^{-1}$ which can last for decades or more (Herbig, 1977, 2008). This variability has been attributed to instabilities in the inner disk creating an irregular flow of material to the inner disk edge, and unstable disk and magnetic field interactions (Hartmann & Kenyon, 1996). Once the mass of the protostar is high enough deuterium burning ignites in the core followed by hydrogen burning resulting in a main sequence star (McKee & Ostriker, 2007).

The evolutionary scenario described above is for low-mass star formation, i.e., $M_{star} \lesssim 2$ $M_\odot$. Stars with masses greater than this are fully radiative rather than having the radiative core and convective envelope of low mass stars. These intermediate mass YSOs, Herbig Ae/Be stars, have a mass range from $2$ $M_\odot \lesssim M_{Star} \lesssim 8$ $M_\odot$. Herbig Ae/Be stars follow a similar SED evolution as for low mass stars (Waters & Waelkens, 1998). Herbig Ae/Be sources exhibit signatures of magnetospheric accretion but have lower accretion rates. Over this intermediate mass range the accretion mechanism is thought to switch from magnetospheric accretion to direct accretion from a disk. This is due to their radiative envelopes resulting in weaker magnetic fields. There are still questions regarding how more massive stars form (Tan *et al.*, 2014), but there is now evidence for rotating Keplerian-like disks around O-type stars which supports a disk accretion theory of massive star formation (e.g., Johnston *et al.*, 2015).

## 1.2 Disk evolution

As described in Section 1.1, during core collapse a circumstellar disk forms which mediates the transfer of material from the in-falling envelope to the protostar. At this early stage in the disk's life time it maybe susceptible to gravitational in-

stabilities (GI; Kratter & Lodato, 2016). GI is associated with non-axisymmetric spirals which will influence the physical and chemical conditions in the disk. These spirals are local enhancements in the disk density and temperature that sweep through the disk. This will do several things to the gas and the dust. The trapping of dust in the spirals enhances the rate of grain growth and shock heating of the gas will, in turn, affect the local chemical composition (e.g., Ilee *et al.*, 2011; Rice *et al.*, 2004). As a general rule GI becomes relevant when the disk to star mass ratio is high ($M_{disk}/M_{star} \geq 0.1$). The stability of a disk against spiral instabilities can be quantified via the Toomre Q parameter (Toomre, 1964):

$$Q = \frac{c_s \kappa}{\pi G \Sigma}$$

where $c_s$ is the sound speed of the gas, $\kappa$ is the epicyclic frequency (equal to the angular velocity $\Omega$ in a Keplerian disk) and $\Sigma$ is the surface density of the gas. Disks with $Q \lesssim 1.7$ will be susceptible to the formation of spiral asymmetries or fragmentation, possibly resulting in the formation of bound companions (Durisen *et al.*, 2007).

Protoplanetary disks in the Class II stage are generally thought to have a disk mass of $1 - 10\%$ of the host star's mass. These disks are described as viscous accretion disks and the theoretical framework originated from the seminal papers from Lynden-Bell & Pringle (1974) and Pringle (1981). As mentioned in Section 1.1 disks are essential in removing the angular momentum from the forming star. Due to some source of viscosity, there is net transfer of mass inwards through the disk, which is accreted into the star, and a net transfer of angular momentum radially outwards, causing the disk radius to increase. The underlying viscosity $\nu$ in the disk is parameterized by $\alpha$ where:

$$\nu = \alpha c_s H$$

and $c_s$ is the sound speed and $H$ is the scale height of the disk. Typical values for $\alpha$ range from $10^{-3}$ to $10^{-1}$. This framework allows for the modelling of viscous disks without the difficulty of also modelling the source of the viscosity (Pringle, 1981; Shakura & Sunyaev, 1973). The molecular viscosity alone is not sufficient remove the angular momentum. A primary source of the viscosity is thought to be due to the magneto-rotational instability (MRI; Balbus & Hawley, 1991). This is an instability that arises when a magnetic field is present in a differential rotating fluid. The significance of this depends on the ionisation fraction of the disk as this is the material that will be coupled to the magnetic field.

The general evolution of a protoplanetary disk is as follows and these stages are shown in Figure 1.2 (Williams & Cieza, 2011). Initially, the flared disk loses mass due to accretion of material onto the star. In the outer disk there is the removal of gas via photo-evaporation from high-energy photons. Due to the radial pressure gradient in the disk the gas orbits at a slightly sub-Keplerian velocity. As the grains grow, the surface area to mass ratio decreases and the dust dynamics are decoupled from the gas. The dust then experiences a drag force resulting in a loss of angular momentum causing the orbital radius of the particle to decrease. This drag force (and gravity) dampens the relative inclination of the dust's orbit causing the dust to settle in the midplane of the disk. The dust will travel towards a local pressure maximum in the disk which may result in the grain falling into the star or forming a dust trap or ring (Testi *et al.*, 2014).

The micron-sized dust grains present when star formation begins are the building blocks of Earth-like planets. Terrestrial planet formation begins with the collisional growth of dust from micrometre to centimetre sizes (Testi *et al.*, 2014). Further growth to metre sized bodies via collisions of similar sized particles becomes inefficient as centimetre sized particles tend to bounce rather than stick (Zsom *et al.*, 2010). This "bouncing barrier" can be overcome if particles of dif-

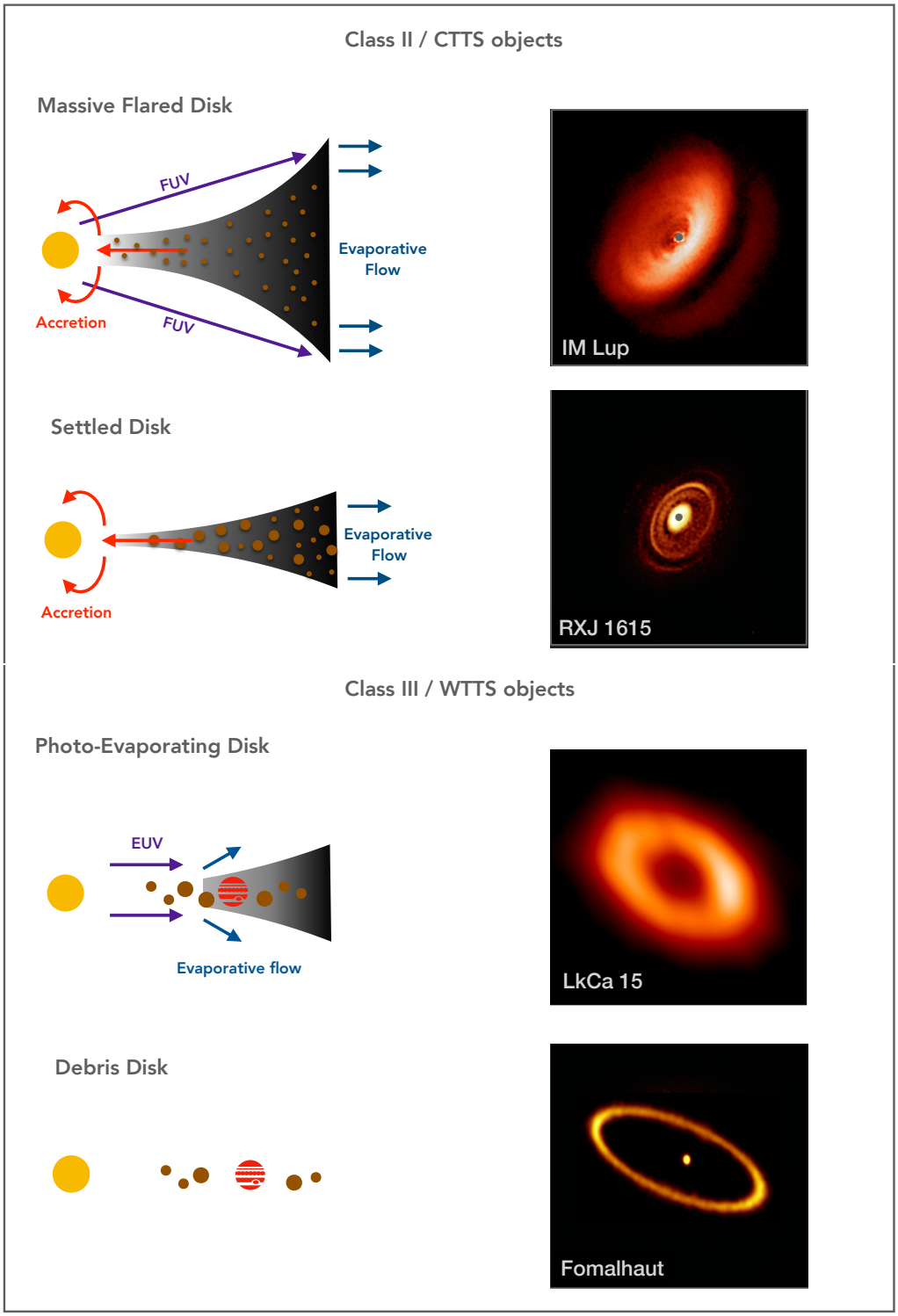


Figure 1.2: Typical stages in protoplanetary disk evolution (based on Williams & Cieza 2011). Disk observations are from Avenhaus *et al.* (2018), Andrews *et al.* (2011) and MacGregor *et al.* (2017).

ferent sizes are colliding. Metre sized objects then face the "drift-fragmentation barrier". Dust in the disk will drift radially inwards once decoupled from the gas motions and this speed depends on the particle size. Collisions with high differential speeds will result in fragmentation or erosion of these larger bodies. Additionally, if the drift timescale is too fast, then a 1-metre size object at 1 AU would fall into the star in $\approx 100$ yrs (Weidenschilling, 1977). There are a number of solutions proposed to overcome this including the streaming instability (e.g., Youdin & Goodman, 2005). This results in a high density concentration of dust that can grow to kilometre-sized via gravitational collapse. The growth from kilometre sized planetesimals to planetary embryos either occurs from the collisions between the planetesimals or via the accretion of smaller particles. The final stage of accretion is chaotic with collisions between embryos and it may take $> 10^7$ yrs for the system to become dynamically stable (Izidoro & Raymond, 2018).

Gas giant planets are proposed to form via two mechanisms: core accretion (CA; Pollack *et al.*, 1996) and gravitational instability (GI; Boss, 1998). Although these two mechanisms have historically been put in opposition it is possible that both are active in disks (Boley, 2009). CA begins in the same way as terrestrial planet formation but in the outer disk beyond molecular snowlines (e.g., $H_2O$, $CO_2$, $N_2$, CO) where there is also icy material available to form the cores. Once the core is $\approx 10$ $M_{Earth}$ it will start accreting a gaseous envelope. When the core and envelope masses are approximately equal the envelope will collapse onto the core and the protoplanet will undergo a run-away gas accretion. Growing the cores required to build giant planets via the collisions of km sized particles is inefficient and in some cases may take longer than the lifetime of the gas disk. The rate of this process can be accelerated by having the core accrete cm sized pebbles instead. This allows gas-giant planets to form in the disk before dissipation (Lambrechts & Johansen, 2012). As described in Section 1.1 disks

with a high mass may be susceptible to gravitational instabilities. In the case where the Toomre Q parameter is $\approx 1$, and where the cooling time is less than the orbital period, the disk will fragment. Giant planets can form via the gravitational collapse of these clumps which are expected to be in the Jupiter mass range with orbits $\gtrsim 10$ au (e.g., Boss, 2011; Rice *et al.*, 2003).

Theoretical models predict that disk dispersal should occur on timescales up to $\approx 10$ times shorter than observed disk lifetimes (Alexander *et al.*, 2014; Panić *et al.*, 2013). Once the accretion rate falls and matches the evaporation rate the outer disk can no longer feed material to the inner disk. UV photons from the star are now able to penetrate the upper atmosphere of the disk more efficiently. An inner hole in the disk forms out to a few au and the gas disperses rapidly. In planet-forming Class II disks, jets/outflows are not the main driver of disk dispersal. Instead, the removal of angular momentum is achieved by slower disk winds ($< 30$ km s$^{-1}$). Disk winds are proposed to be driven by photo-evaporation and/or magneto-hydrodynamical (MHD) effects (Alexander *et al.*, 2014; Ercolano & Pascucci, 2017).

The remnants of protoplanetary disks are called debris disks (Hughes *et al.*, 2018). These are gas poor disks with planetesimals and possibly planets. Their relatively young age but lower dust and gas content make direct imaging potential of exoplanets much easier. For example, in the debris disk around Fomalhaut there is a detection of a giant planet at visible wavelengths interior to the narrow dust ring that has been observed with ALMA (see Figure1.2; Kalas *et al.*, 2008; MacGregor *et al.*, 2017). Similarly, there is a giant planet embedded in the Beta Pic debris disk (Lagrange *et al.*, 2009, 2019). To determine the formation mechanism(s) of these planets we need to constrain the physical and chemical conditions in the younger protoplanetary disks where planet formation is in progress.

## 1.3 Disk structure

### 1.3.1 Physical structure

Protoplanetary disks have strong radial and vertical density and temperate gradients (see the diagram in Figure 1.4). The disk density and temperature structures can be parameterized with analytical formulae. These prescriptions are based on the results from theoretical models of viscous disks and have been shown to be consistent with observations (e.g., Beckwith *et al.*, 1990; Dutrey *et al.*, 1998; Hughes *et al.*, 2011; Williams & Cieza, 2011).

The surface density, $\Sigma(r)$, of a disk can be described as a power law with an exponential taper:

$$\Sigma(r) = \Sigma_0 \left(\frac{r}{r_c}\right)^{-\gamma} \exp\left(-\frac{r}{r_c}\right)^{2-\gamma}.$$

where,

$$\Sigma_0 = (2-\gamma)\frac{M_{\rm d}}{2\pi r_c^2} \exp\left(\frac{r_{\rm in}}{r_c}\right)^{2-\gamma},$$

$M_d$ is the total mass of the disk and $\gamma$ describes the steepness of the surface density slope. $r_c$ is the critical radius where the slope changes from the power law to the exponential and $r_{in}$ is the inner radius of the disk (Hartmann *et al.*, 1998; Lynden-Bell & Pringle, 1974). The 2D gas density distribution, $\rho(r, z)$, can be obtained by solving the equation of hydrostatic equilibrium:

$$\frac{\partial \ln \rho}{\partial z} = -\left[\left(\frac{GM_{\rm star} z}{(r^2+z^2)^{3/2}}\right)\left(\frac{\mu m_{\rm H}}{kT}\right) + \frac{\partial \ln T}{\partial z}\right],$$

where $\mu$ is the mean molecular weight of the gas $(2.2-2.4)$, $n_{\rm H}$ is the mass of a hydrogen nuclei, $T$ is the gas temperature (K) and $k$ is the Boltzmann constant. The smaller micron-sized grains are suspended in the gas but as they grow to millimetre sizes they will settle towards the midplane. At each radius, $r$, $\rho(r, z)$

is normalised such that:

$$\Sigma(r) = \int_{-\infty}^{\infty} \rho(r, z) dz.$$

The temperature of the emitting layer of gas/dust typically follows a power law: $T(r) \sim r^{-q}$ (Beckwith *et al.*, 1990). Initial models used isothermal vertical temperature gradients in the gas but it has been shown from observations that there is also a significant vertical temperature gradient in disks (e.g., Rosenfeld *et al.*, 2013). The temperature structure of the disk is set by a balance of different heating and cooling mechanisms. Heating in the disk comes from the stellar radiation, X-ray and UV radiation and cosmic rays. This energy is then processed by the dust via scattering or absorption and emission, or photo-electric heating. The gas can cool via rotational, vibrational or electronic transitions, forbidden line emission, recombination or collisions (Woitke, 2015). This balance can be computed with full themochemical models (e.g., Woitke *et al.*, 2009a) but the following analytical description is a good approximation. The 2D temperature of the gas can described by two power laws, one for the midplane ($T_{\rm mid}$) and one for the atmosphere ($T_{\rm atm}$):

$$T(r, z) = \begin{cases} T_{\rm mid} + (T_{\rm atm} - T_{\rm mid}) \left[\sin\left(\frac{\pi z}{2 z_q}\right)\right]^{2\delta} & \text{if } z < z_q \\ T_{\rm atm} & \text{if } z \geq z_q \end{cases}$$

where the parameters $\delta$ and $z_q$ describe the steepness of the profile and the height in the disk where the temperature switches to the atmospheric value (e.g., Dartois *et al.*, 2003). Figure 1.3 shows two example disk gas temperature and density structures for a T Tauri and a Herbig Ae disk. The key differences are highlighted in the white contours which show the CO freeze-out temperature (20 K) and the CO photodissociation boundary ($\Sigma(n_{\rm H}) = 1.256 \times 10^{21}$ cm$^{-2}$). This is calculated by integrating the hydrogen nuclei density from the top of the

disk vertically downwards (e.g., Qi *et al.*, 2011). In the outer disk there is a region where the conditions for both freeze-out and dissociation are met. Here, how the CO is processed will depend on the relative rates of both processes.

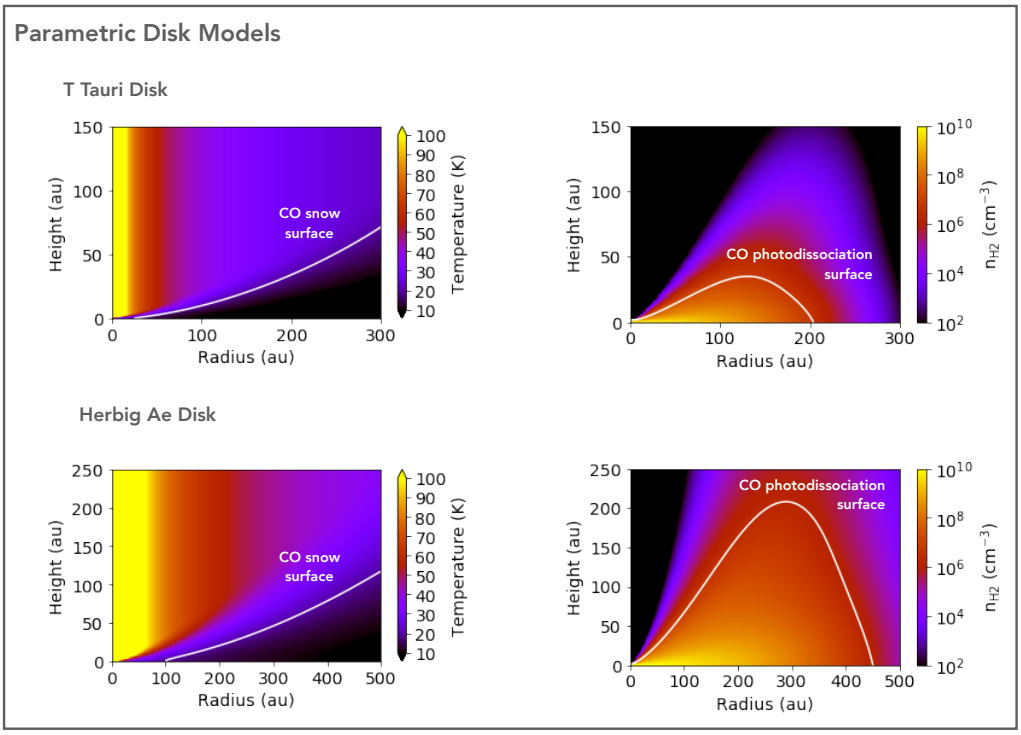


Figure 1.3: Example T Tauri and a Herbig Ae disk parametric models based on Williams & Best (2014). The white contours mark the typical CO freeze-out and photodissociation boundaries.

### 1.3.2 Chemical structure

The initial gas-to-dust mass ratio of the disk is thought to mirror the ISM value of 100. Therefore, the bulk of the mass is made up of gaseous material. Most of this gas is molecular hydrogen and helium, $\approx 98\%$ of the mass, and the remaining mass is dominated by oxygen, carbon, nitrogen and sulphur bearing molecules. These volatiles have a sublimation temperature of less than a few 100 K and can

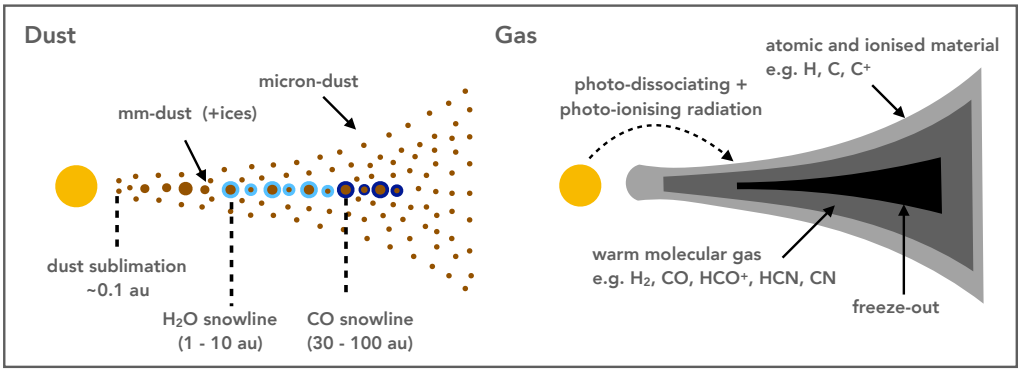


Figure 1.4: The 2D dust (left) and gas (right) distribution in a protoplanetary disk.

exist as ices on the surface of grains or in the gas phase (Pontoppidan *et al.*, 2014). The assumption for the solar system and disks is that they have global stellar elemental abundances as they formed from the same parental cloud of gas and dust (Asplund *et al.*, 2009). Most of the oxygen is in $H_2O$ and CO, and the carbon in CO, $CO_2$, $CH_4$, HCN, $C_2H$, $C_2H_2$ and $C_2H_6$. The main nitrogen reservoir in protoplanetary disks is unclear since we cannot observe $N_2$ directly in disks, but there is expected to be a significant fraction of N in $NH_3$ and HCN (Pontoppidan *et al.*, 2019). Sulphur is observed to be significantly depleted in circumstellar regions with detections of gas-phase S-bearing molecules accounting for $\sim 0.1\%$ only of the estimated cosmic abundance (Dutrey *et al.*, 1997; Ruffle *et al.*, 1999; Tieftrunk *et al.*, 1994). This is despite deep targeted searches in YSOs (e.g., Martín-Doménech *et al.*, 2016). The missing sulphur is thought to reside on the solid dust grains in the disk, the most abundant molecule being $H_2S$ in cometary ices (Bockelée-Morvan *et al.*, 2000). There is also evidence for sulphur chains, e.g., from $S_2$ up to $S_8$ (Jiménez-Escobar & Muñoz Caro, 2011). In refractory form a key sulphur species is iron sulphides (FeS), a main component of primitive comets and meteorites (Keller *et al.*, 2002).

Although the dust only contributes to 1% of the initial disk mass this material is incredibly important as it is this matter that forms terrestrial planets and the cores of giant planets in the core-accretion scenario. In Class II disks the millimetre dust disk tends to be less radially extended with the respect to the gas disk (e.g., Andrews *et al.*, 2016; de Gregorio-Monsalvo *et al.*, 2013; Fedele *et al.*, 2017; Walsh *et al.*, 2014a) as these grains are massive enough to be dynamically decoupled from the gas, whereas the smaller micron sized grains are not. The dust is primarily composed of silicate material. This is evident in the strong absorption resonances at 10 $\mu m$ and 18 $\mu m$ relating to the Si-O and O-Si-O bending modes (Draine, 2003). These features are relatively broad compared with laboratory measurements indicating that interstellar silicates are amorphous rather than crystalline. In addition to this the observed abundance of Si, Fe, and Mg requires almost 100% of the solar abundance of these elements to be condensed into grains. There is also evidence for a mixture of graphite grains and polycyclic aromatic hydrocarbons (PAHs). Dust grains provide a surface for freeze-out of volatile materials to form ices in dark molecular clouds and in the midplane of protoplanetary disks. One of the strongest absorption features of interstellar ice is the O-H bending mode of solid $H_2O$ at 3.1 $\mu$m (Draine, 2003). In T Tauri and Herbig Ae/Be disks there is evidence for grain growth and crystallisation with respect to dust in the ISM (e.g., Przygodda *et al.*, 2003; van Boekel *et al.*, 2003, 2005).

Chemistry in the disk is controlled by the temperature and density structure and the impinging radiation field. Due to the large radial and vertical temperature and density gradients in disks, a range of chemical processes occur and disks are host to a variety of chemical species (see Henning & Semenov, 2013, for a review). Protoplanetary disks can be roughly divided into four regions: the inner and outer midplane, the molecular layer, and the disk atmosphere (see Figure 1.4).

The inner midplane of the disk (approximately $\lesssim$ 20 au but dependent on disk mass) is heated from the dissipation of accretion energy. This region of the disk is very dense and chemistry is dominated by two and three-body neutral-neutral reactions and thermal desorption (e.g., Markwick *et al.*, 2002). In the upper layers of the disk, stellar and interstellar radiation fields are important as the UV radiation dissociates and ionises molecules and atoms facilitating ion-molecule chemistry. The spectral type of the star is important here as T Tauri stars have non-thermal UV emission resulting from accretion and Herbig Ae/Be stars have more thermal UV emission. These differing radiation fields will have different effects on the chemistry in the respective disks since X-rays will result in ion-molecule chemistry and UV radiation will lead to photodissociation (Agúndez *et al.*, 2018; Walsh *et al.*, 2015). In addition to this T Tauri stars have a greater X-ray luminosity than Herbig Ae/Be stars due to their stronger magnetic fields. X-ray photons ionise He in the molecular layer and this ion can then destroy molecules like CO driving gas phase chemistry (Aikawa *et al.*, 1997). Below the atmosphere in the warm molecular layer where temperatures range from $30 - 70$ K, the molecules are partially shielded from radiation allowing more molecule based reactions to proceed (Aikawa *et al.*, 2002). The disk midplane is shielded from most radiation sources aside from cosmic rays and here temperatures can drop below 20 K resulting in freeze-out/adsorption of most molecules onto grain surfaces forming ices. Water freezes out at around 150 K (this temperature depends on the density); in a T Tauri disk this corresponds to a radial distance of $1-3$ au (Notsu *et al.*, 2016). Comparatively, CO is more volatile than $H_2O$ and; therefore, the CO snowline typically lies beyond $\sim$ 20 au (Zhang *et al.*, 2017). In the disk midplane grain surface and hydrogenation reactions are important and materials can be released from grains into the gas phase via non-thermal desorption triggered by, e.g., cosmic rays (e.g., Aikawa *et al.*, 1999; Semenov

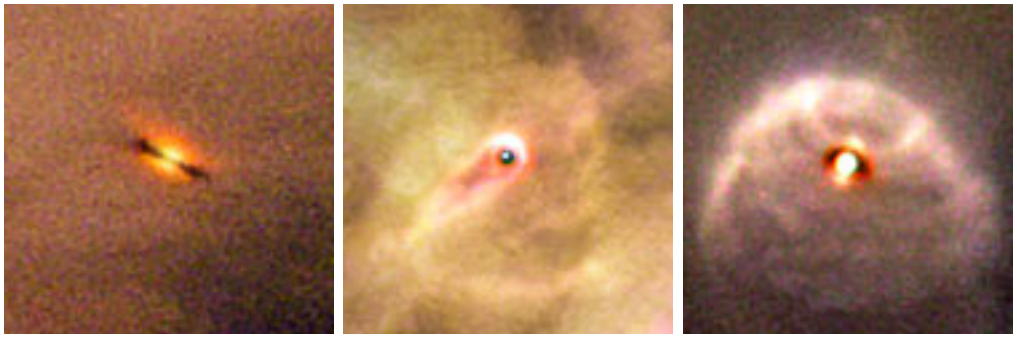

Figure 1.5: Hubble observations of a sample of young disks in the Orion Nebula (taken from Ricci *et al.* 2008).

*et al.*, 2004).

## 1.4 Precursor and complementary observations to ALMA

Before discussing the properties of disks probed via the Atacama Large Millimeter/submillimeter Array (ALMA), it is beneficial to briefly summarize some of the precursor and complementary observations of protoplanetary disks.

The first direct evidence for disks came from observations at visibile wavelenghts. The circumstellar disk around Beta Pic was imaged (Smith & Terrile, 1984) and YSOs in Orion (e.g., O'dell *et al.*, 1993). Visible wavelengths probe the micron-sized dust that scatters light from the flared disk surface and the absorption shadows of the optically thick midplane dust. This can be seen in the images in Figure 1.5 from more recent observations of the Orion Nebula (Ricci *et al.*, 2008). High resolution scattered light observations are executed by telescopes like SPHERE/VLT and these again, probe the light scattered from the disk surface by the micron-sized dust grains that are suspended in the gas disk (e.g., Avenhaus *et al.*, 2018, see Figure 1.2).

Prior to this, the existence of disks was inferred from the infared excess in

SEDs attributed to the thermal emission from the circumstellar dust (e.g., Kenyon & Hartmann, 1987). Transition disks were first identified by Strom *et al.* (1989) by the lack of near-infrared ($< 10$ $\mu$m) excess but with a significant far-infrared ($> 10$ $\mu$m) excess in the SEDs. This lack of emission is attributed to the disk having an inner hole devoid of micron-sized dust grains.

Interferometry at sub-millimetre wavelengths with the Submillimetre Array (SMA), Combined Array for Research in Millimetre-wave Astronomy (CARMA) and NOrthern Extended Millimetre Array (NOEMA, successor to the Plateau de Bure observatory) have provided resolved images of protoplanetary disks and resolved the gaps in transitional disks (for a review see Guilloteau *et al.*, 2011, also see Figure 1.2). Observations with the The Karl G. Jansky Very Large Array (VLA) probe the centimetre-sized dust in the disk (e.g., Rodriguez *et al.*, 1994). These observations show that the larger grains are radially more compact than the millimetre sized grains (e.g., Carrasco-González *et al.*, 2016).

Due to the rich chemistry in the disk, different molecules can be used to trace different regions and properties (see Table 1.1, adapted from Henning & Semenov 2013). Molecules are primarily used as tracers of disk mass, temperature and kinematics but can do much more, for example, CS and $DCO^+$ have been utilised as tracers of disk turbulence and CN has the potential to be a direct measure of disk magnetic field strength (e.g., Flaherty *et al.*, 2015, 2017; Teague *et al.*, 2016; Vlemmings *et al.*, 2019). Over 200 molecules have been detected in space but only $\approx 20$ in protoplanetary disks (McGuire, 2018). This lower number of detections is likely due to the freeze out of molecules onto dust grains in the disk midplane, the destruction of molecules via photodissociation in the disk atmosphere, and the small angular scale that disks subtend on the sky. Space-based infrared observations with *Herschel* and *Spitzer* have detected multiple CO lines and a range of molecules such as $CO_2$, $H_2O$, $C_2H_2$, HCN and OH in disks that are tracing

Table 1.1: Physical and chemical tracers in disks at sub-millimetre wavelengths (adapted from Henning & Semenov, 2013). The superscripts X and Y represent the different mass number of different isotopes, where X = 12,13 and Y = 16,17,18.

| Quantity | Molecule |
|---|---|
| Mass | $^{X}C^{Y}O$, HD |
| Temperature | $^{12}CO$, $^{13}CO$, $H_2$ |
| Kinematics | $^{X}C^{Y}O$, $HCO^+$ |
| Density | CS, $HC_3N$ |
| Ionization | $HCO^+$, $N_2H^+$, $CH^+$ |
| Deuteration | HD, $DCO^+$, DCN, $H_2D^+$ |
| Turbulence | CS, $DCO^+$ |
| Shocks | SiO, SO, $CH_3OH$ |
| Fractionation | $H^{13}CO^+$,$HC^{15}N$ |

warm gas (e.g., Fedele *et al.*, 2013, 2016; Pontoppidan *et al.*, 2010). Interferometry allows for spatially and spectrally resolved observations of molecular lines in disks, and before ALMA, the IRAM Plateau de Bure interferometre (PBdI) and the SMA observatories were driving this science (e.g., Dutrey *et al.*, 1996; Guilloteau *et al.*, 1999; Öberg *et al.*, 2010; Qi *et al.*, 2004). Sub-millimetre interferometry probes the warm and cold gas in the outer disk (> 10 au).

## 1.5 Disk properties via ALMA observations

### 1.5.1 Mass

The mass of a disk is its most fundamental property as this sets a limit on the material available to form a planetary system and can influence the mode of giant planet formation. The initial gas-to-dust ratio of protoplanetary disks is thought to mirror the interstellar medium (ISM) ratio of 100; therefore, the bulk mass carrier in young disks is the gas. With ALMA, the mass of a protoplanetary disk can be determined from observations of the dust emission and CO rotational transitions (see Figure 1.6 and Bergin & Williams, 2017, for a recent review). The

sensitivity of ALMA has allowed for the robust detection of the cold millimetre dust and the rarer CO isotopologue, $C^{18}O$, in $\approx 100$ disks resulting in improved disk gas mass estimates and the ability to study disk demographics.

The dust emits radiation over a continuum where the brightness is dependent on the temperature and the optical depth. As observations with ALMA are at millimetre wavelengths these observations are most sensitive to the millimetre-sized dust. Under the assumption that the millimetre emission is optically thin, the dust mass can be calculated as follows:

$$M_{\rm dust} = \frac{F_\nu d^2}{\kappa_\nu B_\nu(T_{dust})}$$

where $F_\nu$ is the flux at a particular frequency $\nu$, $d$ is the distance to the source in pc, $\kappa_\nu$ is the wavelength dependent dust opacity and $B_\nu(T_{dust})$ is the Planck function assuming a constant dust temperature for the disk (typically 20 K). The opacity $\kappa_\nu$ can be expressed as:

$$\kappa_\nu = \kappa_0 \Big(\frac{\nu}{\nu_0}\Big)^\beta$$

where the constants $\kappa_0$ and the spectral index $\beta$ depend on the dust size distribution and composition (Draine, 2006). A typical value for $\beta$ is 1 and for $\kappa_0$ it is 0.1 g cm$^{-2}$ for a $\nu_0$ of $10^{12}$ Hz (Beckwith *et al.*, 1990).

The above method will no longer trace all of the dust mass if the emission is optically thick at the observed wavelength. In the simplest case, ignoring any dust sub-structure in the disk, the dust optical depth will increase with decreasing radius (see Figure 1.6). For example, the dust disk around HL Tau (Class I/II) has been observed with both ALMA and the VLA and the resulting dust mass derived from the centimetre wavelength observations is 2 to 20 times higher than that with the millimetre wavelength ALMA observations (ALMA Partnership *et al.*, 2015; Carrasco-González *et al.*, 2016). Another indication of optically thick dust

is the deficit of line emission at the location of high continuum optical depth. For example, in the HD 163296 disk there is a deficit of $C^{18}O$ emission where the dust emission peaks in the inner disk (e.g., Isella *et al.*, 2016). Additionally, there has been recent theoretical work showing that at 1 mm the apparent low optical depth ($\tau \approx 0.6$) derived from observations is underestimated due to scattering (Huang *et al.*, 2018a; Zhu *et al.*, 2019).

Most of the gas mass in disks is in $H_2$ which we cannot directly observe in the bulk of the disk (Carmona *et al.*, 2011). This is because $H_2$ has no permanent dipole and therefore the transitions are very weak. As a result, most disk gas masses rely on observations of CO that are then extrapolated to a total gas mass by assuming a constant $CO/H_2$ abundance ratio in the disk ($\approx 10^{-4}$). The gas mass can be calculated from the total integrated line flux but proper treatment of the disk 2D temperature and density structure, accounting for freeze-out and photodissociation, with radiative transfer is preferred when retrieving disk gas masses (Williams & Best, 2014).

Initial observations tended to target $^{13}CO$ and $C^{18}O$. This is because the most abundant isotopologue $^{12}CO$ is optically thick in gas-rich disks, especially within the CO snowline. If the line is optically thick then the emission is not tracing the bulk gas mass in the disk midplane but rather the gas in the warm molecular layer (see Figure 1.6). The rarer the CO isotopologue, the closer to the midplane the observations are tracing. However, the $^{13}CO$ and $C^{18}O$ are likely not optically thin throughout the entire disk, therefore, gas masses determined with these tracers may be underestimated. For example, $^{13}C^{18}O$ has been detected in the TW Hya disk and this emission is proposed to be optically thin within the snowline whereas the $C^{18}O$ is optically thick (Zhang *et al.*, 2017). Therefore, the $C^{18}O$ is not tracing the full column of CO gas within the snowline. The under-estimation of disk gas mass due to optically thick line emission will be

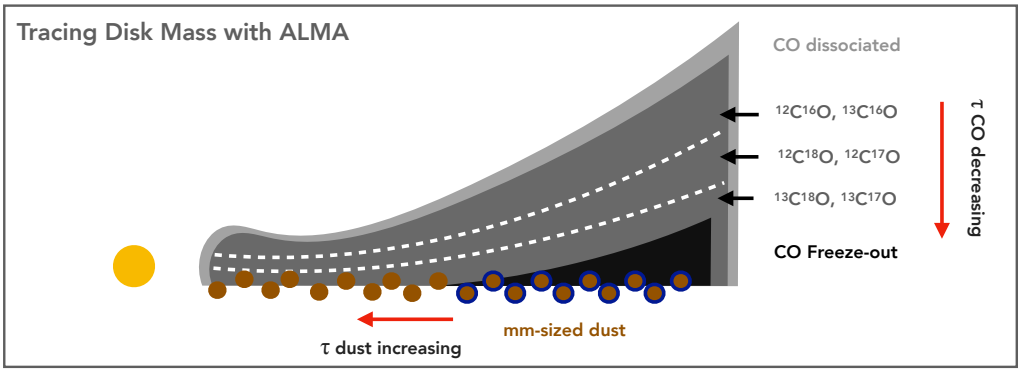


Figure 1.6: Disk mass tracers accessible with ALMA.

more significant in more massive gas-rich disks, i.e., those around Herbig Ae/Be stars versus those around T Tauri stars.

In general, the total (gas and dust) mass measurements of Class II disks in nearby star-forming regions are an order of magnitude less than the Minimum Mass Solar Nebula (MMSN) and the gas to dust mass ratios are $\approx 10$, an order of magnitude lower than in the ISM (Ansdell *et al.*, 2016, 2017, 2018; Long *et al.*, 2018a). Due to the high occurrence rate of exoplanets detected around main sequence stars, it is hard to reconcile this lack of gas mass with the proposition that these disks will not go on to form any planets. Rather, the lack of mass may indicate that planet formation has already taken place in the Class II disks or that these disk masses have been significantly underestimated (e.g., Greaves & Rice, 2011; Manara *et al.*, 2018). These surveys have revealed some trends including the increase in disk dust and gas mass with increasing host star mass, the decrease in disk mass with age, and the decrease in disk mass with increasing proximity to massive stars.

As the CO gas masses measured are low, there is potentially missing disk mass from the conversion from CO to $H_2$ mass. Complimentary HD observations imply the depletion of gas-phase CO in disks relative to that in the ISM (Bergin

*et al.*, 2013; McClure *et al.*, 2016). CO can be depleted from the gas phase via freeze out onto the icy grains in the cold midplane, and subsequent conversion to $CO_2$ and more complex organic species, e.g., $CH_3OH$ (e.g., Bosman *et al.*, 2018). The CO abundance also depends on the gas temperature and the level and type of ionisation in the disk (Schwarz *et al.*, 2018). Photodissociation via far-UV radiation destroys CO in the upper disk atmosphere, and isotope selective photodissociation can enhance the various isotopologue ratios relative to $^{12}C^{16}O$ in the atmosphere (e.g., Miotello *et al.*, 2014). Carbon is observed to be more depleted in the cooler T Tauri disks than in the warmer Herbig Ae/Be disks (Kama *et al.*, 2016a).

### 1.5.2 Temperature

The temperature of the emitting layer of the millimetre dust can be derived from the brightness temperature if the emission is optically thick (e.g., ALMA Partnership *et al.*, 2015). Otherwise, to reliably constrain the dust temperature radiative transfer modelling and multi-wavelength observations are required (Kim *et al.*, 2019; Tazzari *et al.*, 2016).

The temperature in the gas disk can be well constrained with observations of multiple CO lines. SMA and ALMA observations have shown that the gas and dust are thermally decoupled in the disk atmosphere with the gas having a greater vertical temperature gradient than the dust (Qi *et al.*, 2006, 2011; Schwarz *et al.*, 2016). ALMA observations of CO have now been able to spatially resolve emission from both the top and bottom surfaces of inclined flared disks (e.g., de Gregorio-Monsalvo *et al.*, 2013). Similarly, observations of edge on disks can give a direct measure of the gas temperature as a function of radius and height (Dutrey *et al.*, 2017). Other molecular lines, aside from CO, can be used to constrain the gas temperature, for example, multiple lines of $CH_3CN$ have been

used to determine the temperature the $CH_3CN$ emitting layer in the TW Hya disk (Loomis *et al.*, 2018a).

The temperature of the disk can be further constrained by locating key molecular snowlines. The CO midplane snowline in disks is difficult to locate due to the high optical depth of the more abundant CO isotopologues and the vertical temperature gradient of the disk. The CO snowline can be determined directly by observing less abundant, optically thin, CO isotopologues, or by detecting molecules that, due to chemistry, peak in abundance at a location related to the snowline, e.g., $N_2H^+$ and $DCO^+$.

$DCO^+$ is the deuterated form of $HCO^+$ and deuterium chemistry is active in the cold ($< 20$ K), dense ($> 10^6$ cm$^{-3}$) midplane of disks (i.e., near the CO snowline). This results in an increase in the D/H ratio in molecules in the disk due to chemical fractionation:

$$H_3{}^+ + HD \rightleftharpoons H_2D^+ + H_2 + 232 \text{ K}.$$

The elemental D/H ratio is $\approx 10^{-5}$ but at low temperatures the forward reaction dominates. This also leads to an enhancement of deuterium in heavier molecules, e.g.,

$$H_2D^+ + CO \rightarrow DCO^+ + H_2.$$

In dark clouds and disks the observed $DCO^+/HCO^+$ ratios are high $\approx 10^{-2}$, representative of that measured in comets (van Dishoeck *et al.*, 2003). A measure of the level of deuteration of a species can inform on the thermal history of the material which is important as an open question is whether or not cometary ices are inherited from the parent cloud. Similarly, carbon and nitrogen bearing species can also undergo chemical fractionation. This is the preferential transfer of a heavier isotope into a molecule under certain conditions. Current models

primarily focus on $HCO^+$, HCN, and CN and the $^{13}C$ and $^{15}N$ isotopes (Visser *et al.*, 2018; Woods & Willacy, 2009).

### 1.5.3 Dust sub-structure

From the first long baseline ALMA observations of HL Tau it was clear that the radial distribution of dust in disks is likely not smooth (ALMA Partnership *et al.*, 2015). Concentric rings of dust are by far the most common features observed (Andrews *et al.*, 2018a; Long *et al.*, 2018b). Azimuthally asymmetric dust structures are also observed including horse-shoe shaped dust distributions and spirals (e.g; Cazzoletti *et al.*, 2018a; Huang *et al.*, 2018b; Pérez *et al.*, 2016; van der Marel *et al.*, 2013). Figure 1.7 shows recent high spatial resolution ($\approx$ 5 au) 1 mm continuum observations from a survey of nearby protoplanetary disks. The most popular interpretation for these dust structures are planet-disk interactions (Zhang *et al.*, 2018) and this will be discussed further in Section 1.6.

### 1.5.4 Molecular sub-structure

Significantly less detailed sub-structure has been observed in the molecular gas in disks (see Figure 1.8). This is partly due to the longer observing times required to achieve the same spatial resolution and signal-to-noise ratio as the continuum observations, but it is also not expected than the gas and millimetre-sized grains will follow the exact same radial structures. For example, in general the CO gas disks are more radially extended than millimetre dust and this can be explained by radial drift of the millimetre sized grains (Birnstiel *et al.*, 2010).

Gas cavities in the inner disk associated with dust cavities have been resolved in CO isotopologue emission in a number of disks (van der Marel *et al.*, 2015, 2016). Gas density perturbations associated with dust rings $\sim$ 100's of au from the central star are less commonly observed. Examples have been seen with

ALMA in the HD 163296, HD 169142 and AS 209 protoplanetary disks (Isella *et al.* 2016, Fedele *et al.* 2017, Favre *et al.* 2019) where the $^{12}$CO, $^{13}$CO and C$^{18}$O line observations do not follow the exact same radial profiles as the dust, but there is a change in slope of these line intensity profiles that coincides with the location of the dark dust rings. CO isotopologues are a good proxy for total gas density in the disk but only if the CO/$H_2$ ratio is radially constant across the disk, and recent work shows that this may not be the case (Miotello *et al.*, 2018; Nomura *et al.*, 2016; Zhang *et al.*, 2019).

Although CO isotopologues are the most common tracers of the molecular gas in disks, it is beneficial to observe lines from other molecules to gain more information about the physical and chemical conditions of the gas. Species other than CO can be more powerful tracers of physical conditions because the abundances

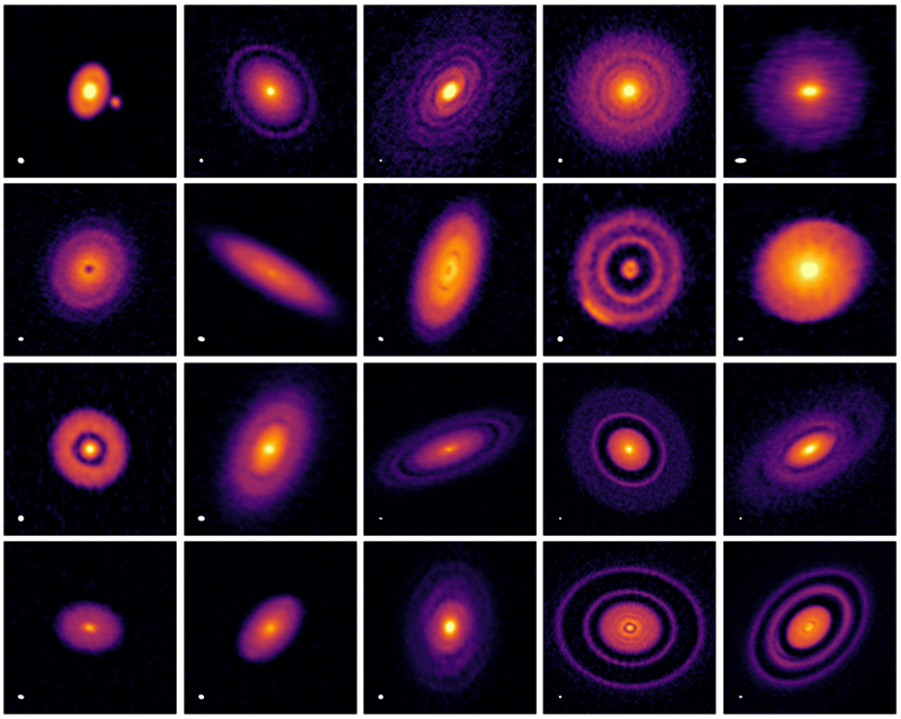

Figure 1.7: ALMA Band 7 continuum emission at $\approx$ 5 au resolution of 20 nearby protoplanetary disks (Andrews *et al.*, 2018a).

are more sensitive to changes in the disk's physical conditions. For most of the disk, the chemistry of CO can be described simply by freeze out and photodissociation, whereas other species' abundances are more dependent on the, e.g., gas number density and the UV and X-ray irradiation. Chemical modelling is required to determine whether or not molecular structures can be linked directly to a change in the total gas surface density. Radial variations in CS emission have been shown to trace a decrease in gas surface density associated with a dust gap in the TW Hya disk (Teague *et al.*, 2017). In comparison, the rings of CN detected in the disks arise naturally without any underlying ringed dust or gas structure (Cazzoletti *et al.*, 2018b). The ringed CN abundance distribution in

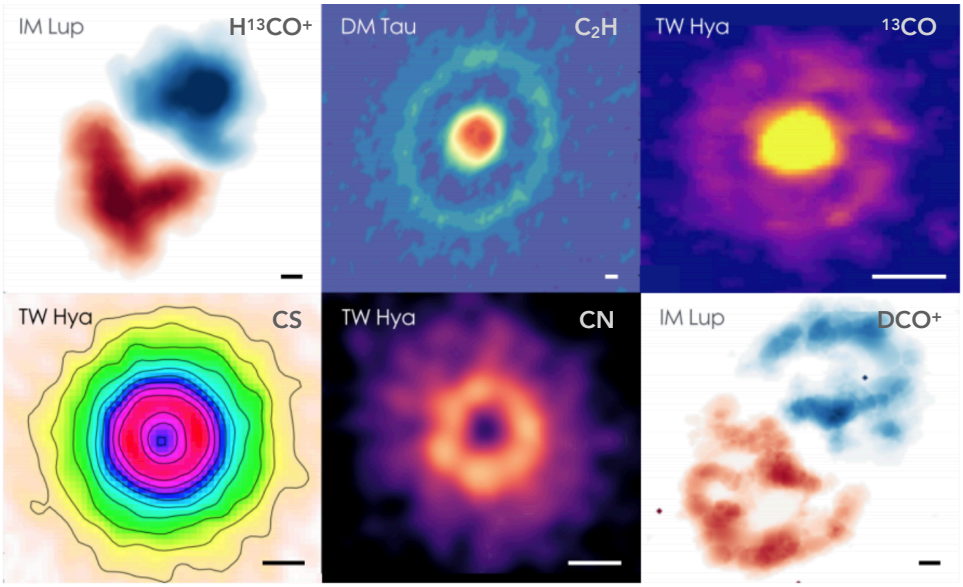


Figure 1.8: Variety of molecule line detections in different disks (Bergin & Cleeves, 2018): (a) IM Lup $H^{13}CO^+$ (Öberg et al. 2015) (b) DM Tau $C_2H$ (Bergin et al. 2016) (c) TW Hya $^{13}CO$ (Schwarz et al. 2016) (d) TW Hya CN (Teague et al. 2016) (e) TW Hya $N_2H^+$ (Qi et al. 2013) (f) IM Lup $DCO^+$ (Oberg et al. 2015.) All colour scales represent the intensity of the line emission but IM Lup has been coloured red and blue to show the regions of the disk where the line emission is red and blue shifted due to the Keplerian shear.

disks is a result of the the impinging UV flux and the flaring angle of the disk surface (Cazzoletti *et al.*, 2018b). Similarly, rings of $C_2H$ and $C_3H_2$ in TW Hya are formed due to UV irradiation and a high C/O ratio in the disk atmosphere (Bergin *et al.*, 2016). Additionally, in the outer gas disk ALMA has detected rings of molecular emission at the edge of the millimetre dust disk, beyond the CO snowline, that can be explained via the non-thermal desorption of CO (Öberg *et al.*, 2015).

Molecular rings of $N_2H^+$ and $DCO^+$ are associated with the CO snowline in disks. $N_2H^+$ is the most robust chemical tracer of the CO snowline due to the anti-correlation between gas phase CO and $N_2H^+$. $N_2H^+$ forms via this reaction:

$$N_2H + H_3{}^+ \rightarrow N_2H^+ + H_2$$

but when CO is present in the gas phase these competing reactions dominate:

$$CO + H_3{}^+ \rightarrow HCO^+ + H_2$$

$$CO + N_2H^+ \rightarrow HCO^+ + N_2$$

Therefore, the location of the CO snowline can be inferred from the presence of ringed $N_2H^+$ emission (TW Hya; Qi *et al.* 2013b and HD 163296; Qi *et al.* 2015). However, the exact location of an $N_2H^+$ ring does not necessarily correspond to directly to the CO snowline location. Chemical models are required to properly interpret the data and $N_2H^+$ line ratios can be used to constrain the emitting gas temperature to see if indeed the gas is tracing the midplane or is optically thick and tracing the warm molecular layer (Qi *et al.*, 2019; Schwarz *et al.*, 2019; van 't Hoff *et al.*, 2017).

### 1.5.5 Disk dispersal

Disk winds can be traced via the velocity profiles of the atomic/molecular gas. Most evidence for disk winds has been seen in blue-shifted line profiles of forbidden lines [O I] and [Ne II] (e.g., Pascucci *et al.*, 2011a). With ALMA there is evidence for a slow $\approx 3$ km s$^{-1}$ disk wind traced in CO isotopologue emission from the T Tauri source DG Tauri (Güdel *et al.*, 2018). Similarly, there is evidence for a radiatively driven disk wind from the edges of the IM Lup disk (Haworth *et al.*, 2017). There is a signature of a rotating MHD wind in molecular line emission from SiO, SO and $SO_2$ emission from a young Class 0 source (Tabone *et al.*, 2017). With ALMA there also is evidence for a rotating disk wind traced in CO but whether or not this is an MHD driven wind is unclear (Klaassen *et al.*, 2013a). The lifetime of the disk and rate of dispersal sets constraints on the timescale and the material available in the disk for planet formation. Directly observing disk dispersal is; therefore, of great interest and importance for understanding planet formation.

## 1.6 Signatures of planets in disks

The observed structures in disks have been proposed to signify planet formation where the apparent gaps and asymmetries are the result of dynamical clearing and gravitational interactions with forming planets (e.g., Zhu *et al.*, 2011). Theoretical simulations of planets in disks show that a planet in a disk will create sub-structures in both the dust and gas. The planet will launch spiral density waves in the disk and will carve out a gap if massive enough. These spirals arise to mediate the exchange of angular momentum between the planet and the disk and can cause orbital migration of the planet. This occurs when the torques from the inner and outer disk are unequal. The direction and timescale of this migration depends on the planet's mass and the physical conditions of the disk

(Kley & Nelson, 2012).

Gas and dust depleted cavities are; therefore, the clearest indirect signposts of giant planet formation. The presence of a massive planet in a disk causes a pressure maximum at the outer edge of the gap it has created (Dong *et al.*, 2015; Pinilla *et al.*, 2012). This pressure maximum will halt the inward radial drift of the mm-sized dust resulting in the formation of a ring of mm-sized dust. Dust gaps are the most common features detected in disks but there are only a few cases where corresponding dust and gas gaps have been detected (e.g., Isella *et al.*, 2016). This is likely due to different sizes of gaps formed in the different tracers. The edge of the gap traced in the micron-sized dust and in the gas are located much closer to the perturbing planet as these particles are less efficiently trapped (de Juan Ovelar *et al.*, 2013). There are analytical relationships to determine the mass of the forming planet from the gap width and depth (e.g., Dong & Fung, 2017; Kanagawa *et al.*, 2016; Rosotti *et al.*, 2016). However, these relationships are limited by the spatial resolution of the observations and the assumption for the disk viscosity. Grids of 2D hydrodynamic simulations of both the gas and dust in a disk with varying $\alpha$, scale height and planet masses can explain all of the structures seen in the recent high angular resolution dust observations (Figure 1.7 and Zhang *et al.*, 2018). Intuitively, one gap would correspond to one planet but models show that one super-Earth mass planet, in a low viscosity disk ($\alpha \leq 10^{-4}$), can induce multiple gaps in the mm-dust but the features in the gas are an order of magnitude smaller (Dong *et al.*, 2018).

The lack of a clear trend in the location and width of the dust ring with host star properties favours planets as the likely explanation (Huang *et al.*, 2018a). If the rings were due to an intrinsic property of the host star, e.g., luminosity, there should be a correlation between ring positions and spectral type of which there is not. But, with the lack of planet candidates detected in gaps other

mechanisms need to be considered. Rings in the dust distribution have been shown to arise at the condensation fronts of volatile species in the disk due to either increased pebble growth or dust sintering (e.g., Okuzumi *et al.*, 2016; Zhang *et al.*, 2015). Additionally, multiple gaps and rings have been shown to form in magneto-hydrodynamic simulations (e.g., Flock *et al.*, 2015; Pinilla *et al.*, 2016; Ruge *et al.*, 2016).

Non-asymmetric features were actually the first dust structures observed in disks (van der Marel *et al.*, 2013). These horseshoe shaped dust traps can form via the Rossby Wave Instability (RWI) in a disk where self-gravity is negligible. An axisymmetric bump in the disk surface density induces a non-axisymmetric vortice (Lovelace & Romanova, 2014). A change in the radial gas density, i.e., a gap due to a forming planet or a massive companion, or, a change in viscosity at the dead zone can create the conditions for a vortex to form. If not excited by planets or companions, spiral asymmetries can arise due to gravitational instability or flyby encounters with unbound objects (Cuello *et al.*, 2019; Hall *et al.*, 2018).

The gas kinematics are encoded in the molecular line emission. The gravitational interactions between a planet and its disk will perturb the local velocity field. Local deviations from Keplerian motions have been detected in multiple disks and can be linked to Jupiter mass planets (see Figure 1.9; Pinte *et al.*, 2018, 2019; Teague *et al.*, 2018). Also a local increase in line width can be attributed to a forming planet (Dong *et al.*, 2019). Larger scale super-Keplerian velocities have been measured in the inner regions ($< 100$ au) in a few disks and these can be explained by warped inner disks or fast radial flows (e.g., Casassus *et al.*, 2013; Loomis *et al.*, 2017; Walsh *et al.*, 2017). Both of these are due to planet-disk interactions. A forming planet is also expected to alter the chemical composition of the disk locally via heating due to its inherent luminosity; therefore, there

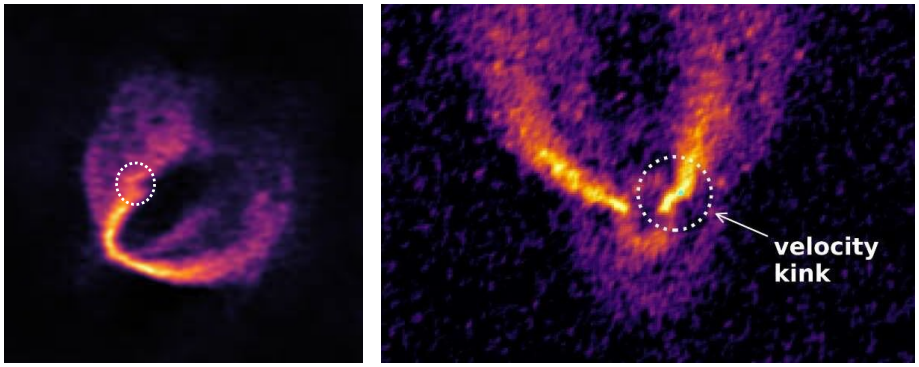


Figure 1.9: Single channels maps showing the local deviations in $^{12}$CO emission (left) and $^{13}$CO (right) from the Keplerian velocity pattern in the HD 163296 (left) and HD 97048 (right) disks (Pinte *et al.*, 2018, 2019).

is the potential for planets to be detected from observed chemical asymmetries (Cleeves *et al.*, 2015).

Planets will accrete material from the disk though their own disks and these are another potential observable in both the gas and dust (Perez *et al.*, 2015; Szulágyi *et al.*, 2016). These circumplanetary disks (CPDs) regulate the growth of the planet and are the potential formation sites for moons. The most convincing detection of a CPD is in the PDS 70 disk. In this source there is a coincident gap in both the gas and dust disk (Long *et al.*, 2018c) and within this gap VLT and Gemini observations detected a point source, PDS 70b (Keppler *et al.*, 2018). Follow up observations detected H$\alpha$ emission from PDS 70b indicative of ongoing accretion and ALMA millimetre continuum emission associated with the point source (Keppler *et al.*, 2019; Wagner *et al.*, 2018). Similarly, recent ALMA observations of TW Hya have detected a compact au-scale feature in the continuum emission that is potentially a CPD in the outer disk (Tsukagoshi *et al.*, 2019).

Overall, ALMA observations have given unprecedented insight into the formation of planets. The observations and modelling of the millimetre dust have

given us valuable information on disk properties but the same degree of importance also needs to be given to the molecular lines. Different molecules give vital diagnostics on the physical and chemical structure as well as the kinematics.

## 1.7 This thesis

This thesis presents a study of molecular line emission from planet-forming disks around young stars. Chapter 1 provided an overview of the formation, evolution and structure of protoplanetary disks.

Chapter 2 outlines the different methods in this thesis including: interferometry with ALMA, chemical modelling and line radiative transfer. This thesis uses both ALMA observations of disks and chemical models with the aim of constraining some of the physical and chemical conditions associated with giant planet formation.

Chapter 3 presents the first detections of $^{13}C^{17}O$ in protoplanetary disks. These data are used to constrain the total gas mass of the HD 163296 and HL Tau disks. In both cases the detection of $^{13}C^{17}O$ shows model independently that the disk gas masses have been underestimated from existing $C^{18}O$ observations by a factor of 2 to 10 times. These updated mass measurements provide insight into the gravitational stability of each star-disk system.

Chapter 4 presents the first detection of $H^{13}CO^+$ and $HC^{15}N$ in the HD 97048 disk. In particular, this work looks at the radial abundance distribution of the $H^{12}CO^+$ and $H^{13}CO^+$. The observed ratio is low and various models are investigated to see if chemistry alone can explain this or if modifications to the underlying disk gas density or temperature structure are required. This analysis highlights the need to consider isotope-fractionation chemistry and suggests that in the outer disk the gas temperature is much colder than previously thought.

Chapter 5 presents the first detection of SO in the HD 100546 disk. In disks S

bearing volatiles are observed to be depleted, but, in other environments SO is a unique tracer of shocks. The spatial distribution of the emission is very compact and the kinematics are not consistent with solely Keplerian rotation. There is significant blue-shifted emission that is not spatially coincident with the blue-shifted disk emission. Therefore, it is proposed that the SO is tracing a disk wind or a circumplanetary disk given that SO is a known shock tracer.

Chapter 6 presents an analysis of the Si and S-bearing volatiles in the HD 97048 and HD 100546 disks. Like sulphur, silicon bearing volatiles are also observed to be significantly depleted in disks, similar to dark clouds. Multiple lines of SO and SiO are targeted towards HD 100546 and HD 97048. Upper limits on the disk averaged column densities are derived for the non-detections of the SiO and SO lines. These values are compared to the results from disk specific chemical models. With this analysis the different reservoirs of volatile silicon and sulphur can be constrained in each disk and reveals that SiS, an as-yet undetected disk molecule, as a significant source of both.

Chapter 7 provides a summary of this thesis, details plans future projects and shows how the work presented here informs the wider protoplanetary disk, planet formation and exoplanet communities.

# Chapter 2

# Methods

## 2.1 Observations with ALMA

Protoplanetary disks subtend a small angular scale on the sky and therefore, in most cases, we need subarcsecond resolution observations in order to spatially resolve them. The mm-sized dust in disks emits radiation at predominately millimetre wavelengths and the rotational transitions of the simple molecules in disks, e.g., CO, $HCO^+$, are also at sub-millimetre wavelengths. The angular resolution, $\theta$, of a telescope is given by:

$$\theta = \frac{\lambda}{D}$$

where $\lambda$ is the observing wavelength and $D$ is the size of the aperture. Single dish telescopes which would meet resolution requirements at sub-millimetre wavelengths to resolve protoplanetary disks are simply too big to construct. The alternative is to synthesise a large continuous aperture telescope by summing separated pairs of smaller telescopes. This is this the principle behind interferometers such as ALMA.

ALMA is the product of an international collaboration between Europe, the United States, Canada, Japan, South Korea, Taiwan, and Chile. This interferometer is located on the Chajnantor plain of the Chilean Andes where the weather

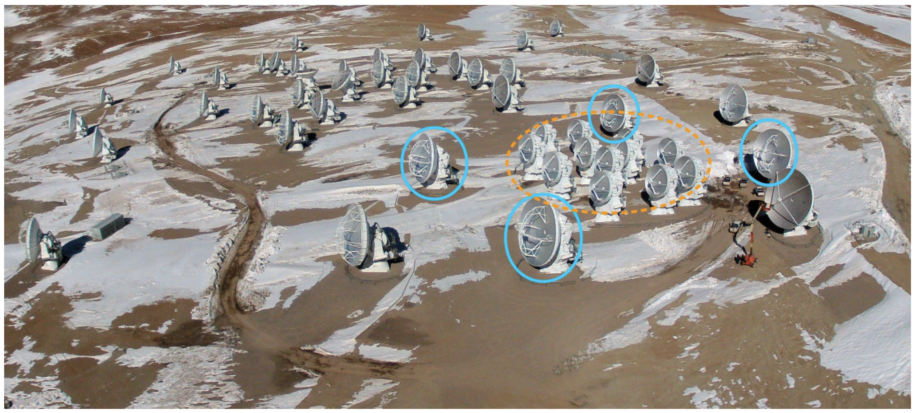

Figure 2.1: The 66 ALMA antenna in a compact configuration. The Total Power array is highlighted in blue and the Atacama Compact Array in orange.

conditions are very dry, reducing the effect of absorption from the atmospheric water vapor. Figure 2.1 shows the 66 antenna that make up ALMA. There are 50 12 m antennas which make up the main array and these are complemented by the 12 7 m antennas in the Atacama Compact Array (ACA) and the 4 12 m antennas in the total Power (TP) array. The following section covers the basics of interferometry and the general steps in working with ALMA data (Remijan, 2019).

### 2.1.1 The basics of interferometry

For a single dish antenna the brightness (specific intensity) is defined as:

$$I_\nu = \frac{\delta P}{\delta\Omega\ \delta A\ \delta\nu}$$

where $\delta P$ is the electromagnetic power received to a surface area $\delta A$ over a given bandwidth $\delta\nu$ from a particular solid angle $\delta\Omega$ on the sky. ALMA can receive signals from 8.5 to 0.32 mm ($35 - 950$ GHz) (Remijan, 2019) and this is divided into different different observing bands (see Table 2.1). The total flux density is

Table 2.1: ALMA observing bands

| Band | Wavelength (mm) | Frequency (GHz) |
|---|---|---|
| 3 | 2.6 - 3.6 | 84 - 116 |
| 4 | 1.8 - 2.4 | 125 - 163 |
| 5 | 1.4 - 1.8 | 163 - 211 |
| 6 | 1.1 - 1.4 | 211 - 275 |
| 7 | 0.8 - 1.1 | 275 - 373 |
| 8 | 0.6 - 0.8 | 385 - 500 |
| 9 | 0.4 - 0.5 | 602 - 720 |
| 10 | 0.3 - 0.4 | 787 - 950 |

given by:

$$S_\nu = \int I_\nu d\nu.$$

The units of $S_\nu$ are $\mathrm{Wm}^{-2}$ $\mathrm{Hz}^{-1}$ but as the flux density received is typically very low the convention is to use Janskys where 1 Jy $\equiv 10^{-26}$ $\mathrm{Wm}^{-2}$ $\mathrm{Hz}^{-1}$.

The antenna has a parabolic surface and the total power received is the sum of the focused radiation. This power response has a Gaussian-like central component with a full width half maximum that is called the primary beam. This determines the field of view and is given by:

$$\text{Primary Beam} = 1.03 \times \frac{\lambda}{D}$$

where D is the diameter of the dish. Beyond this central maximum there are successive lobes of constructive and destructive interference. The amplitude of these side-lobes is typically only an order of a few percent of the central component.

In aperture synthesis the signals from multiple antennas are combined. For an ideal 1-D two-antenna interferometer (A1 and A2) this works as follows. When A1 and A2 both point towards some source S the radiation will reach A2 before A1. To account for this the electrical signal collected at A2 has an artificial delay applied. The voltage response from A1 can therefore be expressed as the response

from A2 with a delay factor:

$$\mathrm{v}_1 = \mathrm{v}_2 \; e^{2\pi i(ul)}$$

where $u$ is the projected baseline and $l$ is the spatial coordinate on the sky. Expanding this 1-D example to 2-D introduces equivalent terms for $u$ and $l$ in the second dimension, $v$ and $m$. This results in:

$$\mathrm{v}_1 = \mathrm{v}_2 \; e^{2\pi i(ul+vm)}.$$

The purpose of the correlator is to multiply and average these incoming signals. Since $\mathrm{v}^2 \propto P$ and $P \propto I$ this becomes:

$$\langle \mathrm{v}_1 \mathrm{v}_2 \rangle \sim \int\int I_\nu(lm) e^{2\pi i(ul+vm)} dldm$$

where the intensity at point $(l, m)$ on the sky is $I_\nu(l, m)$. The correlator therefore is measuring a complex visibility:

$$V(u, v) = \int\int I_\nu(l, m) e^{2\pi i(ul+vm)} dldm.$$

This is a complex number that is defined by an amplitude and a phase which describes the sky brightness at a position relative to the phase centre given the spatial frequencies $u$ and $v$. This visibility is the Fourier transform of the sky brightness distribution, therefore the sky brightness distribution can be recovered from measuring the complex visibilities with different spatial frequencies. Each pair of antennas results in one point in the $(u, v)$ plane defined by their separation distance, or baseline. It is impossible to observe all of the potential points in the $(u, v)$ plane therefore the $uv$-coverage limits the final image fidelity - the accuracy of the reconstruction of the sky brightness distribution. $N$ antennas results in $N(N-1)/2$ different baselines, therefore the 50 12 m array has 1225 different

baselines.

The resolution of the interferometer is limited by the longest baseline:

$$\theta_{res} = \frac{\lambda}{L_{max}}.$$

The highest angular resolution achievable with ALMA at at 345 GHz is 0.″01. Therefore for a disk at 100 pc this is equivalent to 1 au. The largest recoverable angular scale is limited by the shortest baseline:

$$\theta_{LAS} = 0.6 \times \frac{\lambda}{L_{min}}.$$

For example, the shortest baseline in the Cycle 0 observations from Walsh *et al.* (2014a), also presented in Chapter 5, is 21 m corresponding to a largest recoverable angular scale of 4.″5 at 345 GHz (after converting radians to arc-seconds). The ALMA antennas can be moved into a range of compact and extended configurations in order to sample different maximum (15 km) and minimum (15 m) baselines.

### 2.1.2 Working with ALMA data

The measured visibilities need to be calibrated before being Fourier inverted. To work with these data we use the Common Astronomy Software Applications package (CASA; McMullin *et al.*, 2007a). The calibrators, chosen are sources of bright, constant radiation with a well known position, e.g., Titan. The primary calibration of the data is executed by the ALMA staff. They check though the data and will flag any potential issues. Due to the high sensitivity of ALMA which leads to high signal-to-noise observations a self-calibration for the phase and amplitude is then executed by the project PI/team (Brogan *et al.*, 2018). In this step the calibrations are applied to the continuum data only and then the solutions are applied to the line data which are then continuum subtracted.

The visibilities are then Fourier inverted and deconvolved in order create an image. This deconvolution is in order to suppress the side-lobes of emission corrupting the image fidelity. The typical algorithm used for this is CLEAN (Högbom, 1974) and this is a built in function in CASA. CLEAN weighs all of the baselines equally but there are also options to omit particular baselines using a *uv* taper or to give the longer/shorter baselines higher significance in order to improve the science products (Briggs, 1995). The use of a taper or a particular weighting scheme is generally done to optimise both the signal-to-noise ratio and the angular resolution of the image products.

Continuum observations result in a 2D map of the intensity that has been integrated over the bandwidth of the observations. For the line data an image cube (see Figure 2.2), or the channel maps, are the native form of the data. The data cube can then be collapsed to make different moment maps including: integrated intensity, intensity-weighted velocity, velocity dispersion, and peak intensity. Spectra can also be extracting using different apertures, e.g., elliptical, Keplerian mask or pixel.

## 2.2 Chemical modelling

From observations of disks, and in other astrophysical environments, it is clear that different molecules have different abundance distributions. In order to connect the observed column densities to the physical conditions of the environment we need chemical models. The chemical model used in this thesis was first presented in Walsh *et al.* (2010) and Walsh *et al.* (2012). The input parameters are the 2D disk physical structure, radiation field, initial atomic/molecular abundances, and the chemical reactions and their respective reaction rates. The model used in this work is a single point model and this means that the chemistry is solved in time at each point independently in the disk, given the static physical

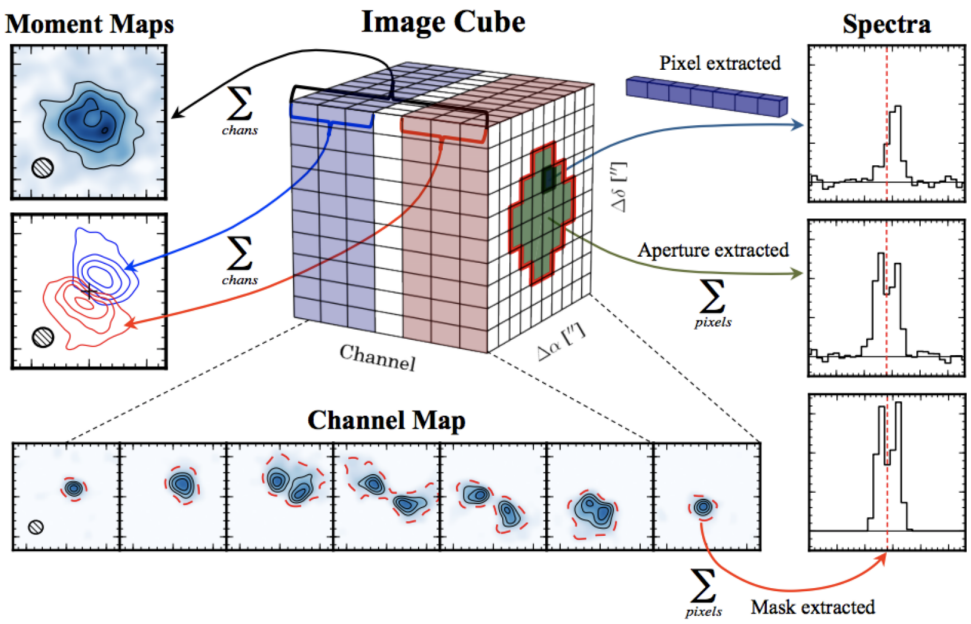


Figure 2.2: A diagram showing the different ways to view an image cube. Counter-clockwise from the top-left: Velocity-integrated moment maps, made by integrating slices of the cube along the frequency axis; channel maps, where each panel corresponds to a channel of the cube; spectra, generated from top to bottom from a single pixel, integrated over an aperture, and integrated using a matched spatio-kinematic mask (dashed red contours in channel maps). The synthesized beam is shown in the lower left of the moment and channel maps (Loomis *et al.*, 2018b).

conditions, temperature and density, and the radiation field.

The initial abundances used in disk models can fall into two categories: atomic or molecular. Molecular abundances assumes that all of the disk material has the same composition as in dark clouds. Atomic abundances assumes that during star (and disk) formation that the increase in temperature and radiation is such that all of the molecular material is broken down into its respective atomic constituents. The reality is likely a mix of both scenarios. Eistrup *et al.* (2016) show that these two different initial conditions do affect the resulting atomic and molecular abundances therefore it is something to consider when setting up a model.

The different types of chemical reactions can be divided into four categories: bond formation, bond destruction, bond rearrangement and ionization. Chemistry in space is not in thermal equilibrium therefore to calculate abundances models use chemical kinetics. This relies on knowing the rate at which a particular reaction occurs at a given temperature ($T$). Table 2.2 summarises some of the types of reactions and their typical reaction rates.

Reaction rates for two body reactions are given as:

$$k_{ij} = \alpha \ (T/300)^{\beta} e^{(-\gamma/T)} \quad \mathrm{cm}^3 \ \mathrm{s}^{-1}.$$

This is the Arrhenius form of the rate equation where $\alpha$ is the pre-exponential factor, $\beta$ determines the temperature dependence of the reaction, and $\gamma$ is the activation energy of the reaction in K. These are all measured experimentally and the two main databases are the UMIST Database for Astrochemistry[1] (McElroy *et al.*, 2013) and the KInetic Database for Astrochemistry[2] (KIDA) (Wakelam *et al.*, 2012).

[1]UMIST: http://udfa.ajmarkwick.net/
[2]KIDA: http://kida.obs.u-bordeaux1.fr/

Table 2.2: Types of chemical reactions with typical rate coefficients (adapted from van Dishoeck (2014)).

| Process | | Rate Coefficient ($cm^3$ $s^{-1}$) |
|---|---|---|
| Bond formation | | |
| Radiative association | $X + Y \rightarrow XY + h\nu$ | $10^{-17} - 10^{-14}$ |
| Grain surface formation | X + Y:gr $\rightarrow$ XY + gr | $\sim 10^{-17}$ |
| Associative detachment | $X^- + Y \rightarrow XY + e^-$ | $\sim 10^{-9}$ |
| Bond destruction | | |
| Photodissociation | $XY + h\nu \rightarrow X + Y$ | $10^{-10} - 10^{-8}$ |
| Dissociative recombination | $XY^+ + e^- \rightarrow X + Y$ | $\sim 10^{-9}$ |
| Collisional dissociation | XY + M $\rightarrow$ X + Y + M | $10^{-26}$ |
| Bond restructuring | | |
| Neutral-neutral | X + YZ $\rightarrow$ XY + Z | $10^{-11} - 10^{-9}$ |
| Charge transfer | $X^+ + YZ \rightarrow X + YZ^+$ | $10^{-9}$ |
| Ion-molecule exchange | $X^+ + YZ \rightarrow XY^+ + Z$ | $10^{-9} - 10^{-8}$ |
| Unchanged bond | | |
| Photoionization | $XY + h\nu \rightarrow XY^+ + e^-$ | $10^{-18} - 10^{-12}$ |
| Ionization by CRP | $XY + h\nu \rightarrow XY^+ + e^-$ | $\sim 10^{-17}$ |

For the photo-induced reactions, photo-ionisation and photo-dissociation, these rates depend on the thermal and non-thermal UV spectrum from the star. Similarly, X-ray ionization is dependent on the stellar X-ray flux. X-rays provide a significant source of ionisation in the denser regions of disks and in particular ionize He. This cation can then go on to destroy species such as CO. Deeper in the disk cosmic rays are the primary ionization source. The galactic cosmic ray ionisation rate is generally taken as $5 \times 10^{17}$ $s^{-1}$ but this is potentially reduced in disks by up to 2 orders of magnitude due to the exclusion of cosmic rays by stellar winds and magnetic fields (Cleeves *et al.*, 2013). An important reaction in molecular clouds and disk midplanes is cosmic ray induced photo-ionisation. This provides a secondary source of ionisation in dense regions where the material is shielded from other sources of ionising radiation.

Another key determining factor in abundance distributions is phase changes. The rate of freeze-out, or accretion, onto the dust grains $k_{acc}$ and the rate of

desorption $k_{des}$ are given by:

$$k_{acc} = \langle v \rangle \ \sigma_{grain} \ n_{grain} \ S \quad \mathrm{s}^{-1}$$

and

$$k_{des} = \nu_0 \exp(-E_b/T_d) \quad \mathrm{s}^{-1},$$

where $\langle v \rangle$ is the mean thermal velocity of molecules, $\sigma_{grain}$ is the surface area per dust grain, $n_{grain}$ is the number of disk grains and $S$ is the sticking coefficient ($\approx 1$ for CO), $\nu_0$ is the characteristic vibrational frequency of an adsorbed species in its potential well, $E_b$ is the binding energy, $T_d$ is the dust grain temperature.

Taking all of the above processes into account, the rate of change of the abundance, $n(i)$, of a particular species $i$ with respect to time is calculated as follows:

$$\frac{\mathrm{d}n_i}{\mathrm{d}t} = \sum_{j,k} k_{jk} n_j n_k + \sum_l k_l n_l - n_i \left[ \sum_m k_{im} n_m + \sum_n k_n \right] + k_{des} n_{i,s} - k_{acc} n_i = 0.$$

The first two terms are the sum over all of two-body reactions and photo-processes and/or cosmic-ray processes that result in the formation of species $i$. The bracketed terms sum over all of the potential destruction reactions for species $i$. The last two terms describe accretion and desorption of $i$. For some cations in the disk, e.g., $HCO^+$ and $N_2H^+$, there are only a few reactions to consider and thus the chemistry can be solved analytically (Aikawa *et al.*, 2015). In most cases though all of these coupled ODEs need to be solved numerically. In dark clouds and the cold midplane of disks grain surface reactions also need to be considered. These facilitate the formation of complex organic molecules (COMs) (Hasegawa *et al.*, 1992; Walsh *et al.*, 2014b). More complex chemical models be built from the same framework as described above. For example an intuitive next step is to modifying the physical conditions at each time step (e.g.; Drozdovskaya *et al.*,

2015; Eistrup *et al.*, 2018) or to include dust dynamics (Booth & Ilee, 2019).

## 2.3 Radiative transfer

Radiative transfer allows for the comparison of observations to models. The theory behind this, for both dust and gas modelling, are described clearly in Pinte (2015), Dionatos (2015) and Kamp (2015) and are summarised in the following section.

### 2.3.1 Molecular excitation

Unlike dust which emits radiation over a continuum, molecules emit photons of discrete energies. Molecules can undergo rotational, vibrational or electronic transitions (Hollas, 2004). The frequency range covered by ALMA is most applicable to the lowest energy transitions, the pure rotational transitions. In the simplest case, for the closed shell diatomic molecules, e.g., CO, in the rigid rotor approximation the energy of a transition, $E_r$, is defined by the rotational quantum number $J$ and moment of inertia $I$:

$$E_r = \frac{h^2}{8\pi^2 cI} J(J+1).$$

Since $E_r \ \alpha \ I^{-1}$, heavier molecules will have a lower frequency and more closely spaced energy levels. For a transition to be allowed the molecule must have a permanent dipole and follow the selection rule that $\Delta J = \pm 1$. This means that homonuclear molecules such as $H_2$ have no allowed pure rotational transitions. Instead, $H_2$ undergoes electric quadrapole transitions where $\Delta J = \pm 2$. Similarity, spherical top molecules, e.g., $CH_4$, have no purely rotational spectrum. The unpaired electron(s) in radicals, e.g., SO, lead to substructure within these rotational transitions (Lique *et al.*, 2006). There are fine structure lines to each rotational transition due to spin-orbital coupling and these follow the selection

rules $\Delta J = \pm 1$ and $\Delta F = 0, \pm 1$. For, e.g., HCN, there are hyperfine structure lines due to the interaction between the nuclei and internally generated magnetic and electric fields. Non-linear molecules, e.g., $NH_3$ and $H_2O$, have more complex spectra. $NH_3$ and $H_2O$ are called symmetric and asymmetric tops and instead of just one quantum number, two and three are needed to describe the total angular momentum of the molecule, respectively.

The strength of a molecular line depends on the level populations, i.e., the number of molecules in that particular energy state. In the case of local thermodynamic equilibrium, LTE, then the level populations are given by the Boltzmann equation and depend on the excitation temperature where $T_{\rm kin} = T_{\rm ex}$ and:

$$\frac{n_i}{n_j} = \frac{g_i}{g_j} \exp -\Delta E/kT_{ex}$$

where $g_i$ and $g_j$ are the degeneracies of each state $n_i$ and $n_j$ and $\Delta E$ is their difference in transition energy.

The gas is only in LTE if collisions dominate the de-excitation and excitation of the gas. For this to be the case the density must be greater than the critical density. The critical density is determined by:

$$n_{cr} = \frac{A_{ij}}{\sum\limits_{j'<i} C_{ij'}}$$

where $A_{ij}$ and $C_{ij}$ are the Einstein A and collisional rates coefficients of the transition. These data are available from the Leiden Atomic and Molecular Database (LAMDA; Schöier *et al.*, 2005)[1]. If the gas in not in LTE then $T_{\rm kin} \neq T_{\rm ex}$ and the full non-LTE statistical equilibrium equation has to be solved. This takes into account both the radiative and collisional processes. Statistical equilibrium is given by:

[1]Leiden Atomic and Molecular Database:https://home.strw.leidenuniv.nl/~moldata/

$$\frac{dn_i}{dt} = \sum_{j>i} n_j \left(A_{ji} + B_{ji} P\left(y_{ji}\right)\right) + \sum_{j<i} n_j B_{ji} P\left(y_{ji}\right) + \sum_{j\neq i} n_j C_{ji}$$
$$- n_i \sum_{j<i} \left(A_{ij} + B_{ij} P\left(v_{ij}\right)\right) - n_i \sum_{j>i} B_{ij} P\left(v_{ij}\right) - n_i \sum_{j\neq i} C_{ij} = 0$$

where $B_{ij}$ and $B_{ji}$ are the rates of stimulated emission and absorption. The first line describes the gain in molecules at a particular energy state ($i$) and the second line describes the loss. This includes spontaneous and stimulated emission from a higher level ($j$) to a lower level ($i$), stimulated absorption from a lower level ($j$) to level ($i$), and all collisional excitation from lower and higher levels to level ($i$). The second line describes the inverse processes.

### 2.3.2 Equation of radiative transfer

The observed and modelled dust and line emission from protoplanetary disks can be described by radiative transfer. This general equation

$$\frac{\mathrm{d}I_\nu(s)}{\mathrm{d}s} = j_\nu(s) - \alpha_\nu(s) I_\nu(s)$$

describes the change in the intensity, $I_\nu(s)$, of light due to emission, $j_\nu$, and absorption, $\alpha_\nu$, along the line of sight, $ds$.

The source function is the ratio of the emission to absorption coefficients and is defined as:

$$S_\nu = \frac{j_\nu}{\alpha_\nu}$$

and the optical depth is given by

$$\tau_\nu = \int_{s1}^{s2} \alpha_\nu(s)\, ds.$$

For $\tau < 1$ emission is considered to be optically thin and for $\tau > 1$ it is optically

thick. Taking the above two relationships the radiative transfer equation can be re-written as:

$$\frac{\mathrm{d}I_\nu(s)}{\mathrm{d}\tau} = S_\nu - I_\nu.$$

The formal solution is given by the integration along the line of sight:

$$I_v(s_2) = I_v(s_1)e^{-\tau_v(s_1,s_2)} + \int_{s_1}^{s_2} j_v(s)e^{-\tau_v(s_1,s_2)}\mathrm{d}s.$$

This equation works on the assumption that the timescales for changes in physical conditions that would change the emission/absorption of light are significantly longer than the light travel time.

For dust modelling, the extinction depends on the density and the cross section:

$$\alpha_\nu = \rho\sigma_\nu$$

and is commonly given as the opacity per unit mass:

$$\kappa_\nu = \alpha_\nu/\rho.$$

If the dust is in thermal equilibrium then the emission is given by

$$j_\nu = \alpha_\nu \; B_\nu(T)$$

where $B_\nu(T)$ is the Planck function.

For molecular lines the equivalent emission and absorption coefficients are given by:

$$\epsilon_\nu^{ij} = \frac{h\nu_{ij}}{4\pi} n_{ij} \; A_{ij} \; \phi_{ij}(\nu),$$

and

$$\alpha_{\nu}^{ij} = \frac{h\nu_{ij}}{4\pi}(n_j B_{ji} - n_i B_{ij})\phi_{ij}(\nu)$$

where $\phi_{ij}$ is the line profile function. The minimum line width is set by the uncertainty principle and this is then broadened by collisions and thermal and/or turbulent motions. In inclined disks, Doppler broadening due to the Keplerian sheer is the dominant line broadening mechanism.

The equation of radiative transfer needs to be solved self-consistently in order to achieve thermal balance between the radiation field and the dust/gas temperaure. The inclusion of dust scattering and optical depth effects can make this computationally expensive.

### 2.3.3 Radiative transfer with LIME

The line radiative transfer calculations in this Thesis are executed using the LIne Modeling Engine[1] (LIME Brinch & Hogerheijde, 2010). LIME is a 3D non-LTE (semi-)Monte Carlo molecular excitation, radiative transfer and ray tracing code.

The inputs to the code are the physical structure, molecular data, and velocity field (assumed to be Keplerian in this instance). The physical structure consists of the gas density, gas and dust temperatures, global gas-to-dust mass ratio and molecular abundance.

LIME is innovative in the way in which the grid is determined. The grid is unstructured and points are chosen from a probability distribution function based on one of the model parameters (e.g., density, molecular abundance). Therefore, the grid has an automatic refinement with the most points in the regions of most interest. The points are then connected via a Delauny Triangulation using QHull (Barber *et al.*, 1996). In 3D this means that four points are connected to form an irregular tetrahedron which contains no points within its volume. Each point

[1]Publicly available at: https://github.com/lime-rt/lime

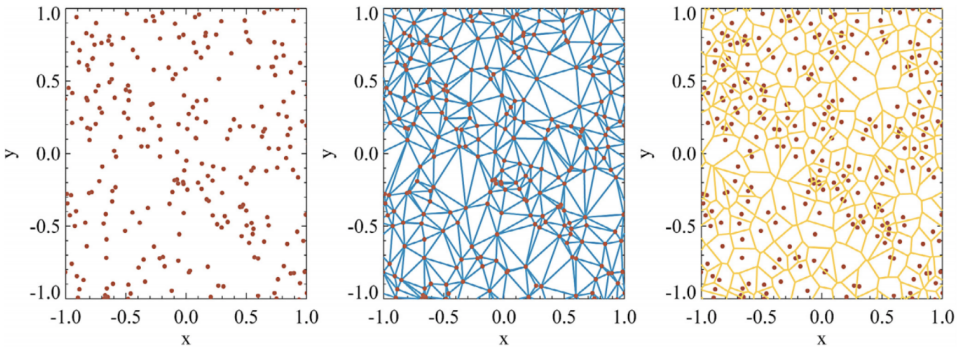


Figure 2.3: Left: a random point distribution. Middle: Delaunay triangulation of the points. Right: the corresponding Voronoi tessellation from Brinch & Hogerheijde 2010).

is connected to $\approx$ 16 other points. Around each point is a Voronoi cell. This is defined as the region surrounding the point which contains all the space that lies closer to that point than any other points. See Figure 2.3 for a visual. Each cell is allocated model parameters which are interpolated from the input files. Photons propagate along the Delauny lines where the subsequent direction at each interface is determined probabilistically. This makes LIME a semi-Monte Carlo code. This is quite efficient as all of the possible paths are predetermined by the grid. At each point the radiative transfer and statistical equilibrium equations are solved iteratively until the level populations converge. The ray tracing step projects the 3D model onto a 2D grid, as defined by the user. The rays travel in straight lines stepping though the Voronoi cells.

The outputs of LIME are the image FITS files of the requested transitions, the level populations and the generated grid. The image is the 2D representation of the sky brightness distribution as would be seen by the observer.

## 2.4 Summary

This Chapter summarises the different methods used in this Thesis. All of the science chapters make use ALMA observations of different molecular lines in disks. In Chapters 3, 4 and 5 LIME is used to make synthetic observations to compare directly to the data. In these Chapters existing 2D disk models are utilised with analytical predictions for the molecular abundances of CO, $HCO^+$ and SO. In Chapter 6 molecular column densities derived from observational fluxes are compared to the results from disk specific chemical models.

# Chapter 3

# $^{13}C^{17}O$ as a tracer of disk gas mass

## 3.1 Introduction

Gas is the dominant mass carrier in disks, hence, measurements of the total gas mass are necessary to determine the planet formation potential of protoplanetary disks, i.e., the mass available to form planets. Observations of rare CO isotopologues are typically used to determine disk gas masses. However, if the line emission is incorrectly assumed to be optically thin this will result in an underestimated disk mass. This Chapter presents the first detections of the rarest stable CO isotopologue, $^{13}C^{17}O$, in protoplanetary disks. The abundance of $^{13}C^{17}O$ is predicted to be $\approx 120,000$ times less than that of the main isotopologue $^{12}C^{16}O$. The two sources, HD 163296 and HL Tau, are two of first disks in which multiple concentric rings of millimeter-sized dust were detected with ALMA and both have been proposed to host forming gas-giant planets (ALMA Partnership *et al.*, 2015; Isella *et al.*, 2016). The newly derived gas masses from the $^{13}C^{17}O$ are compared to existing estimates with $C^{18}O$ and using these masses the gravitational stability or otherwise of the disks is determined.

## 3.2 HD 163296

### 3.2.1 The HD 163296 disk

HD 163296 is a 1.95 $M_\odot$ A0 Vep type pre-main sequence star (Wichittanakom *et al.*, 2020) that is not associated with a young star-forming region (The *et al.*, 1985). The protoplanetary disk around HD 163296 has been well characterised at sub-millimeter wavelengths with both the SMA and ALMA. The most recent high-spatial resolution observations with ALMA at Band 6 ($\approx$ 1.3 mm) and 7 ($\approx$ 1.0 mm) observations show multiple rings in both the continuum and the CO gas emission (e.g. Isella *et al.*, 2016; Notsu *et al.*, 2019, and see Figure 3.1a). There are four proposed $\approx$ 0.5 - 2 $M_J$ planets in this disk inferred from the dust and gas rings, and localised deviations from Keplerian motion in the CO gas kinematics (see Figure 1.9 in Chapter 1: Isella *et al.*, 2016; Liu *et al.*, 2018; Pinte *et al.*, 2018; Teague *et al.*, 2018). Recently, $\approx$ 5 au resolution observations of the continuum emission revealed an additional gap and ring in the inner disk as well as an azimuthal asymmetry in one of the previously detected rings (see Figure 3.1a: Isella *et al.*, 2018). Hence, the proposed planet-induced structures in the HD 163296 disk make it an excellent observational laboratory to study planet formation.

### 3.2.2 Line identification and imaging

HD 163296 was observed by ALMA at Band 7 during Cycle 3 (2015.1.01259.S, PI: S. Notsu). The work presented here began with the self-calibrated measurement set from Notsu *et al.* (2019). The $^{13}C^{17}O$ was initially detected via a matched filter analysis[1] (Loomis *et al.*, 2018b) using a Keplerian mask assuming a disk position angle of 132° and an inclination of 42° (e.g. Isella *et al.*, 2016). Since

[1] A python-based open-source implementation of VISIBLE is available at http://github.com/AstroChem/VISIBLE

the position-velocity pattern of a disk in Keplerian rotation is well characterised, matched filtering can be used to detect weak spectral lines in disks (Loomis *et al.*, 2018b). The Keplerian filter is sampled in the *uv* plane and these visibilities are cross-correlated with the low signal-to-noise (S/N) observed visibilities. This is done by sliding the filter though the data channel-by-channel along the velocity axis. If there is a detectable signal, i.e. emission with a similar position and velocity distribution as the filter, the filter response will peak at the source velocity of the emission. The filter response is shown in Figure 3.1b with the black line marking the $^{13}C^{17}O$ J=3-2 transition after correction for the source velocity (5.8 km s$^{-1}$). The filter response has a S/N of $\approx$ 3.5. There are 14 $^{13}C^{17}O$ J=3-2 hyperfine structure lines that lie between 321.851 and 321.852 GHz. All lines lie within a frequency range less than the spectral resolution of the data ($1.953125\times10^{-3}$ GHz); hence, the observations are a blend of all of the hyperfine lines. The $^{13}C^{17}O$ molecular data is from Klapper *et al.* (2003) and was accessed via the Cologne Database for Molecular Spectroscopy (CDMS, Müller *et al.*, 2005).

The line imaging was conducted using CLEAN with CASA version 4.6.0. The native spectral resolution of the data is 1.8 km s$^{-1}$; however, in order to optimise the S/N the final images were generated with a 3 km s$^{-1}$ channel width and a *uv* taper (as mentioned in Chapter 2) of 0.″5 resulting in a synthesised beam of 0.″87 $\times$ 0.″51 (100°). The channel maps reach a peak of 0.079 Jy beam$^{-1}$ per channel and the line-free channels have a rms noise ($1\sigma$) of 0.010 Jy beam$^{-1}$ per channel resulting in a S/N of 7. Figures 3.1c and d present the $^{13}C^{17}O$ integrated intensity map and the intensity-weighted velocity map, respectively. The integrated intensity map was made using channels $\pm$ 6 km s$^{-1}$ about the source velocity and shows that the emission is centrally peaked and compact compared to the dust disk. The peak integrated intensity is 0.55 Jy beam$^{-1}$ km s$^{-1}$ with an rms noise

level of 0.08 Jy beam$^{-1}$ km s$^{-1}$ (S/N = 7), the latter of which was extracted from the spatial region beyond the detected line emission. The intensity-weighted velocity map was made in the same manner but also with a $3\sigma$ noise clip. There is a velocity gradient across the major axis of the disk that is consistent with the expectation of Keplerian rotation of the gas disk.

Archival data is used to benchmark the line emission modelling (see Table 3.1), including the $^{12}C^{16}O$, $^{13}C^{16}O$, $^{12}C^{18}O$ J=2-1 transitions observed from Isella *et al.* (2016), and the $^{12}C^{16}O$ J=3-2 ALMA Science Verification data.[1] All integrated intensity maps were de-projected and azimuthally averaged and are shown in Figures 3.2 and 3.3a to e. This is an effective method to increase S/N assuming that the emission is azimuthally symmetric (e.g., Yen *et al.*, 2016a). All pixels in each map were placed into radial bins depending on the deprojected radius, and the average value per bin calculated. The errors are the standard deviation of intensity of the pixels in each bin divided by the square root of the number of beams per annulus (e.g. Carney *et al.*, 2018). In addition, Figure 3.2e shows the $^{12}C^{17}O$ J=3-2 transition total integrated intensity value with associated errors (Qi *et al.*, 2011). All data plotted assumes a source distance of 122 pc (van den Ancker *et al.*, 1998). Although the GAIA DR2 parallaxes put this source at $101.5^{+0.2}_{-1.9}$ pc (Gaia Collaboration *et al.*, 2018), in order to compare to previous analyses the previous value is used. The impact of the revised distance is discussed in Section 3.2.4.

[1] https://almascience.nrao.edu/alma-data/science-verification

Table 3.1: List of the HD 163296 modelled CO isotopologue lines.

| Species | Transition | Frequency (GHz) | Beam Size | Reference |
|---|---|---|---|---|
| $^{12}$CO | J=3-2 | 345.796 | 0.″22 x 0.″15 (-89.8°) | ALMA Science Verification |
| $^{12}$CO | J=2-1 | 230.538 | 0.″22 x 0.″15 (-89.8°) | Isella et al. 2016 |
| $^{13}$CO | J=2-1 | 220.399 | 0.″22 x 0.″16 (-89.8°) | Isella et al. 2016 |
| C$^{18}$O | J=2-1 | 219.560 | 0.″23 x 0.″17 (-89.4°) | Isella et al. 2016 |
| C$^{17}$O | J=3-2 | 337.061 | 0.″24 x 0.″17 (-89.6°) | Qi et al. 2011 |
| $^{13}$C$^{17}$O | J=3-2 | 321.852 | 0.″87 x 0.″51 (100°) | This work |

The values for the line frequencies are from the Cologne Database for Molecular Spectroscopy (CDMS; Müller *et al.*, 2001).

### 3.2.3 Line radiative transfer modelling

Previous observations of the HD 163296 disk with ALMA and the SMA have detected multiple CO isotopologues: $^{12}C^{16}O$, $^{13}C^{16}O$, $^{12}C^{18}O$ and $^{12}C^{17}O$ (Isella *et al.*, 2016; Qi *et al.*, 2011). The models that were used to reproduce the line emission in Qi *et al.* (2011) recover the following global isotope ratios;

$$n(^{12}C^{16}O)/n(^{13}C^{16}O) = 67 \pm 8,$$
$$n(^{12}C^{16}O)/n(^{12}C^{18}O) = 444 \pm 88,$$
$$n(^{12}C^{18}O)/n(^{12}C^{17}O) = 3.8 \pm 1.7,$$

where $n(^{X}C^{Y}O)$ is the number density of the molecule. These are consistent with the carbon and oxygen isotope ratios observed in the ISM (Wilson, 1999).

A first estimate of the column density of gas traced by the $^{13}C^{17}O$ emission can be made under the assumption of optically thin emission in local thermodynamic equilibrium (LTE) with:

$$N = 2.04 \frac{\int I_\nu dv}{\theta_a \theta_b} \frac{Q_{\rm rot} \exp\left(E_u/T_{\rm ex}\right)}{\nu^2 \langle S_{\rm ul}\mu^2 \rangle} \times 10^{20} {\rm cm}^{-2}, \quad (3.1)$$

where $\int I_\nu dv$ is the integrated line intensity in Jy beam$^{-1}$ km s$^{-1}$, $\theta_a$ and $\theta_b$ are the semi-major and semi-minor axes of the synthesized beam in arcseconds, $T_{\rm ex}$ is the excitation temperature in K, and $\nu$ is the rest frequency of the transition in GHz (Remijan *et al.*, 2003). The partition function ($Q_{\rm rot}$), upper energy level ($E_u$, in K), and the temperature-independent transition strength and dipole moment ($S_{ul}\mu^2$, in debye$^2$) are taken from CDMS (Müller *et al.*, 2005). The average column density for the $^{13}C^{17}O$ within 50 au, assuming an excitation temperature of 50 K, is 7.1 $\times$ $10^{15}$ cm$^{-2}$. This is equivalent to an $n_{\rm H}$ column density of 2.65 $\times$ $10^{25}$ cm$^{-2}$ (44.4 g cm$^{-2}$) at 50 au. In comparison, the corresponding value for the $^{12}C^{18}O$ is 1.7 $\times$ $10^{16}$ cm$^{-2}$, resulting in an $n(^{12}C^{18}O)/n(^{13}C^{17}O)$

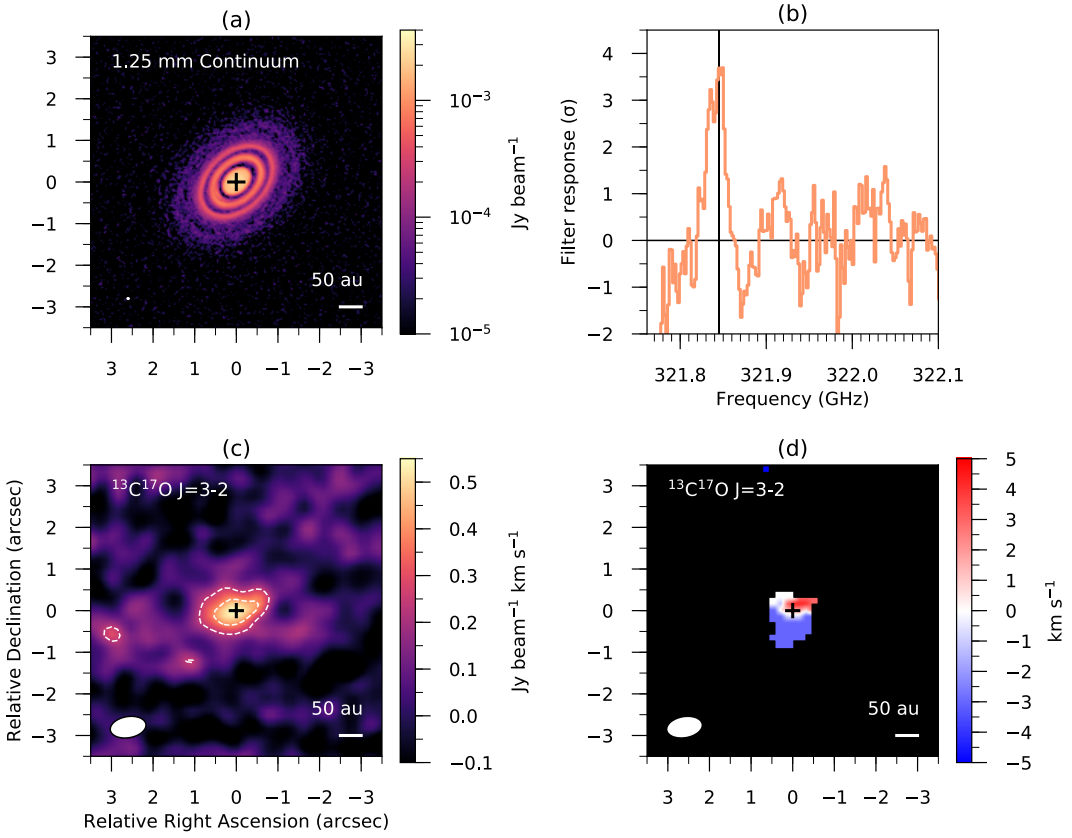


Figure 3.1: a) The 1.25 mm continuum image from Isella *et al.* (2018) plotted on a log colour scale to highlight the rings and extended emission. b) The matched filter response for the $^{13}C^{17}O$ J=3-2 detection where the black line marks the frequency of the hyperfine transitions. c) The $^{13}C^{17}O$ J=3-2 integrated intensity map where the white dashed contours mark 3 and 5 $\sigma$. d) The $^{13}C^{17}O$ J=3-2 intensity-weighted velocity map.

ratio of 2.5. Under the assumption that both the lines are optically thin (and taking the previously derived isotopic ratios), this value is a factor of 100 too low. Therefore, the $^{12}C^{18}O$ line emission is optically thick and the resulting gas mass derived from this tracer will be underestimated.

To quantify this more robustly, an existing disk model that has been shown to fit emission lines from multiple CO isotopologues ($^{12}C^{16}O$, $^{13}C^{16}O$, $^{12}C^{18}O$ and $^{12}C^{17}O$) is employed to model the new $^{13}C^{17}O$ detection (Qi *et al.*, 2011). The density (hydrogen nuclei density, $n_{\rm H}$) and gas temperature of the disk are shown in Figures 3.4a and b. The CO abundance distribution, shown in Figure 3.4c, was determined by setting $n$(CO) to a constant fractional abundance of $6.0\times10^{-5}$ with respect to $H_2$ in the molecular layer following Qi *et al.* (2011). This abundance was reduced by a factor of $10^{-4}$ in the midplane where $T_{\rm gas} \leq 19$ K (the approximate CO freeze-out temperature) and by a factor of $10^{-8}$ in the atmosphere where CO is photo-dissociated. This is where the vertically-integrated hydrogen column density, $\sigma(n_{\rm H})$, from the disk surface is $< 1.256 \times 10^{21}$ cm$^{-2}$. The depleted value in the midplane beyond the snowline is consistent with the CO abundances derived from chemical models that include non-thermal desorption (e.g. Walsh *et al.*, 2010). The photodissociation and freeze out boundaries are shown in white contours overlaid on Figures 3.4a and b.

The first model, Model 1, uses a constant $^{13}C^{17}O$ fractional abundance of $5.39 \times 10^{-10}$ relative to $H_2$. This assumes isotope ratios that are consistent with the observations and modelling from Qi *et al.* (2011). Model 1 has a total disk mass of 0.089 $M_\odot$. Using the CDMS data for $^{13}C^{17}O$ a LAMDA[1]-like file was generated in order to model the J=3-2 hyper-fine components in LIME[2] (the Line Modeling Engine, Brinch & Hogerheijde, 2010). Synthetic images cubes were computed assuming the appropriate position angle and inclination of the source,

[1]LAMDA: https://home.strw.leidenuniv.nl/~moldata/
[2]LIME: https://github.com/lime-rt/lime

and the resulting images were smoothed with a Gaussian beam to the spatial resolution of the observations using the CASA task, *imsmooth*. The generated integrated intensity map was then de-projected and azimuthally averaged. The radial profiles from Model 1 (orange) are shown alongside the observations in Figure 3.2 a to e.

Model 1 underpredicts the $^{13}C^{17}O$ peak emission in the integrated intensity map by a factor of 2.5, yet provides a reasonable fit to the other lines (within a factor of two). The higher spatial resolution observations are affected by dust opacity within $\approx$ 50 au (see Isella *et al.*, 2016); therefore, the focus is to reproduce the data beyond 50 au.

To better fit the $^{13}C^{17}O$ observations the disk mass in Model 1 is increased globally. This was done by initially multiplying $n_{\rm H}$ by a factor of 1.5 and then increasing this factor in steps of 0.5 until the best by-eye fit of 3.5 was found. The results for Model 2 are shown in Figure 3.2 (purple). Model 2 provides a better fit to most of the lines. The $^{12}C^{16}O$ J=2-1 emission is over predicted but this line is optically thick and will therefore be tracing the gas in the warm molecular layer; hence the line strength is more dependent on the gas temperature than density. This model assumes a smooth radial gas density structure contrary to the most recent observations. However, this work is focused on reproducing the global disk mass rather than the underlying small scale gas surface density variations. Model 2 has a total disk mass of 0.31 $M_\odot$.

A similar fit can be obtained using a different CO snowline location at 90 au as determined in Qi *et al.* (2015). This requires a corresponding increase in gas mass ($\times$ 3.5) within the snowline, and obtains a similar $^{12}C^{18}O$ column density profile as in Qi *et al.* (2015) beyond the snowline. Both of these models use the same underlying physical structure but have different CO snowline locations and levels of CO depletion beyond the snowline. The Qi *et al.* (2011) model has

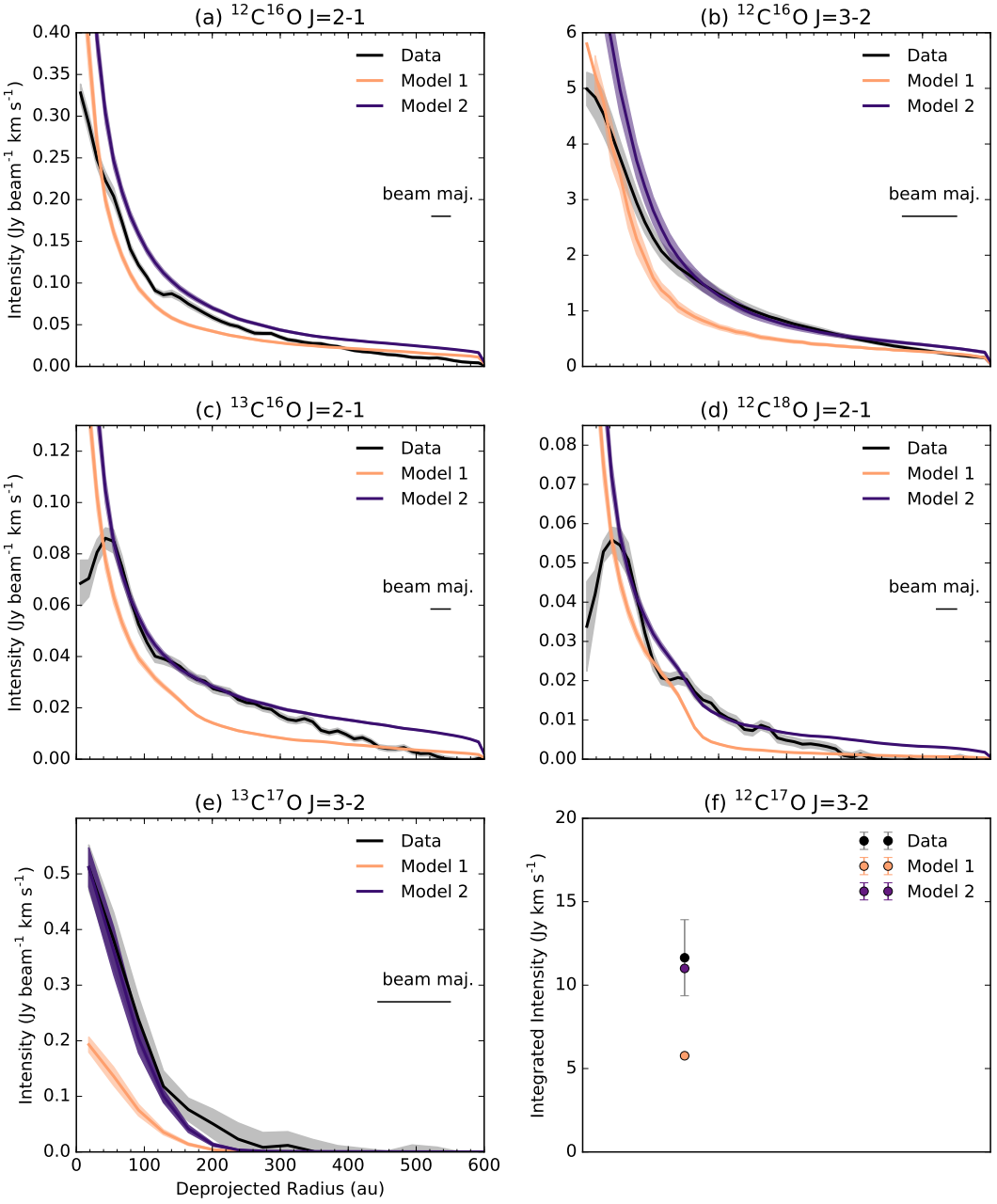


Figure 3.2: a-e) The deprojected and azimuthally averaged radial profiles of the observed and modelled CO lines. f) The value of integrated flux of the observed and modelled $C^{17}O$ J=3-2 line. The shaded regions are the errors as described in the text. Model 1 has a total disk mass of 0.089 $M_\odot$ and Model 2 has a total disk mass of 0.31 $M_\odot$.

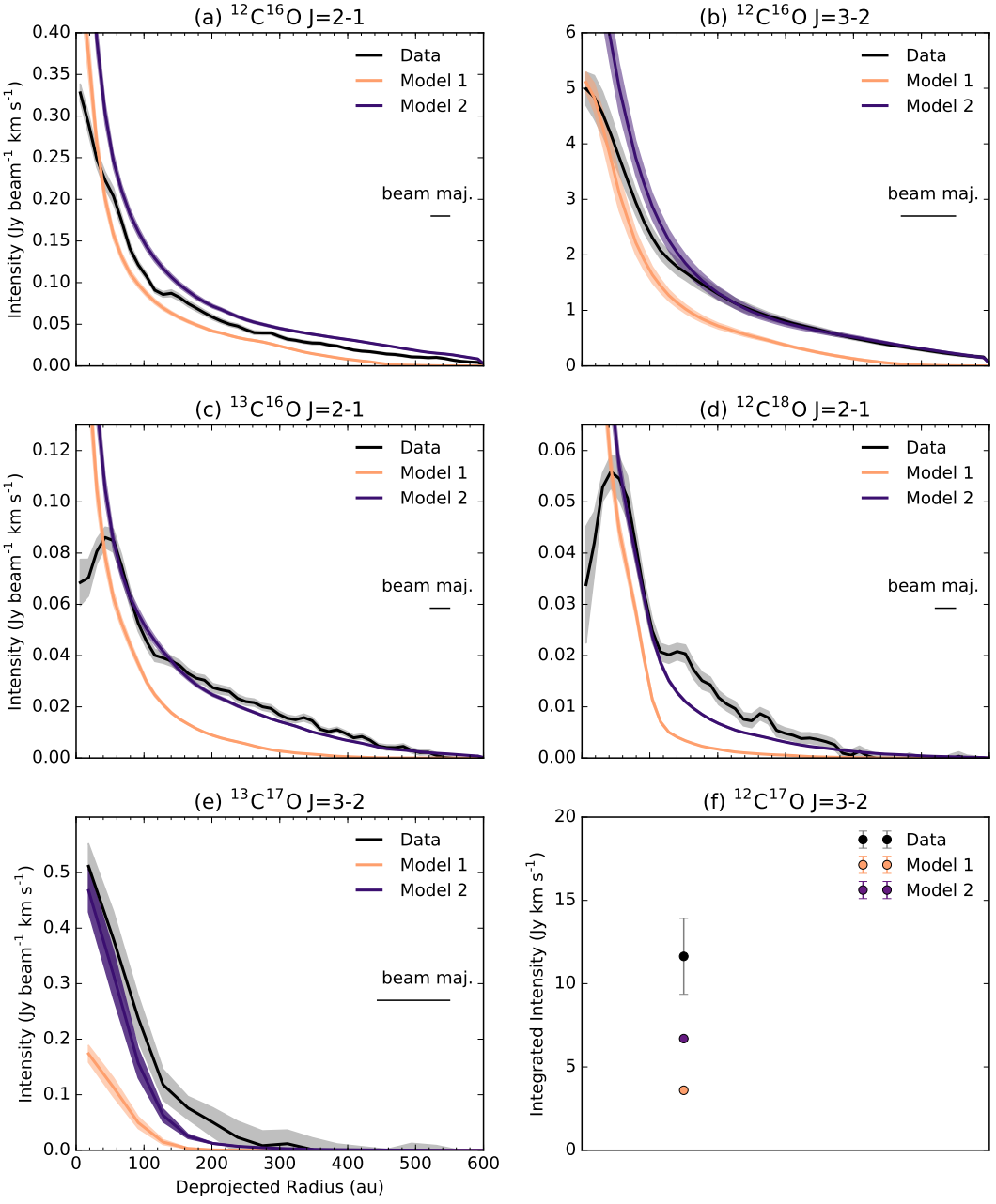


Figure 3.3: Same as Figure 3.2 but for the Qi *et al.* (2015) model.

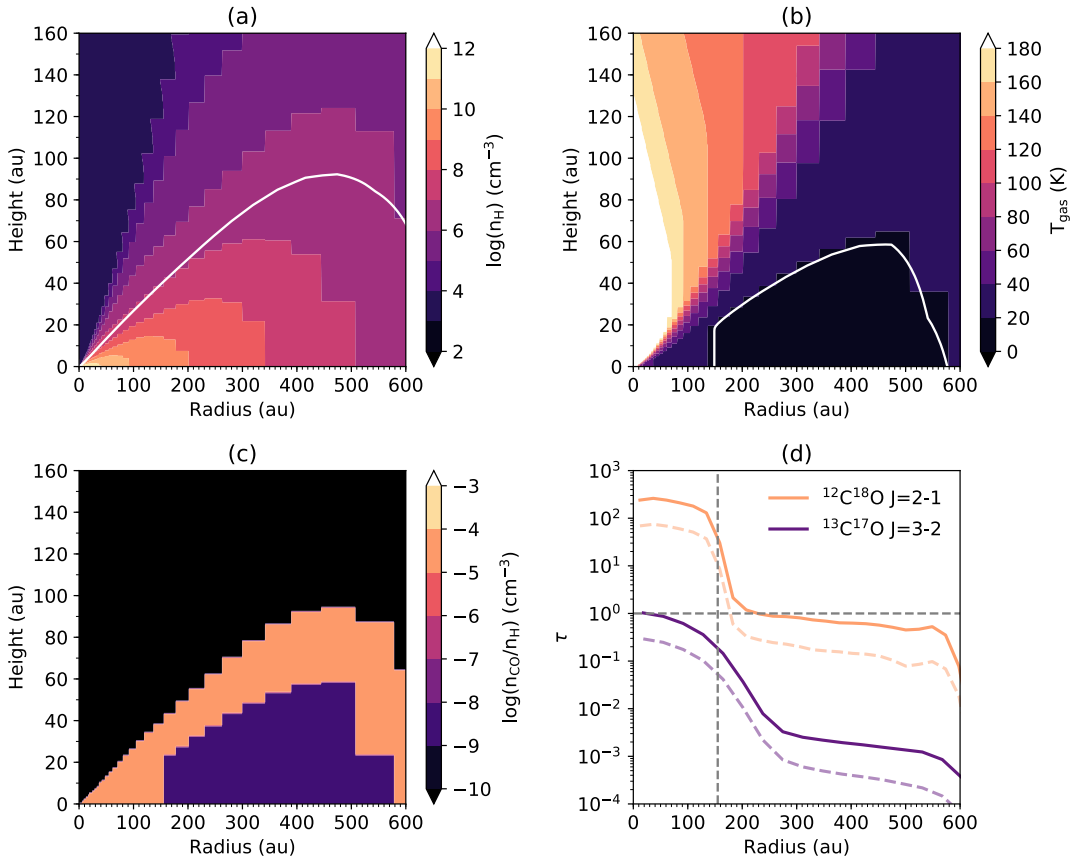


Figure 3.4: The disk physical structure from Qi *et al.* (2011). a) The $n_{\rm H}$ density. b) The gas temperature. The white contours mark $\Sigma(n_{\rm H}) = 1.256 \times 10^{21}$ cm$^{-2}$ and $T_{\rm gas} = 19$K, respectively. c) The $n({\rm CO})/n_{\rm H}$ distribution. d) The radially averaged optical depth ($\tau$) of the $^{12}C^{18}O$ J=2-1 and $^{13}C^{17}O$ J=3-2 transitions from Model 1 (light purple and orange dashed lines) and Model 2 (dark purple and orange solid lines) assuming a face on disk. The vertical dashed line marks the location of the CO snowline in both models (155 au) and the horizontal dashed line marks where $\tau = 1$.

simpler assumptions regarding the freeze-out of CO, consistent with other work (e.g., Williams & Best, 2014), and was found to be a slightly better fit to the observations (see Figures 3.2 and 3.3).

Optical depth maps for a face on disk were generated in LIME to recover the maximum value of $\tau$ for each transition. These maps were radially averaged and the resulting optical depth of the $^{12}C^{18}O$ J=2-1 and $^{13}C^{17}O$ J=3-2 transitions for both models are shown in Figure 3.4d. It can be seen that $^{12}C^{18}O$ is optically thick within the CO snowline (155 au) in both models, whereas the $^{13}C^{17}O$ remains optically thin across the full radial extent of the disk.

### 3.2.4 Comparison to other mass estimates

Observations of $^{13}C^{17}O$ have been used to derive a new gas mass for the HD 163296 disk of 0.31 $M_\odot$ at an assumed distance of 122 pc. The total disk mass depends on the gas to dust mass ratio (g/d), and using the dust mass from Isella *et al.* 2007 this results in a g/d $\approx$ 260. The total disk mas (dust + gas) is therefore 0.31 $M_\odot$ to two significant figures. Here this new result is compared to previous works.

The HD 163296 disk has been well studied and there are many mass measurements in the literature. In general, the mass estimate in this work is the highest by a factor of 2 to 6 compared to previous studies using $^{12}C^{18}O$ (e.g. 0.17 $M_\odot$ and 0.048 $M_\odot$ from Isella *et al.* 2007 and Williams & McPartland 2016 respectively). There are a range of g/d values in the literature that span four orders of magnitude. Tilling *et al.* (2012) and Boneberg *et al.* (2016) models require a low g/d = 20. Isella *et al.* (2016) have a radially varying g/d covering a range from $\approx$ 30 to $\approx$ 1100. Recent work from Powell *et al.* (2019) recover a total disk mass of 0.21 $M_\odot$ with a high g/d $\sim 10^4$ in the outer disk. The one documented mass higher than this work's result is 0.58 $M_\odot$ with a g/d = 350 (Woitke *et al.*,

2019). The inconsistencies in these mass measurements and g/d from different models may be explained by trying to recover the gas density structure with optically thick lines and different assumptions about the 2D gas and (micron and millimeter sized) dust distribution.

Despite these challenges, CO remains the best and most accessible tracer of mass available for disks (Molyarova *et al.*, 2017), and more robust lower limits to the gas mass can only be made by targeting the most optically thin isotopologues ($^{12}C^{17}O$, $^{13}C^{18}O$, and $^{13}C^{17}O$). These masses have all been determined using a source distance of 122 pc. Considering the revised distance of 101.5 pc, the total disk gas mass from this work is thus 0.21 $M_\odot$ (mass $\propto$ flux / distance$^2$). This results in a disk-to-star mass ratio of 0.1.

### 3.2.5 The impact of CO chemistry on the disk mass

CO is susceptible to isotope-selective photodissociation which can reduce the abundance of the rarer isotopologues relative to $^{12}C^{16}O$ in the disk atmosphere. However; the observations are well fit with interstellar isotopic abundances. Because the $^{12}C^{16}O$, $^{13}C^{16}O$ and $^{12}C^{18}O$ line emission is optically thick, testing the significance of isotope-selective photodissociation in this disk requires higher sensitivity observations of the rarer isotopologues that emit from higher in the disk atmosphere.

Observations have shown that CO is depleted with respect to $H_2$ in disks; however, without a better tracer of the $H_2$ column density, e.g., HD, the level of depletion is difficult to constrain (Bergin *et al.*, 2013; McClure *et al.*, 2016). Recent work from (Kama *et al.*, 2020) derived an upper limit on the total disk mass of 0.067 $M_\odot$ from a non-detection of HD. This indicates that there is no carbon depletion, i.e., the average CO/H2 abundance in the disk needs to be $\approx 1.9 \times 10^{-4}$ which is comparable to the ISM value. It has not yet been shown that this model

can reproduce the $^{13}C^{17}O$ emission presented in this Chapter. Carbon depletion effects are less significant in warmer disks around Herbig Ae stars compared to their T Tauri counterparts. This is because in T Tauri disks the chemical conversion of CO to other species is more efficient where there is CO freeze-out. Observations show moderate carbon depletion in the Herbig disk around HD 100546 with a model-derived [C]/[H] abundance ratio of 0.1 to 1.5 $\times$ $10^{-4}$ (Kama *et al.*, 2016b), and the value for CO adopted in this works model is within this range. Consistent with this, models have also suggested that these disks have a close to canonical $n(\mathrm{CO})/n(\mathrm{H_2})$ abundance (Bosman *et al.*, 2018). A detection of the $^{13}C^{18}O$ J=2-1 line in the disk has been used as evidence for a super-solar abundance of CO within the CO snowline (Zhang *et al.*, 2020). This, model-dependant, result can reconcile a higher CO gas mass with the HD upper-limit with a total gas mass of 0.14 $M_{\odot}$. This CO abundance step-function is where the CO abundance is depleted outside the snowline by at least and order of magnitude and then enhanced by a factor of a few inside the snowline. This can be explained by the inward radial drift and subsequent evaporation of CO ice-rich dust grains from the outer disk as it crosses the snowline Krijt *et al.* (2018). Further observations of the rare CO isotopologues in disks that have been targeted in HD are required to determine the level of CO depletion/enhancement in disks. Overall, there is still uncertainty as to how the CO gas masses of disks can used to infer a total disk mass and both observations of rare CO isotopologues and HD are required to make the most robust estimates.

### 3.2.6 Constraints on the location of the CO snowline

Locating the midplane CO snowline in disks is difficult due to the high optical depth of the more abundant CO isotopologues and the vertical temperature gradient of the disk, however the location of the CO snowline can be determined

directly by observing less abundant, optically thin, CO isotopologues

Figure 3.5 shows the radial emission profiles of the $C^{18}O$ J=2-1 and the $^{13}C^{17}O$ J=3-2 lines from high spatial resolution models (5 au beam). This analysis shows that the $C^{18}O$ emission in both models tested is optically thick, and thus cannot be used to directly locate the midplane CO snowline. However, the $^{13}C^{17}O$ emission is optically thin, so future observations at a higher spatial resolution and sensitivity could be used to directly constrain the radius of the midplane CO snowline. The drop off in emission is quite steep but it may still be hard to distinguish between a drop off in emission due to sensitivity. This will only work if the beam-size is much smaller than the expected snowline distance and if the observations are of high enough sensitivity. The effectiveness of this could be tested by attempting to retrieve the snowline location from parametric models run through LIME and the ALMA observing simulator.

The new, closer, source distance moves the absolute snowline locations to 75 au and 128 au (depending on the freezeout temperature, 25 K v 19 K respectively). The former location is close to one of the observed dust gaps in the disk and it may be the case that the drop in CO surface density detected here is due to gas depletion rather than the snowline. It is important to note that the snowline is not a simple sharp transition at the condensation temperature, but is instead determined by the balance of the rates of freezeout and thermal desorption, which should be considered in future disk models (e.g. van 't Hoff *et al.*, 2017).

### 3.2.7 Is the disk gravitationally stable?

The potential exoplanet population currently probed with ALMA, via the ringed depletion of continuum emission, are gas giant planets on wide orbits. In the case of HD 163296 this would imply a multiple giant planet system and indeed, the presence of such a system has already been proposed (Isella *et al.*, 2016; Liu

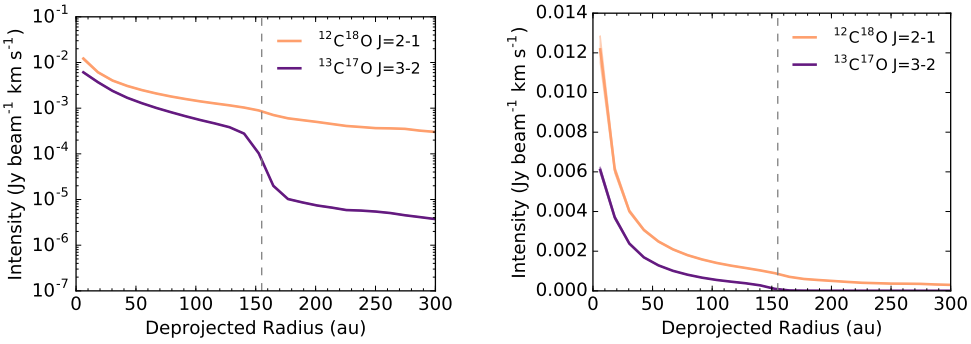


Figure 3.5: Radial emission profiles of the C$^{18}$O J=2-1 and the $^{13}$C$^{17}$O J=3-2 line from models convolved with a 5 au beam (left: log y-axis, right: linear y-axis). The dashed grey line marks radial position of the model snowline.

*et al.*, 2018; Pinte *et al.*, 2018; Teague *et al.*, 2018). The formation of massive planets on wide orbits can in some cases be achieved by core accretion, but a more economical route might involve the gravitational fragmentation of the outer regions of the disk (Boss, 2011). The new, higher, disk mass estimate prompts an investigation into whether such processes may have occurred (or be occurring) in the HD 163296 disk.

As discussed in Section 1.2, the stability of a disk against fragmentation can be quantified via the Toomre Q parameter (Toomre, 1964). Toomre Q values of 1.7 or less imply that the disk is susceptible to instabilities in the form of non-axisymmetric spirals and the disk may fragment (Durisen *et al.*, 2007). Q is calculated across the disk (Figure 3.6, orange) accounting for the lower mass due to the new source distance, assuming a g/d of 260, and the midplane temperature structure of the model (Figure 3.4b). The minimum value of Q is $\approx 6$ at $\approx 110$ au, suggesting that the disk is currently gravitationally stable (in agreement with recent work from Powell *et al.* 2019).

The relatively old age of the HD 163296 system brings into question its stability earlier in its lifetime. The determination of previous disk masses is complicated

by processes including episodic accretion (e.g. Mendigutía *et al.*, 2013) and the decrease in accretion rate with time (e.g. Venuti *et al.*, 2014). The magnitude of these effects are still under debate (see Hartmann *et al.*, 2016, for a review), therefore it is assumed that all of the accreted mass once resided in the disk, and that the accretion rate ($\dot{M}$) has been constant over disk lifetime. HD 163296 has an estimated age of $6.03^{+0.43}_{-0.14}$ Myr and current $\log \dot{\mathrm{M}} = -6.81^{+0.16}_{-0.15}\,\mathrm{M_\odot\,yr^{-1}}$ (Wichittanakom *et al.*, 2020); thus under these assumptions, the disk mass at 0.1 Myr is estimated to be $1.13^{+0.51}_{-0.28}$ $\mathrm{M_\odot}$. The four proposed planets in the disk would add an additional mass of $\approx$ 4 $\mathrm{M_J}$ or $\approx$ 0.004 $\mathrm{M_\odot}$.

The resulting minimum Toomre Q values for this star-disk configuration[1] would be in the range of 1.3–0.7 (Figure 3.6, purple), placing regions of the disk from ∼50–220 au in the regime of instability. Such behaviour early in the disk lifetime has implications for the trapping and growth of dust (Rice *et al.*, 2004) and the chemical composition of the disk (Evans *et al.*, 2015). This previous unstable state could also be the source of the four massive planets currently proposed to reside in the disk around HD 163296 (Isella *et al.*, 2016; Liu *et al.*, 2018; Pinte *et al.*, 2018; Teague *et al.*, 2018).

## 3.3 HL Tau

### 3.3.1 The HL Tau disk

HL Tau is located in the nearby (140 pc) Taurus-Auriga star forming region (Rebull *et al.*, 2004). SED modelling shows it to be a Class I–II protostar surrounded by both a circumstellar disk and envelope (Robitaille *et al.*, 2007). It also appears to be accreting at a high rate ($\dot{M} \sim 10^{-7}$ $\mathrm{M_\odot\,yr^{-1}}$; Beck *et al.* 2010). This observational evidence makes HL Tau an example of a young embedded, disk-hosting

[1] Note this does not account for any change in the stellar mass over this time period, which would decrease Q further.

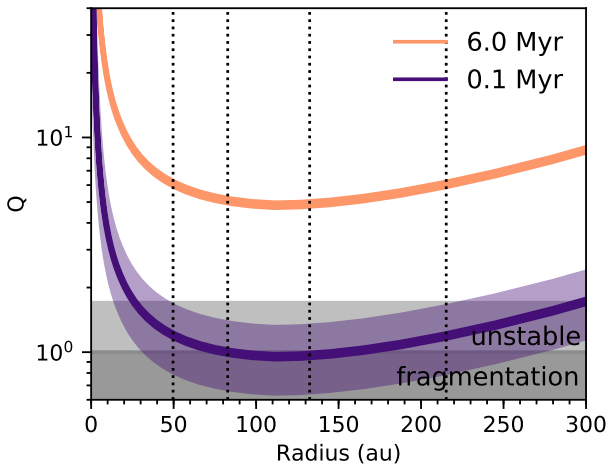


Figure 3.6: Toomre Q parameter for the new disk mass derived from Model 2 and extrapolated back to 0.1 Myr. The shaded regions incorporate both the errors in stellar age and mass accretion rate. Vertical dashed lines mark the radial positions of gaps in the mm dust and kinematic perturbations which may be due to accreting protoplanets.

star ($\sim$ 1 Myr; Briceño *et al.*, 2002).

HL Tau has been a prime target for studies aiming to characterise young disks (Carrasco-González *et al.*, 2009; Greaves *et al.*, 2008). In particular, HL Tau was the first circumstellar disk observed using long baselines with ALMA. This revealed an ordered series of concentric rings and gaps in the disk across multiple millimeter wavelengths (2.9 mm, 1.3 mm, 0.9 mm; ALMA Partnership *et al.*, 2015). Many theories have been put forward to explain the origin of these structures (such as dust sintering and ice lines; Okuzumi *et al.*, 2016; Zhang *et al.*, 2015), but one of the most persistent involves the growth of planets within the disk (Dipierro *et al.*, 2015b). While efforts to detect thermal emission from young planets in the gaps have been unsuccessful, the corresponding upper limits on their masses still lie at the higher end of the giant planet regime (10–15 $M_{Jup}$; Testi *et al.*, 2015).

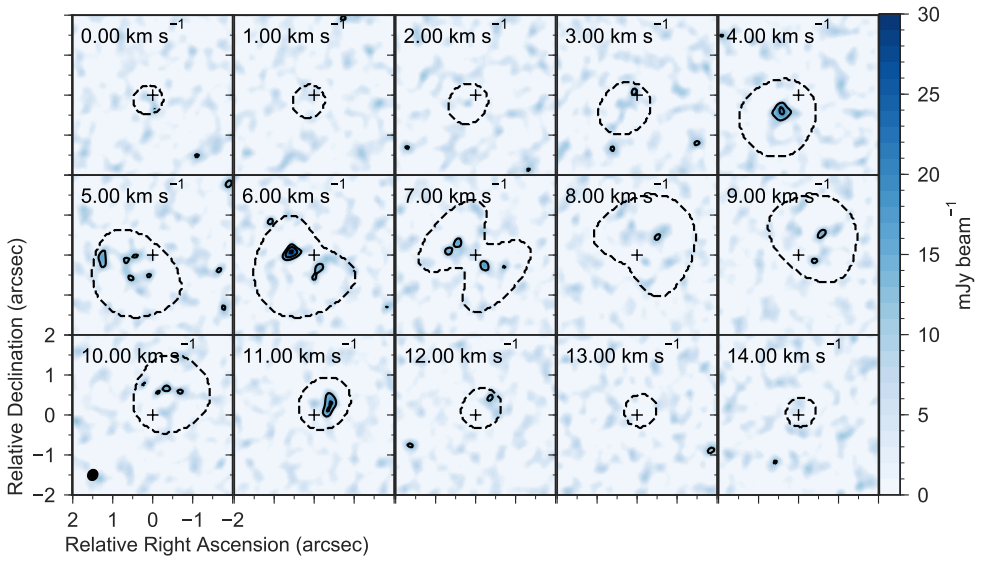


Figure 3.7: The HL Tau $^{13}C^{17}O$ J=3-2 channel maps at 1 km s$^{-1}$. Contours mark the 3, 5 and 7 $\sigma$ levels where $\sigma$ is 6 mJy beam$^{-1}$ channel$^{-1}$. The dashed black lines show the Keplerian mask used in the cleaning procedure.

The combination of the potential for massive planets at large radii, coupled with evidence of a high disk mass ($\sim 0.1 - 0.13\,M_\odot$; Guilloteau *et al.*, 2011; Kwon *et al.*, 2011) has seen gravitational instability (GI; Boss 1997) being invoked to explain both the observed dust structures in HL Tau (Akiyama *et al.*, 2016; Takahashi & Inutsuka, 2016), along with the origin of any planetary companions (Nero & Bjorkman, 2009). However, recent measurements of the gas mass in the HL Tau disk using $C^{18}O$ appear to be too low for GI to be active ($M_{\rm gas}$ = 2–40 $\times\, 10^{-3}\,M_\odot$; Wu *et al.*, 2018).

### 3.3.2 Line imaging

HL Tau was observed by ALMA in Band 7 during Cycle 5 for 1.46 hours with 49 antennae in configuration C43-8 under project code 2017.1.01178.S; P.I. E. Humphreys). The raw data was downloaded from the archive and was calibrated then self-calibrated. Two rounds of phase calibration and then one round of

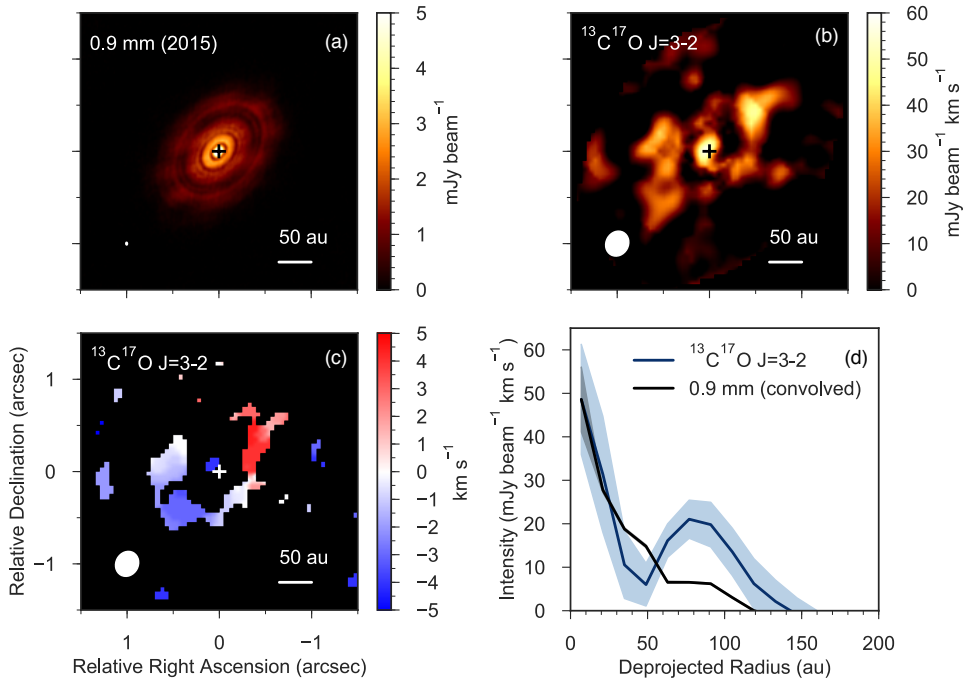


Figure 3.8: **(a)** The 0.9 mm continuum image from ALMA Partnership *et al.* (2015). **(b)** The $^{13}C^{17}O$ $J = 3$–2 integrated intensity map. **(c)** The $^{13}C^{17}O$ $J = 3$–2 intensity-weighted velocity map. **(d)** The $^{13}C^{17}O$ $J = 3$–2 and 0.9 mm continuum (normalised to the line emission peak) de-projected and azimuthally averaged radial profiles. The shaded regions are the errors given by the standard deviation of intensity points in each bin (0.″1) per beam per annulus

amplitude calibration resulting in an increase in the continuum signal-to-noise ratio. The continuum was then subtracted. The spectral window (SPW) covering the $^{13}C^{17}O$ $J = 3$–2 transition (321.852 GHz) had a native spectral resolution of 0.908 km s $^{-1}$ (note this does not resolve the $J = 3$–2 hyperfine structure).

Data (self-)calibration and imaging were performed with CASA version 5.1.1 (McMullin *et al.*, 2007b). Line imaging was performed with the CLEAN algorithm, using a Keplerian mask with the measured position and inclination angles of the disk (e.g. PA = 138° and $i = 46°$; ALMA Partnership *et al.*, 2015). The use of such a mask generates moment maps with less noise as only the emission with the position-velocity pattern coincident with disk emission is integrated (e.g. Salinas *et al.*, 2017). The native resolution of the data resulted in a natural beam size of $0\farcs14 \times 0\farcs11$ ($-13°$). A $0\farcs2$ *uv*-taper was used, which was found to maximise the signal-to-noise (S/N) of the line emission, resulting in a final beamsize of $0\farcs28 \times 0\farcs24$ ($-36°$). The emission is detected across 9 1.0 km s $^{-1}$ wide channels with an rms of 4 mJy beam$^{-1}$ per channel measured from the line-free channels and a peak line emission of 30 mJy beam$^{-1}$ per channel (S/N of 7.5). These channel maps are shown in Figure 3.7 along with the Keplerian mask that was used.

Figure 3.8 shows the ALMA Science Verification Band 7 (∼345 GHz, ∼0.9 mm) continuum image alongside the new $^{13}C^{17}O$ $J = 3$–2 Keplerian-masked integrated intensity map and the $^{13}C^{17}O$ $J = 3$–2 intensity-weighted velocity map made with a 2.5 $\sigma$ clip. Also shown are the deprojected and azimuthally averaged $^{13}C^{17}O$ $J = 3$–2 integrated intensity and 0.9 mm continuum profiles derived from our dataset, binned to the same radial resolution.

The $^{13}C^{17}O$ emission is detected out to approximately 140 au from the central star, with a velocity pattern that is consistent with observations of other gas tracers (e.g. ALMA Partnership *et al.*, 2015). There appears to be a deficit of emission (seen in both the integrated intensity map and radial emission profile)

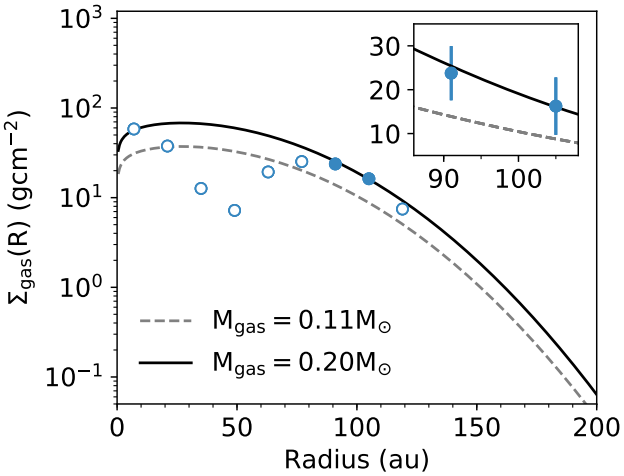


Figure 3.9: Comparison of the total gas surface density derived from the $^{13}C^{17}O$ integrated intensity profile (circles) with our initial and final disk model (dashed and solid lines, respectively). Filled circles show the points used to fit the model, which the inset shows in more detail. Errors are propagated from the observations.

at approximately 50 au. This feature is not coincident with any substructure in the dust continuum or molecular gas observed at higher spatial resolution than our data (e.g., CO, $HCO^+$; Yen *et al.*, 2016b). Multi-wavelength continuum observations have shown that the optical depth of the HL Tau disk at frequencies comparable to the $^{13}C^{17}O$ $J = 3$–2 transition ($\sim$ 330 GHz) is high, with $\tau \sim 8$ between $40 - 50$ au (Carrasco-González *et al.*, 2019). This deficit of emission is therefore likely due to the high continuum opacity at Band 7 obscuring the line emission originating from the midplane, rather than a bona-fide gap in the disk. The central peaking of the $^{13}C^{17}O$ profile may indicate that the line emission at radii $< 10$ au becomes optically thick at a higher height in the disk atmosphere than the dust at this frequency. Beyond approximately 70 au, the intensity profile follows the expected radially-decreasing power law trend.

### 3.3.3 Conversion of line flux to gas mass

The $^{13}C^{17}O$ observations can be used to indirectly measure the total gas mass of the disk. In Section 3.2 for the HD 163296 disk 2D radiative transfer models of multiple CO isotopologues and transitions from a well tested 2D physical structure were used to constrain the disk mass. Many molecular line observations toward HL Tau are significantly affected by absorption and complex velocity gradients from the surrounding cloud (see, e.g., ALMA Partnership *et al.*, 2015; Yen *et al.*, 2019); hence a similar wealth of observational data is not readily available. A simpler method of determing the gas mass is therefore employed here.

The HL Tau mm-dust surface density distribution has been shown to follow a power-law distribution:

$$\Sigma(r) = \Sigma_0 \left(\frac{r}{r_c}\right)^{-\gamma} \exp\left(-\frac{r}{r_c}\right)^{2-\gamma} \tag{3.2}$$

with

$$\Sigma_0 = (2-\gamma)\frac{M_{\rm d}}{2\pi r_c^2} \exp\left(\frac{r_{\rm in}}{r_c}\right)^{2-\gamma} \tag{3.3}$$

where the total disk mass is 0.105 $M_\odot$ (assuming a gas-to-dust mass ratio of 100), $r_c$ is 80 au, $r_{in}$ is 9 au and $\gamma$ is -0.20 (Kwon *et al.*, 2015). This model is shown in Figure 3.9 as the grey dashed line. Although the observed emissivity profiles of the millimeter and centimeter sized dust are more complex, the above profile has been shown to be consistent with these (Pinte *et al.*, 2016) and there is no evidence that these features are also present in the bulk gas distribution.

A range of midplane dust and gas temperature profiles exist for the HL Tau disk (e.g.; Carrasco-González *et al.*, 2019; Kwon *et al.*, 2015; Okuzumi *et al.*, 2016; Zhang *et al.*, 2015). The model from Kwon *et al.* (2015) is consistent with a $T_{\rm mid} = 55\,{\rm K}(r/10\ {\rm au})^{-0.65}$ for $r > 10$ au. While this is colder than other temperature structures (e.g. Zhang *et al.*, 2015), warmer models have no CO

snowline ($\sim 20\,\mathrm{K}$) throughout the radial extent of the disk. This is in tension with recent observations of a chemical tracer of the CO snowline, $N_2H^+$, which has been detected in the HL Tau disk (C. Qi, priv. comm.). Using the above temperature structure places the midplane CO snowline at approximately 50 au.

The observed integrated line intensity of $^{13}C^{17}O$ is converted to a column density of $^{13}C^{17}O$ gas under the assumption of both local thermodynamic equilibrium (LTE) and optically thin line emission. For each point in the radial profile $N(^{13}C^{17}O)$ is calculated via Equation 3.1.

Since the innermost regions of the $^{13}C^{17}O$ emission are affected by continuum absorption, the aim is to match the level of emission between $\sim 90 - 110$ au. As this radial location is beyond the model midplane CO snowline, any emission will be tracing CO gas from the molecular layer down to the CO snow surface (see Miotello *et al.*, 2014). An excitation temperature of $T_{\mathrm{ex}} = 25$ K is adopted for this region (see Akiyama *et al.*, 2011), but note that a range of values for this parameter ($20 - 80$ K) result in values of column density that are well within the observed error in the integrated intensity profile.

To convert from $^{13}C^{17}O$ to $^{12}C^{16}O$ isotope ratios consistent with the ISM are assumed,

$$n(^{12}C^{16}O)/n(^{13}C^{16}O) = 69,$$

$$n(^{12}C^{16}O)/n(^{12}C^{18}O) = 557,$$

$$n(^{12}C^{18}O)/n(^{12}C^{17}O) = 3.6$$

(Wilson, 1999). An $H_2$ column density is calculated assuming a moderately-depleted disk averaged $n(^{12}C^{16}O)/n(H_2)$ ratio of $5 \times 10^{-5}$. A total gas density is then calculated assuming that 80% of the gas mass lies in $H_2$ (e.g Rosenfeld *et al.*, 2013).

Based on the above, an increase in the total disk gas mass to $M_{\rm gas} = 0.20^{+0.6}_{-0.6}$ $M_\odot$ is required to match the observations between $90 - 110$ au (where errors are propagated from the observed radial intensity profile). The lower limit is higher than the current highest mass estimate. The resulting curve is shown in Figure 3.9 alongside the gas surface density values derived from the radial intensity profile of $^{13}C^{17}O$.

### 3.3.4 Assumptions affecting the gas mass

The conversion of line flux to gas mass depends on several assumptions. The derived gas mass is sensitive to the chosen conversion factor between CO and $H_2$ (see Bergin & Williams, 2017, for a review). While this factor is often taken to be $\sim 10^{-4}$, studies of individual protoplanetary disks have revealed carbon depletion from factors of five to orders of magnitude (e.g. Kama *et al.*, 2016a; McClure *et al.*, 2016), and surveys have demonstrated this phenomenon is widespread (e.g. Miotello *et al.*, 2017). The chosen value in this work of $n(^{12}C^{16}O)/n(H_2) = 5 \times 10^{-5}$ therefore accounts for a modest depletion factor of two, in agreement with disk chemical models at ages of $\sim$1 Myr (Bosman *et al.*, 2018; Schwarz *et al.*, 2018). The derived disk gas mass scales linearly with the inverse of the depletion factor, so under the assumption of no carbon depletion (e.g. $10^{-4}$), our derived disk mass would be 0.5 times the above quoted value.

In this analysis it is also assumed that the observations trace the full column of CO on both the 'near' and 'far' sides of the disk. This will not be the case if *i*) there is a significant fraction of CO frozen out in the disk midplane, or *ii*) if the $^{13}C^{17}O$ $J = 3$–2 emission is optically thick. In addition (as discussed in Section 3.3.2), Carrasco-González *et al.* (2019) have determined that the continuum optical depth in the disk is high, with $\tau \sim 8$ at 330 GHz. Therefore, the observations are not sensitive to CO emitting on the far side of the disk. In this

scenario, the true surface density of CO in the disk would be (at least) a factor of two higher in the regions affected by the dust opacity.

Observations of CO rovibrational lines toward the HL Tau envelope have revealed a higher $n(^{12}C^{16}O)/n(^{12}C^{18}O)$ ratio of $760 \pm 80$ compared to the canonical value. This is consistent with isotope-selective photo-dissociation and self-shielding (Smith *et al.*, 2015; Visser *et al.*, 2009). But, as these higher energy infrared transitions do not trace the same reservoir of CO probed in our sub-mm observations, the ISM values were used here. If the higher ratio applies, then a higher column of CO would be required to match the observations, increasing the derived gas mass (though by factors lower than the above examples).

The precise magnitude of these effects cannot be determined without dedicated modelling of the HL Tau disk. Nevertheless, this still implys that the derived gas mass here is a conservative lower limit. Future high spatial and spectral resolution observations of multiple CO isotopologues, also at lower frequencies, toward HL Tau will enable more stringent constraints on the gas mass in the disk, especially in the inner region that is affected by the dust opacity.

### 3.3.5 Comparison to other mass measurements

Tapia *et al.* (2019) use combined dust and gas evolutionary disk models to reproduce ALMA and VLA continuum profiles of the HL Tau disk from to $0.87 - 7.8$ mm. Their best fitting model possesses a dust mass of $4.8 \times 10^{-3}\,M_\odot$ with a gas-to-dust mass ratio of 50, resulting in a disk gas mass of $0.23\,M_\odot$. The result from the $^{13}C^{17}O$ therefore brings mass measurements from dust continuum and molecular line emission into agreement for the first time in this disk.

Wu *et al.* (2018) use $C^{18}O$ $J = 2$–1 SMA observations of HL Tau to derive a total disk gas mass of $2 - 40 \times 10^{-4}$ $M_\odot$, which is between a factor of $50 - 1000$ smaller than the gas mass implied here. However, the above work adopts a

$CO/H_2$ ratio of $2.7 \times 10^{-4}$, which assumes no C depletion, and that all potential volatile carbon in the disk is the form of CO (given an ISM C/H ratio of $1.4 \times 10^{-4}$; Cardelli *et al.* 1996). If the same ratio as Wu *et al.* (2018) is adopted, the resulting gas mass from the $^{13}C^{17}O$ would be $\sim$0.04 $M_\odot$, which is still a factor of $10 - 200$ higher than the gas mass derived from $C^{18}O$.

Using Equation 3.1 the values for $n(^{13}C^{17}O)$ and $n(^{12}C^{18}O)$ can be compared. A column density ratio of $\sim 250$ would imply that both lines are optically thin. However, using the data from the radial profile presented in Wu *et al.* (2018) for a radius of 100 au, the ratio is only $\sim 4$. This demonstrates that the $C^{18}O$ $J = 2 - 1$ emission is optically thick in the HL Tau disk, and is therefore not tracing the bulk gas mass in the molecular layer (also found for HD 163296 in Section 3.2).

### 3.3.6 The (in)stability of the disk

As in Section 3.2.7, the gravitational stability of the higher mass disk can be assessed using the Toomre $Q$ parameter (Toomre, 1964), assuming a central star mass of 1.7 $M_\odot$, (Pinte *et al.* 2016). The resulting radial profile of $Q$ is shown in Figure 3.10a. The $^{13}C^{17}O$ observations therefore support a picture in which the disk around HL Tau is gravitationally unstable ($Q < 1.7$) from approximately $50 - 110$ au (with minimum $Q = 1.1^{+0.5}_{-0.2}$ at $r = 77$ au). Taking into account observational uncertainties, it is also possible that $Q < 1$ between $60 - 100$ au.

If the disk around HL Tau is threaded by a magnetic field, then this may offer an additional mechanism to support the disk against self-gravity. In these cases, $Q$ is modified by a factor $\sqrt{1 + 1/\beta_{\rm p}}$. The plasma parameter is given by:

$$\beta_{\rm p} = \frac{2P\mu_0}{B^2}$$

where $P$ is the gas pressure, $\mu_0$ is he permeability of free space and $B$ is the

magnetic field strength. The threshold for instability lies within the range $Q \lesssim 1.2 - 1.4$ (Kim & Ostriker, 2001). In general, values of $\beta_{\rm p}$ range from $\sim 10$ under ideal MHD conditions (Forgan *et al.*, 2017) and up to $10^4$ for non-ideal MHD (Hasegawa *et al.*, 2017). Such values do not alter the minimum Toomre $Q$ value by more than $\sim 5$ per cent, suggesting that even if the HL Tau disk possesses a strong magnetic field ($\beta_{\rm p} \sim 10$), it would not be sufficient to move the disk into a stable regime.

### 3.3.7 The region of instability in context

Figure 3.10b shows the region of instability in the HL Tau disk with respect to the Band 7 (0.9 mm) continuum observations of ALMA Partnership *et al.* (2015). The unstable region spans several of the bright rings and dark gaps identified in the dust disk (B3 - B7 and D4 - D7). Modelling of unstable disks with a decoupled dust component shows grains concentrating in spiral arms (e.g. Dipierro *et al.*, 2015a; Rice *et al.*, 2004). Therefore it is not immediately clear how to reconcile such an apparently unstable disk with the ordered concentric rings observed in the dust.

Several studies have shown that the 'double gap' feature from $\sim 65 - 74$ au (D5 - B5 - D6) can be reproduced by the presence of a planet with mass between $\sim 0.2 - 0.6$ $\rm M_{Jup}$ (Dipierro *et al.*, 2015b; Dong *et al.*, 2018; Jin *et al.*, 2016), which is supported by mm–cm observations across this radial region (Carrasco-González *et al.*, 2019). The higher gas surface density revealed by the $^{13}$C$^{17}$O observations implies that mm-sized grains would be better coupled to gas than in the above works. Therefore, larger planet masses would be required to match the observed dust structures. When considering the lower bound of the observational errors, $Q \leq 1$ from $\sim$ $60 - 100$ au. Here the local cooling time is expected to be short (e.g. Clarke & Lodato, 2009; Rafikov, 2005), meaning that this region of the disk

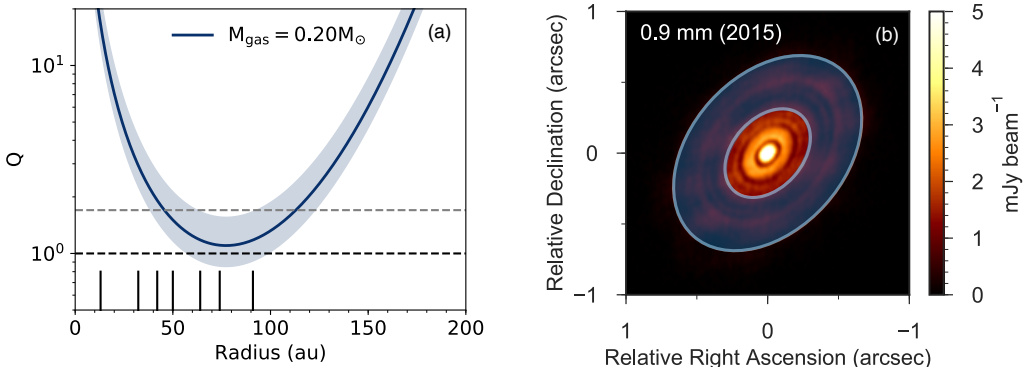


Figure 3.10: **(a)** Radial Toomre $Q$ parameter for our derived disk mass. Shaded regions denote the errors propagated from the radial intensity profile. Dashed grey and black lines mark the $Q = 1.7$ and $Q = 1.0$ levels, respectively. The radial locations of the 'D' gaps reported in ALMA Partnership *et al.* (2015) are shown with vertical black ticks. **(b)** Same as Figure 3.8(a), where the blue shaded area highlights the unstable region of the disk, with $Q < 1.7$ from (a).

would undergo gravitational fragmentation. This scenario is in agreement with dedicated modelling of star-disk systems with similar properties as HL Tau, which form fragments with masses between $1 - 5$ $M_{Jup}$ (Boss, 2011). Therefore, if such a planet is confirmed to be the origin of this observed gap structure, then it is posssible that it has formed via gravitational fragmentation.

Recently, Yen *et al.* (2019) detected a spiral feature in observations of $HCO^+$ $J = 3$–2 toward HL Tau. While they attribute the spiral to in-falling material from the surrounding envelope, this feature crosses our region of instability in the disk. Chemical models of gravitationally unstable disks have predicted $HCO^+$ to be a tracer of spiral structure (Douglas *et al.*, 2013; Ilee *et al.*, 2011). In light of this, it is possible that the spiral structure on small ($\lesssim 100$ au) scales could be due to gravitational instability within the disk.

## 3.4 Conclusions

This chapter presents the first detections of $^{13}C^{17}O$ in protoplanetary disks showcasing the power of this isotopologue as a tracer of disk gas mass. This work provides robust evidence that disks are more massive than previously assumed (see also Zhu *et al.*, 2019). The $^{13}C^{17}O$ J=3-2 detections show that the $C^{18}O$ J=2-1 lines are not optically thin throughout the radial extent of these disks. The updated CO gas mass for the HD 163296 disk is factor of 3.5 higher and a factor of 10 higher in the HL Tau disk. This work shows, model independently, that $C^{18}O$ is not a reliable tracer of disk gas mass. Future observations of this tracer in more sources may help to address the discrepancy between the masses of disks and the observed exoplanet population (Manara *et al.*, 2018). These new disk masses also offer GI and planet formation via disk fragmentation as a possible mechanism for the origin of the structures and proposed gas-giant planets observed in both Class I and II disks.

# Chapter 4

# $H^{13}CO^+$ and $HC^{15}N$ in the HD 97048 Disk

## 4.1 Introduction

In Chapter 3 it was demonstrated that $^{13}C^{17}O$ emission is a robust tracer of total CO gas mass. However, molecular lines aside from CO can be valuable probes of the disk physical conditions. A legacy of observations of protoplanetary disks with single dish telescopes have shown that $HCO^+$ and HCN are two of the brightest molecules in these objects (e.g., Chapillon *et al.*, 2012; Dutrey *et al.*, 1997; Kastner *et al.*, 1997; Piétu *et al.*, 2007; Thi *et al.*, 2004; van Zadelhoff *et al.*, 2001). $HCO^+$ and HCN emission is commonly interpreted to reflect the disk ionization level and impinging UV field respectively. Emission from $HCO^+$ and HCN and selected isotopologues have now been spatially resolved in a number of disks with ALMA (see Section 1.5.4 and e.g. Guzmán *et al.*, 2017; Huang *et al.*, 2017) and exhibit centrally peaked or ringed radial emission profiles. These observed morphologies highlight that there are likely different physical and chemical processes that shape the abundance distributions of different molecules in disks.

This chapter presents the first detections of $H^{13}CO^+$ and $HC^{15}N$ in the HD 97048 disk. As discussed in Section 1.5.4, molecular sub-structure can arise without

any underlying ringed gas and/or dust structure due to the interplay between chemistry and, e.g., radiation. This chapter therefore investigates whether or not chemistry alone can explain the radial emission profiles of molecular lines detected in the HD 97048 disk, or if modifications to the underlying disk gas density or temperature structure are required.

## 4.2 The HD 97048 disk

HD 97048 is a 2.4 $M_\odot$ Herbig Ae/Be star with spectral type B9/A0 (van den Ancker *et al.*, 1998; van Leeuwen, 2007; Wichittanakom *et al.*, 2020) located in the Chameleon I star-forming region. The HD 97048 disk has been well studied over optical to infra-red wavelengths with observations revealing much substructure in the warm gas and small dust grains. High-resolution observations with VLT/SPHERE show four rings in the disk with observations probing disk radii from 45 to 400 au (Ginski *et al.*, 2016). The first spatially resolved observations of the mm-sized dust and molecular gas were presented by Walsh *et al.* (2016a) using ALMA and these data revealed the full spatial extent of the molecular disk. The mm-sized dust is observed to extend to 400 au in radius; while, in comparison, the flared molecular disk, revealed in CO $J = 3 - 2$ emission, is significantly larger and extends to 860 au. There is a decrease in the continuum flux within 55 au and there are three continuum emission rings peaking at 55, 160 and 290 au. There is also an inner cavity in the CO emission but only out to 11 au (van der Plas *et al.*, 2009, 2015). The origin of the CO cavity is proposed to be due to photodissociation of the CO gas by stellar radiation. The detected $HCO^+$ emission is more compact than that for CO, extending out to 540 au only (van der Plas *et al.*, 2017). Recently, Pinte *et al.* (2019) reported the indirect detection of a few Jupiter mass planet at 130 au via kinematic analyses of the $^{13}CO$ line emission (see Figure 1.9). Hence, the HD 97048 disk is another prime

source in which to study the impact of potential gas-giant planets on the disk structure and chemistry. This source differs to HD 163296 as the HD 97048 disk is an extremely flared disk (Lagage *et al.*, 2006; Walsh *et al.*, 2016a) whereas HD 163296 disk is relatively flat in comparison (Muro-Arena *et al.*, 2018).

Although this is the brightest disk observed at sub-mm wavelengths, it remains poorly studied in terms of its molecular content. Particularly lacking are spatially resolved observations of key molecular tracers aside from those reported above. Nevertheless, thanks in part to observations with *Herschel*, it is known to host a chemically-rich gaseous disk. Spatially unresolved emission lines that have been observed include those from $H_2$, [OI], [CII], OH and $CH^+$ (Carmona *et al.*, 2011; Fedele *et al.*, 2013; Meeus *et al.*, 2012, 2013a).

### 4.2.1 Line imaging

The HD 97048 disk was observed at ALMA Band 7 during Cycle 0 (2011.0.00863.S, PI: C. Walsh). This work begins with self-calibrated, phase-corrected, and continuum-subtracted measurement sets from Walsh *et al.* (2016a). This Chapter also makes use of the archival data from ALMA Band 7 Cycle 2 observations (2013.1.00658.S; P.I. G. van der Plas). The $HCO^+$ $J = 4-3$ was first presented in van der Plas *et al.* (2017). These data were self-calibrated using CASA. The data set consists of four spectral windows, two of which were tuned for continuum observations and two of which were centred on the CO $J = 3-2$ and $HCO^+$ $J = 4-3$ spectral lines. The two broadband continuum windows were self-calibrated after flagging the line containing channels. Two rounds of phase calibration were applied then one amplitude calibration. The resulting measurement sets were then used to self-calibrate the respective higher spectral resolution CO $J = 3 - 2$ and $HCO^+$ $J = 4 - 3$ line containing spectral windows. The continuum emission was then subtracted from the two line containing spectral windows using the CASA

task, *uvcontsub*.

The data and lines targeted are listed in Table 4.1 were imaged in CASA using CLEAN with natural weighting and using a Keplerian mask. The Keplerian mask was set to encompass emission from 1 au to 800 au. Table 4.1 lists the rms noise ($\sigma$) of each line imaged at its respective Hanning-smoothed spectral resolution, as well as the image parameters, and the intrinsic properties of the transitions. A comparison of the peak flux densities and integrated intensities for the CO $J = 3 - 2$ line that was observed in both data-sets used here shows that they agree to within 10%.

The CO $J = 3-2$ line emission suffers from missing emission about the source velocity, from 3.4 to 5.7 km $s^{-1}$ inclusive. This is the result of either spatial filtering due to bright background emission or foreground absorption. Spatial filtering is a possibility because the source is in proximity to the Chameleon I molecular cloud. This effect is seen in both the channel maps and line profiles presented by Walsh *et al.* (2016a) and van der Plas *et al.* (2017). This work focuses on the detection of $H^{13}CO^+$ and $HC^{15}N$ and there is no indication that they are also affected by this phenomenon. A possible explanation is that this is due to the higher-lying energy levels of these transitions (see Table 4.1), or due to the lower abundances of $HCO^+$, $H^{13}CO^+$, and $HC^{15}N$, in either background or foreground material, when compared with CO.

Table 4.1: ALMA Band 7 observations and detected molecular lines in the HD 97048 protoplanetary disk.

| Observations | Cycle 0 (2011.0.00863.S) | | | Cycle 2 (2013.1.00658.S) | |
|---|---|---|---|---|---|
| Date observed | 14 December 2012 | | | 22 May 2015 | |
| Baselines (m) | 15.1 - 402 | | | 21.4 - 555.5 | |
| On source integration time (min,sec) | 23,59 | | | 7,10 | |
| Number of antenna | 22 | | | 36 | |
| CLEAN image weighting | natural | | | | |
| Molecule | CO | $H^{13}CO^+$ | $HC^{15}N$ | CO | $HCO^+$ |
| Transition | $J = 3 - 2$ | $J = 4 - 3$ | $J = 4 - 3$ | $J = 3 - 2$ | $J = 4 - 3$ |
| Frequency (GHz) | 345.796 | 346.998 | 344.200 | 345.796 | 356.734 |
| Einstein A coefficient ($s^{-1}$) | 2.497e-06 | 3.288e-03 | 1.879e-03 | 2.497e-06 | 3.627e-03 |
| $E_{up}$(K) | 33.19 | 41.63 | 41.30 | 33.19 | 42.80 |
| Synthesised beam | $0\farcs74 \times 0\farcs51$ | $0\farcs74 \times 0\farcs51$ | $0\farcs74 \times 0\farcs52$ | $0\farcs71 \times 0\farcs44$ | $0\farcs67 \times 0\farcs42$ |
| Beam P.A. | -26° | -26° | -27° | -161° | -161° |
| Spectral resolution (km $s^{-1}$) | 0.21 | 0.21 | 0.21 | 0.10 | 0.10 |
| $\sigma$ (Jy $beam^{-1}$ per channel[a]) | 0.016 | 0.016 | 0.016 | 0.016 | 0.019 |

The values for the line frequencies, Einstein A coefficients, and upper energy levels ($E_{up}$) are from the Leiden Atomic and Molecular Database: http://home.strw.leidenuniv.nl/~moldata/ (LAMDA; Schöier *et al.*, 2005).

[a] At the stated spectral resolution.

## 4.3 Results

### 4.3.1 Channel maps, moment maps, and line profiles

Figure 4.1 shows the $HCO^+$ and $H^{13}CO^+$ channel maps at the native spectral resolution of the $H^{13}CO^+$ data, 0.21 km $s^{-1}$. The $HCO^+$ data is slightly over-sampled in order to allow a direct comparison between the two molecules. Both channel maps have a $1\sigma$ rms noise level of 0.019 Jy $beam^{-1}$ $channel^{-1}$ and reach a S/N of 23 and 6, respectively. To obtain a robust detection of $HC^{15}N$ in the channel maps the data were re-binned to a velocity resolution of 0.5 km $s^{-1}$, and these channel maps are shown in Figure 4.2. The $H^{13}CO^+$ channel maps at the same velocity resolution are also shown in Figure 4.2 for ease of comparison.

For $HCO^+$, the highest velocities at which emission is robustly detected ($> 3\sigma$ within a $0\farcs5$ aperture) are in channels at -0.17 km $s^{-1}$ and 9.55 km $s^{-1}$, for the blue- and red-shifted emission, respectively. Assuming a disk inclination of 41°and a stellar mass of 2.5 $M_\odot$, $HCO^+$ emission is detected down to an average radial distance of $41 \pm 2$ au. This is different to the value of 28 au stated by van der Plas *et al.* (2017); however, note that different imaging parameters are used. Here, natural weighting is adopted in the imaging to enhance the S/N for the detected lines. On the other hand, van der Plas *et al.* (2017) used Briggs weighting in their imaging resulting in a smaller synthesised beam. In comparison, the highest velocity CO emission from both the Cycle 0 and Cycle 2 data as determined here corresponds to emission detected down to an average radial distance of $14 \pm 1$ au. This is in agreement with van der Plas *et al.* (2017). The errors in these radii are propagated from the velocity resolution of the channel maps (see Table 4.1).

The integrated intensity maps and the intensity-weighted velocity maps for $HCO^+$, $H^{13}CO^+$ and $HC^{15}N$ are presented in Figure 4.3. The moment 0 maps were made using a Keplerian mask and the moment 1 maps were made using

a $3\sigma$ clip. The $HCO^+$ intensity-weighted velocity map has a clear Keplerian velocity pattern on large spatial scales and both the $H^{13}CO^+$ and $HC^{15}N$ intensity-weighted velocity maps are consistent with this.

Figure 4.4 shows the $H^{13}CO^+$ and $HC^{15}N$ line profiles mirrored about the source velocity. The $H^{13}CO^+$ line profile was extracted from within the region defined by the $3\sigma$ contour of the $HCO^+$ integrated intensity (see Figure 4.3). The extraction region for the $HC^{15}N$ line profile was chosen by eye due to the low S/N. An ellipse that encompassed the extent of the emission in the integrated intensity map and centred on source was used. The line profiles cover a velocity range of $\pm$ 15 km s$^{-1}$ about the source velocity and are shown at a velocity resolution of 0.5 km s$^{-1}$. They reach a S/N of 5 and 3 with a $1\sigma$ noise level of 0.048 Jy and 0.035 Jy, respectively. The residuals of the mirrored line profiles were calculated to show that the emission is not significantly asymmetric and to further confirm the Keplerian nature of the emission.

### 4.3.2 Deprojection and azimuthal averaging

To better quantify the radial structure of the emission from each molecular transition, the Keplerian-masked integrated intensity maps were deprojected and azimuthally averaged (as described in Section 3.2.2). The radial intensity profiles and the associated errors for CO, $HCO^+$, $H^{13}CO^+$, and $HC^{15}N$ are shown in Figure 4.6. Also plotted is the mm-dust radial profile from Walsh *et al.* (2016a) where the image was generated using super-uniform weighting in CLEAN. The continuum profile shown by the grey dashed line in Figure 4.5 is that derived from modelling the emission in the *uv* domain. The profile has rings which peak at 55 and 160 au with a gap at 110 au and an additional shoulder of emission at 290 au. Although these data were lower spatial resolution than that presented in van der Plas *et al.* (2017), modelling the continuum emission in the *uv* domain

successfully predicted the presence and location of the outer ring(s) that were subsequently imaged in that work (see also Zhang *et al.*, 2016).

The radial profiles of the CO and $HCO^+$ emission show no deviation from a monotonically decreasing radial distribution. As discussed previously, the CO $J = 3 - 2$ emission suffers from missing emission about the source velocity, from 3.4 to 5.7 km $s^{-1}$; therefore, the radial profile likely underestimates the CO flux from the disk. The profile is centrally peaked because the observations do not have the spatial resolution to resolve the inner CO cavity detected in CO ro-vibrational lines (van der Plas *et al.*, 2009). The $HCO^+$ $J = 4 - 3$ is also expected to be optically thick and the radial profile is also centrally peaked. In comparison, the more optically thin tracers, $H^{13}CO^+$ and $HC^{15}N$, show a different radial behaviour. Whilst the $H^{13}CO^+$ $J = 4-3$ radial profile is also centrally peaked but the intensity does not fall off as steeply as the profile for $HCO^+$. Additionally, the intensity profile appears to have a step-like morphology compared to the smooth $HCO^+$ profile. These changes in slope coincide approximately with the locations of the second and third continuum emission rings.

Comparatively, the $HC^{15}N$ profile appears to have a ring-like morphology with the peak in emission occurring at $\approx 100$ au. This is consistent with the moment 0 map shown in Figure 2, but due to the low S/N of the data a centrally peaked smooth radial intensity profile cannot be ruled out. Also plotted in Figure 4.5 with a black dashed line is the mm-dust radial profile from Walsh *et al.* (2016a) convolved with a 50 au beam. The $HC^{15}N$ follows the mm-sized dust distribution at the spatial resolution of the currently available observations. Further analysis of the $HC^{15}N$ emission is not conducted here due to the unavailability of observations of line emission from the main isotopologue, HCN.

The $HCO^+$ to $H^{13}CO^+$ integrated intensity ratio across the disk is shown in Figure 4.6. To directly compare the $HCO^+$ and $H^{13}CO^+$ emission from the

disk, the channel maps have been smoothed to the same beam size using the CASA task, *imsmooth*. The new beam is $0\farcs7 \times 0\farcs6$ with a position angle of -26°. The same analysis using a *uvtaper* when CLEANing the lines (see Chapter 2) to enforce a common beam was also tested and found that the results were consistent with using *imsmooth*. New moment maps were generated and radial profiles from the resulting integrated intensity maps used to calculate the $HCO^+$ to $H^{13}CO^+$ integrated intensity ratio across the disk. The smoothed radial profiles are also shown in Figure 4.6. The plotted ratio is truncated at the point where the $H^{13}CO^+$ profile falls below the noise level. The computed errors have been propagated from the standard error for each profile generated during azimuthal averaging. The expected ratio is $\approx 69$ for the case where both lines are optically thin, reflecting the underlying elemental ratio for $^{12}C/^{13}C$ in the ISM (e.g., Wilson, 1999). The observed ratio decreases slightly with radius but is constant across the disk within the error bars, and has an average value of $12 \pm 3$. This is much lower than the canonical value and confirms that at least the $HCO^+$ emission is optically thick.

## 4.4 Chemical modelling

In this section the origin of the radial distribution of the detected $H^{13}CO^+$ emission and the $HCO^+/H^{13}CO^+$ integrated intensity ratio is investigated. The line emission is modelled for both molecules to explore two hypotheses i) whether or not chemistry alone can explain the radial emission profiles, or, ii) if modifications to the underlying disk structure need to be invoked (e.g., gas cavities). The $HC^{15}N$ emission is not modelled since complementary observations of the main isotopologue HCN do not exist. However, this detection and related chemistry is discussed in Section 4.5.3.

The underlying physical disk structure is the publicly available HD 97048

disk structure from the DIscANAlysis project (DIANA)[1]. The aim of this large collaboration is to generate disk models that can reproduce multi-wavelength (from UV to sub-mm) observations of sources for which data are available (see Woitke *et al.* 2016, Kamp *et al.* 2017, and Woitke *et al.* 2019, for further details on the models). The underlying model assumes a parametric disk model, and for which the gas temperature is self-consistently calculated considering the balance between cooling and heating mechanisms for the gas. The resulting model fits the SED of the source and aims to reproduce the integrated flux from far-IR gas emission lines. The underlying disk structure is assumed to be smooth; however, to better fit SEDs at near to mid-IR wavelengths, models are adapted to include a dust (and gas) cavity if required. Generally, models have not been generated to account for dust gaps and rings as seen in spatially-resolved mm dust continuum images.

This work uses the gas density, gas temperature, and ionisation structure from the DIANA model of HD 97048. This model has a total disk (gas plus dust) mass of $\approx$ 0.1 $M_{\odot}$. Assuming a global gas-to-dust mass ratio of $\sim$ 100, this disk mass is consistent with the upper limit for the dust mass derived from the (sub)mm continuum emission observed with ALMA and corrected for the revised distance ($184^{+2}_{-2}$ pc) to the source ($\lesssim$ 0.09 $M_J$; Walsh *et al.*, 2016a). The ionisation rate throughout the disk is the sum of both the cosmic-ray and X-ray ionisation rates. Maps of the disk physical structure as a function of disk radius and height are shown in Figure 4.7. The best-fit DIANA model has a cavity out to 65 au in both the gas and the dust and a small inner ring of gas and dust out to 6 au. We note here that the size of this cavity is greater than that observed with ALMA in the mm-dust continuum ($\approx$ 50 au).

Due to chemistry, the abundance distribution of $HCO^+$ will not have a con-

[1]The full DIANA models are publicly available: http://www-star.st-and.ac.uk/~pw31/DIANA/DIANAstandard/

stant value relative to the underlying gas density as is commonly assumed in parametric models. Following Aikawa *et al.* (2015), the $HCO^+$ abundance is derived analytically, $n(HCO^+)$ cm$^{-3}$, throughout the disk under a few acceptable and tested assumptions. Because the chemical timescale in a disk is significantly shorter than the disk lifetime steady state is a reasonable assumption, i.e.,

$$\frac{dn(HCO^+)}{dt} = R_f - R_d = 0,$$

where $R_f$ and $R_d$ are the rates of $HCO^+$ formation and destruction, respectively. The main formation reaction for $HCO^+$ is via CO,

$$H_3{}^+ + CO \longrightarrow HCO^+ + H_2,$$

and the primary destruction reaction is dissosiative recombination with an electron,

$$HCO^+ + e^- \longrightarrow H + CO.$$

The destruction of $HCO^+$ via grain-surface recombination is ignored as this is only dominant in the inner $< 10$ au of the disk in the dense midplane where dust grains become the main charge carrier and this region of the disk is not modelled. It is also assumed that $HCO^+$ is the dominant cation in the molecular region of the disk as has been confirmed by full chemical models (e.g.; Walsh *et al.* 2012, Aikawa *et al.* 2015). The resultant abundance of $HCO^+$ is given by;

$$n(HCO^+) = \frac{k_3\ n(CO)\ n(H_3{}^+)}{k_4\ n(e^-)}.$$

The reaction rate coefficients, $k_i$, are given in Table 4.2, where $i$ is the number of the reaction as compiled by Aikawa *et al.* (2015).

The CO abundance distribution is parameterized as described by Williams &

Table 4.2: Reaction rate coefficients from UDFA RATE12[1] used in the analytical formula from Aikawa *et al.* (2015).

| $i$ | Reactions | $\alpha$ | $\beta$ |
|---|---|---|---|
| 1 | $H_2 + crp \longrightarrow H_2^+ + e^-$ | - | - |
| 2 | $H_2^+ + H_2 \longrightarrow H_3^+ + H$ | 2.08(-9) | 0.0 |
| 3 | $H_3^+ + CO \longrightarrow HCO^+ + H_2$ | 1.61(-9) | 0.0 |
| 4 | $HCO^+ + e \longrightarrow H + CO$ | 2.40(-7) | -0.69 |
| 5 | $H_3^+ + e \longrightarrow H_2 + H$ or $H + H + H$ | 7.20(-8) | -0.5 |

Rate coefficients are given in the form of $k = \alpha \times (T/300.0)^{\beta}$ $cm^3s^{-1}$ and $A(B)$ stands for $A \times 10^B$
[1] http://udfa.ajmarkwick.net/index.php, (McElroy *et al.*, 2013)

Best (2014). CO is present in the disk with a relative abundance of $n(CO)/n_H = 1.4 \times 10^{-4}$ if the temperature is greater than 20 K (the approximate freezeout temperature of CO) and if the vertical column density of $H_2$ (integrated vertically downwards from the disk surface) is greater than $1.3 \times 10^{21}$ $cm^{-2}$. Hence, there is no CO depletion factor applied here, because, as confirmed by Kama *et al.* (2016a) HD 97048 exhibits no evidence of carbon depletion. Here, $n_H$ is the total number density of hydrogen nuclei. This simple prescription takes into account the two primary destruction pathways for CO: freezeout onto dust grain surfaces in the midplane, and photodissociation in the atmosphere. The column density upper limit comes from modelling work by Visser *et al.* (2009) and observations of HD 163296 by Qi *et al.* (2011). The $H_3^+$ and electron abundances are given by

$$n(H_3^+) = \frac{1}{2}\, n_H\, \frac{\zeta}{k_5\, n(e^-)\; +\; k_3\, n(CO)},$$

and

$$n(e^-) = \sqrt{\frac{\zeta\, n_H}{2\, k_4}},$$

(Aikawa *et al.*, 2015). Here $\zeta$ is the sum of the cosmic ray and X-ray ionisation rates from the DIANA model. These equations are determined by solving the rate equations for each species under the steady state assumption.

The $H^{13}CO^+$ abundance is determined by simply assuming that

$$H^{12}CO^+/H^{13}CO^+ = {}^{12}C/{}^{13}C \;=\; 69$$

(e.g., Wilson, 1999). Although isotope fractionation processes (e.g., fractionation reactions and isotope-selective photodissociation) will cause the $^{12}CO/^{13}CO$ and $H^{12}CO^+/H^{13}CO^+$ abundance ratios to vary throughout the disk (Woods & Willacy, 2009), developing and running a full chemical model that includes fractionation is beyond the scope of this work and best addressed in a future dedicated study. In a previous study, Woods & Willacy (2009) show that the $n(H^{12}CO^+)/n(H^{13}CO^+)$ ratio has a value of $\approx 40-60$ in the layer in the inner disk ($\lesssim 30$ au) at which $HCO^+$ reaches the highest fractional abundance ($\sim 10^{-9}$). The resulting abundance distributions as a function of disk radius and height for CO, $HCO^+$ and $H^{13}CO^+$ are shown in Figure 4.7.

Synthetic channel maps were generated using LIME version 1.6 (LIne Modelling Engine; Brinch & Hogerheijde, 2010) using the molecular data files for $HCO^+$ and $H^{13}CO^+$ from the LAMDA molecular database[1]. To check whether or not the assumption of LTE was appropriate, the critical density of the $HCO^+$ $J = 4-3$ transition was calculated using the collisional rates from Flower (1999). The critical density was determined to be $10^6$ cm$^{-3}$ in the temperature range from 30 to 100 K. In the region of the disk model where the $HCO^+$ is present the gas density is above this value (see Figure 4.7); therefore, it was confirmed that LTE is an appropriate assumption. The models were made using the same position and inclination angles of the source. The resulting image cubes were then smoothed to the same Gaussian beam as the $HCO^+$ and $H^{13}CO^+$ observations. The simulated channel maps were used to generate azimuthally-averaged radial profiles from the resulting integrated intensity maps and then directly compared

[1]LAMDA data files are available online at: http://home.strw.leidenuniv.nl/~moldata/

with the observations. For the $H^{12}CO^+/H^{13}CO^+$ integrated intensity ratio the images were smoothed to the same common beam as described for the observational dataset. A range of models were run step-by-step altering the initial model to find a best by-eye fit to the observed radial profiles. The specifics of the models are summarised in Table 4.3. The resulting modelled radial intensity profiles for $HCO^+$ and $H^{13}CO^+$, and the line ratio, are shown in Figure 4.8 where the coloured lines are the observations and the black lines are the models.

### 4.4.1 Fiducial model results

Model 1 is the fiducial model as described above and this model is found to overestimate the magnitude of the emission for both the $HCO^+$ and $H^{13}CO^+$ lines. The difference between the modelled and observed peak flux for $HCO^+$ and $H^{13}CO^+$ are around a factor of 1.3 and 2.4, respectively. The morphology of the modelled emission also does not match the observed profiles. The latter are centrally peaked whereas the modelled profiles peak in emission at $\approx 100$ au. The resulting line ratio also does not exhibit the same radial behaviour as the observation as it increases radially from 6 to $26 \pm 1$.

### 4.4.2 Modifications to the fiducial model

Since the fiducial model is a poor fit to the observations the next step is to modify this model step by step in order to better reproduce the data. The first aim is to fit the radial profiles beyond a radius of $\approx 100$ au. In Model 2 the abundance of $HCO^+$ was multiplied by a factor, $\kappa_{HCO^+}$, of 0.2 relative to the abundance calculated using the analytical chemical model. This factor was determined by gradually reducing the multiplication factor in steps of 0.1 in each test, i.e., [0.9, 0.8, ...], until an acceptable by-eye fit to the $HCO^+$ was found. The multiplicative factor $\kappa_{H^{13}CO^+}$ is additionally applied to the $H^{13}CO^+$ abundance

which alters the $n(H^{12}CO^+)/n(H^{13}CO^+)$ ratio in the disk. For Model 2 $\kappa_{H^{13}CO^+}$ is 1 i.e. $n(H^{12}CO^+)/n(H^{13}CO^+)$ is 69. A comparison with the observed profiles shows that good agreement with the radial integrated intensity profile for $HCO^+$ emission is now obtained beyond 100 au. The overall decrease in abundance of a factor of 5 that is required here indicates that either the gas surface density is overestimated by this factor in the disk, or that the disk temperature of the emitting layer is over-estimated, or that the analytical chemical model describing $HCO^+$ is over-predicting the fractional abundance. However, in this model the $H^{13}CO^+$ peak flux is now under-predicted. The resulting $H^{12}CO^+/H^{13}CO^+$ integrated intensity ratio still does not exhibit the same radial behaviour as the observations and is increasing radially from 16 to $44 \pm 2$.

The next iterations of the model are to reconcile the $HCO^+$ model and observations in the inner disk and apply the same changes to the $H^{13}CO^+$ in order to retain their abundance ratio throughout. In Model 3 the disk structure is modified by hand to include gas in the cavity from $\approx$ 6 to $\approx$ 65 au. The gas density, temperature, and molecular abundances within the cavity are set equal to the values at the inner edge of the model gas disk. An LTE model with gas in the cavity and with 0.2 times the $HCO^+$ abundance ($\eta_{cavity}$) used in Model 2 reproduces well the observed radial profile (see Figure 4.8). The continued disagreement with the $H^{13}CO^+$ observations and models shows that the initial assumption of a globally constant value for $n(H^{12}CO^+)/n(H^{13}CO^+)$ of 69 may not be appropriate.

For the $H^{13}CO^+$, further modifications to this model are required to better reproduce the observations. The disk $n(H^{12}CO^+)/n(H^{13}CO^+)$ abundance ratio is altered globally by increasing $n(H^{13}CO^+)$ relative to the values in Model 3. The best by-eye fit for $\kappa_{H^{13}CO^+}$ was found to be 2 relative to the abundances in Model 2. This results in a global disk $n(H^{12}CO^+)/n(H^{13}CO^+)$ abundance

ratio of 35. This is not unrealistic as chemical models that include chemical isotope fractionation processes do predict a decrease in $n(^{12}\mathrm{CO})/n(^{13}\mathrm{CO})$ and $n(\mathrm{H}^{12}\mathrm{CO}^+)/n(\mathrm{H}^{13}\mathrm{CO}^+)$ by at most a factor of two in the midplane (Miotello *et al.*, 2014; Woods & Willacy, 2009). This model provides a much improved fit in the inner disk within 200 au in the $\mathrm{H}^{13}\mathrm{CO}^+$, but there is still not enough $\mathrm{H}^{13}\mathrm{CO}^+$ emission in the outer disk.

In Model 5 the $n(\mathrm{H}^{12}\mathrm{CO}^+)/n(\mathrm{H}^{13}\mathrm{CO}^+)$ ratio is decreased in the outer disk (>200 au) further to better fit the $\mathrm{H}^{13}\mathrm{CO}^+$ observations. The best by-eye fit for $\kappa_{\mathrm{H}^{13}\mathrm{CO}^+}$ was found to be 6 relative to the abundances in Model 2 resulting in a $n(\mathrm{H}^{12}\mathrm{CO}^+)/n(\mathrm{H}^{13}\mathrm{CO}^+)$ ratio of 14 in the outer disk . This suggests the presence of two carbon chemical fractionation regimes traced in $\mathrm{H}^{13}\mathrm{CO}^+$ in the HD 97048 disk. The feasibility of this scenario and possible explanations will be discussed in Section 4.5.

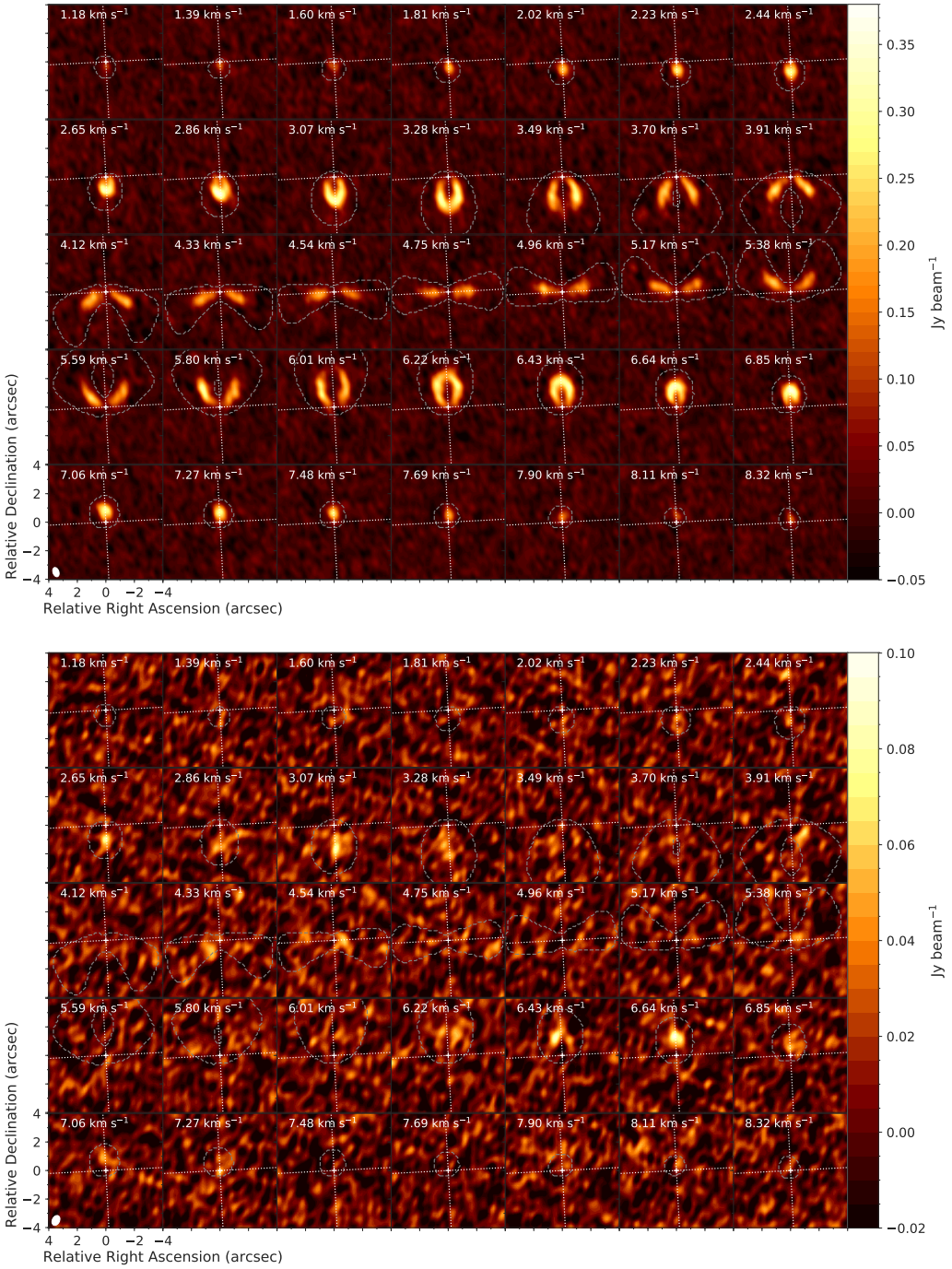


Figure 4.1: $HCO^+$ (top) and $H^{13}CO^+$ (bottom) channel maps with a velocity resolution of 0.21 km s$^{-1}$. The rms noise, $\sigma$, is 0.016 Jy beam$^{-1}$ per channel in both maps and the emission is detected with a S/N of 25 and 7 respectively. The grey dashed contour shows the Keplerian mask used and the dotted white lines mark the major and minor axes of the disk.

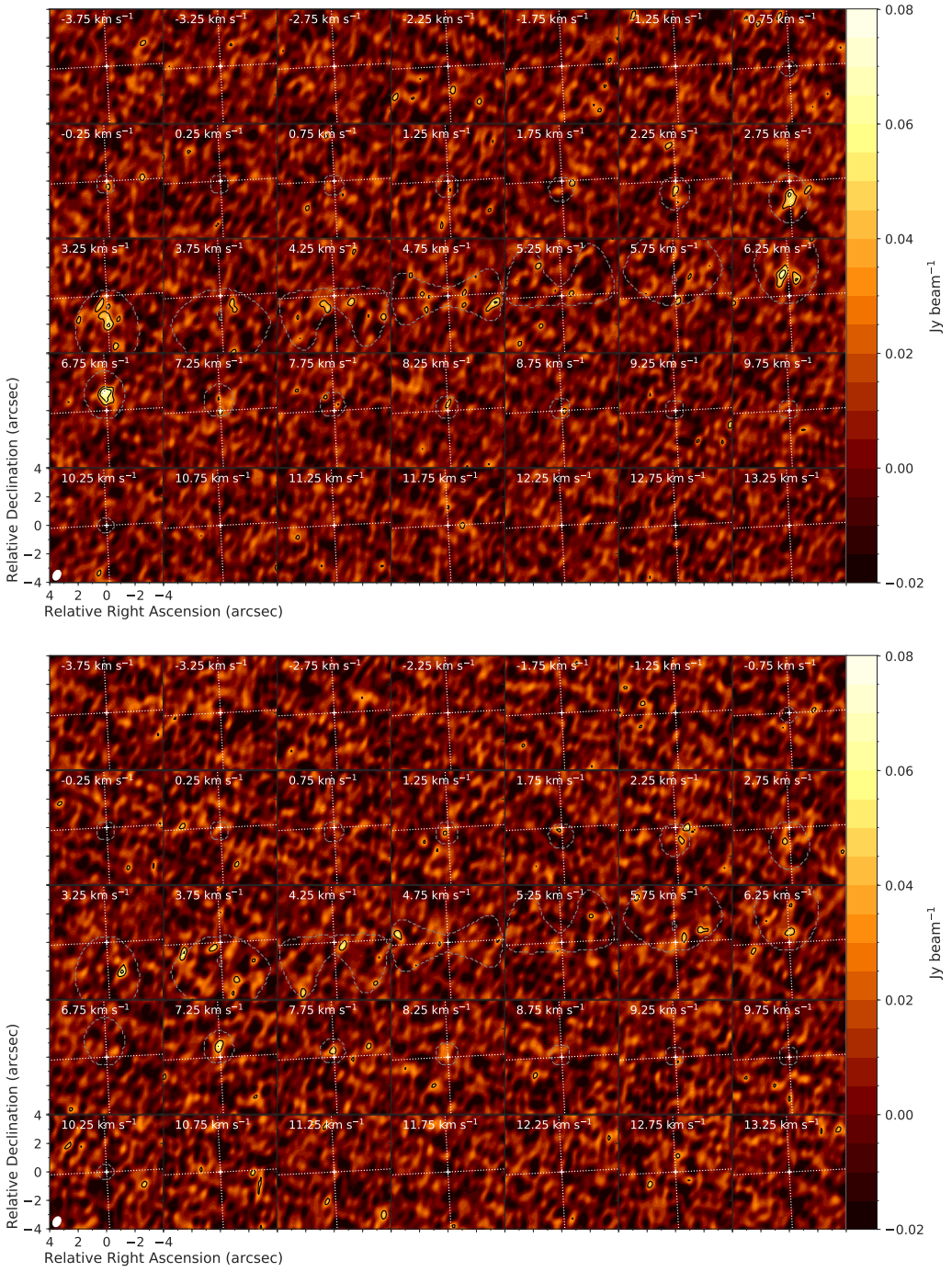


Figure 4.2: $H^{13}CO^+$(top) and $HC^{15}N$ (bottom) channel maps with a velocity resolution of 0.5 km $s^{-1}$. The r.m.s. for each map are 0.011 Jy $beam^{-1}$ km $s^{-1}$ $channel^{-1}$ and 0.012 Jy $beam^{-1}$ km $s^{-1}$ $channel^{-1}$ respectively. Emission is detected in each map with a S/N of 6.8 and 5.7 respectively. The black contours are at the 3 and 5$\sigma$ level. The grey dashed contour shows the Keplerian mask used and the dotted white lines mark the major and minor axes of the disk.

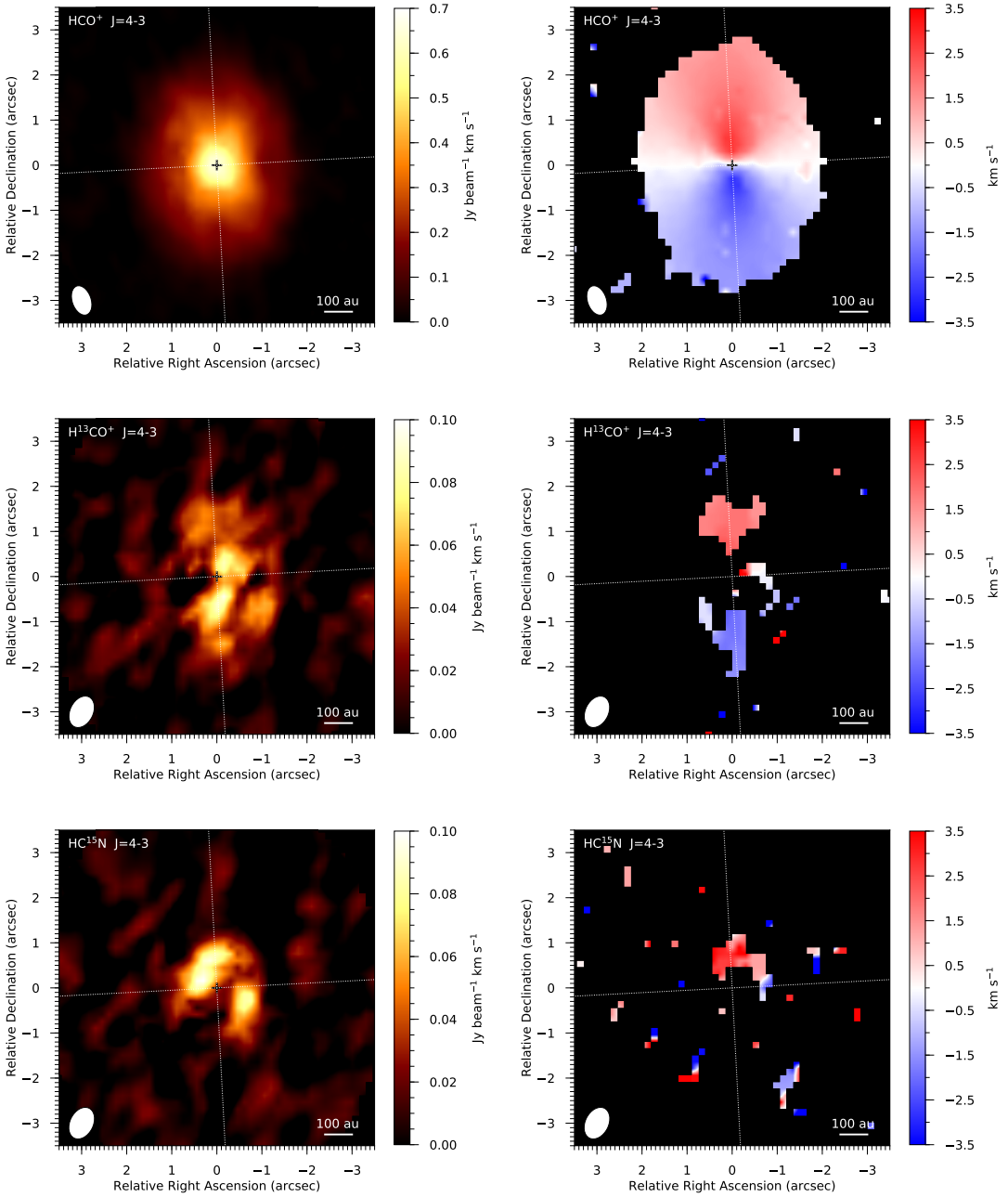


Figure 4.3: The integrated intensity maps (left) and the intensity-weighted velocity (right) for the $HCO^+$ $J = 4-3$ (top), $H^{13}CO^+$ $J = 4-3$ (middle) and $HC^{15}N$ $J = 4-3$ (bottom) transitions generated using the Keplerian masks shown in Figures 4.1, and 4.2. The S/N of the integrated intensity maps are 20, 3 and 3 respectively. The intensity-weighted velocity maps were made using a $3\sigma$ clip in the channel maps. The dotted white lines mark the major and minor axes of the disk.

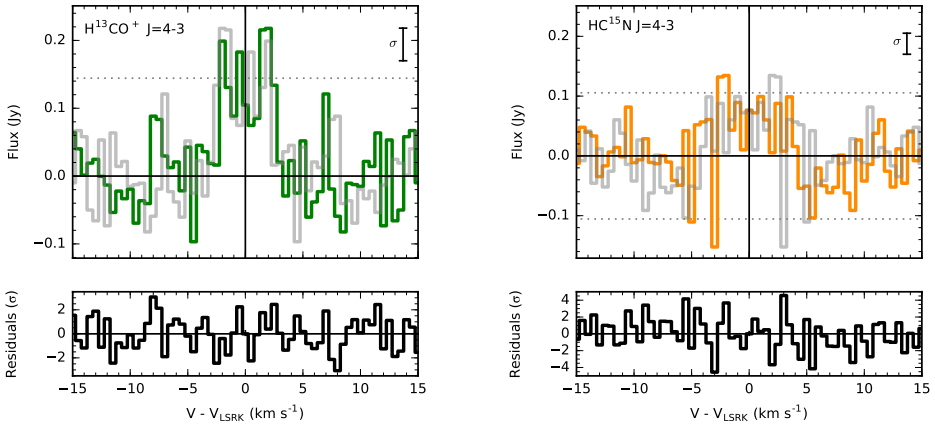


Figure 4.4: Line profiles of the $H^{13}CO^+$ (left) and $HC^{15}N$ (right) emission at a velocity resolution of 0.5 km $s^{-1}$ and mirrored about the source velocity. The $H^{13}CO^+$ line profile is extracted from within the region encompassing the $3\sigma$ extent of the $HCO^+$ integrated intensity and the $HC^{15}N$ extraction region is an ellipse centred on source and chosen by eye. The residuals from the mirrored line profiles are also shown.

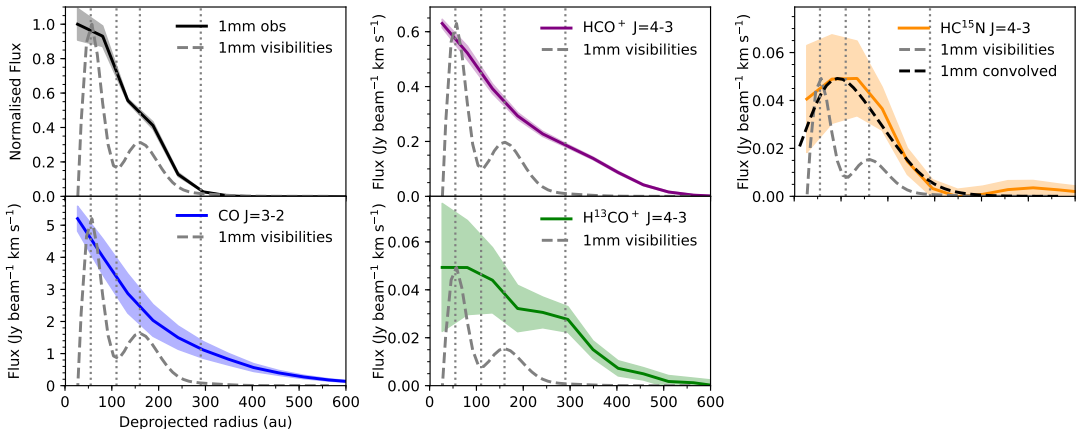


Figure 4.5: Deprojected and azimuthally-averaged radial profiles of the continuum emission, and CO, $HCO^+$, $H^{13}CO^+$, $HC^{15}N$ line emission ratio (from top to bottom, then left to right). The coloured shaded region on each profile represents the errors (see text for details). The vertical dashed grey lines highlight the rings and gaps in the mm-dust continuum profile and the dashed grey profile is the best-fit model of the continuum *uv* data from Walsh *et al.* (2016a) and is normalised to the peak value in each plot. The dotted black line on the $HC^{15}N$ plot is the continuum model convolved with a 50 au beam from Walsh *et al.* (2016a) and is normalised to the peak value in each plot.

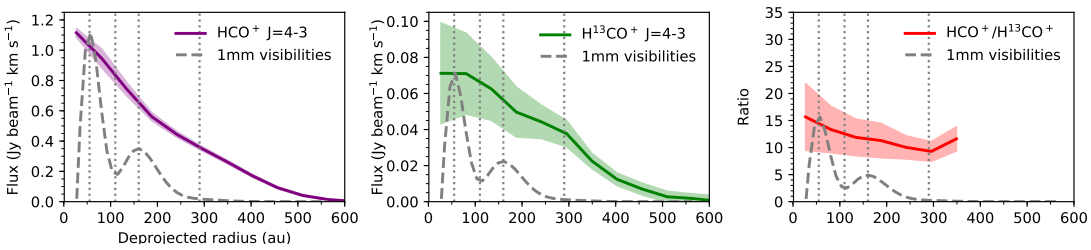


Figure 4.6: Deprojected and azimuthally-averaged radial profiles of the $HCO^+$ and $H^{13}CO^+$ line emission smoothed to a common beam and the subsequent $HCO^+/H^{13}CO^+$ ratio (from left to right). The coloured shaded region on each profile represents the errors (see text for details). The vertical dashed grey lines highlight the rings and gaps in the mm-dust continuum profile and the dashed grey profile is the best-fit model of the continuum *uv* data from (Walsh *et al.*, 2016a) and is normalised to the peak value in each plot.

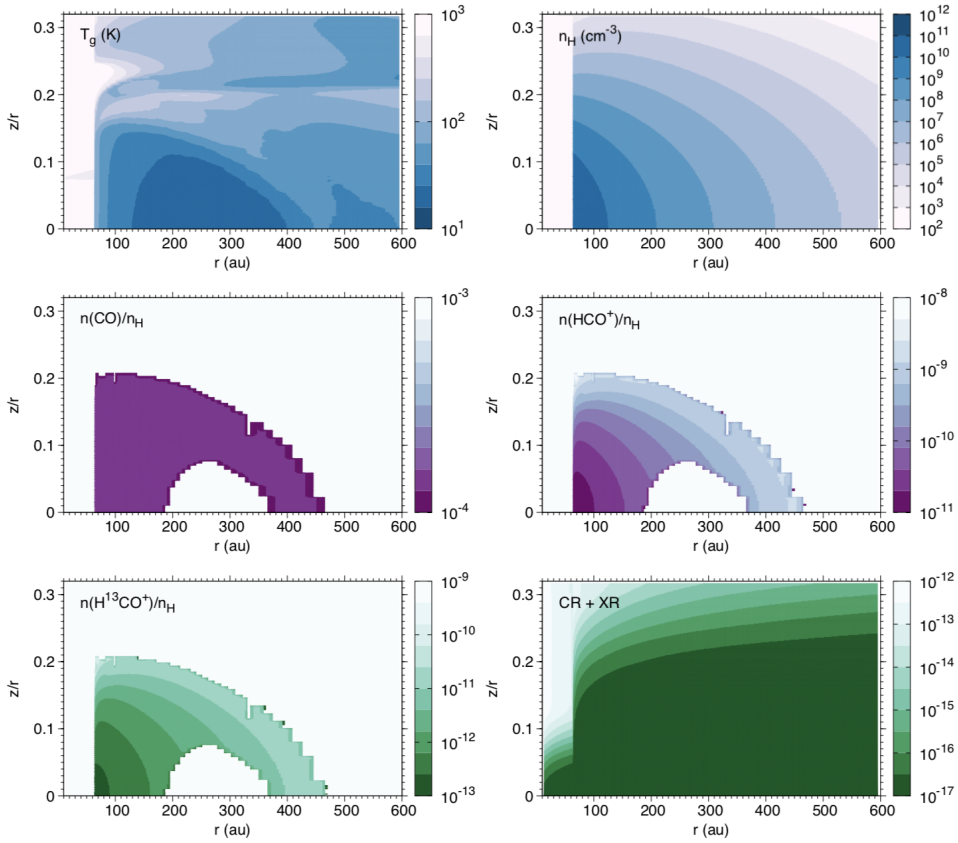


Figure 4.7: The physical disk structure of the HD 97048 protoplanetary disk and the results from the analytical chemical model. Quantities shown are the gas temperature (top left), total H nuclei number density (top right), CO number density relative to H nuclei (middle left), $HCO^+$ number density relative to H nuclei (middle right), $H^{13}CO^+$ number density relative to H nuclei (bottom left) and the sum of the cosmic ray and X-ray ionisation rates (bottom right).

Table 4.3: The different models as described in Section 4.4 along with the parameters that are varied in each model. The ticks and crosses denote if the model fits the specified observation.

| Model | $\kappa_{\mathrm{HCO^+}}$ | $\kappa_{\mathrm{H^{13}CO^+}}$ | Gas in cavity | $\eta_{cavity}$ | $\frac{n(\mathrm{HCO^+})}{n(\mathrm{H^{13}CO^+})}$ | $\mathrm{HCO^+}$ | $\mathrm{H^{13}CO^+}$ | $\frac{\mathrm{HCO^+}}{\mathrm{H^{13}CO^+}}$ |
|---|---|---|---|---|---|---|---|---|
| 1 | - | - | no | - | 69 | x | x | x |
| 2 | [0.9, 0.8,...,**0.2**] | 1 | no | - | 69 | x | x | x |
| 3 | 0.2 | 1 | yes | [0.9, 0.8,...,**0.2**] | 69 | ✓ | x | x |
| 4 | 0.2 | 2 | yes | 0.2 | 34.5 | ✓ | x | x |
| 5 | 0.2 (< 200 au)<br>0.2 (> 200 au) | 2 (< 200 au)<br>[2, 3,...,**6**](> 200 au) | yes | 0.2 | 35 (< 200 au)<br>11.5 (> 200 au) | ✓ | ✓ | ✓ |

The residual channel maps (observations minus Model 5) are shown in Figure 4.9 for $HCO^+$ and $H^{13}CO^+$, respectively. These channel maps show that the flux from the $HCO^+$ line (purple contours) is under-predicted by the model despite the reasonably good fit to the integrated intensity profile. These residuals may be due to the model emission originating from a lower height in the disk than the observations. This would mean that the $HCO^+$ gas is optically thick higher in the disk than the model used here predicts such that the model is either underestimating the disk temperature and hence the disk scale height (i.e., it is more flared than predicted), or that the disk is more massive than suggested by the DIANA model. The $H^{13}CO^+$ residuals are insignificant.

To investigate the effect of the gas temperature on the $HCO^+$ and $H^{13}CO^+$ line emission a set of exploratory models were run. Reducing the gas temperature by a factor of 2 throughout the disk led to a good by-eye fit to the observations in the inner disk ($< 200$ au) using the canonical abundance ratio. However, a significant increase in the $H^{13}CO^+$ abundance relative to $HCO^+$ in the outer disk is still required to better reproduce the emission here. This supports the claim of the presence of two carbon fractionation regimes in this protoplanetary disk, and also supports enhanced fractionation in the outer disk due to the disk being colder than previously inferred from previous modelling work. A more robust determination of the gas temperature structure of this source will require high spatial resolution observations of multiple lines of molecular tracers of gas temperature e.g. $^{12}CO$ and $^{13}CO$.

## 4.5 Discussion

This Chapter presents the first detections of $H^{13}CO^+$ and $HC^{15}N$ in the HD 97048 protoplanetary disk. The radial emission profiles of these tracers are compared with the mm continuum emission profile and the line emission from CO and

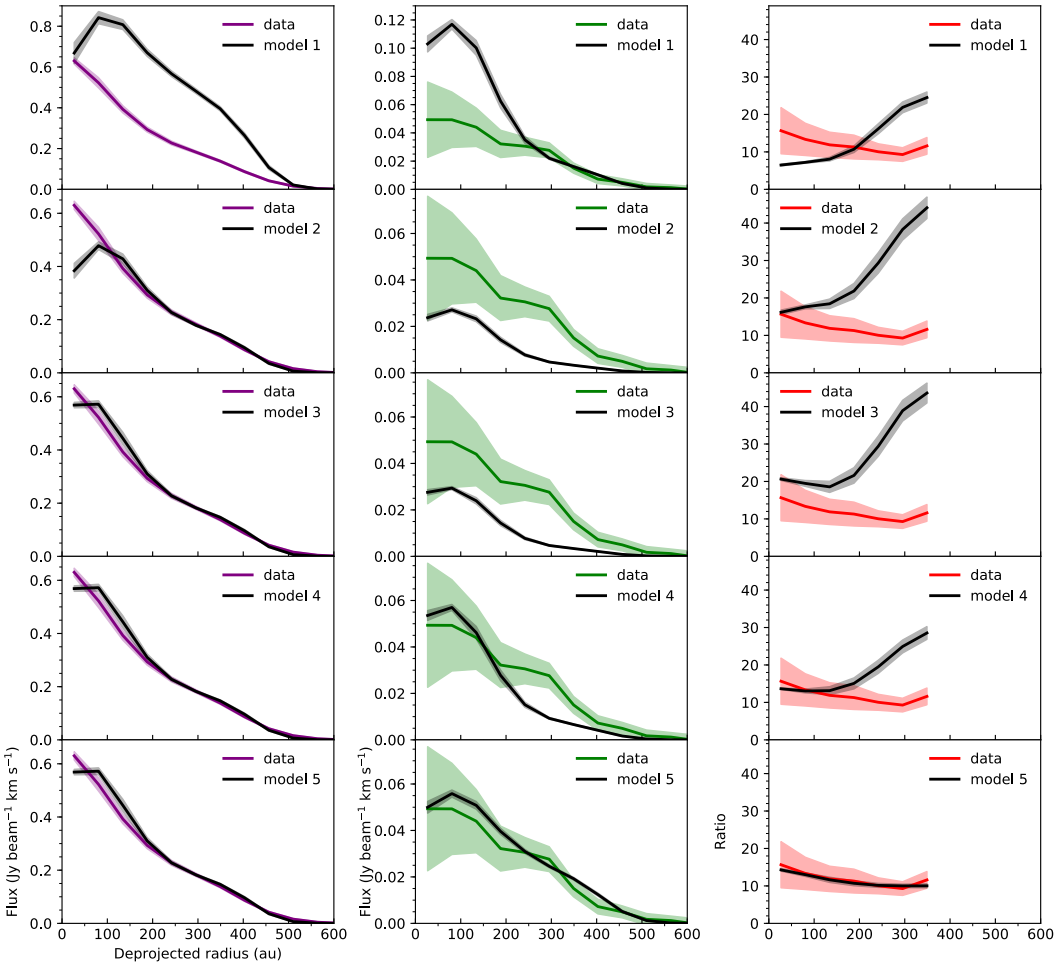


Figure 4.8: Deprojected and azimuthally-averaged radial integrated intensity profiles for $HCO^+$, $H^{13}CO^+$ and the $HCO^+$ /$H^{13}CO^+$ ratio from the observations (in colour) and the LIME models (black). The coloured shaded region on each profile represents the errors (see text for details). The specifics of each model are detailed in Table 4.4.2 and Section 4.4.

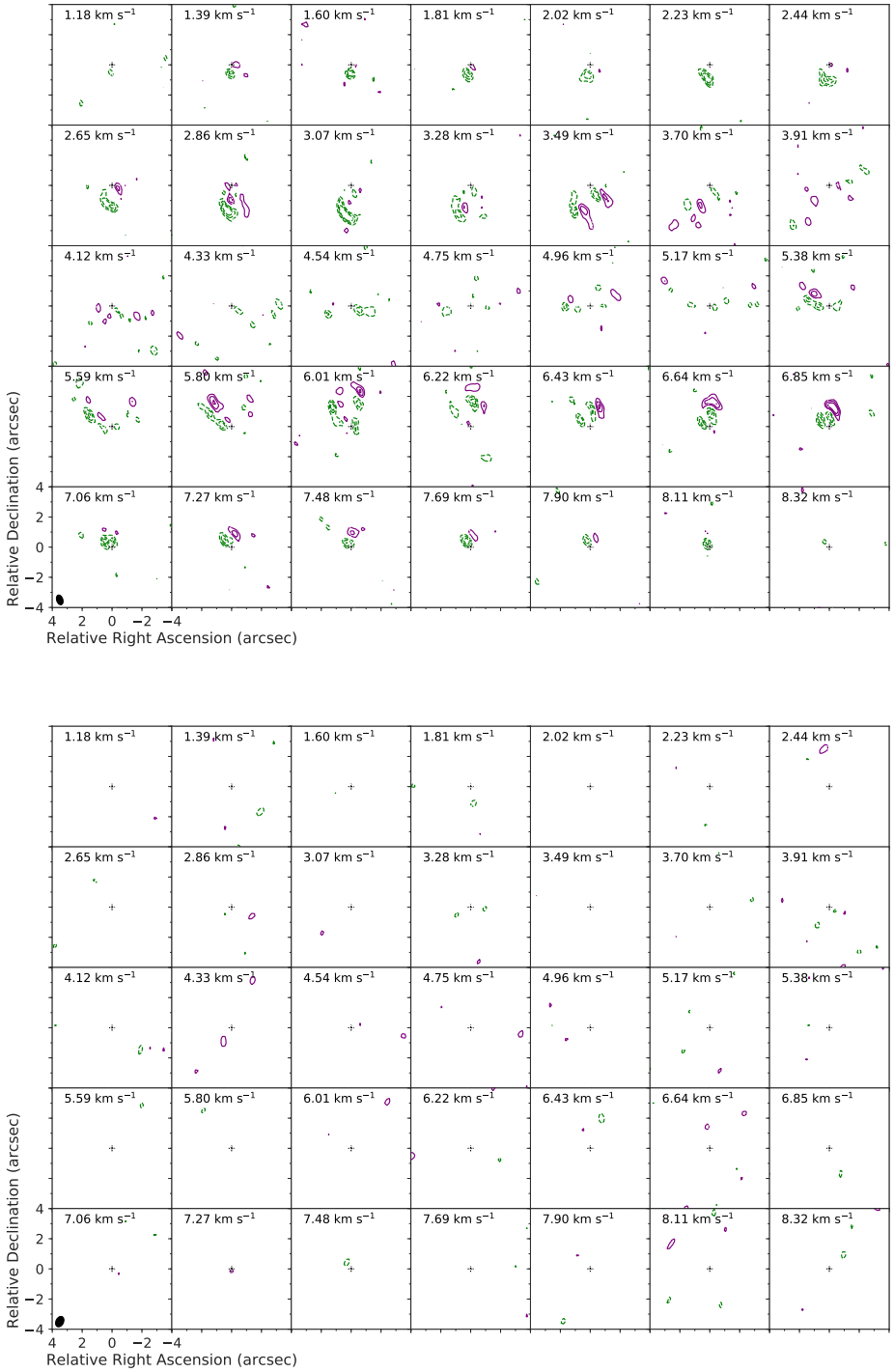


Figure 4.9: Residual (data - model) $HCO^+$ (top) and $H^{13}CO^+$ (bottom) channel maps at a velocity resolution of 0.21 km s$^{-1}$. The rms is 0.016 Jy beam$^{-1}$ km s$^{-1}$ channel$^{-1}$ the purple and green contours are $\pm$ 3, 5, 7$\sigma$ respectively.

$HCO^+$. The optically thin tracers, $H^{13}CO^+$ and $HC^{15}N$, appear to exhibit radial variations in their integrated intensity profiles in contrast to the optically thick tracers, CO and $HCO^+$. Contrary to the $HCO^+$ $J = 4 - 3$ data, the $H^{13}CO^+$ $J = 4 - 3$ radial intensity profile shows a step-like radial structure. The $H^{12}CO^+/H^{13}CO^+$ intensity ratio across the disk is constant with an average value of $12 \pm 3$. This value is consistent with observations of other disks where the disk-integrated $H^{12}CO^+/H^{13}CO^+$ ($J = 3 - 2$) flux ratios range from 13 to 25 (Huang *et al.*, 2017; Öberg *et al.*, 2010, 2011). This low ratio ($< 69$) is consistent with optically thick $HCO^+$ emission. However, using radiative transfer models, consideration of optical depth effects alone cannot explain the data. These models show that radial variations in the abundance ratio of $H^{12}CO^+$ to $H^{13}CO^+$ are necessary to explain the radial behaviour in the observed intensity ratio. The one model that provides a good by-eye fit to the data is Model 5. This model requires an enhancement relative to the canonical ratio of $H^{13}CO^+$ to $H^{12}CO^+$ by a factor of 2 in the inner disk ($< 200$ au) and 5 in the outer disk ($> 200$ au).

The $HC^{15}N$ intensity profile appears to peak in a ring which appears to match well with the mm-sized dust distribution at the same spatial resolution. Higher spatial resolution observations are required to confirm this association. Without complementary observations of the main isotopologue, HCN, it is difficult to investigate further the origin of the $HC^{15}N$ emission. However, the suppression of line emission by the dust opacity in the inner disk can likely be ruled out, within the first dust ring ($<$ 55 au), as the potential origin of a molecular ring as there is not sufficient millimeter dust in this region of the disk.

The remainder of this Section explores if isotope-selective chemistry can explain the structure seen in the $H^{13}CO^+$ emission profile and $H^{12}CO^+/H^{13}CO^+$ ratio across the disk. There is also an estimate of the level of gas depletion in the inner cavity of the disk. These results are compared to observations towards

other Herbig Ae/Be disks, and there is also a speculative discussion on alternative physical/chemical processes that could explain the results presented here.

### 4.5.1 Can isotope-selective chemistry explain the $H^{13}CO^+$ emission?

The best fit model requires multiple $H^{12}CO^+/H^{13}CO^+$ fractionation regimes. Isotope selective chemistry could be responsible for the radial intensity profile of the $H^{13}CO^+$ emission and the observed $H^{12}CO^+/H^{13}CO^+$ ratio but chemical models with isotope selective chemistry only predict a change in the $H^{12}CO^+/H^{13}CO^+$ ratio over very narrow radial and vertical regions of the disk (Miotello *et al.*, 2014; Woods & Willacy, 2009). While detailed chemical modelling of this is beyond the scope of this work, this section explores how isotope selective chemistry could influence the emergent $HCO^+$ and $H^{13}CO^+$ line emission.

Isotope selective photodissociation enhances the ratio of $^{12}CO/^{13}CO$ in the disk atmosphere due to the different self-shielding column densities of the different isotopologues (Miotello *et al.*, 2014; Visser *et al.*, 2009). The relative abundances of $^{12}CO$ and $^{13}CO$ are the least affected of the different CO isotopologues since they are the most abundant. However, the shielding column for $^{13}CO$ will be reached slightly deeper into the disk atmosphere than that for $^{12}CO$ (Miotello *et al.*, 2014). Hence, there will exist a layer in the disk surface where $^{12}CO/^{13}CO > 69$ such that $H^{12}CO^+/H^{13}CO^+$ is also $> 69$ due to the coupled chemistry between the two species. In the model of a T Tauri disk in Miotello *et al.* (2014) that includes comprehensive isotope-selective chemistry, the peak abundance ratio for $^{12}CO/^{13}CO$ is only $\approx$ 2 $\times$ the underlying elemental ratio and only in a narrow layer of the disk atmosphere. The models of carbon isotope fractionation in the inner 30 au of a T Tauri disk by Woods & Willacy (2009) show that there is an increase in the isotopologue ratio in $HCO^+$ relative to that for CO in

the more tenuous and irradiated disk atmosphere (i.e., $n(\mathrm{H}^{12}\mathrm{CO}^+)/n(\mathrm{H}^{13}\mathrm{CO}^+) > n(^{12}\mathrm{CO})/n(^{13}\mathrm{CO})$ with a maximum $n(\mathrm{H}^{12}\mathrm{CO}^+)/n(\mathrm{H}^{13}\mathrm{CO}^+)$ of $\approx 110$). However, this cannot explain the results for HD 97048 because isotope selective photodissociation leads to an enhancement of the main isotopologue relative to the rare isotopologue, which acts in the opposite direction to that required to explain the observations.

Additionally, there are isotope exchange reactions which enhance the abundance of $^{13}$CO relative to $^{12}$CO and $\mathrm{H}^{13}\mathrm{CO}^+$ relative to $\mathrm{H}^{12}\mathrm{CO}^+$ at low temperatures, $< 35$ K and $< 9$ K respectively (as measured by Smith & Adams, 1980). Models of the carbon isotope fractionation in protoplanetary disks show that the chemical $\mathrm{HCO}^+$ fractionation follows the CO fractionation for warm temperatures $> 60$ K but for lower temperatures the fractionation is more extreme for $\mathrm{HCO}^+$ than CO. In the Woods & Willacy (2009) models the $^{13}\mathrm{CO}/^{12}\mathrm{CO}$ reaches $\approx 40$ in the disk midplane whereas the $\mathrm{H}^{13}\mathrm{CO}^+/\mathrm{H}^{12}\mathrm{CO}^+$ ratio is lower ($\approx 30$). Since the density in the disk is relatively high this process is roughly in equilibrium and can be calculated as follows:

$$\frac{n(\mathrm{H}^{12}\mathrm{CO}^+)}{n(\mathrm{H}^{13}\mathrm{CO}^+)} = \exp\left(\frac{-9\mathrm{K}}{\mathrm{T_{gas}}}\right) \frac{n(^{12}\mathrm{CO})}{n(^{13}\mathrm{CO})}.$$

Figure 4.10 shows the $n(\mathrm{H}^{12}\mathrm{CO}^+)/n(\mathrm{H}^{13}\mathrm{CO}^+)$ ratio as a function of gas temperature and underlying $n(^{12}\mathrm{CO})/n(^{13}\mathrm{CO})$ ratio. The white contours mark the three $n(\mathrm{H}^{12}\mathrm{CO}^+)/n(\mathrm{H}^{13}\mathrm{CO}^+)$ ratios used in Models 1 to 3, 4, and 5 respectively. The dashed black line marks the lowest gas temperature in the disk model ($\approx 16$ K). This calculation shows us that the fractionation required in Model 4 is reasonable, but in order to reach the level of fractionation in Model 5, depending on the underlying $n(^{12}\mathrm{CO})/n(^{13}\mathrm{CO})$ ratio, the gas temperature needs to be between 5 and 10 K and this is less than the minimum gas temperature in the disk

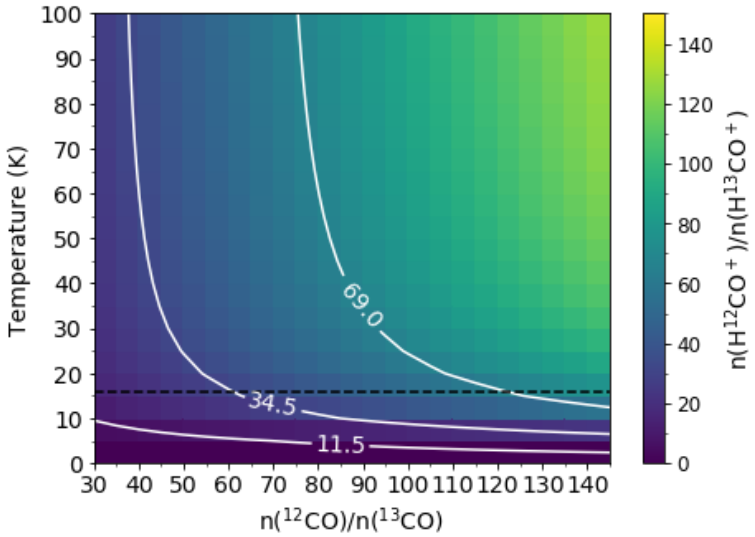


Figure 4.10: The $n(H^{12}CO^+)/n(H^{13}CO^+)$ ratio as a function of gas temperature and underlying $n(^{12}CO)/n(^{13}CO)$ ratio. The white contours mark the three $n(H^{12}CO^+)$ / $n(H^{13}CO^+)$ ratios used in Models 1 to 3, 4 and 5 respectively. The dashed black line marks the lowest gas temperature in the disk model.

model employed in this work. For chemical fractionation to explain the results the gas temperature in the outer disk needs to be significantly cooler than current models predict.

The radial abundance profiles of best-fit models for the $HCO^+$ and $H^{13}CO^+$ emission shows that isotope-selective processes are occurring in this disk; however, the enhancement factors required for $H^{13}CO^+$ are needed across a significantly larger column density of the disk compared to predictions from models, and there needs to be a radial change in the ratio. Comprehensive chemical models are required to determine if the $H^{12}CO^+/H^{13}CO^+$ abundance ratio exhibits variations more than a factor of a few relative to the elemental ratio in the outer disk (100's of au) and how the observed line emission will reflect this.

### 4.5.2 Estimating the gas depletion in the cavity

The $HCO^+$ emission in the channel maps is detected down to at least 40 au whereas the model assumes a gas cavity size of 65 au. Adding gas to the cavity in Model 3 with an abundance 0.2 times that at the edge of the disk well reproduces the radial profile of the $HCO^+$ emission. The fractional abundance of $HCO^+$ in the dust cavity reaches a maximum value of $6 \times 10^{-9}$. Chemical models show that the $HCO^+$ fractional abundance in the inner ($< 50$ au) regions of full disks can be as high as $\sim 10^{-7}$ (Aikawa *et al.*, 2015; Walsh *et al.*, 2010). Hence, if this value represents an absolute ceiling value for the $HCO^+$ fractional abundance then the gas surface density is $\approx$500 times less that in the dust cavity than in the inner edge of the outer disk. However, there remain caveats to this estimate related to chemistry. Because there is a central dust cavity in this disk then the gas will be less shielded from ionising radiation resulting in potentially higher $HCO^+$ abundances than calculated in chemical models of disks without dust cavities. $HCO^+$ is not an optimal tracer of gas mass; hence, the gas depletion in the cavity be should be estimated using CO isotopologue observations.

### 4.5.3 A comparison with other Herbig Ae/Be disks

Molecular line emission from Herbig Ae/Be disks has been shown to trace both sub-structure associated with an underlying ringed dust structure and radial structure that arises due to chemistry, such as snowlines (e.g., HD 163296, HD 169142: Carney *et al.*, 2018; Fedele *et al.*, 2017; Isella *et al.*, 2016; Mathews *et al.*, 2013; Qi *et al.*, 2013a, 2015). With ALMA we now have spatially resolved detections of the $HCO^+$ and HCN isotopologues in multiple protoplanetary disks (see Figure 4.11) . Although these molecules are commonly detected in disks around T Tauri stars, e.g., IM Lup, AS 209, V4046 Sgr, DM Tau, LkCa 15 (Guzmán *et al.*, 2015, 2017; Huang *et al.*, 2017; Öberg

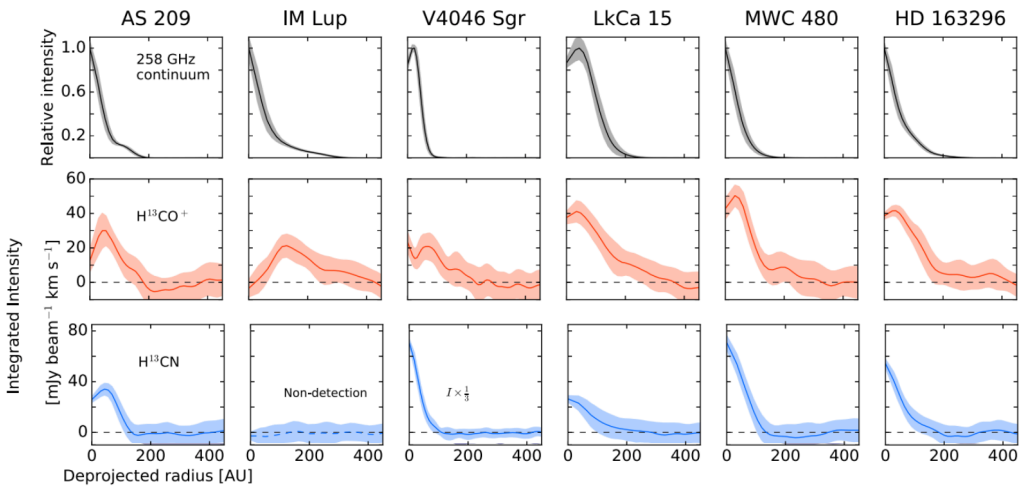


Figure 4.11: Gallery of 1.1 mm continuum and $H^{13}CO^+$ and $HC^{15}N$ J=3-2 radial emission profiles in disks (adapted from from Huang *et al.* (2017) ).

*et al.*, 2015; Piétu *et al.*, 2007), this section will primarily discuss the detections towards HD 97048 in the context of other Herbig Ae/Be disks given the differences in chemistry expected between these two disk types (e.g., Agúndez *et al.*, 2018; Walsh *et al.*, 2015).

Both HCN and $HCO^+$ have been detected towards the dust-trap-hosting transition disk around the Herbig Ae star, HD 142527 (Casassus *et al.*, 2013, 2015a; Rosenfeld *et al.*, 2014; van der Plas *et al.*, 2014). However, for this source, the molecular emission is strongly influenced by the large cavity (140 au) and the lop-sided dust trap. The $HCO^+$ emission from within the cavity traces non-Keplerian motions that have been attributed to radial flows through the gap (Casassus *et al.*, 2013, 2015a; Rosenfeld *et al.*, 2014), and the HCN emission is strongly anti-coincident with the dust trap. This anti-coincidence is proposed to be due to either the lower dust temperatures in the trap (leading to enhanced freezeout) or a high continuum optical depth in the dust trap that is suppressing the emergent line emission (van der Plas *et al.*, 2014). The disk around HD 142527

is a clear example demonstrating the influence that extreme dust structure has on the emergent molecular emission. Emission from $H^{13}CO^+$ ($J = 8 - 7$) from HD 142527 has been targeted with ALMA; however, it was reported as a non-detection (Casassus *et al.*, 2015b).

Evidence for multiple rings of $H^{13}CO^+$ have been detected in the HD 163296 disk and one ring of $H^{13}CO^+$ has been detected in the MWC 480 disk, but their relation to the underlying dust and/or gas structure has not yet been fully investigated using detailed models (see Figure 4.11; Huang *et al.*, 2017). These observations have a spatial resolution of $\approx$ 60 to 70 au. In both of these sources there is a central cavity in the $H^{13}CO^+$ emission and this has been primarily attributed to optically thick continuum emission in the inner disk which suppresses the emergent line emission. For the specific case of $H^{13}CO^+$, this may also be partially due to chemistry in the inner disk. Depending on the location of the $H_2O$ snowline, which can reside at $\sim$ 10s of au from the star in Herbig Ae/Be disks (e.g., Notsu *et al.*, 2017; Woitke *et al.*, 2009b), gaseous $H_2O$ may be present which facilitates another destruction pathway for $HCO^+$. Hence, the absence of $H^{13}CO^+$ emission in the inner regions of protoplanetary disks and protostars has been proposed as an indirect indication of the radial location of the water snow line. This effect has yet to be conclusively demonstrated for a protoplanetary disk but has been demonstrated for the protostellar envelope encompassing NGC1333-IRAS2A (van 't Hoff *et al.*, 2018). As yet, there is no evidence for a central cavity strongly depleted in dust in neither HD 163296 nor MWC 480, unlike as has been found for HD 97048. This explains why the $H^{13}CO^+$ emission profile for HD 97048 is centrally peaked: the emergent emission is not suppressed due to the presence of a significant reservoir of mm-sized dust.

The first detection of $HC^{15}N$ in a protoplanetary disk was reported in the MWC 480 disk (Guzmán *et al.*, 2015). In this source, and in the TW Hya disk

(Hily-Blant *et al.*, 2019), the HCN, $H^{13}CN$ and $HC^{15}N$ all show similar radial distributions which follow the smoothly decreasing dust emission profile. From the same study, HCN emission from the DM Tau disk, a T Tauri source, shows a second ring of emission beyond the mm-dust emission at $\sim$ 300 au. The ring is proposed to arise as a result of increased photodissociation of HCN due to the depletion of micron sized dust interior to the detected molecular ring. The $HC^{15}N$ emission appears to follow the radial emission profile of the mm-dust to the spatial resolution of the observations. Observations of the main isotopologue HCN with improved spatial resolution in the HD 97048 disk are needed confirm the presence of rings in this tracer that align with the dust rings. The $H^{13}CN$ emission in the AS 209 disk, another T Tauri disk, is also ringed (Guzmán *et al.*, 2017), and recent ALMA observations have shown clearly that this disk has multiple rings of dust (Fedele *et al.*, 2018). This, again, is another example disk with rings of dust and rings of molecular gas. $HC^{15}N$ has since been detected in the HD 163296 disk but the observations are not of high enough S/N to make assertions about the radial distribution in relation to the dust rings (Guzmán *et al.*, 2017). Nevertheless, there is growing evidence, including in the analysis presented here, that molecular line mission from optically thin tracers may be following, and is thus influenced by, the underlying dust distribution in Herbig Ae/Be disks making them interesting test cases.

### 4.5.4 What is the effect of the ringed dust (and gas) structure on the chemistry?

A radially smooth profile cannot fit the $H^{13}CO^+$ observations and the $H^{12}CO^+/H^{13}CO^+$ abundance ratio across the disk. As this is not wholly consistent with predictions from chemical fractionation models this section now explores the possible effect of the dust rings on the disk chemistry.

From ALMA observations the mm-sized dust is distributed in three rings (van der Plas *et al.*, 2017; Walsh *et al.*, 2016a). Scattered light observations with SPHERE show that at the disk surface there are four rings, two of which are located at comparable positions to the mm-sized dust rings (Ginski *et al.*, 2016). Due to the matching rings in both the mm-sized and micron-sized grains planet-disk interactions have been proposed as the best explanation for the dust rings in the HD 97048 disk (Ginski *et al.*, 2016; van der Plas *et al.*, 2017; Walsh *et al.*, 2016a). From the non-detections of direct emission from planets in the gaps and by comparing the observed rings to models, limits can be placed on the masses of the anticipated planets. van der Plas *et al.* (2017) estimated the mass of the inner-most planet, located between 2.5 and 11 au, to be $\approx 0.7$ $M_J$ guided by models from Rosotti *et al.* (2016). Low-mass planets, $\approx 1$ $M_J$, will create a narrower and shallower cavity in the gas surface density than in the mm-sized dust which forms more distinct rings (de Juan Ovelar *et al.*, 2013, 2016; Zhu *et al.*, 2012). Pinte *et al.* (2019) indirectly detect a planet of a few Jupiter masses at 130 au, which is consistent with upper-limits from VLT/SPHERE (Ginski *et al.*, 2016). Hence, it is possible that perturbations in the gas surface density are sufficiently shallow that they are not visible in the CO and $HCO^+$ isotopologue observations, or conversely, that the gas gaps are deep, but also sufficiently narrow that subsequent chemical inhomogeneities are resolved out.

It is also a possibility that variations in the underlying gas density due to forming planets may be responsible for the observed radial variation in the $H^{12}CO^+/H^{13}CO^+$ abundance ratio. This is in contrast to the scenario discussed in Section 4.6.1 (see Figure 4.12a). Although these data do not have the resolution to resolve the proposed gas gaps, the presence of such gaps may be revealed through analysing global abundance ratios, that average over the chemical substructure. A drop in the column density of small dust grains at the location of

the millimetre-sized dust gaps will provide less shielding from photodissociating *and* photoionising radiation. This will increase the ionisation fraction within the dust gaps relative to the dust rings. Given that $HCO^+$ is the dominant cation in the molecular layer, its abundance may also increase in the dust gaps and this may mask the presence of gas depletion therein because the overall column density of $HCO^+$ may not change significantly. In this case the difference between the $HCO^+$ and $H^{13}CO^+$ abundance distributions would only be due to isotope-selective chemistry (Figure 4.12b). Also, because of the non-linear nature of the chemistry, a reduction in gas density can have a profound effect on the abundances of more minor species because the rates of two-body ion-molecule reactions are proportional to $n^2$. Hence, it is possible that this can amplify the effects of isotope-selective photodissociation by e.g., slowing down the reformation of $^{13}CO$ relative to $^{12}CO$. This would reduce the abundance of $H^{13}CO^+$ relative to $HCO^+$ in the disk, in contrast to the observations presented here (Figure 4.12c).

An additional explanation to consider is the effect of the dust structure on the gas temperature. Models show that the gas temperature relative to the dust temperature can decrease in the disk atmosphere due to grain growth and settling and at the location of the dust gaps (Facchini *et al.*, 2017; van der Marel *et al.*, 2018). A decrease in gas temperature could be traced by isotope fractionation (see Figure 4.12d) but this remains speculation until dedicated physio-chemical models are available that include isotope-selective chemistry as well as ringed dust structure.

## 4.6 Conclusion

This chapter shows, for the first time, that the disk molecules $H^{13}CO^+$ and $HC^{15}N$, are may be tracing sub-structure in the HD 97048 protoplanetary disk. The favoured by-eye fit to the $H^{13}CO^+$ observations require a model with an en-

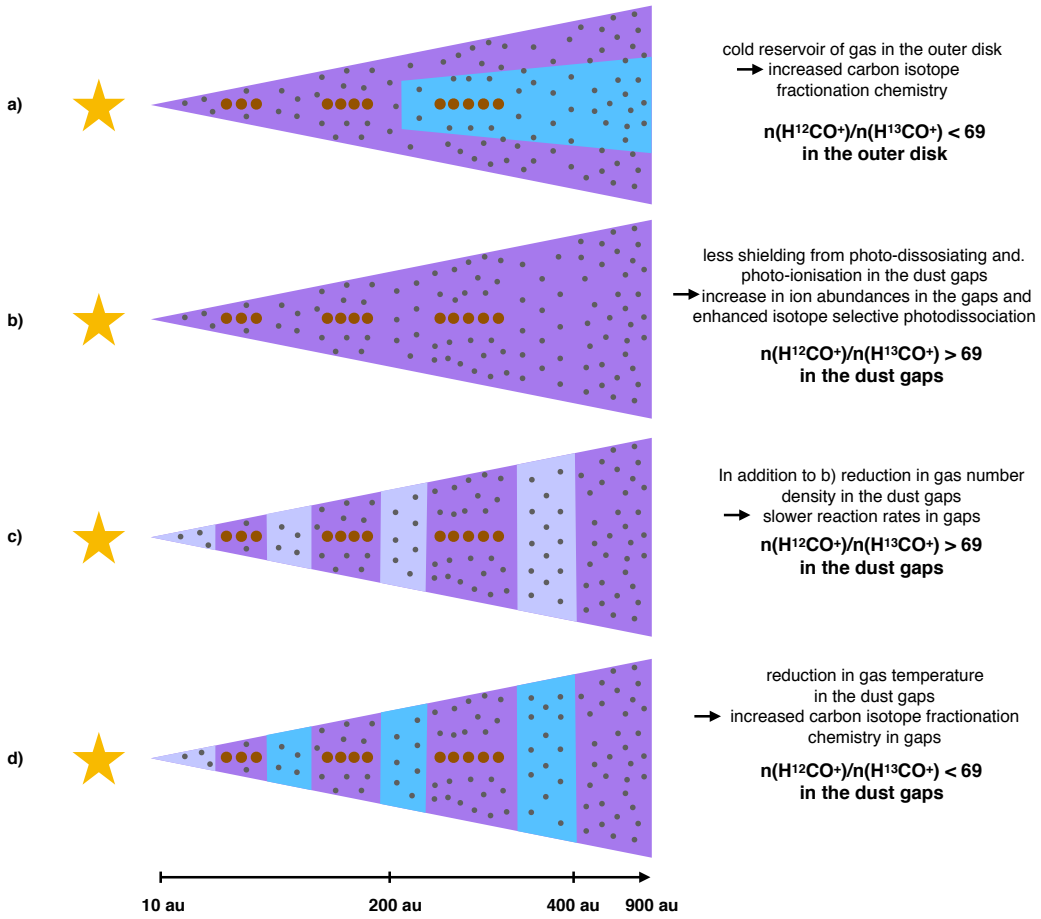


Figure 4.12: Cartoon illustrating the possible gas and dust distributions in the HD 97048 disk. The mm-sized dust is represented by brown circles, the micron-sized dust is represented by grey circles, the gas and depleted gas are represented by purple and lilac respectively and the light blue corresponds to a cold gas reservoir.

hancement in fractional abundance relative to the canonical isotope ratio in the outer disk. Since the $HCO^+$ models do not require such enhancement factors, chemical fractionation is the simplest explanation for the emergent line emission. The enhancement in $H^{13}CO^+$ relative to $HCO^+$ can be explained by a cold reservoir of gas in the outer disk ($\lesssim$ 10 K, $\gtrsim$ 200 au). Through a comparison with disk models that include carbon fractionation, isotope selective chemistry cannot solely explain the observations. Future ALMA observations of HD 97048 need to have the spatial resolution to properly resolve the ringed structure in the dust and in the different gas tracers, and will allow for the determination of the size of central cavity in different tracers. This will enable a detailed study on the dominant chemical processes in the disk and allow a clearer distinctions between the different scenarios presented and provide insight on the physical and chemical nature of planet-carved gaps.

# Chapter 5

# SO in the HD 100546 Disk

## 5.1 Introduction

As discussed in Chapter 1, sulphur is observed to be depleted in molecular rich gas. Despite this depletion issue, sulphur-bearing species are useful tracers of physical processes in interstellar and circumstellar material. For example, SO is frequently detected as a tracer of shocked gas associated with the bipolar outflows from Class 0 and I protostars, (e.g., Tafalla *et al.* 2010 and Podio *et al.* 2015). Searches for SO have found that detections in outflows are ubiquitous but in protoplanetary disks infrequent (Fuente *et al.*, 2010; Guilloteau *et al.*, 2013). ALMA observations have also revealed ring components of SO emission in Class 0 protostars (Sakai *et al.*, 2016) that have been interpreted as accretion shocks at the disk-envelope interface. It is evident from existing observations that SO is a tracer of shocks in Class 0 and I protostars. However, SO is an elusive disk molecule requiring high sensitivity observations for its detection: this is now possible with ALMA. This Chapter presents the first detection of SO in the disk around HD 100546. This is an important source for the study of planet-disk interactions due to the verified discovery of a point source in the disk at 50 au that is proposed to be a young giant planet (Quanz *et al.*, 2013, 2015).

## 5.2 The HD 100546 disk

HD 100546 is an isolated 2.4 $M_*$ Herbig Be star at a distance of 109 pc (van den Ancker *et al.*, 1998; Wichittanakom *et al.*, 2020). Similar to both the HD 163295 and HD 97048 disks, ALMA Band 7 observations show that the millimeter-sized dust grains in the HD 100546 disk are distributed in two rings: one ring is 21 au wide centred at 26 au and the other is 75 au wide centred at 190 au (Walsh *et al.*, 2014a). The best fit evolutionary model for the data is a scenario where there are two planets in the disk: a 20 $M_J$ planet at 10 au and 15 $M_J$ planet at 68 au (Pinilla *et al.*, 2015). This is in agreement with observations of an embedded protoplanet and a possible companion in the cavity of the disk (Avenhaus *et al.*, 2014; Benisty *et al.*, 2017; Brittain *et al.*, 2014; Currie *et al.*, 2014, 2015; Garufi *et al.*, 2016; Mulders *et al.*, 2013; Quanz *et al.*, 2013, 2015).

Various molecular and atomic lines have been detected with single-dish telescopes. Although spatially unresolved, these observations suggest a warm disk atmosphere above the disk midplane with the highest abundances of the detected species coinciding with the outer edge of the cavity which is thought to be puffy (Carmona *et al.*, 2011; Fedele *et al.*, 2013; Goto *et al.*, 2012; Hein Bertelsen *et al.*, 2014; Liskowsky *et al.*, 2012; Panić *et al.*, 2010; Sturm *et al.*, 2010; Thi *et al.*, 2011). The disk hosts a large molecular gas disk with the CO gas extending out to $\approx$ 400 au (Pineda *et al.*, 2014; Walsh *et al.*, 2014a). In addition to this, there is evidence for thermal decoupling of gas and dust in the disk atmosphere and radial drift of millimeter-sized dust grains (see Bruderer *et al.*, 2012; Meeus *et al.*, 2013b; Walsh *et al.*, 2014a), now a common property of protoplanetary disks (Andrews, 2020).

Table 5.1: ALMA band 7 observational parameters and sulphur monoxide transitions for HD 100546

| | | | | | |
|---|---|---|---|---|---|
| Date observed | 18th November 2012 | | | | |
| Baselines | 21 - 375 m | | | | |
| Weighting | natural | | | | |
| SO rotational transitions | $7_7 - 6_6$ | $7_8 - 6_7$ | $8_8 - 7_7$ | $3_2 - 1_2$ | $7_7 - 6_6 + 7_8 - 6_7$ |
| Rest frequency (GHz) | 301.286 | 304.078 | 344.311 | 345.704 | - |
| Synthesised beam | $1\farcs1 \times 0\farcs6$ | $1\farcs1 \times 0\farcs6$ | $1\farcs0 \times 0\farcs5$ | $1\farcs0 \times 0\farcs5$ | $1\farcs1 \times 0\farcs6$ |
| Beam P.A. | 24° | 23° | 40° | 40° | 24° |
| Spectral resolution ( km $s^{-1}$) | 0.24 | 0.24 | 0.21 | 0.21 | 1.00 |
| rms noise (mJy $beam^{-1}$) $channel^{-1}$ | 10.9 | 9.9 | 17.4 | 16.2 | 4.2 |
| Peak emission (mJy $beam^{-1}$) | - | - | - | - | 24.7 |
| $E_u$ (K) | 71.0 | 62.1 | 87.5 | 21.1 | - |
| Einstein A coefficient ($s^{-1}$) | 3.429e-04 | 3.609e-04 | 5.186e-04 | 1.390e-07 | - |

The values for the line frequencies and Einstein A coefficients are from the Cologne Database for Molecular Spectroscopy (CDMS; Müller *et al.*, 2001) as listed in the Leiden Atomic and Molecular Database (LAMDA; Schöier *et al.*, 2005).

## 5.3 Line imaging

The HD 100546 disk was observed at ALMA Band 7 during Cycle 0 (2011.0.00863.S, PI: C. Walsh). This work began with the self-calibrated, phase-corrected, and continuum-subtracted measurement sets from Walsh *et al.* (2014a).

The observations of HD 100546 and the four SO transitions analysed in this work are detailed in Table 5.1. Imaging of the data was done using CASA version 4.6.0. The individual lines were each imaged at the spectral resolution of the observations (0.21 - 0.24 km s$^{-1}$, applying Hanning smoothing) and then at a coarser resolution of 1 km s$^{-1}$. Only the $J = 7_7 - 6_6$ and $J = 7_8 - 6_7$ transitions were detected. These two SO lines were then stacked in the *uv* plane to increase the signal-to-noise ratio (S/N) in the resulting channel maps (see Table 5.1). This was done as follows. The central frequency of each spectral window was transformed to the central frequency of the SO line it contained using the CASA tool *regridspw*. These measurement sets were then concatenated using the CASA task *concat*. The line emission was imaged at a velocity resolution of 1 km s$^{-1}$ using the CLEAN algorithm with natural weighting and a channel-by-channel mask guided by the spatial extent of the CO $J = 3 - 2$ emission ($3\sigma$). The SO $J = 3_2 - 1_2$ transition has a low excitation energy (21 K) and it is expected that the inner region of this disk is warm ($> 20$ K). Hence, the detection of the higher energy transitions only is consistent with the expected temperature of emitting molecular gas. Further, the lower energy transition is significantly weaker (see Table 5.1). Including the $J = 8_8 - 7_7$ transition in the stacking increased the noise level in the channel maps thus degrading the S/N in the resulting images. Stacking wholly in the image plane gave the same results but with a slightly lower S/N than using the *regrid* plus *concat* method (seen also in the analysis conducted by Walsh *et al.* 2016a).

## 5.4 Results

### 5.4.1 Detected SO emission

Figure 5.1 shows the integrated intensity maps of the two SO lines detected in the imaging. They encompass the significant ($> 3\sigma$) on source emission detected in the 1 km s$^{-1}$ channel maps. This is integrated across 11 channels from $-7$ km s$^{-1}$ to 5 km s$^{-1}$ with respect to the source velocity. The source velocity of the emission, as inferred from the CO $J = 3 - 2$ emission (Walsh *et al.*, 2014a, 2017), is 5.7 km s$^{-1}$. The $J = 7_7 - 6_6$ and $J = 7_8 - 6_7$ transitions are detected with a peak S/N of 7 and 11 respectively in the integrated intensity maps. The rms noise was extracted from the region beyond the $3\sigma$ contour of the integrated intensity.

Stacking these two transitions results in a robust detection of SO in the channel maps ($6\sigma$) and line profile ($5\sigma$). Figure 5.2 shows the channel maps of the stacked SO emission at a velocity resolution of 1 km s$^{-1}$ and with respect to the source velocity. The emission reaches a peak S/N of 6 with an rms noise of 4.2 mJy beam$^{-1}$ channel$^{-1}$. The noise in the channel maps was determined by taking the rms of the line-free channels either side of those with significant emission. The CO emission ($> 3\sigma$) is also plotted to allow a comparison between the emission morphology of these two molecules. When comparing the SO and CO, the SO emission is significantly more compact than the CO emission and there is an excess blue-shifted component of SO emission that is not spatially consistent with the blue-shifted disk emission traced in CO. This is further highlighted by comparing the SO and CO line profiles shown in Figure 5.3.

Figure 5.4 shows the line profile extracted from within the $3\sigma$ contour of the stacked integrated intensity and covers a velocity range of $-$ 50 km s$^{-1}$ to + 50 km s$^{-1}$ about the source velocity. This large velocity range was chosen to highlight the significance of the emission with respect to the underlying noise.

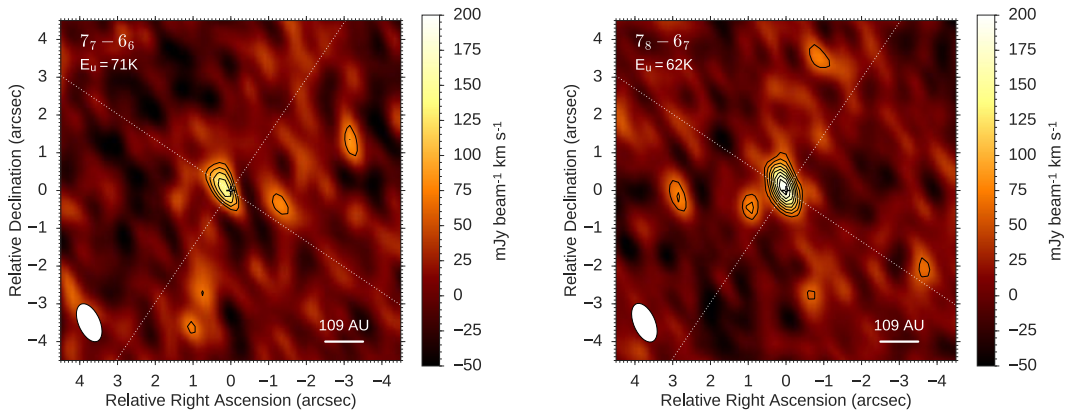


Figure 5.1: Integrated intensity maps of the two SO transitions integrated over a 11 km s$^{-1}$ velocity range. Left: the $J = 7_7 - 6_6$ transition with an rms of 22 mJy beam$^{-1}$ km s$^{-1}$ and a peak emission of 151 mJy beam$^{-1}$ km s$^{-1}$ resulting in a S/N of 6.9. Right: the $J = 7_8 - 6_7$ transition with an rms of 19 mJy beam$^{-1}$ km s$^{-1}$ and a peak emission of 206 mJy beam$^{-1}$ km s$^{-1}$ resulting in a S/N of 10.8. The black contours are at intervals of $\sigma$ going from $3\sigma$ to peak.

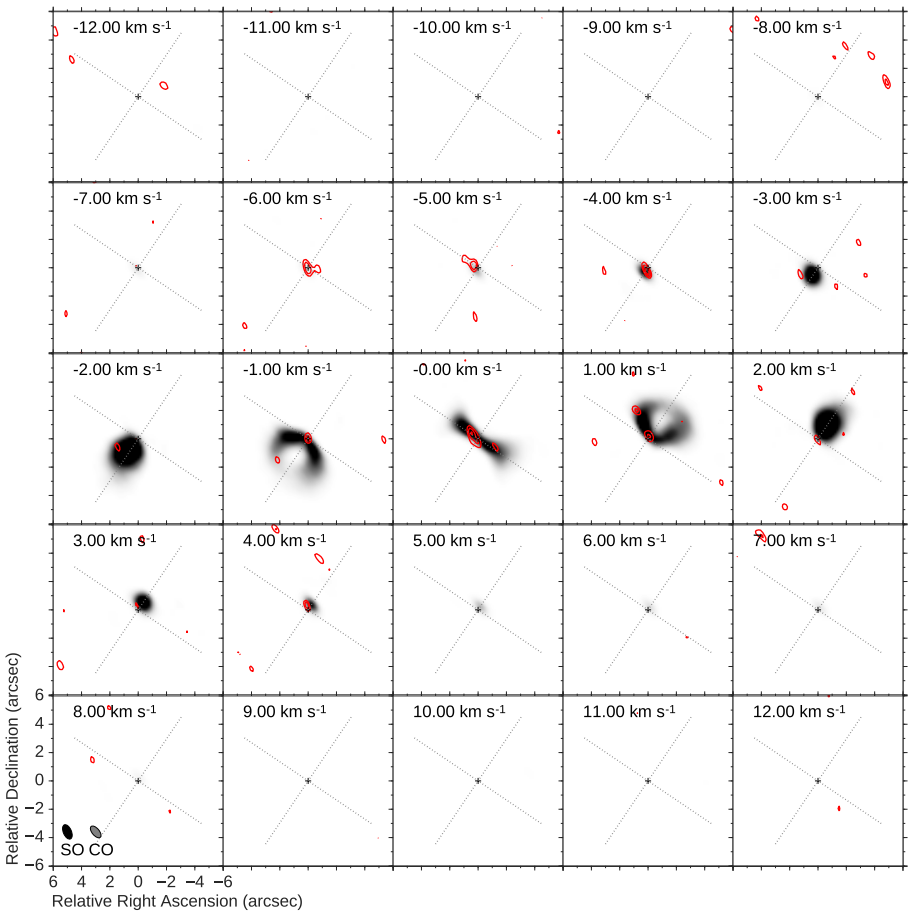


Figure 5.2: Channel maps of the stacked SO emission (red contours) and the CO $J = 3-2$ emission with a $3\sigma$ clip (grey colour map). The stacked SO emission has an rms noise of 4.2 mJy beam$^{-1}$ channel$^{-1}$ and peak emission of 24.7 mJy beam$^{-1}$ resulting in a S/N of 5.9. The contours are from $3\sigma$ to peak in intervals of $\sigma$. The stated velocities are with respect to the source velocity of the emission.

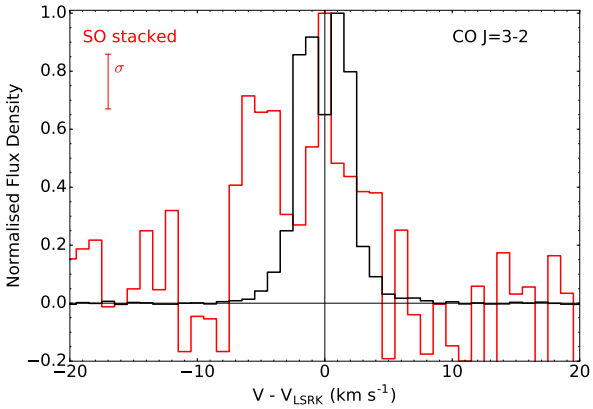


Figure 5.3: SO stacked (red) line profile and CO $J = 3 - 2$ (black) line profile extracted from within the $3\sigma$ extent of their respective integrated intensity maps. The SO stacked line profile reaches a S/N of 5.3 and the CO $J = 3 - 2$ reaches a S/N of 375. Note that the rms for the CO $J = 3 - 2$ is not visible on this scale (81 mJy).

The rms of the line profile was determined from the line-free channels either side of the channels with significant emission. The line profile is double peaked which could indicate that the emission is originating from an inclined disk in Keplerian rotation. However, the trough of the profile is 2 km s$^{-1}$ blueshifted from the CO-determined source velocity. Because the emission is clearly peaking on source, numerous checks were done to see if the blue-shifted emission shift is real. The CASA velocity reference frame is LSRK as is needed, the line frequencies are correct, and there are no other emission lines within the considered velocity range that could attribute to the blue-shifted emission. In addition to this, with the removal of 5% to 10% of the longer and shorter baselines and the double-peaked line profile persists. This was done to check that this was not an imaging artifact. We also confirmed that the frequency axis of the spectral cube was correctly indexed. The line profiles of the individual transitions (see Figure 5.4) both have the same line profile shape. Therefore, any additional signal was not induced through stacking.

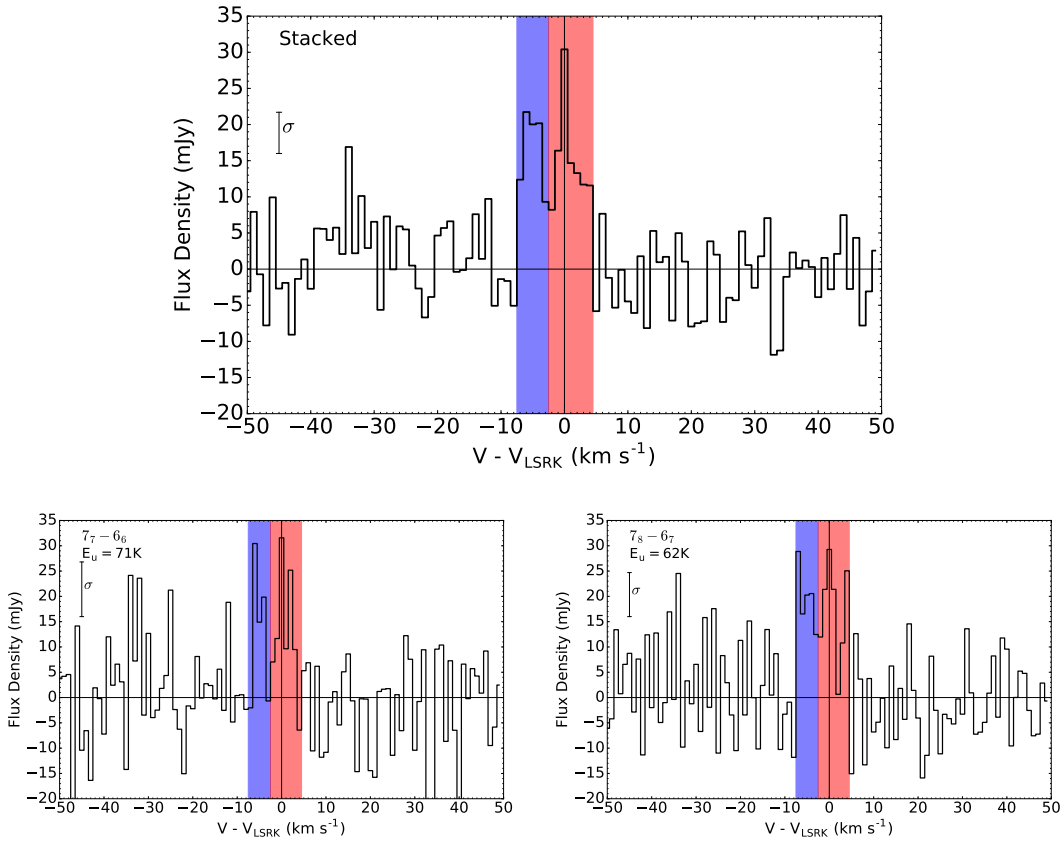


Figure 5.4: Top: Line profile extracted from within the $3\sigma$ extent of the SO stacked integrated intensity with an rms noise of 5.7 mJy and a peak flux of 30.4 mJy resulting in a S/N of 5.3. Bottom: Line profiles of the individual J=$7_7 - 6_6$ (left) and J=$7_8 - 6_7$ (right) transitions extracted from within the $3\sigma$ extent of their respective intensity maps. Both line profiles reach a S/N of 3 with rms noise of 10.8 mJy and 8.7 mJy respectively. Highlighted in red and blue are the velocity ranges of emission used in the moment maps of the individual lines in Figure 5.1.

Table 5.2: Moment map S/N and rms.

| Moment map | | S/N | rms. (mJy beam$^{-1}$ km s$^{-1}$) |
|---|---|---|---|
| $J = 7_7 - 6_6$ | disk component | 4.8 | 17 |
| $J = 7_7 - 6_6$ | wind component | 5.0 | 15 |
| $J = 7_8 - 6_7$ | disk component | 8.4 | 15 |
| $J = 7_8 - 6_7$ | wind component | 6.8 | 13 |

To investigate the spatial distribution of both components of emission (on source emission and blue shifted emission, respectively), a moment zero map was created for both. Figure 5.5 shows the integrated intensity maps from -7.5 km s$^{-1}$ to -2.5 km s$^{-1}$ and from -2.5 km s$^{-1}$ to 4.5 km s$^{-1}$. These velocity ranges are highlighted in the stacked line profile and the individual lines profiles (Figure 5.4). The peak S/N and rms. for each of these integrated intensity maps are listed in Table 5.2. The peak emission in the two maps is spatially offset but the exact separation of these two components is unclear because the emission is of the order of the same size as the beam. The ratio of the peak emission in the moment zero maps of the $J = 7_7 - 6_6$ transition to the $J = 7_8 - 6_7$ transition is higher in the blue-shifted component of emission compared with the emission at the source velocity. This likely indicates that the blue-shifted component is tracing warmer gas. The stacked moment maps over the two velocity ranges are shown in Figure 5.6 in which the spatial offset between the two components is more significant.

From this analysis it can be said that there are two components of emission and not just Keplerian disk emission that is blue-shifted relative to the source velocity. The emission in the line profile that peaks on source and aligns kinematically with the CO in the channel maps (Figure 5.2) can be attributed to disk emission. The morphology of the on-source singly-peaked disk component might be explained by asymmetric SO emission which is arising from the north-east side of the disk only.

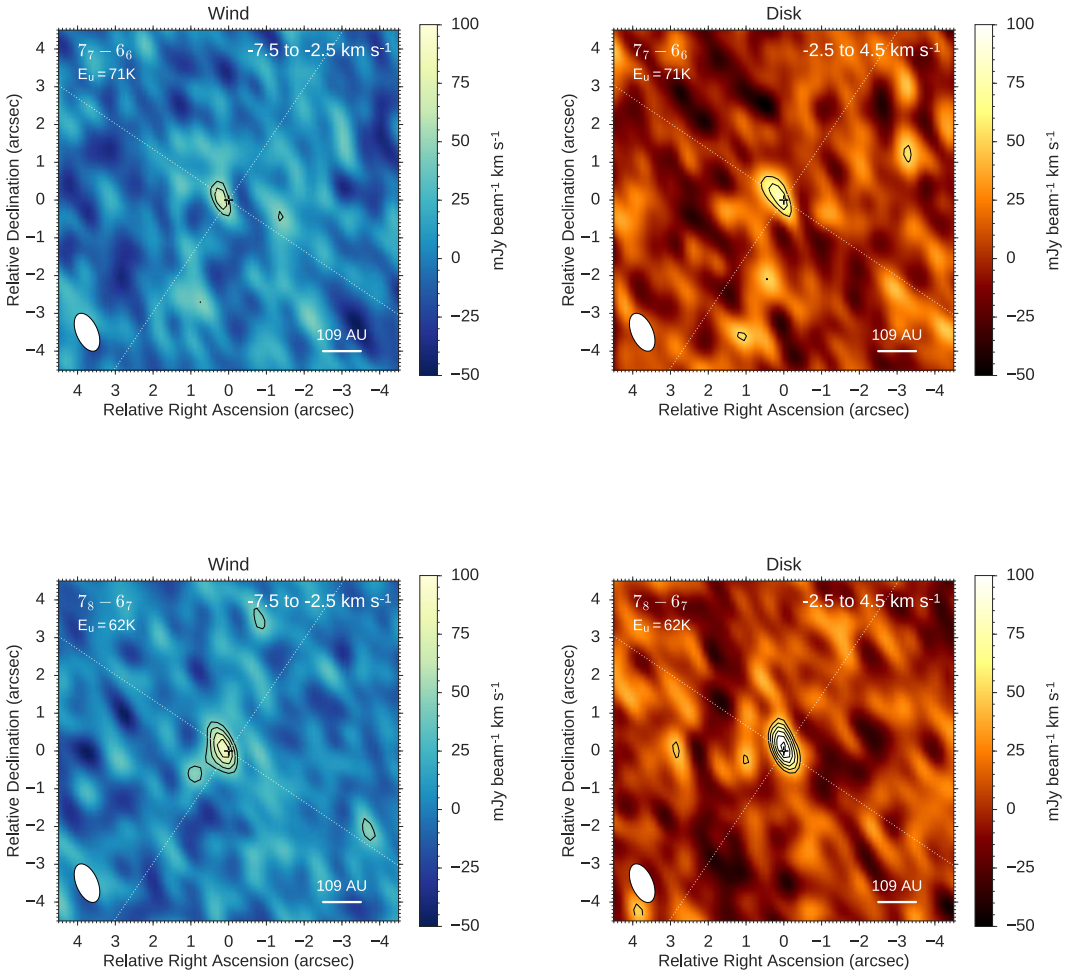


Figure 5.5: Integrated intensity maps of the two SO transitions over two velocity ranges. Top: the $J = 7_7 - 6_6$ transition from -7.5 km s$^{-1}$to -2.5 km s$^{-1}$ (left) and -2.5 km s$^{-1}$to 4.5 km s$^{-1}$ (right). Bottom: the $J = 7_8 - 6_7$ transition from -7.5 km s$^{-1}$to -2.5 km s$^{-1}$ (left) and -2.5 km s$^{-1}$to 4.5 km s$^{-1}$ (right). The peak S/N and rms. for each of these maps are listed in Table 5.2. The black contours are at intervals of $\sigma$ going from $3\sigma$ to peak.

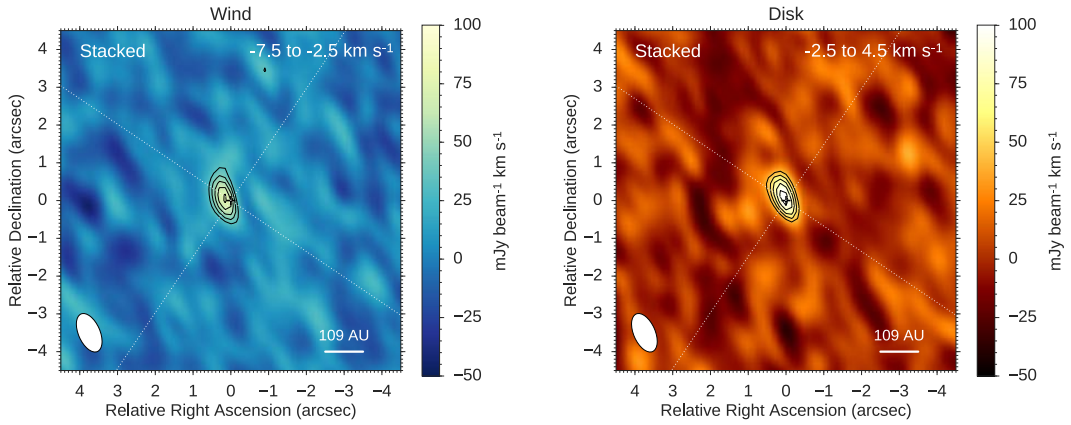


Figure 5.6: Integrated intensity maps of the stacked SO emission over two velocity ranges: -7.5 km $s^{-1}$to -2.5 km $s^{-1}$ (left) with a S/N of 7 and -2.5 km $s^{-1}$to 4.5 km $s^{-1}$ (right) with a S/N of 9. The r.m.s. noise reached in these maps is 11 and 14 mJy $beam^{-1}$ km $s^{-1}$ and the peak emission is 80 and 123 mJy $beam^{-1}$ km $s^{-1}$ respectively. The black contours are at intervals of $\sigma$ from $3\sigma$ to peak.

This is investigated further in Section 5.6. The blue-shifted emission peaks off source spectrally and potentially spatially too ($\approx$ 1-2 pixels, a projected distance of 15 - 30 au) and it is attributed to a disk wind where material is being driven from the surface of the disk resulting in a blue-shift along the line of sight.

### 5.4.2 Relative line strengths via matched filter analysis

As discussed in Chapter 3 a matched filter[1] can be used to detect lines in the *uv* data (Loomis *et al.*, 2018b). This is utilised to derive the relative line strengths of the deteced SO lines. A CLEANed image of the CO line ($J = 3 - 2$) and the best fit LIME model (see Section 5.5 for details) are used as filters. The CO image has been scaled down to one quarter of its size and this is motivated

[1]vis_sample is publicly available at:
https://github.com/AstroChem/vis_sample

by the compact nature of the SO emission (as seen in the channel maps and the integrated intensity: Figures 5.1 and 5.2). Application of the matched filter results in a measure of the response of the filter to the data at a given frequency. The response is scaled to $\sigma$ with the rms noise normalised to 1.

Figure 5.7 shows the response of the three detected SO lines to the compact CO and best fit LIME wedge model filters (see Section 5.5). For the CO filter three of the four lines were detected, the $J = 7_8 - 6_7$, $J = 7_7 - 6_6$, and $J = 8_8 - 7_7$ transitions. They have a peak response of 6.8, 4.2 and 4.0 respectively. There is no detection of the lower energy J=$3_2 - 1_2$ transition. Different CO filters were tested with different compression factors of 1/2, 1/3 and 1/4. The $J = 7_8 - 6_7$ transition is picked up in all the filters but the higher excitation lines have an improved response with the more compact filters. The best fit LIME model also detects the same three SO lines. The $J = 8_8 - 7_7$ filter response is approximately the same as with the compact CO filter but the other two lines responses are quite different.

The peak of the responses are not all at the expected source velocity supporting the theory that there are multiple velocity components of emission including a possible disk wind. The matched filter has confirmed the detection of the two lines detected in the image plane and they are observed at a substantially higher S/N than in the channel maps. It has also facilitated the detection of a line that was not detected in the imaging. Further, as the matched filter line response scales with intensity, there is now rudimentary excitation information on the three lines to motivate further modelling.

## 5.5 Line radiative transfer modelling

The abundance of SO was estimated by matching the observed emission with simulated emission generated using a HD 100456 physical disk structure (from

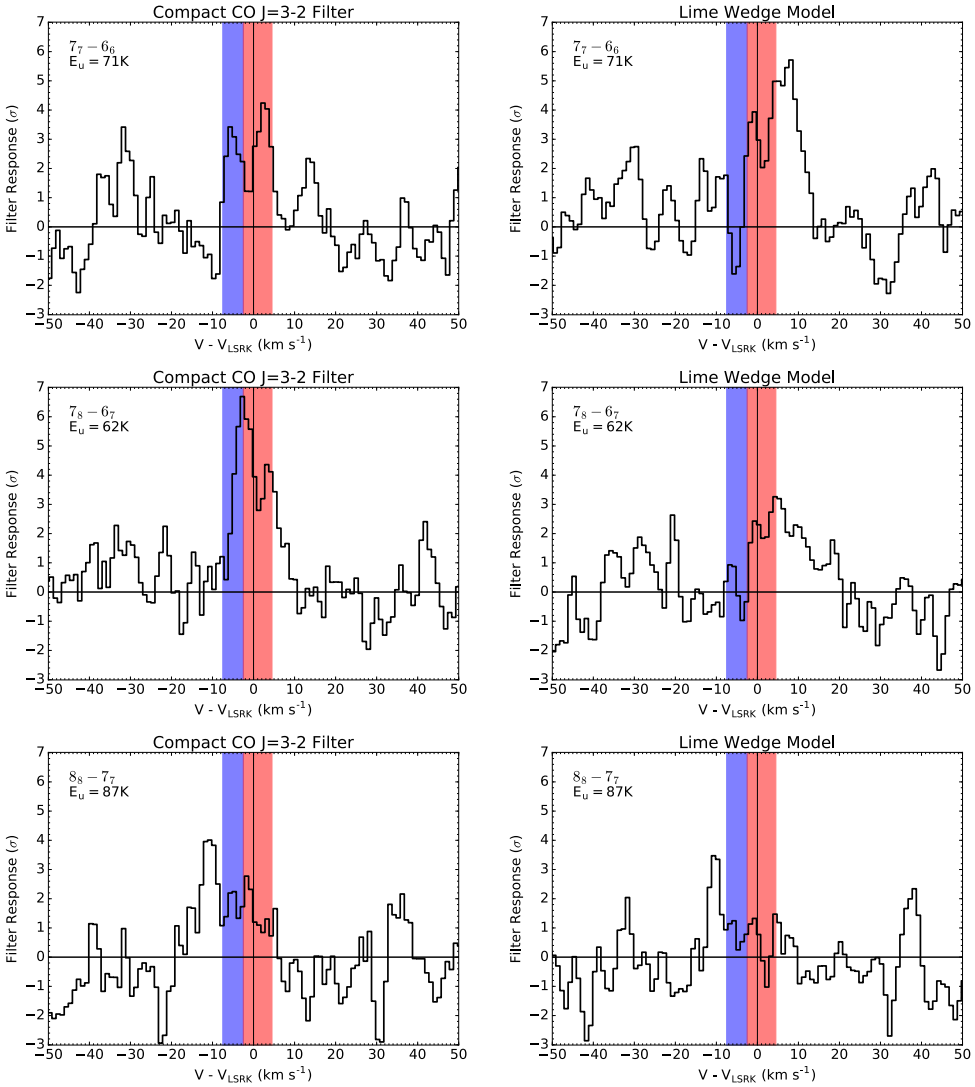


Figure 5.7: Matched filter responses for the three detected SO transitions. Left: the results using a spatially compact (1/4) version of the CO channel maps as a filter. Right: the results using the best fit LIME wedge model as a filter (see Section 5 for details). Highlighted in red and blue are the velocity ranges of emission attributed to a disk and a wind component respectively.

Kama *et al.* 2016a, see Figure 5.8) and LIME version 1.5 (LIne Modelling Engine; Brinch & Hogerheijde, 2010). Ray-tracing calculations were done assuming LTE and the appropriate distance, inclination and position angle for the source. The molecular data files for sulphur monoxide were taken from the Leiden Atomic and Molecular Database (LAMDA[1]). To check that LTE calculations were a good approximation the critical density of the transitions was calculated . The critical density for the SO $J = 7_7 - 6_6$ transition was determined to be $6 \times 10^6$ cm$^{-3}$ at 100 K using the LAMDA molecular data with the collisional rates from Lique *et al.* (2006). The other transitions are of a similar order of magnitude.

Because the matched filter is a linear process the relative responses for a pair of lines can be used as a proxy for their relative intensities after correcting for the difference in noise levels in each line. These relative intensities were converted to line ratios and this information was used to confine the location of the SO in the disk with respect to the temperature and density conditions. Model line ratios were calculated from line intensities determined using the RADEX [2] radiative transfer code assuming an SO column density of $10^{14}$ cm$^{-2}$ motivated by full chemical models (Kama *et al.*, 2016b, priv. comm.). RADEX is a non-LTE 1D radiative transfer code that can be used with the intensity of an observed particular molecular line to estimate the excitation temperature and column density of the gas, assuming an isothermal, homogeneous medium with no significant velocity gradient (van der Tak *et al.*, 2007). The line ratios of the three lines were calculated over a grid of temperatures and densities and the results are shown in Figure 5.9. These model line ratios were compared to the observed line ratios from the matched filter responses. Within the velocity range defined as disk emission, these are 1.5, 1.6 and 1.1 for the $J = 7_8 - 6_7/J = 7_7 - 6_6$, $J = 7_8 - 6_7/J = 8_7 - 7_6$ and $J = 7_7 - 6_6/J = 8_7 - 7_6$ line ratios respectively. A selection of the RADEX

[1] http://home.strw.leidenuniv.nl/~moldata/SO.html
[2] http://home.strw.leidenuniv.nl/~moldata/radex.html

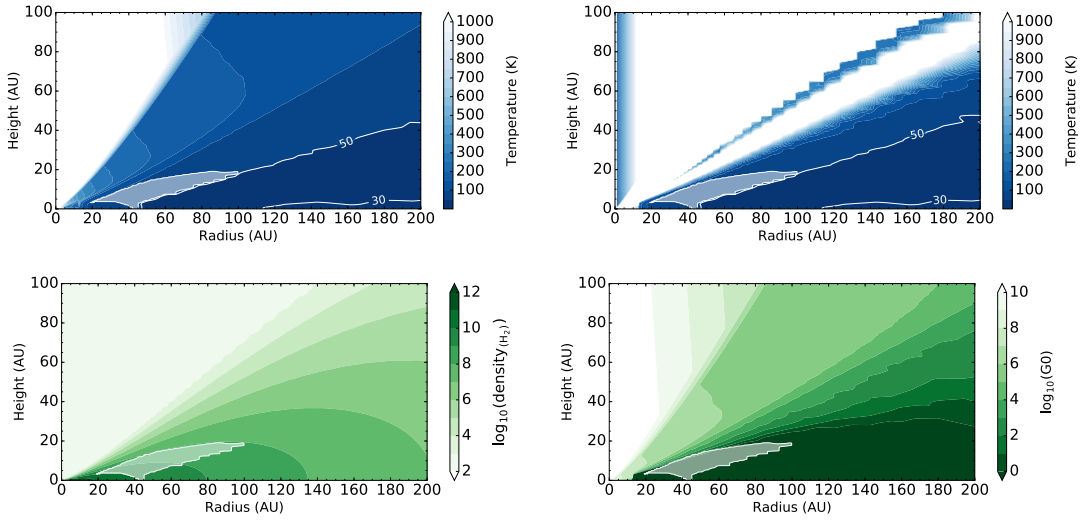


Figure 5.8: The HD 100546 disk physical structure from Kama *et al.* (2016a). Top left and moving clockwise: the dust temperature (K), gas temperature (K), UV flux (in units of the interstellar radiation field) and number density ($cm^{-3}$). The two white contours in each of the temperature plots correspond to a temperature of 30 K and 50 K. The shaded region highlights the location of the SO motivated by RADEX calculations and used in the LIME modelling.

results are shown in Table 5.3 along with the observed ratios and their associated errors. The regime that best fits our observations is a $H_2$ density from $10^8$ to $10^{10}$ $cm^{-3}$ and a gas temperature between 50 and 100 K. These conditions result in the SO being distributed in a ring from 20 to 100 au in a layer above the midplane (see Figure 5.8). This is in agreement with previous modelling of sulphur volatiles in disks (e.g.; Dutrey *et al.*, 2011) and is in agreement with the compact nature of the SO emission. Placing the SO in a region of lower density and higher temperature resulted in significantly more extended emission than in our observations. Only the near surface of the disk is modelled as it is assumed that this region of the disk ($< 100$ au) the optically thick dust emission will block the emission from the molecular gas in the far surface of the disk.

A set of models were run varying the fractional abundance of SO with respect

Table 5.3: Model and observed line ratios for the detected SO transitions.

| Observed line ratios | | | | |
|---|---|---|---|---|
| - | - | 1.5±0.4 | 1.6±0.4 | 1.1±0.4 |
| Radex model line ratios | | | | |
| $n_{H_2}$ ($cm^{-3}$) | $T_k$ (K) | J=$7_8-6_7$/J=$7_7-6_6$ | J=$7_8-6_7$/J=$8_7-7_6$ | J=$7_7-6_6$/J=$8_7-7_6$ |
| $10^5$ | 25 | 1.909 | 7.000 | 3.667 |
| $10^6$ | 25 | 1.726 | 3.982 | 2.296 |
| $10^7$ | 25 | 1.607 | 2.481 | 1.544 |
| $10^8$ | 25 | 1.587 | 2.302 | 1.451 |
| $10^9$ | 25 | 1.583 | 2.288 | 1.446 |
| $10^{10}$ | 25 | 1.583 | 2.288 | 1.446 |
| $10^5$ | 50 | 1.659 | 4.056 | 2.444 |
| $10^6$ | 50 | 1.489 | 2.285 | 1.535 |
| $10^7$ | 50 | 1.386 | 1.530 | 1.104 |
| $10^8$ | 50 | 1.367 | 1.449 | 1.060 |
| $10^9$ | 50 | 1.364 | 1.442 | 1.058 |
| $10^{10}$ | 50 | 1.364 | 1.442 | 1.058 |
| $10^5$ | 100 | 1.546 | 2.930 | 1.895 |
| $10^6$ | 100 | 1.400 | 1.683 | 1.203 |
| $10^7$ | 100 | 1.296 | 1.197 | 0.924 |
| $10^8$ | 100 | 1.273 | 1.150 | 0.903 |
| $10^9$ | 100 | 1.269 | 1.144 | 0.902 |
| $10^{10}$ | 100 | 1.270 | 1.145 | 0.902 |
| $10^5$ | 250 | 1.555 | 2.348 | 1.510 |
| $10^6$ | 250 | 1.371 | 1.318 | 0.961 |
| $10^7$ | 250 | 1.239 | 1.015 | 0.819 |
| $10^8$ | 250 | 1.212 | 0.990 | 0.816 |
| $10^9$ | 250 | 1.211 | 0.984 | 0.812 |
| $10^{10}$ | 250 | 1.203 | 0.978 | 0.813 |
| $10^5$ | 500 | 1.551 | 2.182 | 1.407 |
| $10^6$ | 500 | 1.358 | 1.203 | 0.886 |
| $10^7$ | 500 | 1.218 | 0.962 | 0.790 |
| $10^8$ | 500 | 1.192 | 0.939 | 0.788 |
| $10^9$ | 500 | 1.191 | 0.939 | 0.789 |
| $10^{10}$ | 500 | 1.193 | 0.939 | 0.787 |

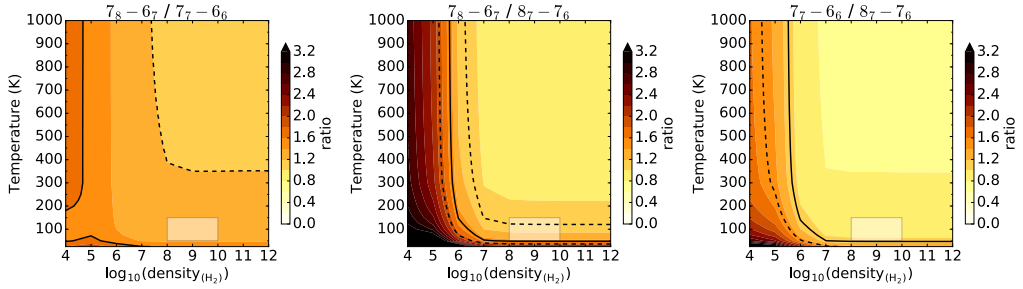


Figure 5.9: The RADEX modelling results of the selected SO line ratios. From left to right are the three ratios: $J = 7_8 - 6_7/J = 7_7 - 6_6$, $J = 7_8 - 6_7/J = 8_7 - 7_6$ and $J = 7_7 - 6_6/J = 8_7 - 7_6$. The solid black line is the observed line ratio and the dotted black lines are the error bars. The shaded region highlights the temperature and density conditions chosen for the location of the SO in the LIME modelling.

to $H_2$. This was done in order to match the observed peak in the integrated intensity of the disk component for each of the two transitions: 80 mJy beam$^{-1}$ km s$^{-1}$ for the $J = 7_7 - 6_6$ transition and 124 mJy beam$^{-1}$ km s$^{-1}$ for the $J = 7_8 - 6_7$. A model for a full disk was calculated with a fractional abundance of $3.5\times\ 10^{-7}$ with respect to $H_2$ resulting in a peak intensity for each of the lines of 92 mJy beam$^{-1}$ km s$^{-1}$ and 109 mJy beam$^{-1}$ km s$^{-1}$ respectively. These values match the peak emission of the observations within $\pm\ 1\sigma$. The residual maps of the observed integrated intensity minus the model integrated intensity for the two lines are shown in Figure 5.10. The residuals show that the observed emission is asymmetric peaking in the north east region of the disk and that a full disk is not an accurate representation of the data. A second model was run restricting the SO to a specific angular region of the disk. A 45° wedge of emission was calculated with the optimal position picked by eye from the residual maps to be from 0° to 45° from the disk's major axis. A fractional abundance of $5.0\times\ 10^{-6}$ with respect to $H_2$ resulted in a peak intensity for each of the lines of 93 mJy beam$^{-1}$ km s$^{-1}$ and 96 mJy beam$^{-1}$ km s$^{-1}$ respectively. These values match the peak emission

of the observations within $\pm$ 2$\sigma$. This fractional abundance is more than an order of magnitude greater than the 'depleted' sulphur fractional abundance observed dark clouds ($SO/H_2 \approx 10^{-8}$; Ruffle *et al.* 1999). This suggests that there are energetic processes occurring in HD 100546 releasing a source of refractory sulphur into the gas phase. The fractional abundance of SO derived from the LIME modelling is model dependent as it depends on the gas density of the region of the disk where the SO is located. This model well reproduces the integrated intensity; however, the kinematics trace red-shifted disk emission. The peak in both of the line profiles for the wedge models is 1.7$\times$ the observed line profile peaks and the model emission is over a narrower velocity range. The model line profiles for both the disk and the wedge models are compared with the observed line profiles in Figure 5.11. Further refinement of the disk emission component requires better data as the emission is the same size scale as the beam.

## 5.6 Discussion

### 5.6.1 Location and abundance of the detected SO emission

This Chapter presents the first detection SO in the protoplanetary disk around HD 100546. In the image plane there is a clear detection of two lines in the integrated intensity maps and the the S/N in the channel maps and line profile is improved by stacking. From the morphology of the line profile and the asymmetric distribution of the emission it is likely there are two components of emission: a wedge of disk emission and a blue-shifted component (at $\approx$ -5 km s$^{-1}$). We use a matched filter to better determine the relative intensities of the SO lines in the data set and confirm the detection of three transitions and a non detection of the lowest energy transition. The relative intensities of the three detected lines are used to motivate the location of SO in the disk using LIME radiative transfer

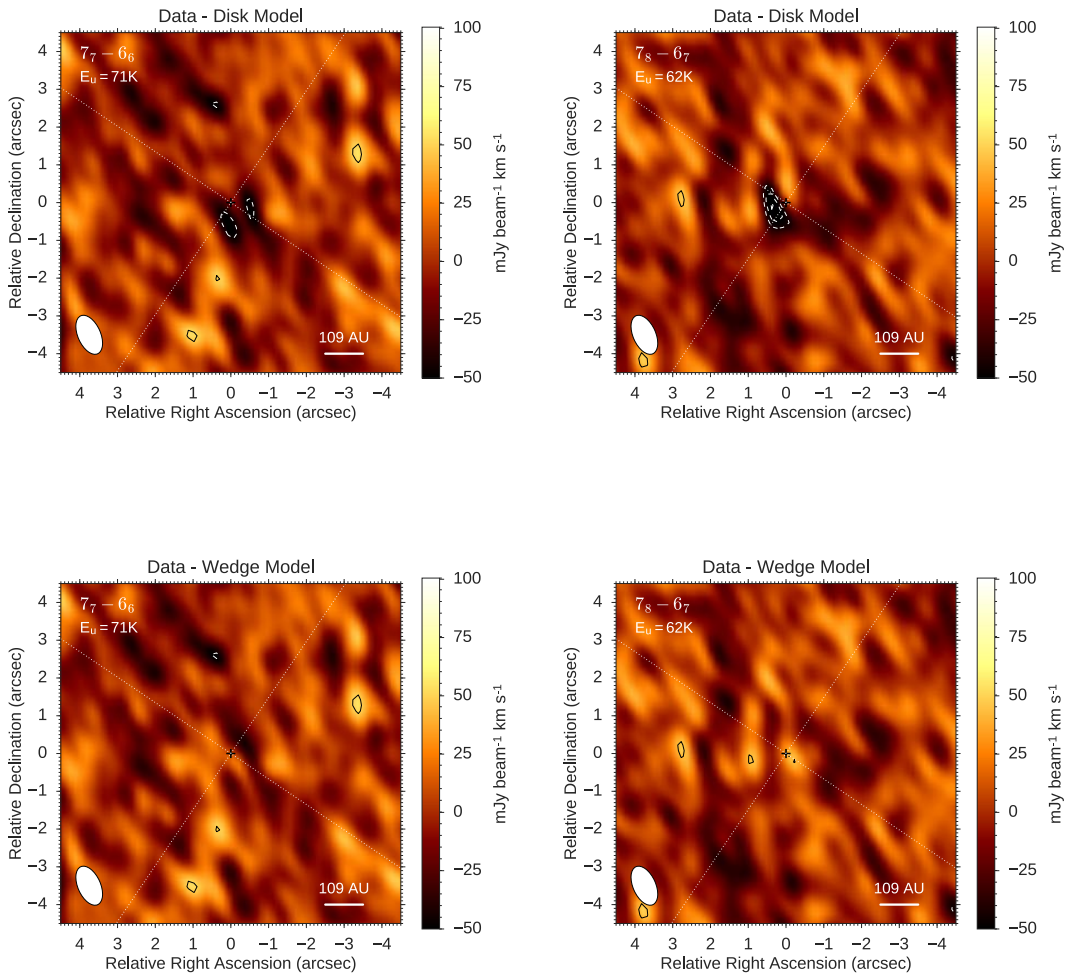


Figure 5.10: Residual maps from the disk emission integrated intensity and the LIME models for each of the transitions. Top: disk emission minus disk model. Bottom: disk emission minus wedge model. Overlaid are dashed -5,-4 and -3$\sigma$ contours and solid 3, 4 and 5$\sigma$ contours.

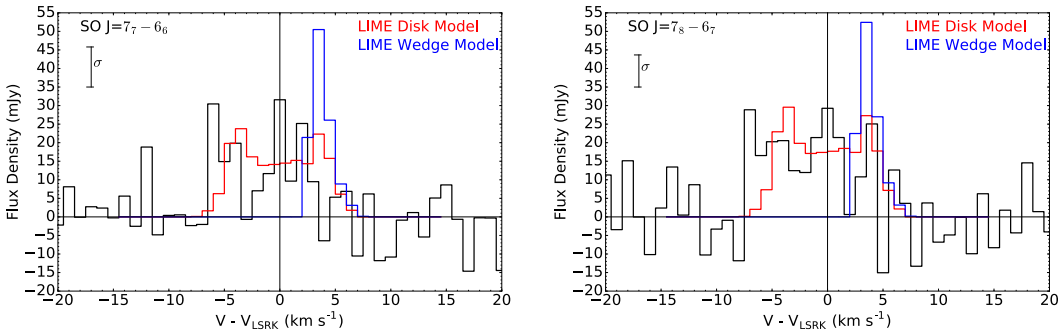


Figure 5.11: Line profiles of the individual J=$7_7 - 6_6$ (left) and J=$7_8 - 6_7$ (right) transitions with the LIME model line profiles plotted on the top: disk model (red) and wedge model (blue).

modelling. The residuals from the observed and modelled integrated intensity maps reveal that the integrated emission is indeed asymmetric peaking north-east of the source position. This is coincident with a 'hot-spot' observed in CO emission relating to a possible disk warp (Walsh *et al.*, 2017). The CO $J = 3 - 2$ emission from the HD 100546 disk is asymmetric along the minor axis with the emission peaking in the north east region of the disk. Since this CO emission is optically thick it should be tracing the temperature of the gas and therefore reflects an non-axisymmetric temperature structure. The SO can be modelled as a wedge of emission in this region. The excess blue-shifted component (-5 km s$^{-1}$ with respect to the source velocity) is spatially inconsistent with the expected location of blue-shifted Keplerian disk emission. This emission could be attributed to a disk wind. This hypothesis is summarised in a cartoon in Figure 5.12.

None of the four SO lines in the complementary HD 97048 Cycle 0 data (see Walsh *et al.*, 2016a) using the imaging methods detailed in Sections 5.3 and 5.4. The stacked emission in the channel maps at a velocity resolution of 1 km s$^{-1}$ reaches an rms noise of 6 mJy beam$^{-1}$, and there was no significant response using the matched filter analysis. This supports the hypothesis that SO is tracing a

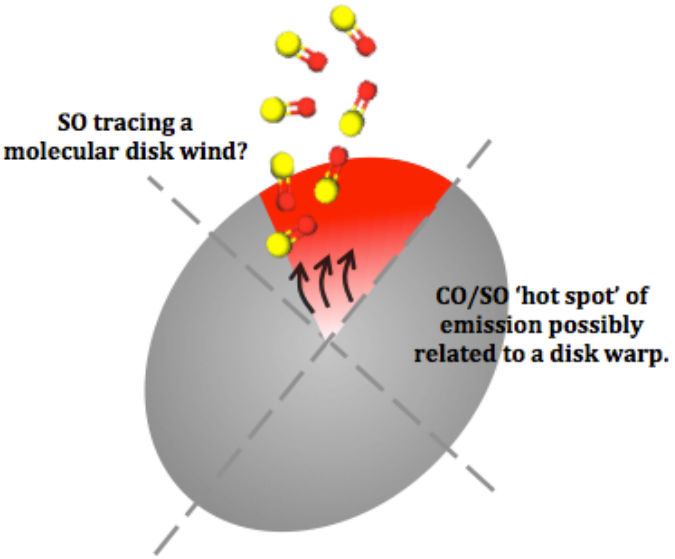


Figure 5.12: Cartoon of HD 100546 showing the wedge region of disk emission and the disk wind traced in SO.

physical mechanism unique to HD 100546. The disks around HD 100546 and HD 97048 have significantly different structures: the gap(s) in the sub-mm dust are further from the star in HD 97048 and there are no protoplanet candidates directly detected in this disk (Quanz *et al.*, 2012; van der Plas *et al.*, 2017; Walsh *et al.*, 2016a). But, there is a recent indirect detection of a planet at 130 au (Pinte *et al.*, 2019). Further detailed modelling is required to determine the chemical origin of the SO emission in the HD 100546 disk and how the physical and chemical conditions differ from those in the HD 97048 disk.

The only other disk from which SO emission has been imaged is AB Aur (Pacheco-Vázquez *et al.*, 2016). In this transition disk the SO is located further from the star in a ring from approximately 145 to 384 au with a maximum modelled abundance of $2\times10^{-10}$ with respect to $H_2$. The SO, like in HD 100456, is thought to reside in a layer between the surface and the midplane of the disk. The relative abundance of SO observed in AB Aur is a few orders of magnitude less

than in HD 100546, so the emission is not necessarily tracing the same process. In AB Aur, SO is proposed as a chemical tracer of the early stages of planet formation as the abundance of SO appears to decrease towards the disk's dust trap, a local pressure maximum thought to be the site of future planet formation (e.g.; van der Marel *et al.*, 2013).

### 5.6.2 Sulphur chemistry

Sulphur chemistry, particularly the evolution of S-bearing molecules on grain surfaces, is not fully understood as current models fail to reproduce observed abundances (e.g.; Guilloteau *et al.*, 2016). If the observations are probing a wedge or partial ring of SO, the inner edge of the emission coincides with the inner edge of the sub-millimetre dust ring at approximately 20 au. Since HD 100546 is a transition disk the midplane material is exposed to far-UV photons from the central star. This will cause the desorption of molecules from icy grain mantles. $H_2O$ ice has been observed in this disk (Honda *et al.*, 2016) and $H_2S$ ice is a primary component of cometary ices (Bockelée-Morvan *et al.*, 2000). The photodissociation of these molecules originating from cosmic rays or UV photons, depending on the height of the gas in the disk, would create the reactants needed to form SO;

$$\mathrm{H_2O} + h\nu \longrightarrow \mathrm{OH} + \mathrm{H} \tag{5.1}$$

$$\longrightarrow \mathrm{O} + \mathrm{H} + \mathrm{H} \tag{5.2}$$

$$\mathrm{H_2S} + h\nu \longrightarrow \mathrm{HS} + \mathrm{H} \tag{5.3}$$

$$\longrightarrow \mathrm{S} + \mathrm{H} + \mathrm{H} \tag{5.4}$$

$$\mathrm{HS} + \mathrm{O} \longrightarrow \mathrm{SO} + \mathrm{H} \tag{5.5}$$

$$\mathrm{S} + \mathrm{OH} \longrightarrow \mathrm{SO} + \mathrm{H}. \tag{5.6}$$

These two SO formation reactions have no reaction barrier (KIDA: KInetic Database for Astrochemistry http://kida.obs.u-bordeaux1.fr/). There are a few possible reactions for the destruction of SO to form $SO_2$ (Millar & Herbst, 1990);

$$SO + O \longrightarrow SO_2 + h\nu \tag{5.7}$$

$$SO + OH \longrightarrow SO_2 + H. \tag{5.8}$$

In AB Aur the abundance of SO decreases with increasing density towards the disk's dust trap. This is attributed to the increase in conversion of SO to $SO_2$ via radiative association with atomic oxygen and then freeze out of $SO_2$ onto dust grains (Pacheco-Vázquez *et al.*, 2016). In HD 100546, the density and temperature of the disk may have been perturbed creating the conditions for the localised formation of the observed asymmetric SO. However, chemical modeling of warped disks and associated temperature perturbations are required to confirm this hypothesis.

From observations of cometary volatiles, and for the particular case of 67P, the total abundance of sulphur-bearing species detected is consistent with the solar abundance of sulphur (Calmonte *et al.*, 2016). This means that if our solar system is typical then the observed depletion of sulphur in circumstellar regions may be an observational effect as we have not been able to detect the various forms of sulphur. The form of the sulphur, whether it resides in refractory or volatile form in planet-forming disks is still an open question. For the SO detected in HD 100546 it is unclear as to its origin, e.g., if it is a result of the volatile reactions described above or whether it has been released from refractory materials due to a shock as suggested by the high abundance in the models. Further observations may make this clearer.

### 5.6.3 What is the SO tracing?

The influence of the massive companion at approximately 10 au in the disk may cause the disk velocity structure to depart from simple Keplerian rotation in the inner region. The protoplanet embedded in the disk at 50 au may also have an effect (Quillen, 2006). If the disk is warped, the line of sight inclination will vary radially changing the velocity structure. Previous observations with APEX show that the $^{12}$CO emission from the HD 100546 protoplanetary disk is asymmetric (Panić *et al.*, 2010) suggesting that one side of the outer disk is colder by 10-20 K than the other or that there is a shadow on the outer disk caused by a warped geometry of the inner disk. Shadows resulting from disk warps and their effect on gas kinematics have been observed in a few other sources, e.g., HD 142527 (Casassus *et al.*, 2015a). There is evidence for a possible warp in the inner 100 au of the HD 100546 disk from a detailed study of the CO $J = 3 - 2$ kinematics (Walsh *et al.*, 2017). The spatial resolution of the HD 100546 Cycle 0 observations is limited to approximately 100 au along the minor axis of the disk so it is unclear what is causing the non-Keplerian motions. Since previous observations point towards this star hosting at least one massive companion, a warped disk is a favoured hypothesis. A warp would directly expose the north-east side of the disk to heating by the central star, creating locally the conditions for the formation of SO and the launching of a disk wind. The non-Keplerian motions in the inner 100 au of this disk could explain the discrepancy in the kinematics of the best fit model for the SO and the observations.

Disk dispersal is predicted to occur on a timescale up to 10 times shorter than observed disk lifetimes (Alexander *et al.*, 2014). This process limits the time available for giant planet formation, decreases the gas to dust ratio in the disk, and the mass loss will have an effect on the chemical content of the disk. In planet-forming Class II disks, jets and/or outflows are not the main driver of disk

dispersal. Instead the removal of angular momentum from the disk material can be achieved by slower disk winds ($< 30$ km s$^{-1}$). Photoevaporative disk winds are thought to be the primary disk dispersal mechanism (Alexander *et al.*, 2014). MHD disk winds also drive disk dispersal but are less well understood (Ercolano & Pascucci, 2017). Evidence of photoevaporative disk winds has been detected from a number of sources in the form of blue-shifted (up to 10 km s$^{-1}$) line profiles of forbidden line emission in the optical (e.g.; Ercolano & Owen, 2016; Pascucci *et al.*, 2011b). In addition to this, ALMA observations show a spatially resolved molecular disk wind originating from the HD 163296 disk (Klaassen *et al.*, 2013b), and a molecular protostellar outflow from TMC1A launched by a disk wind originating from a Keplerian disk (Bjerkeli *et al.*, 2016). We checked for any large scale or high velocity (>10 km s$^{-1}$) CO or SO emission from HD 100546 but none was detected. Gas launched from the HD 100546 disk surface with a velocity of a few km s$^{-1}$ would have a blue shift along the line of sight to the observer and could account for the blue-shifted emission. The mechanism for launching this material and why it is traced in the SO emission is unclear. The lack of observed excess blue-shifted CO emission is due to the SO originating from a layer in the disk that is higher than the emitting layer of the CO $J = 3 - 2$ ($E_u$ =33.19 K) gas. To see this effect in CO will require observations of higher J transition lines which will be tracing the warmer gas in the atmosphere. We surmise that the red-shifted counterpart of the disk wind, launching from the far side of the disk, is obscured by the optically thick dust disk. Determination of the chemical origin of the SO will help to shed light on whether the wind is MHD driven (ion-molecule chemistry) or photoevaporative (photon-dominated chemistry) in nature.

An alternative explanation for the SO emission is that it is the result of an accretion shock due to a circumplanetary disk. The position angle of the SO emission coincides with the observed infrared point source in the disk at

approximately 50 au that has been attributed to a protoplanet (see Figure 5.13 Currie *et al.*, 2015; Quanz *et al.*, 2013, 2015). Future ALMA observations at a higher spatial and spectral resolution will help determine if the SO emission is due to an accreting giant planet. As SO is a known shock tracer this is a valid hypothesis that should be tested.

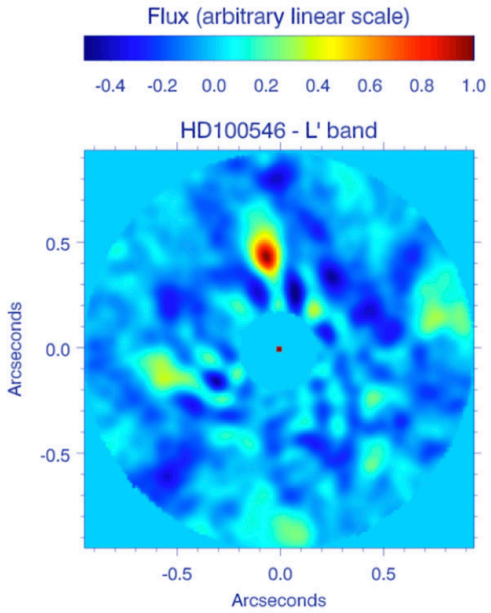


Figure 5.13: Observations of HD 100546 with VLT/NACO at L' band that detect a point source in the disk at a de-projected radius of ≈ 50 au (Quanz *et al.*, 2015)

## 5.7 Conclusions

This work has shown that SO is detectable in protoplanetary disks with ALMA by uncovering a sulphur reservoir in the HD 100546 protoplanetary disk. The S abundance required to reproduce the emission is $> 3$ orders of magnitude larger than the "depleted" value assumed in the ISM. This is strong evidence of a shock origin for the S that is then incorporated into SO. In addition, it is discussed that SO may be a tracer of a molecular disk wind or a circumplanetary disk. New

data with better spatial and spectral resolution are required to truly disentangle the different components of the emission in the case of a wind. Data with a beam less than the semi-major axis of the planets orbit are required to determine if the SO is directly tracing a forming planet. An ALMA Cycle 7 proposal has been accepted on the basis of the work presented in this Chapter and the observations are currently underway.

# Chapter 6

# Tapping into the semi-refractory reservoir in protoplanetary disks

## 6.1 Introduction

As discussed in Chapters 1 and 5, sulphur bearing volatiles are observed to be depleted in protoplanetary disks by a factor of $\approx 10^3$ relative to the cosmic S abundance. A more significant, $\approx 10^{4-5}$ times, level of depletion, is observed in silicon that has a solar abundance of Si/H $= 4 \times 10^{-5}$ (Asplund *et al.*, 2009). SiO is expected to be the most abundant Si bearing molecule in the gas phase at warm temperatures: the observed fractional abundance of SiO in dark clouds on the other hand is very low ($\approx 10^{-12}$; Ziurys *et al.*, 1989). It is therefore proposed that most of the Si is in refractory form as high fractional abundances ($\approx 10^{-6}$) of SiO are only detected in shocks (Martin-Pintado *et al.*, 1992). As Si is a primary constituent of the Earth's crust and the main component of the disk dust grains, the raw materials for building planets, this element is of particular interest. The Si and S abundances relative to other refractory elements in a disk can be derived from spectral observations of the stellar photosphere (Kama *et al.*, 2015). This enrichment in refractory materials in the photosphere is due to the accretion of disk material onto the star. The radiative rather than convective envelopes

Table 6.1: SiO and SO transition data

| | SiO | | SO | |
|---|---|---|---|---|
| Transition | $J = 8 - 7$ | $J = 9 - 8$ | $J = 7_7 - 6_6$ | $J = 7_8 - 6_7$ |
| Frequency (GHz) | 303.9268 | 347.3306 | 301.2861 | 304.0778 |
| $E_{\rm up}$(K) | 58.35 | 75.02 | 71.0 | 62.1 |
| $\rm E_a$ ($\rm s^{-1}$) | $1.464\times10^{-3}$ | $2.204\times10^{-3}$ | $3.429\times10^{-4}$ | $3.609\times10^{-4}$ |

The values for the line frequencies, Einstein A coefficients, and upper energy levels ($E_{\rm up}$) are from the Leiden Atomic and Molecular Database: http://home.strw.leidenuniv.nl/~moldata/ (LAMDA; Schöier *et al.*, 2005).

of the young Herbig Ae/Be stars leads to slow mixing timescales meaning that the accreted material remains near the stellar surface (Jermyn & Kama, 2018). While the photospheric abundances can characterise the level of dust depletion and the elemental ratios of the accreted material (Kama *et al.*, 2015), they do not necessarily reveal the full origin story of the nature of the reservoirs that carried those atoms through the disk. Being able to directly measure the volatile abundances of Si and S in protoplanetary disks provides an additional constraint on the total refractory abundances and gives insight into the nature of their main molecular carriers. This Chapter calculates the column densities of SiO and SO from observations of two SiO and SO lines observed in the HD 100546 and HD 97048 disks. These values are then compared with disk specific chemical models to identify the main molecular carrier and constrain their abundances.

## 6.2 Column density upper limits

The relevant SiO and SO lines targeted in both disks are are listed in Table 6.1. Only the two SO transitions that are robustly detected in HD 100546 are analysed in this Chapter. For each disk none of the SiO lines were detected in the image plane nor via matched filter analysis (Loomis *et al.*, 2018b). This was also the case for SO in the HD 97048 disk. In order to give the lowest upper limits, the non-detections of the two SiO and SO lines were stacked respectively in the

Table 6.2: ALMA Band 7 observations of SiO in the HD 97048 and HD 100546 disks.

| | HD 97048 | | HD 100546 | |
|---|---|---|---|---|
| Molecule | SiO | SO | SiO | SO |
| Synthesised beam | $0\farcs94 \times 0\farcs64$ | $0\farcs94 \times 0\farcs64$ | $1\farcs09 \times 0\farcs59$ | $1\farcs09 \times 0\farcs6$ |
| Beam P.A. | -46° | -46° | 29° | 24° |
| $\sigma_{\rm rms}$ (mJy beam$^{-1}$ per channel[a]) | 6.8 | 4.9 | 5.0 | 4.2 |
| Detected | N | N | N | Y |

[a] At a channel width of 1 km s$^{-1}$

visibility domain for each disk using the CASA tools *mstransform* and *concat*. Spectra were extracted from the stacked channel maps using *specflux* from both Keplerian and elliptical masks (see Figure 6.1). For the HD 97048 disk both the masks were 800 au in radius and for the HD 100546 disk both masks were 500 au in radius. There is no clear signal in the resulting plots as all fluxes are less than the $3\sigma$ level (calculated from the line free channels in the line profile extracted via an elliptical mask) further confirming the non-detections.

The rms noise ($\sigma_{\rm rms}$) from the line free channels in the channel maps was used to calculate an $3\sigma$ flux upper limit for the non-detected lines. Following the method in Carney *et al.* (2019):

$$\sigma = \sqrt{\frac{n_{\rm p}}{n_{\rm ppb}}} \times dv \times \sigma_{\rm rms}, \tag{6.1}$$

where $n_{\rm p}$ is the number of pixels included in the mask, $n_{\rm ppb}$ is the number of pixels per beam and $dv$ is the channel width of 1 km s$^{-1}$. The disk averaged column density is then calculated using Equation 3.1 where the partition function ($Q_{\rm rot}$) and the temperature-independent transition strength and dipole moment ($S_{ul}\mu^3$, in debye$^2$) are taken from CDMS (Müller *et al.*, 2005). The integrated line flux, $\int I_\nu dv$, is 3 $\sigma$ in the case of the non-detections and for the SO detection in HD 100546 this is calculated by integrating the line profile shown in Figure 5.4 and this is 0.191 Jy km s$^{-1}$. A range of excitation temperatures were used and

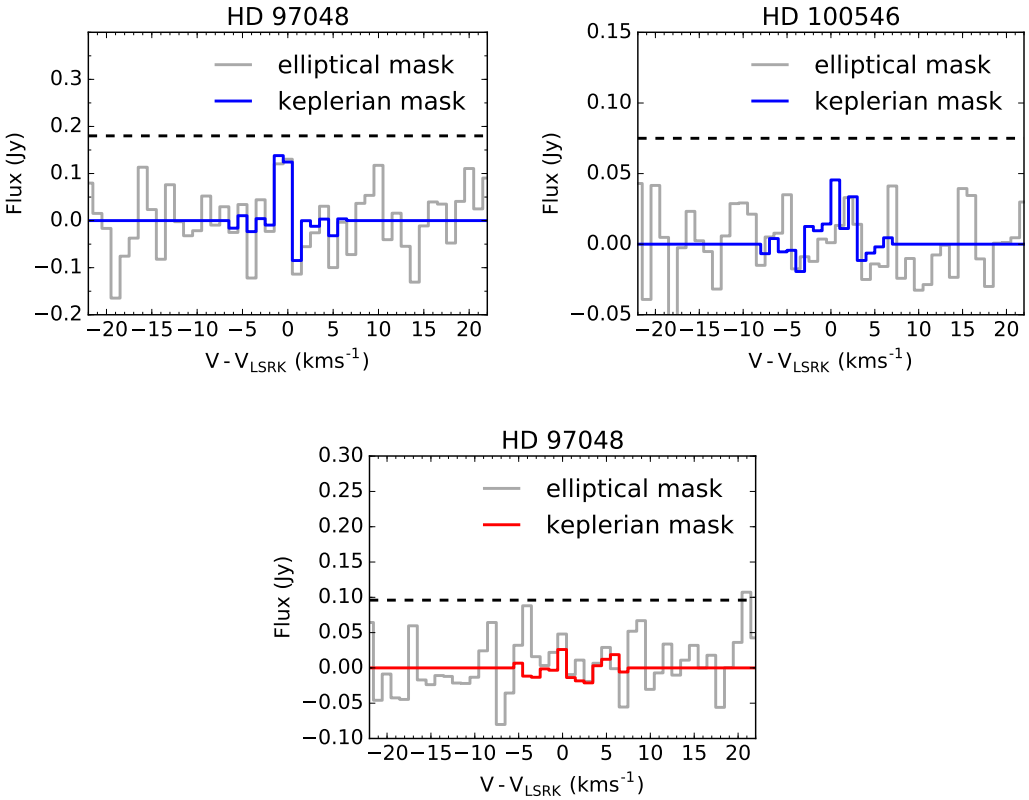


Figure 6.1: Stacked SiO (top) and SO (bottom) spectra extracted from the HD 97048 and HD 100546 disks with both elliptical and Keplerian masks. The black dashed line marks the $3\sigma$ level where $\sigma$ was calculated from the line free channels in the line profile extracted from the channel maps using an elliptical mask.

| HD 97048 | | | HD 100546 | | |
|---|---|---|---|---|---|
| $T_{ex}(K)$ | $N_{SiO}(cm^{-2})$ | $N_{SO}(cm^{-2})$ | $T_{ex}(K)$ | $N_{SiO}(cm^{-2})$ | $N_{SO}(cm^{-2})$ |
| 50 | $<7.8\times10^{12}$ | $<9.7\times10^{13}$ | 50 | $<1.3\times10^{13}$ | $4.3\times10^{13}$ |
| 100 | $<7.4\times10^{12}$ | $<1.1\times10^{14}$ | 100 | $<1.3\times10^{13}$ | $5.0\times10^{13}$ |
| 200 | $<1.0\times10^{13}$ | $<1.7\times10^{14}$ | 200 | $<1.9\times10^{13}$ | $7.6\times10^{13}$ |
| 400 | $<1.3\times10^{13}$ | $<2.2\times10^{14}$ | 400 | $<2.3\times10^{13}$ | $9.8\times10^{13}$ |

Table 6.3: SO and SiO column density upper limits and measurements.

the results are shown in Table 6.3. The upper limits are calculated with the molecular data for each of the stacked transitions but only the lower of the two values are listed in the table in order to give the lowest upper limit. The values are of order $10^{13}$ to $10^{14}$ cm$^{-2}$. To put this into context, the CO surface density in the HD 163296 model in Chapter 3 ranges from $10^{20}$ to $10^{22}$ cm$^{-2}$ within the CO snowline.

## 6.3 Chemical modelling

Chemical modelling enables a determination of which different molecules the S and Si are partitioned into and if they are in the gas or ice phase. This will inform on the dominant S and Si carrier in both disks and allow a direct comparison to the upper limits and direct measurements from the observations and a constraint on the expected volatile abundance of SiO and SO.

### 6.3.1 Model set-up

The HD 100546 and HD 97048 physical disk models are the same as used in Chapters 5 and 4 respectively. Both are shown again in Figure 6.2 with the same color scales to allow for a direct comparison between the two sources. Shown is the gas density ($n_{\rm H}$), the gas temperature, the UV-radiation field and the X-ray ionization rate. Additional parameters in the model are the dust temperature, host star luminosity and the cosmic ray ionisation rate assumed to be $5 \times 10^{-17}$ s$^{-1}$

Table 6.4: Select initial abundances for S and Si bearing volatiles where $n_{\rm H}$ is the number density of H nuclei. Where grain is equivalent to ice.

| Species | $n(X_{\rm gas})/n_{\rm H}$ | $n(X_{\rm grain})/n_{\rm H}$ |
|---|---|---|
| SiO | $8.45 \times 10^{-10}$ | $5.75 \times 10^{-10}$ |
| SO | $1.70 \times 10^{-11}$ | $9.36 \times 10^{-16}$ |
| SiS | $4.00 \times 10^{-17}$ | $5.18 \times 10^{-17}$ |
| CS | $4.16 \times 10^{-9}$ | $8.85 \times 10^{-10}$ |
| $SiH_4$ | $6.21 \times 10^{-14}$ | $4.19 \times 10^{-9}$ |
| $H_2S$ | $6.19 \times 10^{-12}$ | $2.94 \times 10^{-8}$ |

in the HD 100546 disk and $1.7 \times 10^{-17}$ s$^{-1}$ in the HD 97048 disk to keep consistency with Kama *et al.* (2016a) and Bruderer *et al.* (2012), and Woitke *et al.* (2019), respectively. The HD 100546 model is more flared than the HD 970478 model. The HD 100546 has a radially increasing $z/r$ varying from 0.5 to 2.0 and the HD 97048 has a constant $z/r$ of 0.34. The HD 100546 disk gas temperature in the atmosphere and outer midplane is also warmer. The UV field and X-ray ionization rate are both higher in HD 97048 model.

The initial molecular abundances were determined by running a single point dark cloud chemical model from atomic initial conditions for 1 Myr. The gas and dust temperature were set to 10 K, $n_{\rm H}$ to $2.0 \times 10^4$ cm$^{-3}$, and the cosmic ray ionisation rate to $10^{-17}$ s$^{-1}$ (Drozdovskaya *et al.*, 2015). The initial volatile S and Si abundances in this model relative to $n_{\rm H}$ were $8.00 \times 10^{-8}$ and $8.00 \times 10^{-9}$ respectively. Additionally, $n({\rm C})/n_{\rm H} = 1.40 \times 10^{-4}$, $n({\rm O})/n_{\rm H} = 3.20 \times 10^{-4}$ and $n({\rm N})/n_{\rm H} = 7.50 \times 10^{-5}$. The resulting molecular gas and ice phase initial abundances relative to $n_{\rm H}$ are shown in Table 6.4 for a select number of S and Si bearing volatiles after 1 Myr of chemical evolution. The main source of Si and S after 1 Myr are $SiH_4$ and $H_2S$ ice, respectively.

The chemical code as described in Section 2.3, was run for 1 Myr for each disk model using the reaction network from Walsh *et al.* (2015). Gas phase reactions and freeze-out/desorption processes only are included as these are expected to

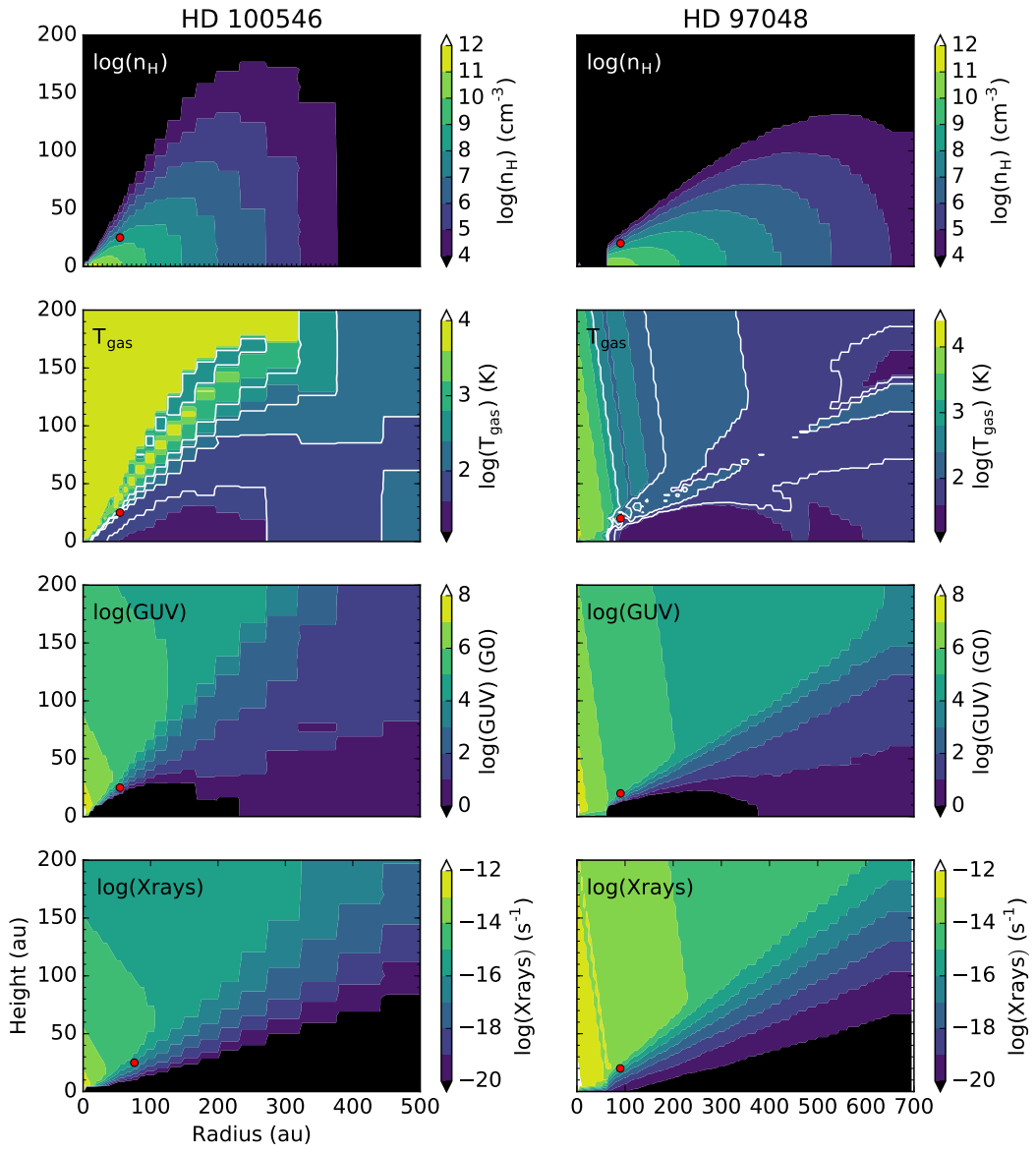


Figure 6.2: HD 100546 (left) and HD 97048 (right) disk models from Bruderer *et al.* (2012); Kama *et al.* (2016a); Woitke *et al.* (2019). From top to bottom: $n_{\rm H}$ density ($\rm cm^{-3}$), gas temperature (K), UV field (G0) and X-ray ionization rate ($\rm s^{-1}$). The red dot marks the point in the disk where the time dependency of the abundances were explored in each model.

dominate in the warmer Herbig Ae/Be disks. After this time the molecular abundances have approached steady state in most regions of the disk.

### 6.3.2 Model results

Figures 6.3, 6.4, 6.5 and 6.6 show the 2D abundance distributions of the most abundant Si and S bearing molecules in both disks. In both cases the gas-phase molecules are constrained to a thin layer in disk atmosphere. This molecular layer is considerably thicker in the HD 100546 disk and this can be attributed to the differences in disk physical structure. The HD 100546 disk is more flared, has a higher gas temperature and lower X-ray ionisation rate and UV flux meaning that there is a larger column of gas in the disk where these molecules can survive in the gas phase.

In HD 100546 SiO is the dominant Si-bearing species but in comparison the SiO abundance in the HD 97048 disk is negligible. In HD 97048 SiS is the dominant Si and S bearing molecule in the molecular layer. There is also significant SiS in the HD 100546 disk ($n(\mathrm{SiS})/n_{\mathrm{H})} \approx 10^{-9}$). SO, $SO_2$, CS have peak abundances in the HD 100546 disk that are at least 3 orders of magnitude greater than those in the HD 97048 disk. In the upper atmosphere atomic and ionised S and Si are present and these species account for rest of S and Si in the disk atmosphere.

There is significant ice-phase SiO in both disks ($n(\mathrm{GSiO})/n_{\mathrm{H})} \approx 10^{-8}$, where G denotes that the molecule is frozen-out onto the dust grain). This and the ice phase $SiH_4$ accounts for almost all of the available volatile Si in this region of the disk. There is negligible gas phase $SiH_4$. Most of the ice-phase S is locked up in the $H_2S$ ice in both disks. There is more ice phase SO in HD 97048 than in the HD 100546 disk and this is likely due to the HD 97048 disk being colder. As the grain surface chemistry is not included in this model care has to be taken when interpreting the ice phase abundances as they may go on to form other ices if a

full chemical model is run.

As the disk has a radial and vertical density gradient it is more intuitive to calculate the vertically integrated column density to determine the most abundant species in the disk. These are shown in Figure 6.7 for SiO, SO, CS and SiS in each disk. From this it is very clear that the HD 100546 model is more molecule rich than the HD 97048 model. This is partly due to the large inner cavity in the HD 97048 model and freeze-out in the colder midplane of HD 97048 disk coupled with enhanced dissociation and ionization in the atmosphere. The differences in chemistry between the two models will be discussed further in the next Section.

## 6.4 Discussion

### 6.4.1 The detectability of SiO and SO

Figure 6.8 shows the model column densities of SiO and SO in each disk as a function of radius and over plotted in the grey box are the column densities calculated in Section 6.2. For both disks there is a radial region where the model SiO abundances are greater than the calculated upper limits. The angular resolution of the observations limits resolving emission on scales of to $\approx$ 180 au and $\approx$ 100 au in the HD 97048 and HD 100546 disks, respectively. As the detectable SiO region in HD 97048 is very close to the upper limit value and $\approx$ 10 au in radius this would not be detectable in the current observations. The detectable SiO region in HD 100546 is $\approx$ 200 au in diameter and on average at least an order of magnitude higher than the upper limit, therefore, this suggests that it should have been detected. While there are no disk specific studies on silicon chemistry with which to compare to, silicon chemistry has been studied in other environments. For example, Herbst *et al.* (1989) modelled SiO in dark clouds and found that the resulting fractional abundances was four orders of magnitude less than the observed upper limit from this work. As SiO is expected to make up 50%

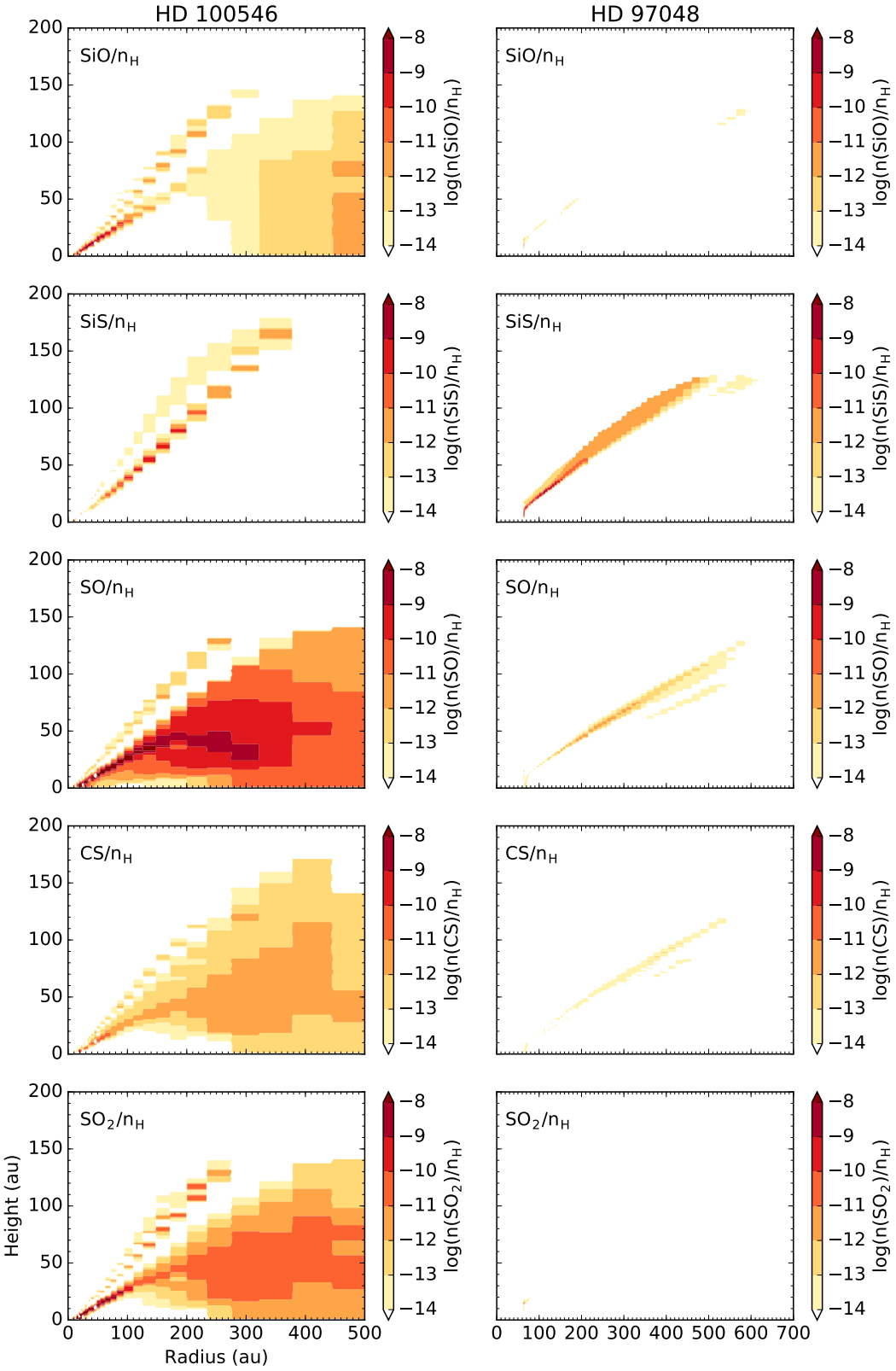


Figure 6.3: Select gas phase molecular abundances with respect to $n_{\rm H}$ in the HD 100546 (left) and HD 97048 (right) disks.

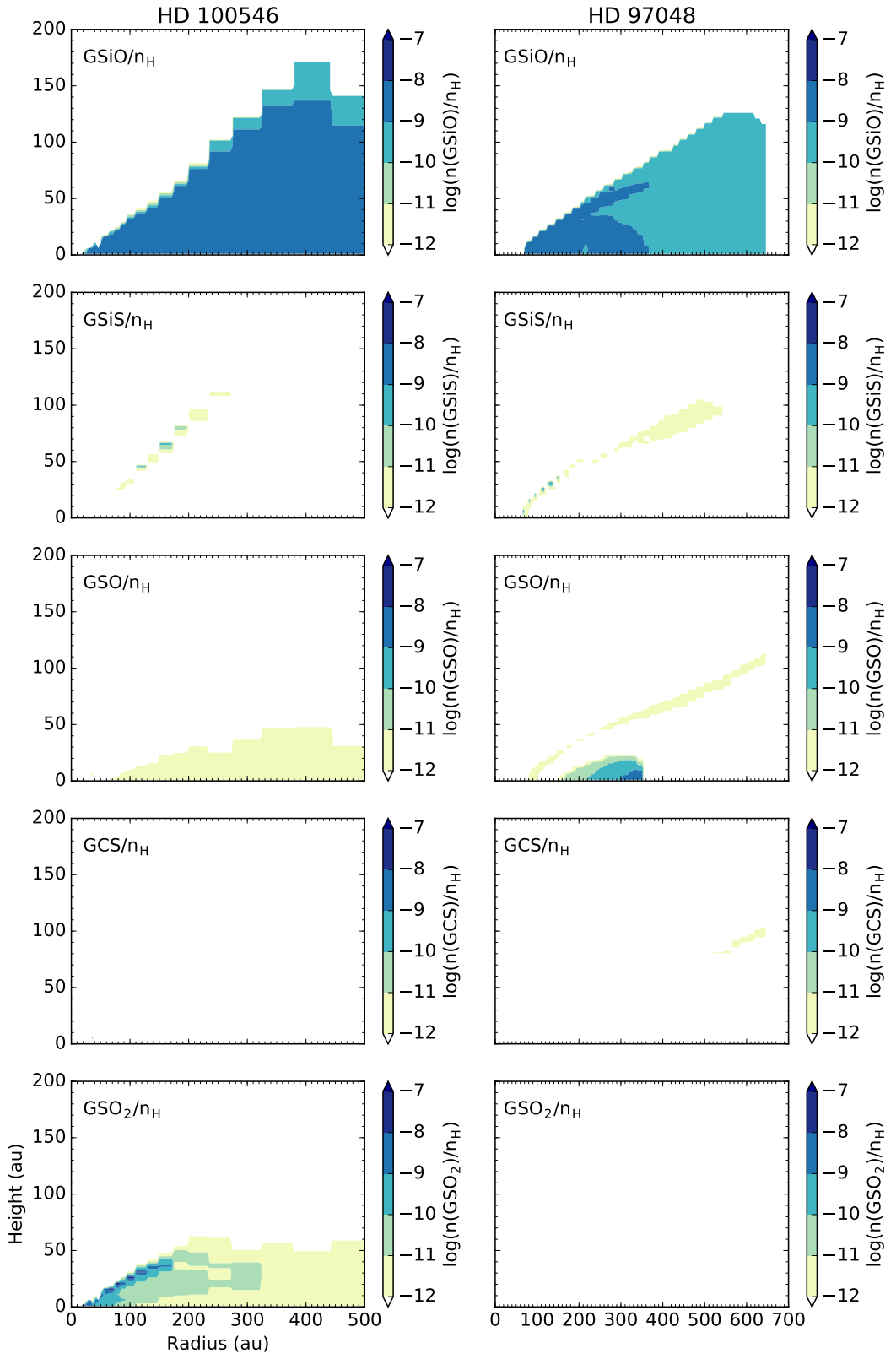


Figure 6.4: Select ice phase molecular abundances with respect to $n_{\mathrm{H}}$ in the HD 100546 (left) and HD 97048 (right) disks.

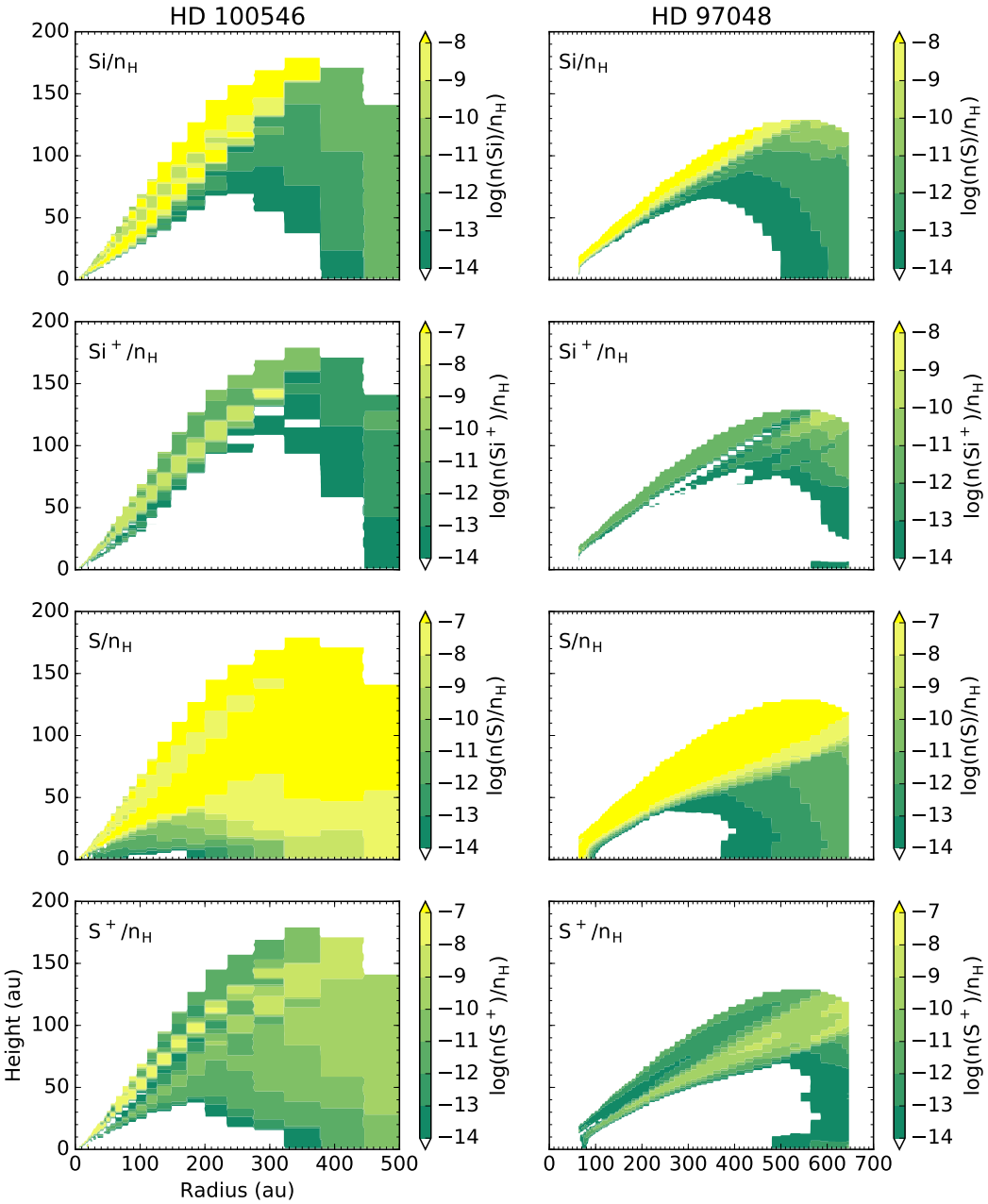


Figure 6.5: Select atomic and ionic abundances with respect to $n_{\mathrm{H}}$ in the HD 100546 (left) and HD 97048 (right) disks.

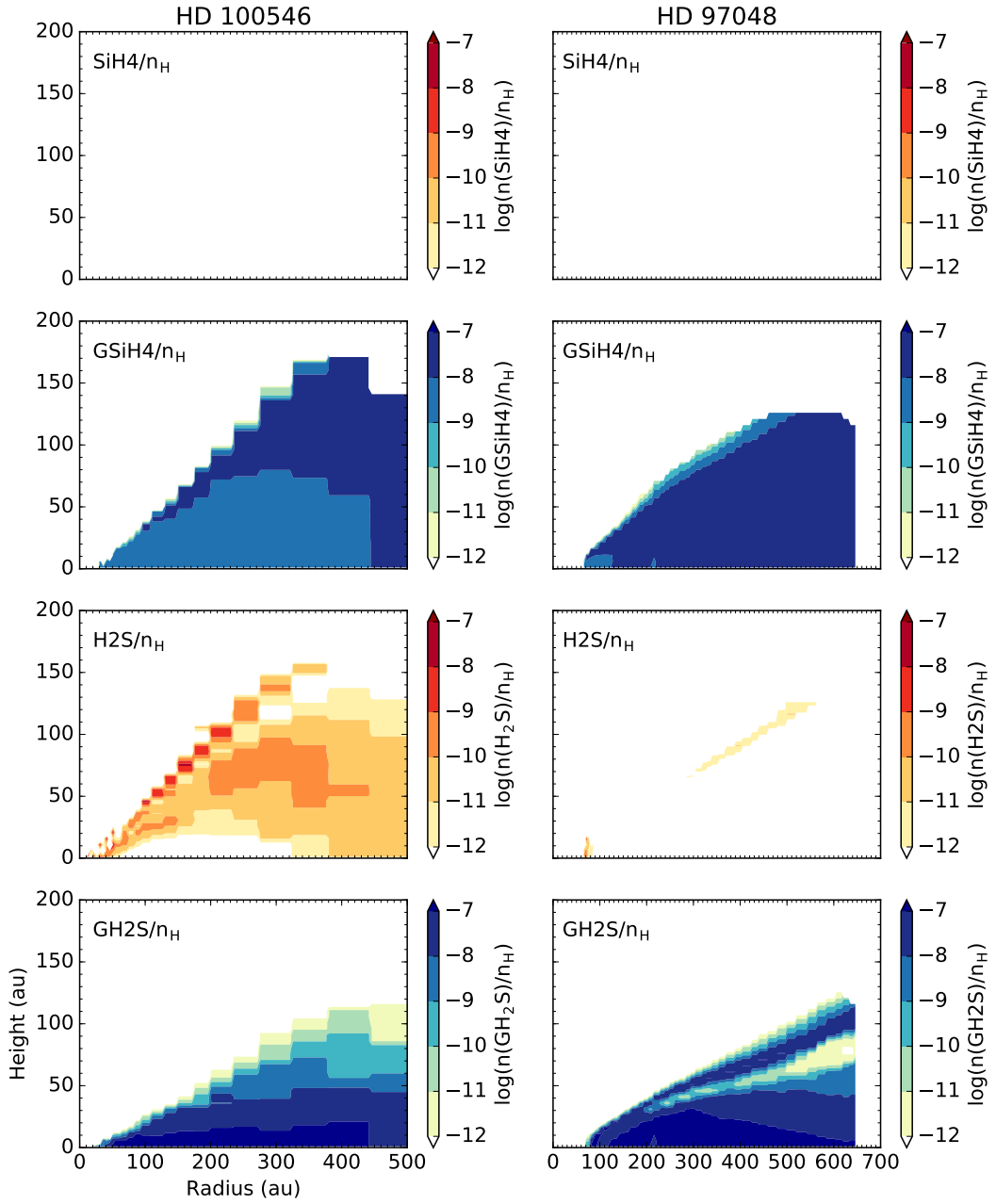


Figure 6.6: Abundances of $SiH_4$ and $H_2S$ gas and ice with respect to $n_H$ in the HD 100546 (left) and HD 97048 (right) disks.

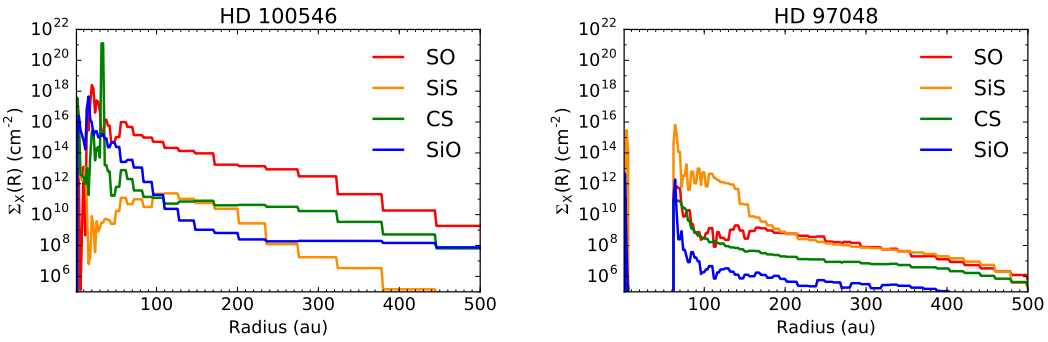


Figure 6.7: Vertically integrated column densities for SiO, SO, CS and SiS in HD 100546 (left) and HD 97048 (right) disk models

of the available volatile silicon this has been attributed to either a more significant Si depletion or an incomplete chemical network. The non-detection of SO in the HD 97048 disk is consistent with the upper limit. On the other hand, the strength of the SO detection in HD 100546 disk appears to be inconsistent with the chemical model predictions. The chemical model predicts a higher column of SO than extracted from the model independent analysis from the observations in Chapter 5. Full line radiative transfer models of the specific transitions detected are required to make a direct comparison, as the observations only probe the region of emitting gas at specific frequencies, not the entire reservoir of SO as shown in the chemical models. In general, sulphur chemical models fail to reproduce the observed SO abundances (e.g.; Guilloteau *et al.*, 2016), again indicating more volatile depletion or incomplete or inaccurate sulphur reaction networks. Agúndez *et al.* (2018) model the gas phase chemistry in both a generic T-Tauri and a Herbig disk model. In their model the sulphur chemistry is calculated but no Si-bearing molecules are included in their network. Additionally X-ray induced processes are not included. In their Herbig disk model the SO has a column density of order $10^{14}$ cm$^{-2}$ from ≈10-100 au (consistent with the HD 100546 observations) and $10^{12}$ cm$^{-2}$ from >100 au. This is is lower than the values in

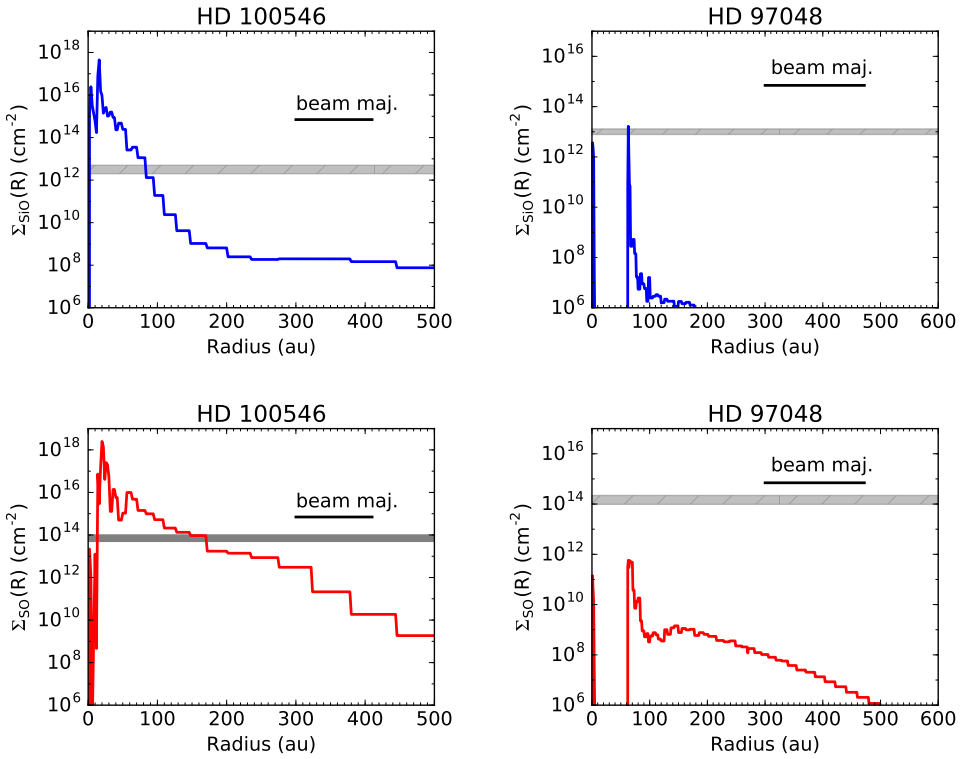


Figure 6.8: Radial column denisties for SiO (top) and SO (bottom) in the HD 100546 (left) and HD 97048 (right) disks. Over-plotted in the grey box are the column densities from Table 6.3

Figure 6.8 for the inner disk shown here.

### 6.4.2 Si and S chemistry

Both SiO and SiS have yet to be detected in a protoplanetary disk. In comparison, a variety of S and Si molecules are routinely detected in the outflows from forming stars and asymptotic giant branch (AGB) stars (e.g.; Brunner *et al.*, 2018; Massalkhi *et al.*, 2019; Wright *et al.*, 2020). The formation and destruction reactions pertinent to SiO, SO and SiS are investigated at $10^4$ and $10^5$ yrs. These are time steps where the rate of change in abundance is high. Figure 6.9 shows the gas and ice phase abundances of these species in time from a point in each

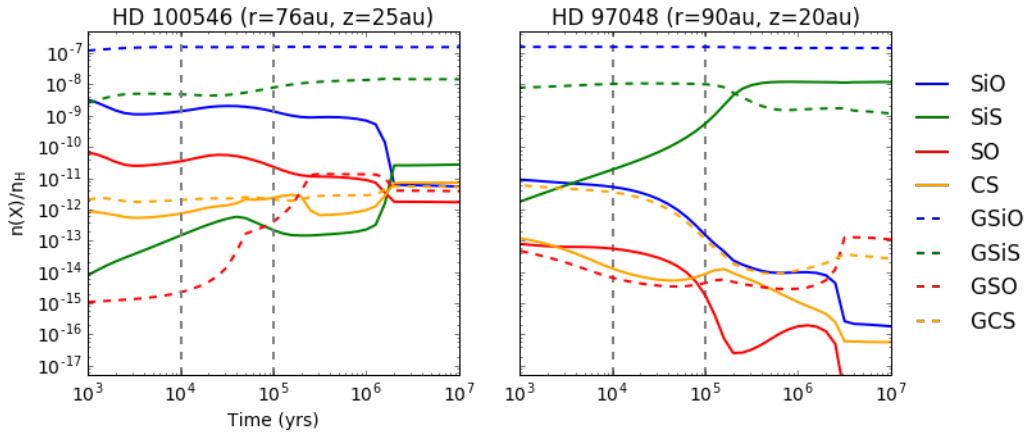


Figure 6.9: Relative abundances of select gas and ice phase Si and S bearing volatiles in time for a point in the HD 100546 (left) and HD 97048 (right) disk models.

disk. The point chosen is where the abundances peak in each disk and this is highlighted in Figure 6.2 with a red dot. This is at ($r$ = 90 au, $z$ = 20 au, $n_H = 3 \times 10^7$ cm$^{-3}$, $T_{gas}$ = 100 K) for HD 97048 and ($r$ = 76 au, $z$ = 25 au, $n_{H=2\times10^8\ cm^{-3}}$, $T_{gas}$ = 200 K) for HD 100546.

In the HD 100546 disk at $10^4$ and $10^5$ yrs SiO is formed via three processes, all of equal significance, and there is an overall net increase in abundance. These are dissociative recombination:

$$SiO^+ + e^- \longrightarrow SiO + H,$$

the neutral-neutral reaction:

$$Si + O_2 \longrightarrow SiO + O$$

and thermal desorption:

$$GSiO \longrightarrow SiO.$$

In comparison, in the HD 97048 disk there is a net decrease in SiO abundance at

the chosen point. At $10^4$ yrs approximately 70% of the SiO is formed via proton transfer:

$$NH_3 + SiOH^+ \longrightarrow {NH_4}^+ + SiO.$$

The dissociative recombination reaction from above accounts for 15% of the SiO formation and the rest is formed via neutral-neutral reactions of Si with $CO_2$, $O_2$ and NO. By $10^4$ years proton transfer accounts for 95% of the SiO formation. The only significant destruction pathway for SiO in both disks is via photo-ionization:

$$SiO + h\nu \longrightarrow SiO^+ + e^-.$$

In the HD 97048 point the $SiOH^+$ ion is a significant reactant compared to the HD 100546 point. The formation of $SiOH^+$ depends on the above destruction recation for SiO and then the subsequent ion-molecule reaction:

$$H_2 + SiO^+ \longrightarrow SiOH^+ + H.$$

The SO has a similar destruction reaction to SiO in both disks via photo-ionization:

$$SO + h\nu \longrightarrow SO^+ + e^-.$$

At both time steps in the HD 100546 disk the dominant formation pathway (80%) is via the neutral-neutral reaction:

$$S + O_2 \longrightarrow SO + O.$$

The reaction with OH accounts for a few percent and the rest is from desorption. In the HD 97048 disk the primary formation reaction for SO is

$$NH_3 + SO^+ \longrightarrow {NH_3}^+ + SO.$$

At the earlier time step the neutral-neutral reaction

$$O + SH \longrightarrow SO + H.$$

is also significant.

There are many more mechanisms for the destruction of SiS in the disk. These are various ion molecule exchange reactions with $C^+$, $H_3{}^+$, $HCO^+$, $He^+$ and are present in both disks at both times. In both disks significant SiS is adsorbed to the grains. This is not seen for the SiO or SO and is because the binding energy of SiS is higher ($3.8\times10^3$ K) than for SiO ($3.5\times10^3$ K) and SO ($3.5\times10^3$ K) meaning it will be frozen out at warmer temperature in the disk. In the HD 100546 disk by $10^3$ and $10^4$ yrs thermal desorption is the primary formation mechanism for the SiS. In comparison, reactions with the $HSiS^+$ ion are significant in the HD 97048 disk where:

$$NH_3 + HSiS^+ \longrightarrow SiS + NH_4{}^+,$$

$$HCN + HSiS^+ \longrightarrow SiS + HCNH^+$$

and

$$HSiS^+ + e^- \longrightarrow SiS + H.$$

Similar to the $SiOH^+$, after thermal desorption, the $HSiS^+$ forms via photo-dissociation:

$$GSiH_4 \longrightarrow SiH_4,$$

$$SiH_4 + h\nu \longrightarrow SiH_2 + H_2,$$

$$SiH_2 + h\nu \longrightarrow SiH_2{}^+ + e^-,$$

$$SiH_2{}^+ + S \longrightarrow HSiS^+ + H.$$

Overall, this is consistent with more SiO and SO formed and retained in the warmer disk (HD 100546) and in which the ionization rate is lower and UV field is weaker. On the other hand, the SiS formation is more efficient in the disk with the higher ionization rate and stronger UV field. A caveat of the above analysis is that no grain surface reactions were included. A follow up from this work would be to investigate the effect of including grain surface reactions that may convert S to $H_2S$ and Si to $SiH_4$ thus reducing the abundances of S and Si in the gas phase. This would also require updating the S and Si reactions in the chemical network from more recent works. For example, Laas & Caselli (2019) recently presented an updated gas-grain chemistry network to describe the depletion of S in dark clouds, but no Si reactions are considered. Nevertheless, SiS is predicted to be a tracer of ionization dominated chemistry in cool and massive protoplanetary disks.

### 6.4.3 Volatile sulphur depletion or enhancement in the HD 100546 disk?

Chapter 5 reported the detection of SO in the HD 100546 disk. The chemical model in this Chapter predicts a layer of SO in the disk out to 100's of  au that would have been detectable out to $\approx$ 150 au. In comparison, the observations show that the SO emission is compact $<$ 100 au and a comparison to models shows that the observed emission is also asymmetric. The SO model column density is also much higher than the value derived from the observations which are sensitive to the column density of the emitting gas through specific rotational transitions. As discussed in Chapter 5 S-bearing volatiles are observed to be depleted in disks. Recently, Kama *et al.* (2019) have shown, using photospheric abundances that $89 \pm 8\%$ of the total sulphur abundance is locked in refractory materials (thought to be FeS). This would mean that $\approx 1 - 10\%$ of the S is in volatile materials, this

is consistent with the $n(\mathrm{S})/n_{\mathrm{H}}$ of $8.00 \times 10^{-8}$ used in this model. Even given this though, model predictions of SO and other species tend to be at least an order of magnitude higher than upper limits and detections (Phuong *et al.*, 2018). This indicates that either (or both) the chemical network for the sulphur reactions is incomplete, the depletion of S is at the higher end of the Kama *et al.* (2019) value, and/or the physical model is not wholly representative of the source.

The SO emission in the HD 100546 disk is proposed to be attributed to either a disk wind or a circumplanetary disk. An MHD disk wind traced in SO has been detected from the HH 212 system and a molecular disk wind traced in CO has been detected originating from the HD 163296 disk (Klaassen *et al.*, 2013a; Tabone *et al.*, 2017). Both are associated with large scale outflows but there is no evidence for such an outflow towards the HD 100546 star and disk system. If the SO is liberated due to an accretion shock then the non-detection of the SiO places an upper limit on the strength of this shock. A proposal of follow up ALMA observations in Cycle 7 was accepted and are currently underway. These will target both SO, SiO and SiS lines in the HD 100546 disk at higher angular resolution and sensitivity.

## 6.5 Conclusion

This chapter takes the first detailed look at the sulphur and silicon chemistry in Herbig Ae disks. Silicon is the primary constituent of the dust in disks but the volatile component remains unconstrained both from an observational and modelling perspective. The non-detection of SiO in the HD 100546 disk is not consistent with the predictions from the chemical model whilst the non-detections of SO and SiO in the HD 97048 disk are consistent with the models. A significant decrease in the SO abundance in the HD 100546 disk model is required to match the observations. Further radiative transfer models of the detected and non-

detected SO transitions using the results from the chemical model are required to confirm this. Given the evidence for gas-phase sulphur depletion and the high percentage of refractory sulphur needed in the models in Chapter 5, the argument for a volatile enhancement of sulphur in this disk via a shock to explain the HD 100546 observations still holds. Additionally, the disk wind interpretation is also still feasible as dedicated chemical models of the chemistry in disk winds do not yet exist. Finally, the chemical models enable mapping of the different reservoirs of gas and ice phase Si and S in both the HD 100546 and HD 97048 disks. This reveals that SiS is a significant reservoir of both S and Si in these warm disks and will provide key insight to the observed volatile depletion of sulphur in protoplanetary disks.

# Chapter 7

# Conclusions

## 7.1 Summary

Molecular lines can be used to gain vital information on the physical and chemical conditions in disks. Constraining the properties of these disks leads to an understanding of the initial conditions of planet formation. This thesis has presented observations, analysis, and modelling of molecular line emission from four protoplanetary disks. These sources are all proposed to be hosting gas-giant planets. The following sections summarise the key findings of this thesis.

### 7.1.1 $^{13}C^{17}O$ as a tracer of disk gas mass

The total gas mass of a protoplanetary disk is most often inferred from observations of the most abundant CO isotopologues: $^{12}CO$, $^{13}CO$ and $C^{18}O$. ALMA has allowed for the routine detection of $C^{18}O$ in disks but the inferred gas masses have been anomalously low compared to the mm-dust derived masses. This has been primarily proposed to be due to the volatile depletion of carbon in disks (Miotello *et al.*, 2017). This can account for the low masses in disks under very chemical specific conditions (Bosman *et al.*, 2018; Schwarz *et al.*, 2018). Another complementary reason for the low gas masses may be that the $C^{18}O$ emission is optically thick and therefore not tracing the full column of gas in the disk. This

can be verified, model independently, through observations of less abundant and therefore optically thinner CO isotopologues. Chapter 3 presents the first detections of $^{13}C^{17}O$ in protoplanetary disks, which is the rarest ($\approx 120,000$ times less abundant than $^{12}C^{16}O$) stable isotopologue. The $^{13}C^{17}O$ J=3-2 transition is detected in the HD 163296 and HL Tau disks, and in both cases, a comparison to existing $C^{18}O$ observations towards these disks reveal that indeed the $C^{18}O$ lines are not optically thin throughout the entire radial extent.

The HD 163296 disk has been particularly well studied with the SMA and ALMA meaning that multiple CO isotopologue lines have been detected and modelled in previous work (Isella *et al.*, 2016; Qi *et al.*, 2011). This thesis utilises an existing 2D model of the gas density and temperature structure that has been shown to reproduce the existing observations. The $^{13}C^{17}O$ J=3-2 line strength from the model is determined using the line radiative transfer code LIME and the existing model flux is significantly less than what is observed. A model with 3.5 times more mass fits well both the new $^{13}C^{17}O$ observations and the existing line observations. The new gas mass of 0.21 $M_{\odot}$ (at 101.5 pc) is $\approx 10\%$ of the stellar mass and brings the gravitational stability of the disk into question. A Toomre Q analysis shows that the disk is currently stable with a minium Q value of $\approx 6$. Considering the disk mass lost through accretion in time, the simplest possible argument, and adding this mass back onto the disk results in a young unstable disk with a minimum Q of $\approx 1$. If this past instability is true then this may have been the origin of the four massive planets currently proposed to reside in the disk (Isella *et al.*, 2016; Liu *et al.*, 2018; Pinte *et al.*, 2018; Teague *et al.*, 2018).

After the 2015 ALMA long baseline observations of HL Tau, this has arguably become one of the most famous protoplanetary disks (ALMA Partnership *et al.*, 2015). Due to the high dust mass in the disk and under the assumption of an ISM gas-to-dust mass ratio ($\approx 100$) this disk has historically been considered

gravitationally unstable. Recent observations of $C^{18}O$ measure too low a gas mass for this to be the case (Wu *et al.*, 2018). Due to the more embedded nature of the HL Tau disk compared to the HD 163296 disk there are fewer observations and well tested disk models of the molecular lines. However, there are many studies that fit the mm-sized dust observations with a radial surface density power law (e.g.; Kwon *et al.*, 2015). Therefore, a similar analysis can be used for the molecular line emission. In this work, a simple power-law model is fit to the radial column density profile of the $^{13}C^{17}O$ derived assuming optically thin emission with the reasonable assumption that the observations are tracing the full column of CO gas from both sides of the disk and not accounting for any CO freeze-out. The greatest uncertainty in this gas mass calculation is the $CO/H_2$ ratio. With a $CO/H_2$ ratio consistent with recent disk chemical models (Bosman *et al.*, 2018; Schwarz *et al.*, 2018) there is now sufficient mass for the disk to be considered gravitationally unstable with $Q_{\rm min}$ of $\approx 1.1$, a disk mass of 0.21 $M_\odot$, and a disk-to-star mass ratio of 0.12. The radial region of instability coincides with the location of a proposed planet-carved gap in the dust disk. This gap has been attributed to a Saturn to Jupiter mass planet (Dipierro *et al.*, 2015b; Dong *et al.*, 2018; Jin *et al.*, 2016). Models of star-disk systems with similar masses as the HL Tau system form fragments with masses between 1-5 $M_{\rm Jup}$ on timescales of $10^3$ years (Boss, 2011). Therefore, the gravitational fragmentation of the HL Tau protoplanetary disk resulting in the formation of giant planet(s) may be the cause of the observed dust structures in the disk.

### 7.1.2 $H^{13}CO^+$ and $HC^{15}N$ in the HD 97048 disk

Observations of different molecular lines in protoplanetary disks provide valuable information on the gas kinematics, as well as constraints on the radial density and temperature structure of the gas. The HD 97048 disk has multiple rings of

mm and micron-sized dust and there is a proposed Jupiter mass planet located in one of the gaps (Ginski *et al.*, 2016; Pinte *et al.*, 2019; van der Plas *et al.*, 2017; Walsh *et al.*, 2016a). Chapter 4 presented the first detections of the $H^{13}CO^+$ and $HC^{15}N$ isotopologues in this disk. These new detections are compared to the ringed continuum mm-dust emission and the spatially resolved CO and $HCO^+$ emission. The $H^{13}CO^+$ and $HC^{15}N$ emission show hints of ringed sub-structure whereas the optically thick tracers, CO and $HCO^+$, do not. The $HCO^+/H^{13}CO^+$ intensity ratio across the disk it is radially constant (within the uncertainties), with a value of $12 \pm 3$ which is consistent with optically thick $HCO^+$ emission.

A physio-chemical parametric disk structure of the HD 97048 disk with an analytical prescription for the $HCO^+$ abundance distribution is used to generate synthetic observations of the $HCO^+$ and $H^{13}CO^+$ disk emission assuming LTE. The best by-eye fit models require radial variations in the $HCO^+/H^{13}CO^+$ abundance ratio and an overall enhancement in $H^{13}CO^+$ relative to $HCO^+$. This highlights the need to consider isotope selective chemistry and in particular low temperature carbon isotope exchange reactions. This also points to the presence of a reservoir of cold molecular gas in the outer disk ($T < 10$ K, $R > 200$ au) despite the disk being hosted by an A-type star. Chemical models are required to confirm that isotope-selective chemistry alone can explain the observations as current models do not extend to the Herbig disks (e.g.; Woods & Willacy, 2009). With these data, it cannot be ruled out that the known dust substructure in the HD 97048 disk is responsible for the observed trends in molecular line emission. Higher spatial resolution observations are required to fully explore the chemistry in planet-carved dust gaps and the potential of different molecular lines to trace these phenomena. Nevertheless, this results shows that disks around Herbig Ae/Be stars may be cold enough for the freeze-out of CO.

### 7.1.3 SO in the HD 100546 disk

Sulphur-bearing volatiles are observed to be significantly depleted in interstellar and circumstellar regions. This missing sulphur is postulated to be mostly locked up in refractory form. Chapter 5 presents the first detection of sulphur monoxide (SO), a known shock tracer, in the HD 100546 protoplanetary disk. Two rotational transitions: J= $7_7 - 6_6$ (301.286 GHz) and J= $7_8 - 6_7$ (304.078 GHz) are detected in their respective integrated intensity maps. The stacking of these transitions results in a clear $5\sigma$ detection in the stacked line profile. The emission is compact but is spectrally resolved and the line profile has two components. One component peaks at the source velocity and the other is blue-shifted by 5 kms$^{-1}$. The kinematics and spatial distribution of the SO emission are not consistent with that expected from a purely Keplerian disk. One explanation is that the blue-shifted emission could be due to a disk wind. The disk component was simulated using LIME and a physical disk structure. The disk emission is asymmetric and best fit by a wedge of emission in the north-east region of the disk coincident with a "hot-spot" observed in the $^{12}$CO $J = 3 - 2$ line. The favoured hypothesis is that a possible inner disk warp directly exposes the north-east side of the disk to heating by the central star, creating the conditions to launch a disk wind across this azimuth. Chemical models of disk winds will help to elucidate why the wind is particularly highlighted in SO emission and whether or not a refractory source of sulphur is needed. An alternative explanation is that the SO is tracing an accretion shock from a circumplanetary disk associated with the proposed protoplanet embedded in the disk at 50 au. Ongoing ALMA Cycle 7 observations will enable a distinction between the two hypotheses.

### 7.1.4 Tapping into the semi-refractory reservoir of protoplanetary disks

Silicon is the primary component of the dust grains in protoplanetary disks, which are building blocks of planets. The refractory silicon abundance in disks is difficult to constrain but the volatile material is more accessible via observations of Si-containing molecules such as SiO. The volatile silicon reservoir in disks is unconstrained, both via observations and chemical models. Chapter 6 calculates upper limits for the non-detections of SiO in the HD 97048 and HD 100546 disk ($\lesssim 10^{14}$ cm$^{-2}$). Additionally, the detected SO in HD 100546 and non-detected SO in HD 97048 are investigated. Two source specific physical models are used in conjunction with a disk chemical model to calculate the 2D abundance distributions of different Si and S-bearing molecules in each disk. The non-detection of SiO and SO in the HD 97048 disk were found to be consistent with the chemical model predictions. The HD 100546 model predicts significantly more SiO and SO than the upper limit and detection respectively. This is potentially due to incomplete chemical networks, disk model structures and/or increased volatile depletion. The models also reveal that SiS is a significant reservoir of both S and Si in these warm disks, particularly in the disk dominated by ionization, HD 97048. If confirmed as a warm molecular gas tracer in disks, SiS will provide key insight to the observed volatile depletion of silicon and sulphur in protoplanetary disks.

## 7.2 Future work

The following section describes follow up projects on the science presented in this thesis and considerations for future research by protoplanetary disk community as a whole.

### 7.2.1 Disk gas masses

The natural extension of the work presented in Chapter 3 is to use ALMA to detect $^{13}C^{17}O$ in other disks to see if these results can be applied to the general population of Class I and Class II disks. Targeting disks with detections of $C^{18}O$ J=2-1 (Band 6) will allow for precise sensitivity estimates for detecting $^{13}C^{18}O$ and $^{13}C^{17}O$. As shown in this thesis, accurate disk masses can be achieved with a moderate angular and spectral resolution (a beam size of $\approx 0\farcs5$ and a velocity resolution 1 km s$^{-1}$). Unfortunately this will not circumvent the greatest source of uncertainty in disk gas masses: the CO/$H_2$ ratio. Recent models have used $C_2H$ observations to constrain the level of carbon depletion in the atmosphere (Miotello *et al.*, 2019). This species can be included in same spectral setting as the CO lines to estimate the carbon depletion factor. Also, including $N_2H^+$ would allow for an additional constraint on the location of the CO snowline and thus the disks' midplane temperaure structure. As demonstrated by Williams & Best (2014), a grid of parametric models with different gas masses, temperature structures, and gas-to-dust mass ratios can be computed and then the model integrated line fluxes calculated and compared to the observations. Repeating and extending this to the less abundant CO isotopologues will enable a determination as to whether or not disk gas masses have been systematically underestimated due to the high optical depth of the $C^{18}O$ line emission. This will contribute necessary information to the current disagreement between disk and exoplanetary system masses (Manara *et al.*, 2018). Additionally, for the more gas rich disks, like HD 100546 and HD 97048, revised gas masses will give important constraints on the gravitational stability of these objects. As ALMA is indicating that planet formation seems to be happening early ($\lesssim 10^6$ yrs), then the formation of the proposed gas-giant planets in these systems will be more feasible via gravitational instability rather than core accretion.

### 7.2.2 Disk midplane temperature structures

Both the HD 163296 and HL Tau disks require dedicated high spatial resolution ($\approx 0\farcs1$) and high sensitivity observations in order to directly determine the location of the CO snowline. The proposed observations would again target $^{13}C^{18}O$ and $^{13}C^{17}O$, but at Band 3. Lower frequency observations are preferred as this will limit the loss in line emission due to the known optically thick dust in these disks. As shown in Chapter 3, $C^{18}O$ will not trace the CO midplane snowline directly in more massive disks due to the high column of gas in the disk atmosphere. Constraining the location of the midplane CO snowline is important for multiple reasons. Grain growth is proposed to be enhanced at snowline locations and therefore these are potential locations for planet formation via core accretion. Dust grains with CO ice mantles are also the feedstock for complex organic molecules like $CH_3OH$ which are in turn the building blocks of more exotic pre-biotic molecules (Walsh *et al.*, 2016b).

### 7.2.3 Key molecular tracers in Herbig Ae/Be disks

The disks around Herbig stars are the formation sites of gas-giant planetary systems. A-type stars have the highest occurrence rate of gas-giant planets across the stellar mass range (Johnson *et al.*, 2010; Reffert *et al.*, 2015, ; detections via the radial velocity method). Therefore, the radial and vertical chemical structure of these disks need to be mapped in order to determine the disk composition and the physical and chemical conditions within planet-carved gaps. This will set the composition of the gas-giant planet atmospheres, therefore future studies will enable the accurate interpretation of future high resolution exoplanet transmission spectra with, e.g., JWST and Ariel. The HD 97048 disk is among one of the brightest Herbig disks. The disk is gas rich but has yet to be fully targeted with ALMA for molecular line observations. This project would target the known key

disk tracers: $^{13}C^{17}O$, $HCO^+$, HCN, CN, $C_2H$, $N_2H^+$ (and isotopologues) with the spatial resolution to resolve emission within and outside the dust gaps ($\approx$ 10 au). These observations will allow for a more accurate 2D physical and chemical disk model to be constructed and the composition of the planet feeding material to be determined. The disk mass and CO snowline could also be constrained. These observations would also validate or disprove the key result from Chapter 4 which is that $H^{13}CO^+$ is tracing a reservoir of cold gas in the outer disk.

### 7.2.4 SO as a tracer of circumplanetary disks

While there is overwhelming evidence that planets have already formed in disks, circumplanetary disks (CPDs) have remained unconvincingly detected in the continuum and molecular line emission. Detecting CPDs are fundamental for understanding how planets assemble from the surrounding protoplanetary disk material. In the HD 100546 disk, there is evidence that SO is tracing an accretion shock from a CPD or a disk wind is another possibility. SO is a known tracer of shocked gas and has been shown to trace accretion shocks at the disk-envelope interface in young Class I sources. The accretion of material from protoplanetary disk to planet can be viewed as a scaled down version of this and it is expected that the same observational tracers of shocks are applicable when studying giant planet formation. Therefore, SO has the potential to be a unique probe of embedded CPDs, which have so far only been convincingly detected in H$\alpha$ emission (PDS 70; Wagner *et al.*, 2018). A proposal based on the work presented in this thesis was accepted in Cycle 7 and the observations are currently underway. These observations target SO, shock tracers (SiO, $CH_3OH$), and SiS in the HD100546 disk. The first successful confirmation of the presence of a CPD traced in a molecular line opens doors to new molecular line diagnostics of planet-disk interactions at high angular resolution and the physics and chemistry of giant

planet formation.

## 7.3 Final remarks

Gas giant planets on wide orbits are the potential exoplanet population currently probed with ALMA via the ringed depletion of continuum emission. These dust structures motivate the need for studies on the distribution of molecular gas in these potentially planet-forming disks. This thesis has shown that molecular lines are powerful probes of disk physical and chemical conditions. Further progress requires observations of molecular lines in disks at high sensitivity with the angular resolution required to properly probe the planet-building environment. The sensitivity of ALMA means that the rarest of isotopologues can be targeted.

Additionally, disk models that accurately represent the dust and gas distribution in disks are sorely needed. Specifically, models which take into account the gas within the dust cavities and multiple rings of gas and dust depletion. Such models will maximise the power of molecular line emission to provide much needed information on the physical and chemical conditions in planet-forming disks. Efforts also need to be made to find models to fit multiple observable from different molecules and at different frequencies, e.g., both HD and rare CO isotopologue lines. Complementary observations of the dust at shorter and longer wavelengths than ALMA at comparable spatial resolution are also needed. The distribution of both the larger and smaller disk grains are important for the disk chemistry. Currently SPHERE is proving incredible scattered light images of disks (Avenhaus *et al.*, 2018) and future observations with ngVLA and SKA will provide unprecedented observations of dust that has grown to centimeter sizes (Andrews *et al.*, 2018b; Wilner, 2004). Similarity SOFIA will allow for observations of HD which will prove an additional constraint on disk gas masses. Molecules like $H_2O$, $CO_2$ and $CH_4$ which are not accessible with ALMA but that will be with JWST will

give information on the composition of the disk atmosphere in the planet-building zone.

Finally, because there is growing evidence that planet formation is happening early (<1 Myr) these younger sources need to be targeted in observing campaigns. Targeting the rarest isotopologues will limit the effect of envelope and cloud contamination at ALMA Band 3. This will allow us to view the initial conditions of planet formation enabling us to connect the dots in the journey from protoplanetary disks to exoplanets.

# References


Adams, F.C., Lada, C.J. & Shu, F.H. (1987). Spectral evolution of young stellar objects. *ApJ*, **312**, 788–806. 3

Agúndez, M., Roueff, E., Le Petit, F. & Le Bourlot, J. (2018). The chemistry of disks around T Tauri and Herbig Ae/Be stars. *A&A*, **616**, A19. 16, 116, 164

Aikawa, Y., Umebayashi, T., Nakano, T. & Miyama, S.M. (1997). Evolution of Molecular Abundance in Protoplanetary Disks. *ApJ*, **486**, L51–L54. 16

Aikawa, Y., Umebayashi, T., Nakano, T. & Miyama, S.M. (1999). Evolution of Molecular Abundances in Protoplanetary Disks with Accretion Flow. *ApJ*, **519**, 705–725. 16

Aikawa, Y., van Zadelhoff, G.J., van Dishoeck, E.F. & Herbst, E. (2002). Warm molecular layers in protoplanetary disks. *A&A*, **386**, 622–632. 16

Aikawa, Y., Furuya, K., Nomura, H. & Qi, C. (2015). Analytical Formulae of Molecular Ion Abundances and the $N_2H^+$ Ring in Protoplanetary Disks. *ApJ*, **807**, 120. 44, 95, 96, 115

## REFERENCES


Akiyama, E., Momose, M., Hayashi, H. & Kitamura, Y. (2011). Thermal Structure of a Protoplanetary Disk around HD 163296: A Study of Vertical Temperature Distribution by CO Emission Lines. *Publications of the Astronomical Society of Japan*, **63**, 1059–1069. 77

Akiyama, E., Hasegawa, Y., Hayashi, M. & Iguchi, S. (2016). Planetary System Formation in the Protoplanetary Disk around HL Tauri. *ApJ*, **818**, 158. 72

Alexander, R., Pascucci, I., Andrews, S., Armitage, P. & Cieza, L. (2014). The Dispersal of Protoplanetary Disks. In H. Beuther, R.S. Klessen, C.P. Dullemond & T. Henning, eds., *Protostars and Planets VI*, 475. 10, 147, 148

ALMA Partnership, Brogan, C.L., Pérez, L.M., Hunter, T.R., Dent, W.R.F., Hales, A.S., Hills, R.E., Corder, S., Fomalont, E.B., Vlahakis, C., Asaki, Y., Barkats, D., Hirota, A., Hodge, J.A., Impellizzeri, C.M.V., Kneissl, R., Liuzzo, E., Lucas, R., Marcelino, N., Matsushita, S., Nakanishi, K., Phillips, N., Richards, A.M.S., Toledo, I., Aladro, R., Broguiere, D., Cortes, J.R., Cortes, P.C., Espada, D., Galarza, F., Garcia-Appadoo, D., Guzman-Ramirez, L., Humphreys, E.M., Jung, T., Kameno, S., Laing, R.A., Leon, S., Marconi, G., Mignano, A., Nikolic, B., Nyman, L.A., Radiszcz, M., Remijan, A., Rodón, J.A., Sawada, T., Takahashi, S., Tilanus, R.P.J., Vila Vilaro, B., Watson, L.C., Wiklind, T., Akiyama, E., Chapillon, E., de Gregorio-Monsalvo, I., Di Francesco, J., Gueth, F., Kawamura, A., Lee, C.F., Nguyen Luong, Q., Mangum, J., Pietu, V., Sanhueza, P., Saigo, K., Takakuwa, S., Ubach, C., van Kempen, T., Wootten, A., Castro-Carrizo, A., Francke, H., Gal-

lardo, J., Garcia, J., Gonzalez, S., Hill, T., Kaminski, T., Kurono, Y., Liu, H.Y., Lopez, C., Morales, F., Plarre, K., Schieven, G., Testi, L., Videla, L., Villard, E., Andreani, P., Hibbard, J.E. & Tatematsu, K. (2015). The 2014 ALMA Long Baseline Campaign: First Results from High Angular Resolution Observations toward the HL Tau Region. *ApJ*, **808**, L3. 20, 23, 25, 53, 71, 73, 74, 76, 81, 82, 174

Andre, P., Ward-Thompson, D. & Barsony, M. (1993). Submillimeter continuum observations of Rho Ophiuchi A - The candidate protostar VLA 1623 and prestellar clumps. *ApJ*, **406**, 122–141. 3

Andrews, S.M. (2020). Observations of Protoplanetary Disk Structures. *arXiv e-prints*, arXiv:2001.05007. 124

Andrews, S.M., Rosenfeld, K.A., Wilner, D.J. & Bremer, M. (2011). A Closer Look at the LkCa 15 Protoplanetary Disk. *ApJ*, **742**, L5. 8

Andrews, S.M., Wilner, D.J., Zhu, Z., Birnstiel, T., Carpenter, J.M., Pérez, L.M., Bai, X.N., Öberg, K.I., Hughes, A.M., Isella, A. & Ricci, L. (2016). Ringed Substructure and a Gap at 1 au in the Nearest Protoplanetary Disk. *ApJ*, **820**, L40. 15

Andrews, S.M., Huang, J., Pérez, L.M., Isella, A., Dullemond, C.P., Kurtovic, N.T., Guzmán, V.V., Carpenter, J.M., Wilner, D.J., Zhang, S., Zhu, Z., Birnstiel, T., Bai, X.N., Benisty, M., Hughes, A.M., Öberg, K.I. & Ricci, L. (2018a). The Disk Substructures at High Angular Resolution Project (DSHARP). I. Motivation, Sample, Calibration, and Overview. *ApJ*, **869**, L41. 25, 26

Andrews, S.M., Wilner, D.J., Macias, E., Carrasco-Gonzalez, C. & Isella, A. (2018b). Science with an ngVLA: Resolved Substructures in Protoplanetary Disks. *arXiv e-prints*, arXiv:1810.06598. 182

Ansdell, M., Williams, J.P., van der Marel, N., Carpenter, J.M., Guidi, G., Hogerheijde, M., Mathews, G.S., Manara, C.F., Miotello, A., Natta, A., Oliveira, I., Tazzari, M., Testi, L., van Dishoeck, E.F. & van Terwisga, S.E. (2016). ALMA Survey of Lupus Protoplanetary Disks. I. Dust and Gas Masses. *ApJ*, **828**, 46. 22

Ansdell, M., Williams, J.P., Manara, C.F., Miotello, A., Facchini, S., van der Marel, N., Testi, L. & van Dishoeck, E.F. (2017). An ALMA Survey of Protoplanetary Disks in the $\sigma$ Orionis Cluster. *AJ*, **153**, 240. 22

Ansdell, M., Williams, J.P., Trapman, L., van Terwisga, S.E., Facchini, S., Manara, C.F., van der Marel, N., Miotello, A., Tazzari, M., Hogerheijde, M., Guidi, G., Testi, L. & van Dishoeck, E.F. (2018). ALMA Survey of Lupus Protoplanetary Disks. II. Gas Disk Radii. *ApJ*, **859**, 21. 22

Asplund, M., Grevesse, N., Sauval, A.J. & Scott, P. (2009). The Chemical Composition of the Sun. *ARA&A*, **47**, 481–522. 14, 151

Avenhaus, H., Quanz, S.P., Meyer, M.R., Brittain, S.D., Carr, J.S. & Najita, J.R. (2014). HD100546 Multi-epoch Scattered Light Observations. *ApJ*, **790**, 56. 124

Avenhaus, H., Quanz, S.P., Garufi, A., Perez, S., Casassus, S., Pinte, C., Bertrang, G.H.M., Caceres, C., Benisty, M. & Dominik, C. (2018). Disks around T Tauri Stars with SPHERE (DARTTS-S).

I. SPHERE/IRDIS Polarimetric Imaging of Eight Prominent T Tauri Disks. *ApJ*, **863**, 44. 8, 17, 182

Balbus, S.A. & Hawley, J.F. (1991). A powerful local shear instability in weakly magnetized disks. I - Linear analysis. II - Nonlinear evolution. *ApJ*, **376**, 214–233. 7

Barber, C.B., Dobkin, D.P., Dobkin, D.P. & Huhdanpaa, H. (1996). The quickhull algorithm for convex hulls. *ACM Trans. Math. Softw.*, **22**, 469–483. 49

Beck, T.L., Bary, J.S. & McGregor, P.J. (2010). Spatially Extended Brackett Gamma Emission in the Environments of Young Stars. *ApJ*, **722**, 1360–1372. 70

Beckwith, S.V.W., Sargent, A.I., Chini, R.S. & Guesten, R. (1990). A survey for circumstellar disks around young stellar objects. *AJ*, **99**, 924–945. 11, 12, 20

Benisty, M., Stolker, T., Pohl, A., de Boer, J., Lesur, G., Dominik, C., Dullemond, C.P., Langlois, M., Min, M., Wagner, K., Henning, T., Juhasz, A., Pinilla, P., Facchini, S., Apai, D., van Boekel, R., Garufi, A., Ginski, C., Ménard, F., Pinte, C., Quanz, S.P., Zurlo, A., Boccaletti, A., Bonnefoy, M., Beuzit, J.L., Chauvin, G., Cudel, M., Desidera, S., Feldt, M., Fontanive, C., Gratton, R., Kasper, M., Lagrange, A.M., LeCoroller, H., Mouillet, D., Mesa, D., Sissa, E., Vigan, A., Antichi, J., Buey, T., Fusco, T., Gisler, D., Llored, M., Magnard, Y., Moeller-Nilsson, O., Pragt, J., Roelfsema, R., Sauvage, J.F. & Wildi, F. (2017). Shadows and spirals in the protoplanetary disk HD 100453. *A&A*, **597**, A42. 124

Bergin, E.A. & Cleeves, L.I. (2018). Chemistry During the Gas-Rich Stage of Planet Formation. 137. 27

Bergin, E.A. & Tafalla, M. (2007). Cold dark clouds: The initial conditions for star formation. *ARA&A*, **45**, 339–396. 2

Bergin, E.A. & Williams, J.P. (2017). The Determination of Protoplanetary Disk Masses. **445**, 1. 19, 78

Bergin, E.A., Cleeves, L.I., Gorti, U., Zhang, K., Blake, G.A., Green, J.D., Andrews, S.M., Evans, N.J., II, Henning, T., Öberg, K., Pontoppidan, K., Qi, C., Salyk, C. & van Dishoeck, E.F. (2013). An old disk still capable of forming a planetary system. *Nature*, **493**, 644–646. 22, 66

Bergin, E.A., Du, F., Cleeves, L.I., Blake, G.A., Schwarz, K., Visser, R. & Zhang, K. (2016). Hydrocarbon Emission Rings in Protoplanetary Disks Induced by Dust Evolution. *ApJ*, **831**, 101. 28

Birnstiel, T., Dullemond, C.P. & Brauer, F. (2010). Gas- and dust evolution in protoplanetary disks. *A&A*, **513**, A79. 25

Bjerkeli, P., van der Wiel, M.H.D., Harsono, D., Ramsey, J.P. & Jørgensen, J.K. (2016). Resolved images of a protostellar outflow driven by an extended disk wind. *Nature*, **540**, 406–409. 148

Bockelée-Morvan, D., Lis, D.C., Wink, J.E., Despois, D., Crovisier, J., Bachiller, R., Benford, D.J., Biver, N., Colom, P., Davies, J.K., Gérard, E., Germain, B., Houde, M., Mehringer, D., Moreno, R., Paubert, G., Phillips, T.G. & Rauer, H. (2000). New molecules found in comet C/1995 O1 (Hale-Bopp). Investigating the link between cometary and interstellar material. *A&A*, **353**, 1101–1114. 14, 145

Boley, A.C. (2009). The Two Modes of Gas Giant Planet Formation. *ApJ*, **695**, L53–L57. 9

Boneberg, D.M., Panić, O., Haworth, T.J., Clarke, C.J. & Min, M. (2016). Determining the mid-plane conditions of circumstellar discs using gas and dust modelling: a study of HD 163296. *MNRAS*, **461**, 385–401. 65

Booth, R.A. & Ilee, J.D. (2019). Planet-forming material in a protoplanetary disc: the interplay between chemical evolution and pebble drift. *MNRAS*, **487**, 3998–4011. 45

Borucki, W.J. (2017). Kepler: A Brief Discussion of the Mission and Exoplanet Results. *Proceedings of the American Philosophical Society*, **161**, 38–65. 1

Bosman, A.D., Walsh, C. & van Dishoeck, E.F. (2018). CO destruction in protoplanetary disk midplanes: Inside versus outside the CO snow surface. *A&A*, **618**, A182. 23, 67, 78, 173, 175

Boss, A.P. (1997). Giant planet formation by gravitational instability. *Science*, **276**, 1836–1839. 72

Boss, A.P. (1998). Evolution of the Solar Nebula. IV. Giant Gaseous Protoplanet Formation. *ApJ*, **503**, 923–937. 9

Boss, A.P. (2011). Formation of Giant Planets by Disk Instability on Wide Orbits Around Protostars with Varied Masses. *ApJ*, **731**, 74. 10, 69, 82, 175

Briceño, C., Luhman, K.L., Hartmann, L., Stauffer, J.R. & Kirkpatrick, J.D. (2002). The Initial Mass Function in the Taurus Star-forming Region. *ApJ*, **580**, 317–335. 71

Briggs, E.L. (1995). *Development and Application of Methods for Performing Large Scale Electronic Structure Calculations*. Ph.D. thesis, NORTH CAROLINA STATE UNIVERSITY. 40

Brinch, C. & Hogerheijde, M.R. (2010). LIME - a flexible, non-LTE line excitation and radiation transfer method for millimeter and far-infrared wavelengths. *A&A*, **523**, A25. 49, 50, 60, 97, 137

Brittain, S.D., Carr, J.S., Najita, J.R., Quanz, S.P. & Meyer, M.R. (2014). NIR Spectroscopy of the HAeBe Star HD 100546. III. Further Evidence of an Orbiting Companion? *ApJ*, **791**, 136. 124

Brogan, C.L., Hunter, T.R. & Fomalont, E.B. (2018). Advanced Gain Calibration Techniques in Radio Interferometry. *arXiv e-prints*, arXiv:1805.05266. 39

Bruderer, S., van Dishoeck, E.F., Doty, S.D. & Herczeg, G.J. (2012). The warm gas atmosphere of the HD 100546 disk seen by Herschel. Evidence of a gas-rich, carbon-poor atmosphere? *A&A*, **541**, A91. 124, 156, 157

Brunner, M., Danilovich, T., Ramstedt, S., Marti-Vidal, I., De Beck, E., Vlemmings, W.H.T., Lindqvist, M. & Kerschbaum, F. (2018). Molecular line study of the S-type AGB star W Aquilae. ALMA observations of CS, SiS, SiO and HCN. *A&A*, **617**, A23. 165

Calmonte, U., Altwegg, K., Balsiger, H., Berthelier, J.J., Bieler, A., Cessateur, G., Dhooghe, F., van Dishoeck, E.F., Fiethe, B., Fuselier, S.A., Gasc, S., Gombosi, T.I., Hässig, M., Le Roy, L., Rubin, M., Sémon, T., Tzou, C.Y. & Wampfler, S.F. (2016). Sulphur-bearing species in the coma of comet 67P/Churyumov-Gerasimenko. *MNRAS*, **462**, S253–S273. 146

Calvet, N., Muzerolle, J., Briceño, C., Hernández, J., Hartmann, L., Saucedo, J.L. & Gordon, K.D. (2004). The Mass Accretion Rates of Intermediate-Mass T Tauri Stars. *AJ*, **128**, 1294–1318. 5

Cardelli, J.A., Meyer, D.M., Jura, M. & Savage, B.D. (1996). The Abundance of Interstellar Carbon. *ApJ*, **467**, 334. 80

Carmona, A., van der Plas, G., van den Ancker, M.E., Audard, M., Waters, L.B.F.M., Fedele, D., Acke, B. & Pantin, E. (2011). A survey for near-infrared $H_2$ emission in Herbig Ae/Be stars: emission from the outer disks of HD 97048 and HD 100546. *A&A*, **533**, A39. 21, 87, 124

Carney, M.T., Fedele, D., Hogerheijde, M.R., Favre, C., Walsh, C., Bruderer, S., Miotello, A., Murillo, N.M., Klaassen, P.D., Henning, T. & van Dishoeck, E.F. (2018). Probing midplane CO abundance and gas temperature with $DCO^+$ in the protoplanetary disk around HD 169142. *A&A*, **614**, A106. 56, 115

Carney, M.T., Hogerheijde, M.R., Guzmán, V.V., Walsh, C., Öberg, K.I., Fayolle, E.C., Cleeves, L.I., Carpenter, J.M. & Qi, C. (2019). Upper limits on $CH_3OH$ in the HD 163296 protoplanetary disk. Evidence for a low gas-phase $CH_3OH$-to-$H_2CO$ ratio. *A&A*, **623**, A124. 153

Carrasco-González, C., Rodríguez, L.F., Anglada, G. & Curiel, S. (2009). High Angular Resolution Radio Observations of the HL/XZ Tau Region: Mapping the 50 AU Protoplanetary Disk Around HL Tau and Resolving XZ Tau S Into a 13 AU Binary. *ApJ*, **693**, L86–L90. 71

Carrasco-González, C., Henning, T., Chandler, C.J., Linz, H., Pérez, L., Rodríguez, L.F., Galván-Madrid, R., Anglada, G., Birnstiel, T., van Boekel, R., Flock, M., Klahr, H., Macias, E.,

Menten, K., Osorio, M., Testi, L., Torrelles, J.M. & Zhu, Z. (2016). The VLA View of the HL Tau Disk: Disk Mass, Grain Evolution, and Early Planet Formation. *ApJ*, **821**, L16. 18, 20

Carrasco-González, C., Sierra, A., Flock, M., Zhu, Z., Henning, T., Chandler, C., Galván-Madrid, R., Macías, E., Anglada, G., Linz, H., Osorio, M., Rodríguez, L.F., Testi, L., Torrelles, J.M., Pérez, L. & Liu, Y. (2019). The Radial Distribution of Dust Particles in the HL Tau Disk from ALMA and VLA Observations. *ApJ*, **883**, 71. 75, 76, 78, 81

Casassus, S., van der Plas, G., M, S.P., Dent, W.R.F., Fomalont, E., Hagelberg, J., Hales, A., Jordán, A., Mawet, D., Ménard, F., Wootten, A., Wilner, D., Hughes, A.M., Schreiber, M.R., Girard, J.H., Ercolano, B., Canovas, H., Román, P.E. & Salinas, V. (2013). Flows of gas through a protoplanetary gap. *Nature*, **493**, 191–194. 31, 116

Casassus, S., Marino, S., Pérez, S., Roman, P., Dunhill, A., Armitage, P.J., Cuadra, J., Wootten, A., van der Plas, G., Cieza, L., Moral, V., Christiaens, V. & Montesinos, M. (2015a). Accretion Kinematics through the Warped Transition Disk in HD142527 from Resolved CO(6-5) Observations. *ApJ*, **811**, 92. 116, 147

Casassus, S., Wright, C.M., Marino, S., Maddison, S.T., Wootten, A., Roman, P., Pérez, S., Pinilla, P., Wyatt, M., Moral, V., Ménard, F., Christiaens, V., Cieza, L. & van der Plas, G. (2015b). A Compact Concentration of Large Grains in the HD 142527 Protoplanetary Dust Trap. *ApJ*, **812**, 126. 117

Cazzoletti, P., van Dishoeck, E.F., Pinilla, P., Tazzari, M., Facchini, S., van der Marel, N., Benisty, M., Garufi, A. & Pérez,

L.M. (2018a). Evidence for a massive dust-trapping vortex connected to spirals. Multi-wavelength analysis of the HD 135344B protoplanetary disk. *A&A*, **619**, A161. 25

Cazzoletti, P., van Dishoeck, E.F., Visser, R., Facchini, S. & Bruderer, S. (2018b). CN rings in full protoplanetary disks around young stars as probes of disk structure. *A&A*, **609**, A93. 27, 28

Chapillon, E., Guilloteau, S., Dutrey, A., Piétu, V. & Guélin, M. (2012). Chemistry in disks. VI. CN and HCN in protoplanetary disks. *A&A*, **537**, A60. 85

Clarke, C.J. & Lodato, G. (2009). Limits on the location of planetesimal formation in self-gravitating protostellar discs. *MNRAS*, **398**, L6–L10. 81

Cleeves, L.I., Adams, F.C. & Bergin, E.A. (2013). Exclusion of Cosmic Rays in Protoplanetary Disks: Stellar and Magnetic Effects. *ApJ*, **772**, 5. 43

Cleeves, L.I., Bergin, E.A. & Harries, T.J. (2015). Indirect Detection of Forming Protoplanets via Chemical Asymmetries in Disks. *ApJ*, **807**, 2. 32

Cuello, N., Dipierro, G., Mentiplay, D., Price, D.J., Pinte, C., Cuadra, J., Laibe, G., Ménard, F., Poblete, P.P. & Montesinos, M. (2019). Flybys in protoplanetary discs: I. Gas and dust dynamics. *MNRAS*, **483**, 4114–4139. 31

Currie, T., Muto, T., Kudo, T., Honda, M., Brandt, T.D., Grady, C., Fukagawa, M., Burrows, A., Janson, M., Kuzuhara, M., McElwain, M.W., Follette, K., Hashimoto, J., Henning, T., Kandori, R., Kusakabe, N., Kwon, J., Mede, K., Morino, J.i., Nishikawa, J., Pyo, T.S., Serabyn, G., Suenaga, T., Takahashi, Y., Wisniewski, J.

& Tamura, M. (2014). Recovery of the Candidate Protoplanet HD 100546 b with Gemini/NICI and Detection of Additional (Planet-induced?) Disk Structure at Small Separations. *ApJ*, **796**, L30. 124

Currie, T., Cloutier, R., Brittain, S., Grady, C., Burrows, A., Muto, T., Kenyon, S.J. & Kuchner, M.J. (2015). Resolving the HD 100546 Protoplanetary System with the Gemini Planet Imager: Evidence for Multiple Forming, Accreting Planets. *ApJ*, **814**, L27. 124, 149

Dartois, E., Dutrey, A. & Guilloteau, S. (2003). Structure of the DM Tau Outer Disk: Probing the vertical kinetic temperature gradient. *A&A*, **399**, 773–787. 12

de Gregorio-Monsalvo, I., Ménard, F., Dent, W., Pinte, C., López, C., Klaassen, P., Hales, A., Cortés, P., Rawlings, M.G., Tachihara, K., Testi, L., Takahashi, S., Chapillon, E., Mathews, G., Juhasz, A., Akiyama, E., Higuchi, A.E., Saito, M., Nyman, L.Å., Phillips, N., Rodón, J., Corder, S. & Van Kempen, T. (2013). Unveiling the gas-and-dust disk structure in HD 163296 using ALMA observations. *A&A*, **557**, A133. 15, 23

de Juan Ovelar, M., Min, M., Dominik, C., Thalmann, C., Pinilla, P., Benisty, M. & Birnstiel, T. (2013). Imaging diagnostics for transitional discs. *A&A*, **560**, A111. 30, 119

de Juan Ovelar, M., Pinilla, P., Min, M., Dominik, C. & Birnstiel, T. (2016). Constraining turbulence mixing strength in transitional discs with planets using SPHERE and ALMA. *MNRAS*, **459**, L85–L89. 119

Dionatos, O. (2015). Gas line observations of disks. In *European Physical Journal Web of Conferences*, vol. 102, 00008. 45

Dipierro, G., Pinilla, P., Lodato, G. & Testi, L. (2015a). Dust trapping by spiral arms in gravitationally unstable protostellar discs. *MNRAS*, **451**, 974–986. 81

Dipierro, G., Price, D., Laibe, G., Hirsh, K., Cerioli, A. & Lodato, G. (2015b). On planet formation in HL Tau. *MNRAS*, **453**, L73–L77. 71, 81, 175

Dong, R. & Fung, J. (2017). What is the Mass of a Gap-opening Planet? *ApJ*, **835**, 146. 30

Dong, R., Zhu, Z. & Whitney, B. (2015). Observational Signatures of Planets in Protoplanetary Disks I. Gaps Opened by Single and Multiple Young Planets in Disks. *ApJ*, **809**, 93. 30

Dong, R., Li, S., Chiang, E. & Li, H. (2018). Multiple Disk Gaps and Rings Generated by a Single Super-Earth. II. Spacings, Depths, and Number of Gaps, with Application to Real Systems. *ApJ*, **866**, 110. 30, 81, 175

Dong, R., Liu, S.Y. & Fung, J. (2019). Observational Signatures of Planets in Protoplanetary Disks: Planet-induced Line Broadening in Gaps. *ApJ*, **870**, 72. 31

Douglas, T.A., Caselli, P., Ilee, J.D., Boley, A.C., Hartquist, T.W., Durisen, R.H. & Rawlings, J.M.C. (2013). Simulated observations of young gravitationally unstable protoplanetary discs. *MNRAS*, **433**, 2064–2074. 82

Draine, B.T. (2003). Interstellar Dust Grains. *ARA&A*, **41**, 241–289. 15

Draine, B.T. (2006). On the Submillimeter Opacity of Protoplanetary Disks. *ApJ*, **636**, 1114–1120. 20

Drozdovskaya, M.N., Walsh, C., Visser, R., Harsono, D. & van Dishoeck, E.F. (2015). The complex chemistry of outflow cavity walls exposed: the case of low-mass protostars. *MNRAS*, **451**, 3836–3856. 44, 156

Durisen, R.H., Boss, A.P., Mayer, L., Nelson, A.F., Quinn, T. & Rice, W.K.M. (2007). Gravitational Instabilities in Gaseous Protoplanetary Disks and Implications for Giant Planet Formation. *Protostars and Planets V*, 607–622. 6, 69

Dutrey, A., Guilloteau, S., Duvert, G., Prato, L., Simon, M., Schuster, K. & Menard, F. (1996). Dust and gas distribution around T Tauri stars in Taurus-Auriga. I. Interferometric 2.7mm continuum and ˆ13ˆCO J=1-0 observations. *A&A*, **309**, 493–504. 19

Dutrey, A., Guilloteau, S. & Guelin, M. (1997). Chemistry of protosolar-like nebulae: The molecular content of the DM Tau and GG Tau disks. *A&A*, **317**, L55–L58. 14, 85

Dutrey, A., Guilloteau, S., Prato, L., Simon, M., Duvert, G., Schuster, K. & Menard, F. (1998). CO study of the GM Aurigae Keplerian disk. *A&A*, **338**, L63–L66. 11

Dutrey, A., Wakelam, V., Boehler, Y., Guilloteau, S., Hersant, F., Semenov, D., Chapillon, E., Henning, T., Piétu, V., Launhardt, R., Gueth, F. & Schreyer, K. (2011). Chemistry in disks. V. Sulfur-bearing molecules in the protoplanetary disks surrounding LkCa15, MWC480, DM Tauri, and GO Tauri. *A&A*, **535**, A104. 138

Dutrey, A., Guilloteau, S., Piétu, V., Chapillon, E., Wakelam, V., Di Folco, E., Stoecklin, T., Denis-Alpizar, O., Gorti, U., Teague, R., Henning, T., Semenov, D. & Grosso, N. (2017). The Flying Saucer:

Tomography of the thermal and density gas structure of an edge-on protoplanetary disk. *A&A*, **607**, A130. 23

Eistrup, C., Walsh, C. & van Dishoeck, E.F. (2016). Setting the volatile composition of (exo)planet-building material. Does chemical evolution in disk midplanes matter? *A&A*, **595**, A83. 42

Eistrup, C., Walsh, C. & van Dishoeck, E.F. (2018). Molecular abundances and C/O ratios in chemically evolving planet-forming disk midplanes. *A&A*, **613**, A14. 45

Ercolano, B. & Owen, J.E. (2016). Blueshifted [O I] lines from protoplanetary discs: the smoking gun of X-ray photoevaporation. *MNRAS*, **460**, 3472–3478. 148

Ercolano, B. & Pascucci, I. (2017). The dispersal of planet-forming discs: theory confronts observations. *Royal Society Open Science*, **4**, 170114. 10, 148

Evans, M.G., Ilee, J.D., Boley, A.C., Caselli, P., Durisen, R.H., Hartquist, T.W. & Rawlings, J.M.C. (2015). Gravitational instabilities in a protosolar-like disc - I. Dynamics and chemistry. *MNRAS*, **453**, 1147–1163. 70

Evans, N.J., II (1999). Physical Conditions in Regions of Star Formation. *ARA&A*, **37**, 311–362. 2

Facchini, S., Birnstiel, T., Bruderer, S. & van Dishoeck, E.F. (2017). Different dust and gas radial extents in protoplanetary disks: consistent models of grain growth and CO emission. *A&A*, **605**, A16. 120

Favre, C., Fedele, D., Maud, L., Booth, R., Tazzari, M., Miotello, A., Testi, L., Semenov, D. & Bruderer, S. (2019). Gas Density Pertur-

bations Induced by One or More Forming Planets in the AS 209 Protoplanetary Disk as Seen with ALMA. *ApJ*, **871**, 107. 26

Fedele, D., Bruderer, S., van Dishoeck, E.F., Carr, J., Herczeg, G.J., Salyk, C., Evans, N.J., Bouwman, J., Meeus, G., Henning, T., Green, J., Najita, J.R. & Güdel, M. (2013). DIGIT survey of far-infrared lines from protoplanetary disks. I. [O i], [C ii], OH, $H_2O$, and $CH^+$. *A&A*, **559**, A77. 19, 87, 124

Fedele, D., van Dishoeck, E.F., Kama, M., Bruderer, S. & Hogerheijde, M.R. (2016). Probing the 2D temperature structure of protoplanetary disks with Herschel observations of high-J CO lines. *A&A*, **591**, A95. 19

Fedele, D., Carney, M., Hogerheijde, M.R., Walsh, C., Miotello, A., Klaassen, P., Bruderer, S., Henning, T. & van Dishoeck, E.F. (2017). ALMA unveils rings and gaps in the protoplanetary system HD 169142: signatures of two giant protoplanets. *A&A*, **600**, A72. 15, 26, 115

Fedele, D., Tazzari, M., Booth, R., Testi, L., Clarke, C.J., Pascucci, I., Kospal, A., Semenov, D., Bruderer, S., Henning, T. & Teague, R. (2018). ALMA continuum observations of the protoplanetary disk AS 209. Evidence of multiple gaps opened by a single planet. *A&A*, **610**, A24. 118

Flaherty, K.M., Hughes, A.M., Rosenfeld, K.A., Andrews, S.M., Chiang, E., Simon, J.B., Kerzner, S. & Wilner, D.J. (2015). Weak Turbulence in the HD 163296 Protoplanetary Disk Revealed by ALMA CO Observations. *ApJ*, **813**, 99. 18

Flaherty, K.M., Hughes, A.M., Rose, S.C., Simon, J.B., Qi, C., Andrews, S.M., Kóspál, Á., Wilner, D.J., Chiang, E., Armitage, P.J. & Bai, X.n. (2017). A Three-dimensional View of Turbulence: Constraints on

Turbulent Motions in the HD 163296 Protoplanetary Disk Using $DCO^+$. *ApJ*, **843**, 150. 18

Flock, M., Ruge, J.P., Dzyurkevich, N., Henning, T., Klahr, H. & Wolf, S. (2015). Gaps, rings, and non-axisymmetric structures in protoplanetary disks. From simulations to ALMA observations. *A&A*, **574**, A68. 31

Flower, D.R. (1999). Rotational excitation of HCO+ by H2. *MNRAS*, **305**, 651–653. 97

Forgan, D., Price, D.J. & Bonnell, I. (2017). On the fragmentation boundary in magnetized self-gravitating discs. *MNRAS*, **466**, 3406–3416. 81

Fuente, A., Cernicharo, J., Agúndez, M., Berné, O., Goicoechea, J.R., Alonso-Albi, T. & Marcelino, N. (2010). Molecular content of the circumstellar disk in AB Aurigae. First detection of SO in a circumstellar disk. *A&A*, **524**, A19. 123

Gaia Collaboration, Brown, A.G.A., Vallenari, A., Prusti, T., de Bruijne, J.H.J., Babusiaux, C., Bailer-Jones, C.A.L., Biermann, M., Evans, D.W., Eyer, L. & et al. (2018). Gaia Data Release 2. Summary of the contents and survey properties. *A&A*, **616**, A1. 56

Garufi, A., Quanz, S.P., Schmid, H.M., Mulders, G.D., Avenhaus, H., Boccaletti, A., Ginski, C., Langlois, M., Stolker, T., Augereau, J.C., Benisty, M., Lopez, B., Dominik, C., Gratton, R., Henning, T., Janson, M., Ménard, F., Meyer, M.R., Pinte, C., Sissa, E., Vigan, A., Zurlo, A., Bazzon, A., Buenzli, E., Bonnefoy, M., Brandner, W., Chauvin, G., Cheetham, A., Cudel, M., Desidera, S., Feldt, M., Galicher, R., Kasper, M., Lagrange, A.M., Lannier, J., Maire, A.L., Mesa, D., Mouillet, D., Peretti, S., Perrot, C.,

Salter, G. & Wildi, F. (2016). The SPHERE view of the planet-forming disk around HD 100546. *A&A*, **588**, A8. 124

Ginski, C., Stolker, T., Pinilla, P., Dominik, C., Boccaletti, A., de Boer, J., Benisty, M., Biller, B., Feldt, M., Garufi, A., Keller, C.U., Kenworthy, M., Maire, A.L., Ménard, F., Mesa, D., Milli, J., Min, M., Pinte, C., Quanz, S.P., van Boekel, R., Bonnefoy, M., Chauvin, G., Desidera, S., Gratton, R., Girard, J.H.V., Keppler, M., Kopytova, T., Lagrange, A.M., Langlois, M., Rouan, D. & Vigan, A. (2016). Direct detection of scattered light gaps in the transitional disk around HD 97048 with VLT/SPHERE. *A&A*, **595**, A112. 86, 119, 176

Goodman, A.A., Benson, P.J., Fuller, G.A. & Myers, P.C. (1993). Dense cores in dark clouds. VIII - Velocity gradients. *ApJ*, **406**, 528–547. 2

Goto, M., van der Plas, G., van den Ancker, M., Dullemond, C.P., Carmona, A., Henning, T., Meeus, G., Linz, H. & Stecklum, B. (2012). Warm gas at 50 AU in the disk around Herbig Be star HD 100546. *A&A*, **539**, A81. 124

Greaves, J.S. & Rice, W.K.M. (2011). Do all Sun-like stars have planets? Inferences from the disc mass reservoirs of Class 0 protostars. *MNRAS*, **412**, L88–L92. 22

Greaves, J.S., Richards, A.M.S., Rice, W.K.M. & Muxlow, T.W.B. (2008). Enhanced dust emission in the HL Tau disc: a low-mass companion in formation? *MNRAS*, **391**, L74–L78. 71

Greene, T.P. & Lada, C.J. (1996). Near-Infrared Spectra and the Evolutionary Status of Young Stellar Objects: Results of a 1.1-2.4 Survey. *AJ*, **112**, 2184. 3

Güdel, M., Eibensteiner, C., Dionatos, O., Audard, M., Forbrich, J., Kraus, S., Rab, C., Schneider, C., Skinner, S. & Vorobyov, E. (2018). ALMA detects a radial disk wind in DG Tauri. *A&A*, **620**, L1. 29

Guilloteau, S., Dutrey, A. & Simon, M. (1999). GG Tauri: the ring world. *A&A*, **348**, 570–578. 19

Guilloteau, S., Dutrey, A., Piétu, V. & Boehler, Y. (2011). A dual-frequency sub-arcsecond study of proto-planetary disks at mm wavelengths: first evidence for radial variations of the dust properties. *A&A*, **529**, A105. 18, 72

Guilloteau, S., Di Folco, E., Dutrey, A., Simon, M., Grosso, N. & Piétu, V. (2013). A sensitive survey for 13CO, CN, H2CO, and SO in the disks of T Tauri and Herbig Ae stars. *A&A*, **549**, A92. 123

Guilloteau, S., Reboussin, L., Dutrey, A., Chapillon, E., Wakelam, V., Piétu, V., Di Folco, E., Semenov, D. & Henning, T. (2016). Chemistry in disks. X. The molecular content of protoplanetary disks in Taurus. *A&A*, **592**, A124. 145, 164

Guzmán, V.V., Öberg, K.I., Loomis, R. & Qi, C. (2015). Cyanide Photochemistry and Nitrogen Fractionation in the MWC 480 Disk. *ApJ*, **814**, 53. 115, 117

Guzmán, V.V., Öberg, K.I., Huang, J., Loomis, R. & Qi, C. (2017). Nitrogen Fractionation in Protoplanetary Disks from the $H^{13}CN/HC^{15}N$ Ratio. *ApJ*, **836**, 30. 85, 115, 118

Hall, C., Rice, K., Dipierro, G., Forgan, D., Harries, T. & Alexander, R. (2018). Is the spiral morphology of the Elias 2-27 circumstellar disc due to gravitational instability? *MNRAS*, **477**, 1004–1014. 31

Hartmann, L. & Kenyon, S.J. (1996). The FU Orionis Phenomenon. *ARA&A*, **34**, 207–240. 5

Hartmann, L., Calvet, N., Gullbring, E. & D'Alessio, P. (1998). Accretion and the Evolution of T Tauri Disks. *ApJ*, **495**, 385–400. 11

Hartmann, L., Herczeg, G. & Calvet, N. (2016). Accretion onto Pre-Main-Sequence Stars. *ARA&A*, **54**, 135–180. 4, 70

Hasegawa, T.I., Herbst, E. & Leung, C.M. (1992). Models of Gas-Grain Chemistry in Dense Interstellar Clouds with Complex Organic Molecules. *ApJS*, **82**, 167. 44

Hasegawa, Y., Okuzumi, S., Flock, M. & Turner, N.J. (2017). Magnetically Induced Disk Winds and Transport in the HL Tau Disk. *ApJ*, **845**, 31. 81

Haworth, T.J., Facchini, S., Clarke, C.J. & Cleeves, L.I. (2017). First evidence of external disc photoevaporation in a low mass star forming region: the case of IM Lup. *MNRAS*, **468**, L108–L112. 29

Hein Bertelsen, R.P., Kamp, I., Goto, M., van der Plas, G., Thi, W.F., Waters, L.B.F.M., van den Ancker, M.E. & Woitke, P. (2014). CO ro-vibrational lines in HD 100546. A search for disc asymmetries and the role of fluorescence. *A&A*, **561**, A102. 124

Henning, T. & Semenov, D. (2013). Chemistry in Protoplanetary Disks. *Chemical Reviews*, **113**, 9016–9042. 15, 18, 19

Herbig, G.H. (1977). Eruptive phenomena in early stellar evolution. *ApJ*, **217**, 693–715. 5

Herbig, G.H. (2008). History and Spectroscopy of EXor Candidates. , **135**, 637–648. 5

Herbst, E., Millar, T.J., Wlodek, S. & Bohme, D.K. (1989). The chemistry of silicon in dense interstellar clouds. *A&A*, **222**, 205–210. 159

Hily-Blant, P., Magalhaes de Souza, V., Kastner, J. & Forveille, T. (2019). Multiple nitrogen reservoirs in a protoplanetary disk at the epoch of comet and giant planet formation. *A&A*, **632**, L12. 118

Högbom, J.A. (1974). Aperture Synthesis with a Non-Regular Distribution of Interferometer Baselines. *A&AS*, **15**, 417. 40

Hollas, J.M. (2004). *Modern spectroscopy*. John Wiley & Sons, 2013, iSBN 1118681606, 9781118681602. 45

Honda, M., Kudo, T., Takatsuki, S., Inoue, A.K., Nakamoto, T., Fukagawa, M., Tamura, M., Terada, H. & Takato, N. (2016). Water Ice at the Surface of the HD 100546 Disk. *ApJ*, **821**, 2. 145

Huang, J., Öberg, K.I., Qi, C., Aikawa, Y., Andrews, S.M., Furuya, K., Guzmán, V.V., Loomis, R.A., van Dishoeck, E.F. & Wilner, D.J. (2017). An ALMA Survey of DCN/$H^{13}CN$ and $DCO^+/H^{13}CO^+$ in Protoplanetary Disks. *ApJ*, **835**, 231. 85, 111, 115, 116, 117

Huang, J., Andrews, S.M., Dullemond, C.P., Isella, A., Pérez, L.M., Guzmán, V.V., Öberg, K.I., Zhu, Z., Zhang, S., Bai, X.N., Benisty, M., Birnstiel, T., Carpenter, J.M., Hughes, A.M., Ricci, L., Weaver, E. & Wilner, D.J. (2018a). The Disk Substructures at High Angular Resolution Project (DSHARP). II. Characteristics of Annular Substructures. *ApJ*, **869**, L42. 21, 30

Huang, J., Andrews, S.M., Pérez, L.M., Zhu, Z., Dullemond, C.P., Isella, A., Benisty, M., Bai, X.N., Birnstiel, T., Carpenter, J.M., Guzmán, V.V., Hughes, A.M., Öberg, K.I., Ricci, L., Wilner, D.J. & Zhang, S. (2018b). The Disk Substructures at High Angular Resolution Project (DSHARP). III. Spiral Structures in the Millimeter Continuum of the Elias 27, IM Lup, and WaOph 6 Disks. *ApJ*, **869**, L43. 25

Hughes, A.M., Wilner, D.J., Andrews, S.M., Qi, C. & Hogerheijde, M.R. (2011). Empirical Constraints on Turbulence in Protoplanetary Accretion Disks. *ApJ*, **727**, 85. 11

Hughes, A.M., Duchêne, G. & Matthews, B.C. (2018). Debris Disks: Structure, Composition, and Variability. *ARA&A*, **56**, 541–591. 10

Ilee, J.D., Boley, A.C., Caselli, P., Durisen, R.H., Hartquist, T.W. & Rawlings, J.M.C. (2011). Chemistry in a gravitationally unstable protoplanetary disc. *MNRAS*, **417**, 2950–2961. 6, 82

Isella, A., Testi, L., Natta, A., Neri, R., Wilner, D. & Qi, C. (2007). Millimeter imaging of HD 163296: probing the disk structure and kinematics. *A&A*, **469**, 213–222. 65

Isella, A., Guidi, G., Testi, L., Liu, S., Li, H., Li, S., Weaver, E., Boehler, Y., Carperter, J.M., De Gregorio-Monsalvo, I., Manara, C.F., Natta, A., Pérez, L.M., Ricci, L., Sargent, A., Tazzari, M. & Turner, N. (2016). Ringed Structures of the HD 163296 Protoplanetary Disk Revealed by ALMA. *Physical Review Letters*, **117**, 251101. 21, 26, 30, 53, 54, 56, 58, 61, 65, 68, 70, 115, 174

Isella, A., Huang, J., Andrews, S.M., Dullemond, C.P., Birnstiel, T., Zhang, S., Zhu, Z., Guzmán, V.V., Pérez, L.M., Bai, X.N.,

Benisty, M., Carpenter, J.M., Ricci, L. & Wilner, D.J. (2018). The Disk Substructures at High Angular Resolution Project (DSHARP). IX. A High-definition Study of the HD 163296 Planet-forming Disk. *ApJ*, **869**, L49. 54, 59

Izidoro, A. & Raymond, S.N. (2018). *Formation of Terrestrial Planets, Handbook of Exoplanets*, 142. 9

Jeans, J.H. (1902). The Stability of a Spherical Nebula. *Philosophical Transactions of the Royal Society of London Series A*, **199**, 1–53. 2

Jermyn, A.S. & Kama, M. (2018). Stellar photospheric abundances as a probe of discs and planets. *MNRAS*, **476**, 4418–4434. 152

Jiménez-Escobar, A. & Muñoz Caro, G.M. (2011). Sulfur depletion in dense clouds and circumstellar regions. I. $H_2S$ ice abundance and UV-photochemical reactions in the $H_2O$-matrix. *A&A*, **536**, A91. 14

Jin, S., Li, S., Isella, A., Li, H. & Ji, J. (2016). Modeling Dust Emission of HL Tau Disk Based on Planet-Disk Interactions. *ApJ*, **818**, 76. 81, 175

Johnson, J.A., Aller, K.M., Howard, A.W. & Crepp, J.R. (2010). Giant Planet Occurrence in the Stellar Mass-Metallicity Plane. *PASP*, **122**, 905. 180

Johnston, K.G., Robitaille, T.P., Beuther, H., Linz, H., Boley, P., Kuiper, R., Keto, E., Hoare, M.G. & van Boekel, R. (2015). A Keplerian-like Disk around the Forming O-type Star AFGL 4176. *ApJ*, **813**, L19. 5

Kalas, P., Graham, J.R., Chiang, E., Fitzgerald, M.P., Clampin, M., Kite, E.S., Stapelfeldt, K., Marois, C. & Krist, J. (2008). Optical

Images of an Exosolar Planet 25 Light-Years from Earth. *Science*, **322**, 1345. 10

Kama, M., Folsom, C.P. & Pinilla, P. (2015). Fingerprints of giant planets in the photospheres of Herbig stars. *A&A*, **582**, L10. 151, 152

Kama, M., Bruderer, S., Carney, M., Hogerheijde, M., van Dishoeck, E.F., Fedele, D., Baryshev, A., Boland , W., Güsten, R., Aikutalp, A., Choi, Y., Endo, A., Frieswijk, W., Karska, A., Klaassen, P., Koumpia, E., Kristensen, L., Leurini, S., Nagy, Z., Perez Beaupuits, J.P., Risacher, C., van der Marel, N., van Kempen, T.A., van Weeren, R.J., Wyrowski, F. & Yildiz, U.A. (2016a). Observations and modelling of CO and [C I] in protoplanetary disks. First detections of [C I] and constraints on the carbon abundance. *A&A*, **588**, A108. 23, 78, 96, 137, 138, 156, 157

Kama, M., Bruderer, S., van Dishoeck, E.F., Hogerheijde, M., Folsom, C.P., Miotello, A., Fedele, D., Belloche, A., Güsten, R. & Wyrowski, F. (2016b). Volatile-carbon locking and release in protoplanetary disks. A study of TW Hya and HD 100546. *A&A*, **592**, A83. 67, 137

Kama, M., Shorttle, O., Jermyn, A.S., Folsom, C.P., Furuya, K., Bergin, E.A., Walsh, C. & Keller, L. (2019). Abundant refractory sulfur in protoplanetary disks. *ApJ*, **885**, 114. 169, 170

Kama, M., Trapman, L., Fedele, D., Bruderer, S., Hogerheijde, M.R., Miotello, A., van Dishoeck, E.F., Clarke, C. & Bergin, E.A. (2020). Mass constraints for 15 protoplanetary discs from HD 1-0. *A&A*, **634**, A88. 66

Kamp, I. (2015). Line radiative transfer and statistical equilibrium. In *European Physical Journal Web of Conferences*, vol. 102, 00010. 45

Kamp, I., Thi, W.F., Woitke, P., Rab, C., Bouma, S. & Ménard, F. (2017). Consistent dust and gas models for protoplanetary disks. II. Chemical networks and rates. *A&A*, **607**, A41. 94

Kanagawa, K.D., Muto, T., Tanaka, H., Tanigawa, T., Takeuchi, T., Tsukagoshi, T. & Momose, M. (2016). Mass constraint for a planet in a protoplanetary disk from the gap width. *PASJ*, **68**, 43. 30

Kastner, J.H., Zuckerman, B., Weintraub, D.A. & Forveille, T. (1997). X-ray and molecular emission from the nearest region of recent star formation. *Science*, **277**, 67–71. 85

Keller, L.P., Hony, S., Bradley, J.P., Molster, F.J., Waters, L.B.F.M., Bouwman, J., de Koter, A., Brownlee, D.E., Flynn, G.J., Henning, T. & Mutschke, H. (2002). Identification of iron sulphide grains in protoplanetary disks. *Nature*, **417**, 148–150. 14

Kenyon, S.J. & Hartmann, L. (1987). Spectral energy distributions of T Tauri stars - Disk flaring and limits on accretion. *ApJ*, **323**, 714–733. 18

Keppler, M., Benisty, M., Müller, A., Henning, T., van Boekel, R., Cantalloube, F., Ginski, C., van Holstein, R.G., Maire, A.L., Pohl, A., Samland, M., Avenhaus, H., Baudino, J.L., Boccaletti, A., de Boer, J., Bonnefoy, M., Chauvin, G., Desidera, S., Langlois, M., Lazzoni, C., Marleau, G.D., Mordasini, C., Pawellek, N., Stolker, T., Vigan, A., Zurlo, A., Birnstiel, T., Brandner, W., Feldt, M., Flock, M., Girard, J., Gratton, R., Hagelberg,

J., Isella, A., Janson, M., Juhasz, A., Kemmer, J., Kral, Q., Lagrange, A.M., Launhardt, R., Matter, A., Ménard, F., Milli, J., Mollière, P., Olofsson, J., Pérez, L., Pinilla, P., Pinte, C., Quanz, S.P., Schmidt, T., Udry, S., Wahhaj, Z., Williams, J.P., Buenzli, E., Cudel, M., Dominik, C., Galicher, R., Kasper, M., Lannier, J., Mesa, D., Mouillet, D., Peretti, S., Perrot, C., Salter, G., Sissa, E., Wildi, F., Abe, L., Antichi, J., Augereau, J.C., Baruffolo, A., Baudoz, P., Bazzon, A., Beuzit, J.L., Blanchard, P., Brems, S.S., Buey, T., De Caprio, V., Carbillet, M., Carle, M., Cascone, E., Cheetham, A., Claudi, R., Costille, A., Delboulbé, A., Dohlen, K., Fantinel, D., Feautrier, P., Fusco, T., Giro, E., Gluck, L., Gry, C., Hubin, N., Hugot, E., Jaquet, M., Le Mignant, D., Llored, M., Madec, F., Magnard, Y., Martinez, P., Maurel, D., Meyer, M., Möller-Nilsson, O., Moulin, T., Mugnier, L., Origné, A., Pavlov, A., Perret, D., Petit, C., Pragt, J., Puget, P., Rabou, P., Ramos, J., Rigal, F., Rochat, S., Roelfsema, R., Rousset, G., Roux, A., Salasnich, B., Sauvage, J.F., Sevin, A., Soenke, C., Stadler, E., Suarez, M., Turatto, M. & Weber, L. (2018). Discovery of a planetary-mass companion within the gap of the transition disk around PDS 70. *A&A*, **617**, A44. 32

Keppler, M., Teague, R., Bae, J., Benisty, M., Henning, T., van Boekel, R., Chapillon, E., Pinilla, P., Williams, J.P., Bertrang, G.H.M., Facchini, S., Flock, M., Ginski, C., Juhasz, A., Klahr, H., Liu, Y., Müller, A., Pérez, L.M., Pohl, A., Rosotti, G., Samland, M. & Semenov, D. (2019). Highly structured disk around the planet host PDS 70 revealed by high-angular resolution observations with ALMA. *A&A*, **625**, A118. 32

Kim, S., Nomura, H., Tsukagoshi, T., Kawabe, R. & Muto, T. (2019). The Synthetic ALMA Multiband Analysis of the Dust Properties of the TW Hya Protoplanetary Disk. *ApJ*, **872**, 179. 23

Kim, W.T. & Ostriker, E.C. (2001). Amplification, Saturation, and Q Thresholds for Runaway: Growth of Self-Gravitating Structures in Models of Magnetized Galactic Gas Disks. *ApJ*, **559**, 70–95. 81

Klaassen, P.D., Juhasz, A., Mathews, G.S., Mottram, J.C., De Gregorio-Monsalvo, I., van Dishoeck, E.F., Takahashi, S., Akiyama, E., Chapillon, E., Espada, D., Hales, A., Hogerheijde, M.R., Rawlings, M., Schmalzl, M. & Testi, L. (2013a). ALMA detection of the rotating molecular disk wind from the young star HD 163296. *A&A*, **555**, A73. 29, 170

Klaassen, P.D., Juhasz, A., Mathews, G.S., Mottram, J.C., De Gregorio-Monsalvo, I., van Dishoeck, E.F., Takahashi, S., Akiyama, E., Chapillon, E., Espada, D., Hales, A., Hogerheijde, M.R., Rawlings, M., Schmalzl, M. & Testi, L. (2013b). ALMA detection of the rotating molecular disk wind from the young star HD 163296. *A&A*, **555**, A73. 148

Klapper, G., Surin, L., Lewen, F., Muller, H.S.P., Pak, I. & Winnewisser, G. (2003). Laboratory precision measurements of the rotational spectrum of12c17o and13c17o. *The Astrophysical Journal*, **582**, 262–268. 55

Kley, W. & Nelson, R. (2012). Planet-disk interaction and orbital evolution. *ARA&A*, **50**, 211–249. 30

Kratter, K. & Lodato, G. (2016). Gravitational Instabilities in Circumstellar Disks. *ARA&A*, **54**, 271–311. 6

Krijt, S., Schwarz, K.R., Bergin, E.A. & Ciesla, F.J. (2018). Transport of CO in Protoplanetary Disks: Consequences of Pebble Formation, Settling, and Radial Drift. *ApJ*, **864**, 78. 67

Kwon, W., Looney, L.W. & Mundy, L.G. (2011). Resolving the Circumstellar Disk of HL Tauri at Millimeter Wavelengths. *ApJ*, **741**, 3. 72

Kwon, W., Looney, L.W., Mundy, L.G. & Welch, W.J. (2015). Resolving Protoplanetary Disks at Millimeter Wavelengths with CARMA. *ApJ*, **808**, 102. 76, 175

Laas, J.C. & Caselli, P. (2019). Modeling sulfur depletion in interstellar clouds. *A&A*, **624**, A108. 169

Lagage, P.O., Doucet, C., Pantin, E., Habart, E., Duchêne, G., Ménard, F., Pinte, C., Charnoz, S. & Pel, J.W. (2006). Anatomy of a flaring proto-planetary disk around a young intermediate-mass star. , **314**, 621–623. 87

Lagrange, A.M., Gratadour, D., Chauvin, G., Fusco, T., Ehrenreich, D., Mouillet, D., Rousset, G., Rouan, D., Allard, F., Gendron, É., Charton, J., Mugnier, L., Rabou, P., Montri, J. & Lacombe, F. (2009). A probable giant planet imaged in the $\beta$ Pictoris disk. VLT/NaCo deep L'-band imaging. *A&A*, **493**, L21–L25. 10

Lagrange, A.M., Boccaletti, A., Langlois, M., Chauvin, G., Gratton, R., Beust, H., Desidera, S., Milli, J., Bonnefoy, M., Cheetham, A., Feldt, M., Meyer, M., Vigan, A., Biller, B., Bonavita, M., Baudino, J.L., Cantalloube, F., Cudel, M., Daemgen, S., Delorme, P., D'Orazi, V., Girard, J., Fontanive, C., Hagelberg, J., Janson, M., Keppler, M., Koypitova, T., Galicher,

R., Lannier, J., Le Coroller, H., Ligi, R., Maire, A.L., Mesa, D., Messina, S., Müeller, A., Peretti, S., Perrot, C., Rouan, D., Salter, G., Samland, M., Schmidt, T., Sissa, E., Zurlo, A., Beuzit, J.L., Mouillet, D., Dominik, C., Henning, T., Lagadec, E., Ménard, F., Schmid, H.M., Turatto, M., Udry, S., Bohn, A.J., Charnay, B., Gomez Gonzales, C.A., Gry, C., Kenworthy, M., Kral, Q., Mordasini, C., Moutou, C., van der Plas, G., Schlieder, J.E., Abe, L., Antichi, J., Baruffolo, A., Baudoz, P., Baudrand, J., Blanchard, P., Bazzon, A., Buey, T., Carbillet, M., Carle, M., Charton, J., Cascone, E., Claudi, R., Costille, A., Deboulbe, A., De Caprio, V., Dohlen, K., Fantinel, D., Feautrier, P., Fusco, T., Gigan, P., Giro, E., Gisler, D., Gluck, L., Hubin, N., Hugot, E., Jaquet, M., Kasper, M., Madec, F., Magnard, Y., Martinez, P., Maurel, D., Le Mignant, D., Möller-Nilsson, O., Llored, M., Moulin, T., Origné, A., Pavlov, A., Perret, D., Petit, C., Pragt, J., Szulagyi, J. & Wildi, F. (2019). Post-conjunction detection of $\beta$ Pictoris b with VLT/SPHERE. *A&A*, **621**, L8. 10

Lambrechts, M. & Johansen, A. (2012). Rapid growth of gas-giant cores by pebble accretion. *A&A*, **544**, A32. 9

Larson, R.B. (2003). The physics of star formation. *Reports on Progress in Physics*, **66**, 1651–1697. 2

Lique, F., Dubernet, M.L., Spielfiedel, A. & Feautrier, N. (2006). Rotational excitation of sulfur monoxide in collision with helium at high temperature. *A&A*, **450**, 399–405. 45, 137

Liskowsky, J.P., Brittain, S.D., Najita, J.R., Carr, J.S., Doppmann, G.W. & Troutman, M.R. (2012). High-resolution Near-infrared

Spectroscopy of HD 100546. I. Analysis of Asymmetric Ro-vibrational OH Emission Lines. *ApJ*, **760**, 153. 124

Liu, S.F., Jin, S., Li, S., Isella, A. & Li, H. (2018). New Constraints on Turbulence and Embedded Planet Mass in the HD 163296 Disk from Planet-Disk Hydrodynamic Simulations. *ApJ*, **857**, 87. 54, 68, 70, 174

Long, F., Herczeg, G.J., Pascucci, I., Apai, D., Henning, T., Manara, C.F., Mulders, G.D., Szűcs, L. & Hendler, N.P. (2018a). An ALMA Survey of Faint Disks in the Chamaeleon I Star-forming Region: Why Are Some Class II Disks so Faint? *ApJ*, **863**, 61. 22

Long, F., Pinilla, P., Herczeg, G.J., Harsono, D., Dipierro, G., Pascucci, I., Hendler, N., Tazzari, M., Ragusa, E., Salyk, C., Edwards, S., Lodato, G., van de Plas, G., Johnstone, D., Liu, Y., Boehler, Y., Cabrit, S., Manara, C.F., Menard, F., Mulders, G.D., Nisini, B., Fischer, W.J., Rigliaco, E., Banzatti, A., Avenhaus, H. & Gully-Santiago, M. (2018b). Gaps and Rings in an ALMA Survey of Disks in the Taurus Star-forming Region. *ApJ*, **869**, 17. 25

Long, Z.C., Akiyama, E., Sitko, M., Fernandes, R.B., Assani, K., Grady, C.A., Cure, M., Danchi, W.C., Dong, R., Fukagawa, M., Hasegawa, Y., Hashimoto, J., Henning, T., Inutsuka, S.I., Kraus, S., Kwon, J., Lisse, C.M., Baobabu Liu, H., Mayama, S., Muto, T., Nakagawa, T., Takami, M., Tamura, M., Currie, T., Wisniewski, J.P. & Yang, Y. (2018c). Differences in the Gas and Dust Distribution in the Transitional Disk of a Sun-like Young Star, PDS 70. *ApJ*, **858**, 112. 32

Loomis, R.A., Öberg, K.I., Andrews, S.M. & MacGregor, M.A. (2017). A Multi-ringed, Modestly Inclined Protoplanetary Disk around AA Tau. *ApJ*, **840**, 23. 31

Loomis, R.A., Cleeves, L.I., Öberg, K.I., Aikawa, Y., Bergner, J., Furuya, K., Guzman, V.V. & Walsh, C. (2018a). The Distribution and Excitation of $CH_3CN$ in a Solar Nebula Analog. *ApJ*, **859**, 131. 24

Loomis, R.A., Öberg, K.I., Andrews, S.M., Walsh, C., Czekala, I., Huang, J. & Rosenfeld, K.A. (2018b). Detecting Weak Spectral Lines in Interferometric Data through Matched Filtering. *AJ*, **155**, 182. 41, 54, 55, 134, 152

Lovelace, R.V.E. & Romanova, M.M. (2014). Rossby wave instability in astrophysical discs. *Fluid Dynamics Research*, **46**, 041401. 31

Lynden-Bell, D. & Pringle, J.E. (1974). The evolution of viscous discs and the origin of the nebular variables. *MNRAS*, **168**, 603–637. 6, 11

MacGregor, M.A., Matrà, L., Kalas, P., Wilner, D.J., Pan, M., Kennedy, G.M., Wyatt, M.C., Duchene, G., Hughes, A.M., Rieke, G.H., Clampin, M., Fitzgerald, M.P., Graham, J.R., Holland, W.S., Panić, O., Shannon, A. & Su, K. (2017). A Complete ALMA Map of the Fomalhaut Debris Disk. *ApJ*, **842**, 8. 8, 10

Manara, C.F., Morbidelli, A. & Guillot, T. (2018). Why do protoplanetary disks appear not massive enough to form the known exoplanet population? *A&A*, **618**, L3. 22, 83, 179

Markwick, A.J., Ilgner, M., Millar, T.J. & Henning, T. (2002). Molecular distributions in the inner regions of protostellar disks. *A&A*, **385**, 632–646. 16

Martín-Doménech, R., Jiménez-Serra, I., Muñoz Caro, G.M., Müller, H.S.P., Occhiogrosso, A., Testi, L., Woods, P.M. & Viti, S. (2016). The sulfur depletion problem: upper limits on the gas-phase abundances toward the low-mass warm core IRAS 16293-2422. *A&A*, **585**, A112. 14

Martin-Pintado, J., Bachiller, R. & Fuente, A. (1992). SiO emission as a tracer of shocked gas in molecular outflows. *A&A*, **254**, 315–326. 151

Massalkhi, S., Agúndez, M. & Cernicharo, J. (2019). Study of CS, SiO, and SiS abundances in carbon star envelopes: assessing their role as gas-phase precursors of dust. *A&A*, **628**, A62. 165

Mathews, G.S., Klaassen, P.D., Juhász, A., Harsono, D., Chapillon, E., van Dishoeck, E.F., Espada, D., de Gregorio-Monsalvo, I., Hales, A., Hogerheijde, M.R., Mottram, J.C., Rawlings, M.G., Takahashi, S. & Testi, L. (2013). ALMA imaging of the CO snowline of the HD 163296 disk with $DCO^+$. *A&A*, **557**, A132. 115

McClure, M.K., Bergin, E.A., Cleeves, L.I., van Dishoeck, E.F., Blake, G.A., Evans, N.J., II, Green, J.D., Henning, T., Öberg, K.I., Pontoppidan, K.M. & Salyk, C. (2016). Mass Measurements in Protoplanetary Disks from Hydrogen Deuteride. *ApJ*, **831**, 167. 23, 66, 78

McElroy, D., Walsh, C., Markwick, A.J., Cordiner, M.A., Smith, K. & Millar, T.J. (2013). The UMIST database for astrochemistry 2012. *A&A*, **550**, A36. 42, 96

McGuire, B.A. (2018). 2018 census of interstellar, circumstellar, extragalactic, protoplanetary disk, and exoplanetary molecules. *ApJS*, **239**, 17. 18

McKee, C.F. & Ostriker, E.C. (2007). Theory of star formation. *ARA&A*, **45**, 565–687. 5

McKee, C.F., Zweibel, E.G., Goodman, A.A. & Heiles, C. (1993). Magnetic Fields in Star-Forming Regions - Theory. In E.H. Levy & J.I. Lunine, eds., *Protostars and Planets III*, 327. 2

McMullin, J.P., Waters, B., Schiebel, D., Young, W. & Golap, K. (2007a). CASA Architecture and Applications. In R.A. Shaw, F. Hill & D.J. Bell, eds., *Astronomical Data Analysis Software and Systems XVI*, vol. 376 of *Astronomical Society of the Pacific Conference Series*, 127. 39

McMullin, J.P., Waters, B., Schiebel, D., Young, W. & Golap, K. (2007b). CASA Architecture and Applications. In R.A. Shaw, F. Hill & D.J. Bell, eds., *Astronomical Data Analysis Software and Systems XVI*, vol. 376 of *Astronomical Society of the Pacific Conference Series*, 127. 74

Meeus, G., Montesinos, B., Mendigutía, I., Kamp, I., Thi, W.F., Eiroa, C., Grady, C.A., Mathews, G., Sandell, G., Martin-Zaïdi, C., Brittain, S., Dent, W.R.F., Howard, C., Ménard, F., Pinte, C., Roberge, A., Vandenbussche, B. & Williams, J.P. (2012). Observations of Herbig Ae/Be stars with Herschel/PACS. The atomic and molecular contents of their protoplanetary discs. *A&A*, **544**, A78. 87

Meeus, G., Salyk, C., Bruderer, S., Fedele, D., Maaskant, K., Evans, N.J., van Dishoeck, E.F., Montesinos, B., Herczeg, G., Bouwman, J., Green, J.D., Dominik, C., Henning, T. & Vicente, S. (2013a). DIGIT survey of far-infrared lines from protoplanetary discs. II. CO. *A&A*, **559**, A84. 87

Meeus, G., Salyk, C., Bruderer, S., Fedele, D., Maaskant, K., Evans, N.J., van Dishoeck, E.F., Montesinos, B., Herczeg, G., Bouwman, J., Green, J.D., Dominik, C., Henning, T. & Vicente, S. (2013b). DIGIT survey of far-infrared lines from protoplanetary discs. II. CO. *A&A*, **559**, A84. 124

Mendigutía, I., Brittain, S., Eiroa, C., Meeus, G., Montesinos, B., Mora, A., Muzerolle, J., Oudmaijer, R.D. & Rigliaco, E. (2013). Accretion Variability of Herbig Ae/Be Stars Observed by X-Shooter HD 31648 and HD 163296. *ApJ*, **776**, 44. 70

Millar, T.J. & Herbst, E. (1990). Organo-sulphur chemistry in dense interstellar clouds. *A&A*, **231**, 466–472. 146

Miotello, A., Bruderer, S. & van Dishoeck, E.F. (2014). Protoplanetary disk masses from CO isotopologue line emission. *A&A*, **572**, A96. 23, 77, 100, 112

Miotello, A., van Dishoeck, E.F., Williams, J.P., Ansdell, M., Guidi, G., Hogerheijde, M., Manara, C.F., Tazzari, M., Testi, L., van der Marel, N. & van Terwisga, S. (2017). Lupus disks with faint CO isotopologues: low gas/dust or high carbon depletion? *A&A*, **599**, A113. 78, 173

Miotello, A., Facchini, S., van Dishoeck, E.F. & Bruderer, S. (2018). Probing the protoplanetary disk gas surface density distribution with $^{13}$CO emission. *A&A*, **619**, A113. 26

Miotello, A., Facchini, S., van Dishoeck, E.F., Cazzoletti, P., Testi, L., Williams, J.P., Ansdell, M., van Terwisga, S. & van der Marel,

N. (2019). Bright $C_2H$ emission in protoplanetary discs in Lupus: high volatile C/O > 1 ratios. *A&A*, **631**, A69. 179

Molyarova, T., Akimkin, V., Semenov, D., Henning, T., Vasyunin, A. & Wiebe, D. (2017). Gas Mass Tracers in Protoplanetary Disks: CO is Still the Best. *ApJ*, **849**, 130. 66

Mulders, G.D., Paardekooper, S.J., Panić, O., Dominik, C., van Boekel, R. & Ratzka, T. (2013). Planet or brown dwarf? Inferring the companion mass in HD 100546 from the wall shape using mid-infrared interferometry. *A&A*, **557**, A68. 124

Müller, H.S.P., Thorwirth, S., Roth, D.A. & Winnewisser, G. (2001). The Cologne Database for Molecular Spectroscopy, CDMS. *A&A*, **370**, L49–L52. 57, 125

Müller, H.S.P., Schlöder, F., Stutzki, J. & Winnewisser, G. (2005). The Cologne Database for Molecular Spectroscopy, CDMS: a useful tool for astronomers and spectroscopists. *JMoSt*, **742**, 215–227. 55, 58, 153

Muro-Arena, G.A., Dominik, C., Waters, L.B.F.M., Min, M., Klarmann, L., Ginski, C., Isella, A., Benisty, M., Pohl, A., Garufi, A., Hagelberg, J., Langlois, M., Menard, F., Pinte, C., Sezestre, E., van der Plas, G., Villenave, M., Delboulbé, A., Magnard, Y., Möller-Nilsson, O., Pragt, J., Rabou, P. & Roelfsema, R. (2018). Dust modeling of the combined ALMA and SPHERE datasets of HD 163296. Is HD 163296 really a Meeus group II disk? *A&A*, **614**, A24. 87

Nero, D. & Bjorkman, J.E. (2009). Did Fomalhaut, HR 8799, and HL Tauri Form Planets Via the Gravitational Instability? Placing Limits on the Required Disk Masses. *ApJ*, **702**, L163–L167. 72

Nomura, H., Tsukagoshi, T., Kawabe, R., Ishimoto, D., Okuzumi, S., Muto, T., Kanagawa, K.D., Ida, S., Walsh, C., Millar, T.J. & Bai, X.N. (2016). ALMA Observations of a Gap and a Ring in the Protoplanetary Disk around TW Hya. *ApJ*, **819**, L7. 26

Notsu, S., Nomura, H., Ishimoto, D., Walsh, C., Honda, M., Hirota, T. & Millar, T.J. (2016). Candidate Water Vapor Lines to Locate the H2O Snowline through High-dispersion Spectroscopic Observations. I. The Case of a T Tauri Star. *ApJ*, **827**, 113. 16

Notsu, S., Nomura, H., Ishimoto, D., Walsh, C., Honda, M., Hirota, T. & Millar, T.J. (2017). Candidate Water Vapor Lines to Locate the $H_2O$ Snowline through High-dispersion Spectroscopic Observations. II. The Case of a Herbig Ae Star. *ApJ*, **836**, 118. 117

Notsu, S., Akiyama, E., Booth, A., Nomura, H., Walsh, C., Hirota, T., Honda, M., Tsukagoshi, T. & Millar, T.J. (2019). Dust Continuum Emission and the Upper Limit Fluxes of Submillimeter Water Lines of the Protoplanetary Disk around HD 163296 Observed by ALMA. *ApJ*, **875**, 96. 54

Öberg, K.I., Qi, C., Fogel, J.K.J., Bergin, E.A., Andrews, S.M., Espaillat, C., van Kempen, T.A., Wilner, D.J. & Pascucci, I. (2010). The Disk Imaging Survey of Chemistry with SMA. I. Taurus Protoplanetary Disk Data. *ApJ*, **720**, 480–493. 19, 111

Öberg, K.I., Qi, C., Fogel, J.K.J., Bergin, E.A., Andrews, S.M., Espaillat, C., Wilner, D.J., Pascucci, I. & Kastner, J.H. (2011). Disk Imaging Survey of Chemistry with SMA. II. Southern Sky Protoplanetary Disk Data and Full Sample Statistics. *ApJ*, **734**, 98. 111

Öberg, K.I., Furuya, K., Loomis, R., Aikawa, Y., Andrews, S.M., Qi, C., van Dishoeck, E.F. & Wilner, D.J. (2015). Double $DCO^+$ Rings Reveal CO Ice Desorption in the Outer Disk Around IM Lup. *ApJ*, **810**, 112. 28, 115

O'dell, C.R., Wen, Z. & Hu, X. (1993). Discovery of new objects in the Orion nebula on HST images - Shocks, compact sources, and protoplanetary disks. *ApJ*, **410**, 696–700. 17

Okuzumi, S., Momose, M., Sirono, S.i., Kobayashi, H. & Tanaka, H. (2016). Sintering-induced Dust Ring Formation in Protoplanetary Disks: Application to the HL Tau Disk. *ApJ*, **821**, 82. 31, 71, 76

Pacheco-Vázquez, S., Fuente, A., Baruteau, C., Berné, O., Agúndez, M., Neri, R., Goicoechea, J.R., Cernicharo, J. & Bachiller, R. (2016). High spatial resolution imaging of SO and $H_2CO$ in AB Auriga: The first SO image in a transitional disk. *A&A*, **589**, A60. 144, 146

Panić, O., van Dishoeck, E.F., Hogerheijde, M.R., Belloche, A., Güsten, R., Boland, W. & Baryshev, A. (2010). Observations of warm molecular gas and kinematics in the disc around HD 100546. *A&A*, **519**, A110. 124, 147

Panić, O., Holland, W.S., Wyatt, M.C., Kennedy, G.M., Matthews, B.C., Lestrade, J.F., Sibthorpe, B., Greaves, J.S., Marshall, J.P., Phillips, N.M. & Tottle, J. (2013). First results of the SONS survey: submillimetre detections of debris discs. *MNRAS*, **435**, 1037–1046. 10

Pascucci, I., Sterzik, M., Alexander, R.D., Alencar, S.H.P., Gorti, U., Hollenbach, D., Owen, J., Ercolano, B. & Edwards, S. (2011a). The Photoevaporative Wind from the Disk of TW Hya. *ApJ*, **736**, 13. 29

Pascucci, I., Sterzik, M., Alexander, R.D., Alencar, S.H.P., Gorti, U., Hollenbach, D., Owen, J., Ercolano, B. & Edwards, S. (2011b). The Photoevaporative Wind from the Disk of TW Hya. *ApJ*, **736**, 13. 148

Pérez, L.M., Carpenter, J.M., Andrews, S.M., Ricci, L., Isella, A., Linz, H., Sargent, A.I., Wilner, D.J., Henning, T., Deller, A.T., Chandler, C.J., Dullemond, C.P., Lazio, J., Menten, K.M., Corder, S.A., Storm, S., Testi, L., Tazzari, M., Kwon, W., Calvet, N., Greaves, J.S., Harris, R.J. & Mundy, L.G. (2016). Spiral density waves in a young protoplanetary disk. *Science*, **353**, 1519–1521. 25

Perez, S., Dunhill, A., Casassus, S., Roman, P., Szulágyi, J., Flores, C., Marino, S. & Montesinos, M. (2015). Planet Formation Signposts: Observability of Circumplanetary Disks via Gas Kinematics. *ApJ*, **811**, L5. 32

Phuong, N.T., Chapillon, E., Majumdar, L., Dutrey, A., Guilloteau, S., Piétu, V., Wakelam, V., Diep, P.N., Tang, Y.W., Beck, T. & Bary, J. (2018). First detection of $H_2S$ in a protoplanetary disk. The dense GG Tauri A ring. *A&A*, **616**, L5. 170

Piétu, V., Dutrey, A. & Guilloteau, S. (2007). Probing the structure of protoplanetary disks: a comparative study of DM Tau, LkCa 15, and MWC 480. *A&A*, **467**, 163–178. 85, 116

Pineda, J.E., Quanz, S.P., Meru, F., Mulders, G.D., Meyer, M.R., Panić, O. & Avenhaus, H. (2014). Resolved Images of the Protoplanetary Disk around HD 100546 with ALMA. *ApJ*, **788**, L34. 124

Pinilla, P., Benisty, M. & Birnstiel, T. (2012). Ring shaped dust accumulation in transition disks. *A&A*, **545**, A81. 30

Pinilla, P., Birnstiel, T. & Walsh, C. (2015). Sequential planet formation in the HD 100546 protoplanetary disk? *A&A*, **580**, A105. 124

Pinilla, P., Flock, M., Ovelar, M.d.J. & Birnstiel, T. (2016). Can dead zones create structures like a transition disk? *A&A*, **596**, A81. 31

Pinte, C. (2015). Continuum radiative transfer. In *European Physical Journal Web of Conferences*, vol. 102, 00006. 45

Pinte, C., Dent, W.R.F., Ménard, F., Hales, A., Hill, T., Cortes, P. & de Gregorio-Monsalvo, I. (2016). Dust and Gas in the Disk of HL Tauri: Surface Density, Dust Settling, and Dust-to-gas Ratio. *ApJ*, **816**, 25. 76, 80

Pinte, C., Price, D.J., Ménard, F., Duchêne, G., Dent, W.R.F., Hill, T., de Gregorio-Monsalvo, I., Hales, A. & Mentiplay, D. (2018). Kinematic Evidence for an Embedded Protoplanet in a Circumstellar Disk. *ApJ*, **860**, L13. 31, 32, 54, 69, 70, 174

Pinte, C., van der Plas, G., Ménard, F., Price, D.J., Christiaens, V., Hill, T., Mentiplay, D., Ginski, C., Choquet, E., Boehler, Y., Duchêne, G., Perez, S. & Casassus, S. (2019). Kinematic detection of a planet carving a gap in a protoplanetary disk. *Nature Astronomy*, **3**, 1109–1114. 31, 32, 86, 119, 144, 176

Podio, L., Codella, C., Gueth, F., Cabrit, S., Bachiller, R., Gusdorf, A., Lee, C.F., Lefloch, B., Leurini, S., Nisini, B. & Tafalla, M. (2015). The jet and the disk of the HH 212 low-mass protostar imaged by ALMA: SO and $SO_2$ emission. *A&A*, **581**, A85. 123

Pollack, J.B., Hubickyj, O., Bodenheimer, P., Lissauer, J.J., Podolak, M. & Greenzweig, Y. (1996). Formation of the Giant Planets by Concurrent Accretion of Solids and Gas. *Icarus*, **124**, 62–85. 9

Pontoppidan, K.M., Salyk, C., Blake, G.A., Meijerink, R., Carr, J.S. & Najita, J. (2010). A Spitzer Survey of Mid-Infrared Molecular Emission from Protoplanetary Disks. i. Detection Rates. *ApJ*, **720**, 887–903. 19

Pontoppidan, K.M., Salyk, C., Bergin, E.A., Brittain, S., Marty, B., Mousis, O. & Öberg, K.I. (2014). Volatiles in Protoplanetary Disks. *Protostars and Planets VI*, 363–385. 14

Pontoppidan, K.M., Salyk, C., Banzatti, A., Blake, G.A., Walsh, C., Lacy, J.H. & Richter, M.J. (2019). The Nitrogen Carrier in Inner Protoplanetary Disks. *ApJ*, **874**, 92. 14

Powell, D., Murray-Clay, R., Pérez, L.M., Schlichting, H.E. & Rosenthal, M. (2019). New Constraints From Dust Lines on the Surface Densities of Protoplanetary Disks. *ApJ*, **878**, 116. 65, 69

Pringle, J.E. (1981). Accretion discs in astrophysics. *ARA&A*, **19**, 137–162. 6, 7

Przygodda, F., van Boekel, R., Àbrahàm, P., Melnikov, S.Y., Waters, L.B.F.M. & Leinert, C. (2003). Evidence for grain growth in T Tauri disks. *A&A*, **412**, L43–L46. 15

Qi, C., Ho, P.T.P., Wilner, D.J., Takakuwa, S., Hirano, N., Ohashi, N., Bourke, T.L., Zhang, Q., Blake, G.A., Hogerheijde, M., Saito, M., Choi, M. & Yang, J. (2004). Imaging the Disk around TW Hydrae with the Submillimeter Array. *ApJ*, **616**, L11–L14. 19

Qi, C., Wilner, D.J., Calvet, N., Bourke, T.L., Blake, G.A., Hogerheijde, M.R., Ho, P.T.P. & Bergin, E. (2006). CO J = 6-5 Observations of TW Hydrae with the Submillimeter Array. *ApJ*, **636**, L157–L160. 23

Qi, C., D'Alessio, P., Öberg, K.I., Wilner, D.J., Hughes, A.M., Andrews, S.M. & Ayala, S. (2011). Resolving the CO Snow Line in the Disk around HD 163296. *ApJ*, **740**, 84. xvii, 13, 23, 56, 58, 60, 61, 64, 96, 174

Qi, C., Öberg, K.I. & Wilner, D.J. (2013a). $H_2CO$ and $N_2H^+$ in Protoplanetary Disks: Evidence for a CO-ice Regulated Chemistry. *ApJ*, **765**, 34. 115

Qi, C., Öberg, K.I., Wilner, D.J., D'Alessio, P., Bergin, E., Andrews, S.M., Blake, G.A., Hogerheijde, M.R. & van Dishoeck, E.F. (2013b). Imaging of the CO Snow Line in a Solar Nebula Analog. *Science*, **341**, 630–632. 28

Qi, C., Öberg, K.I., Andrews, S.M., Wilner, D.J., Bergin, E.A., Hughes, A.M., Hogherheijde, M. & D'Alessio, P. (2015). Chemical Imaging of the CO Snow Line in the HD 163296 Disk. *ApJ*, **813**, 128. xvii, 28, 61, 63, 115

Qi, C., Öberg, K.I., Espaillat, C.C., Robinson, C.E., Andrews, S.M., Wilner, D.J., Blake, G.A., Bergin, E.A. & Cleeves, L.I. (2019). Probing CO and $N_2$ Snow Surfaces in Protoplanetary Disks with $N_2H^+$ Emission. *ApJ*, **882**, 160. 28

Quanz, S.P., Birkmann, S.M., Apai, D., Wolf, S. & Henning, T. (2012). Resolving the inner regions of the HD 97048 circumstellar disk with VLT/NACO polarimetric differential imaging. *A&A*, **538**, A92. 144

Quanz, S.P., Amara, A., Meyer, M.R., Kenworthy, M.A., Kasper, M. & Girard, J.H. (2013). A Young Protoplanet Candidate Embedded in the Circumstellar Disk of HD 100546. *ApJ*, **766**, L1. 123, 124, 149

Quanz, S.P., Amara, A., Meyer, M.R., Girard, J.H., Kenworthy, M.A. & Kasper, M. (2015). Confirmation and Characterization of the Protoplanet HD 100546 bDirect Evidence for Gas Giant Planet Formation at 50 AU. *ApJ*, **807**, 64. 123, 124, 149

Quillen, A.C. (2006). The Warped Circumstellar Disk of HD 100546. *ApJ*, **640**, 1078–1085. 147

Rafikov, R.R. (2005). Can Giant Planets Form by Direct Gravitational Instability? *ApJ*, **621**, L69–L72. 81

Rebull, L.M., Wolff, S.C. & Strom, S.E. (2004). Stellar Rotation in Young Clusters: The First 4 Million Years. *AJ*, **127**, 1029–1051. 70

Reffert, S., Bergmann, C., Quirrenbach, A., Trifonov, T. & Künstler, A. (2015). Precise radial velocities of giant stars. VII. Occurrence rate of giant extrasolar planets as a function of mass and metallicity. *A&A*, **574**, A116. 180

Remijan, A., Snyder, L.E., Friedel, D.N., Liu, S.Y. & Shah, R.Y. (2003). A Survey of Acetic Acid toward Hot Molecular Cores. *ApJ*, **590**, 314–332. 58

Remijan, A.e.a. (2019). *ALMA Technical Handbook*. 36

Ricci, L., Robberto, M. & Soderblom, D.R. (2008). THEHUBBLE SPACE TELESCOPE/ADVANCED CAMERA FOR SURVEYS ATLAS OF

PROTOPLANETARY DISKS IN THE GREAT ORION NEBULA. *The Astronomical Journal*, **136**, 2136–2151. 17

Rice, W.K.M., Armitage, P.J., Bate, M.R. & Bonnell, I.A. (2003). The effect of cooling on the global stability of self-gravitating protoplanetary discs. *MNRAS*, **339**, 1025–1030. 10

Rice, W.K.M., Lodato, G., Pringle, J.E., Armitage, P.J. & Bonnell, I.A. (2004). Accelerated planetesimal growth in self-gravitating protoplanetary discs. *MNRAS*, **355**, 543–552. 6, 70, 81

Robitaille, T.P., Whitney, B.A., Indebetouw, R. & Wood, K. (2007). Interpreting Spectral Energy Distributions from Young Stellar Objects. II. Fitting Observed SEDs Using a Large Grid of Precomputed Models. *ApJS*, **169**, 328–352. 70

Rodriguez, L.F., Canto, J., Torrelles, J.M., Gomez, J.F., Anglada, G. & Ho, P.T.P. (1994). Subarcsecond VLA maps of the disk and the jet in HL Tauri. *ApJ*, **427**, L103–L106. 18

Rosenfeld, K.A., Andrews, S.M., Hughes, A.M., Wilner, D.J. & Qi, C. (2013). A Spatially Resolved Vertical Temperature Gradient in the HD 163296 Disk. *ApJ*, **774**, 16. 12, 77

Rosenfeld, K.A., Chiang, E. & Andrews, S.M. (2014). Fast Radial Flows in Transition Disk Holes. *ApJ*, **782**, 62. 116

Rosotti, G.P., Juhasz, A., Booth, R.A. & Clarke, C.J. (2016). The minimum mass of detectable planets in protoplanetary discs and the derivation of planetary masses from high-resolution observations. *MNRAS*, **459**, 2790–2805. 30, 119

Ruffle, D.P., Hartquist, T.W., Caselli, P. & Williams, D.A. (1999). The sulphur depletion problem. *MNRAS*, **306**, 691–695. 14, 141

Ruge, J.P., Flock, M., Wolf, S., Dzyurkevich, N., Fromang, S., Henning, T., Klahr, H. & Meheut, H. (2016). Gaps, rings, and non-axisymmetric structures in protoplanetary disks: Emission from large grains. *A&A*, **590**, A17. 31

Sakai, N., Oya, Y., López-Sepulcre, A., Watanabe, Y., Sakai, T., Hirota, T., Aikawa, Y., Ceccarelli, C., Lefloch, B., Caux, E., Vastel, C., Kahane, C. & Yamamoto, S. (2016). Subarcsecond Analysis of the Infalling-Rotating Envelope around the Class I Protostar IRAS 04365+2535. *ApJ*, **820**, L34. 123

Salinas, V.N., Hogerheijde, M.R., Mathews, G.S., Öberg, K.I., Qi, C., Williams, J.P. & Wilner, D.J. (2017). $DCO^+$, DCN, and $N_2D^+$ reveal three different deuteration regimes in the disk around the Herbig Ae star HD 163296. *A&A*, **606**, A125. 74

Schöier, F.L., van der Tak, F.F.S., van Dishoeck, E.F. & Black, J.H. (2005). An atomic and molecular database for analysis of submillimetre line observations. *A&A*, **432**, 369–379. 46, 89, 125, 152

Schwarz, K.R., Bergin, E.A., Cleeves, L.I., Blake, G.A., Zhang, K., Öberg, K.I., van Dishoeck, E.F. & Qi, C. (2016). The Radial Distribution of $H_2$ and CO in TW Hya as Revealed by Resolved ALMA Observations of CO Isotopologues. *ApJ*, **823**, 91. 23

Schwarz, K.R., Bergin, E.A., Cleeves, L.I., Zhang, K., berg, K.I., Blake, G.A. & Anderson, D. (2018). Unlocking CO depletion in protoplanetary disks. i. the warm molecular layer. *ApJ*, **856**, 85. 23, 78, 173, 175

Schwarz, K.R., Teague, R. & Bergin, E.A. (2019). Line Ratios Reveal $N_2H^+$ Emission Originates above the Midplane in TW Hydrae. *ApJ*, **876**, L13. 28

Semenov, D., Wiebe, D. & Henning, T. (2004). Reduction of chemical networks. II. Analysis of the fractional ionisation in protoplanetary discs. *A&A*, **417**, 93–106. 16

Shakura, N.I. & Sunyaev, R.A. (1973). Black holes in binary systems. Observational appearance. *A&A*, **24**, 337–355. 7

Shu, F.H. (1977). Self-similar collapse of isothermal spheres and star formation. *ApJ*, **214**, 488–497. 2

Shu, F.H., Adams, F.C. & Lizano, S. (1987). Star formation in molecular clouds - Observation and theory. *ARA&A*, **25**, 23–81. 2

Smith, B.A. & Terrile, R.J. (1984). A Circumstellar Disk around $\beta$ Pictoris. *Science*, **226**, 1421–1424. 17

Smith, D. & Adams, N.G. (1980). Laboratory studies of isotope fractionation in the reactions of C+ and HCO+ with CO - Interstellar implications. *ApJ*, **242**, 424–431. 113

Smith, R.L., Pontoppidan, K.M., Young, E.D. & Morris, M.R. (2015). Heterogeneity in $^{12}CO/^{13}CO$ Abundance Ratios toward Solar-type Young Stellar Objects. *ApJ*, **813**, 120. 79

Strom, K.M., Strom, S.E., Edwards, S., Cabrit, S. & Skrutskie, M.F. (1989). Circumstellar material associated with solar-type pre-main-sequence stars - A possible constraint on the timescale for planet building. *AJ*, **97**, 1451–1470. 18

Sturm, B., Bouwman, J., Henning, T., Evans, N.J., Acke, B., Mulders, G.D., Waters, L.B.F.M., van Dishoeck, E.F., Meeus, G., Green, J.D., Augereau, J.C., Olofsson, J., Salyk, C., Najita, J., Herczeg, G.J., van Kempen, T.A., Kristensen, L.E., Dominik, C., Carr, J.S., Waelkens, C., Bergin, E., Blake, G.A., Brown, J.M., Chen, J.H., Cieza, L., Dunham, M.M., Glassgold, A., Güdel, M., Harvey, P.M., Hogerheijde, M.R., Jaffe, D., Jørgensen, J.K., Kim, H.J., Knez, C., Lacy, J.H., Lee, J.E., Maret, S., Meijerink, R., Merín, B., Mundy, L., Pontoppidan, K.M., Visser, R. & Yildiz, U.A. (2010). First results of the Herschel key program "Dust, Ice and Gas In Time" (DIGIT): Dust and gas spectroscopy of HD 100546. *A&A*, **518**, L129. 124

Szulágyi, J., Masset, F., Lega, E., Crida, A., Morbidelli, A. & Guillot, T. (2016). Circumplanetary disc or circumplanetary envelope? *MNRAS*, **460**, 2853–2861. 32

Tabone, B., Cabrit, S., Bianchi, E., Ferreira, J., Pineau des Forêts, G., Codella, C., Gusdorf, A., Gueth, F., Podio, L. & Chapillon, E. (2017). ALMA discovery of a rotating $SO/SO_2$ flow in HH212. A possible MHD disk wind? *A&A*, **607**, L6. 29, 170

Tafalla, M., Santiago-García, J., Hacar, A. & Bachiller, R. (2010). A molecular survey of outflow gas: velocity-dependent shock chemistry and the peculiar composition of the EHV gas. *A&A*, **522**, A91. 123

Takahashi, S.Z. & Inutsuka, S.i. (2016). An Origin of Multiple Ring Structure and Hidden Planets in HL Tau: A Unified Picture by Secular Gravitational Instability. *AJ*, **152**, 184. 72

Tan, J.C., Beltrán, M.T., Caselli, P., Fontani, F., Fuente, A., Krumholz, M.R., McKee, C.F. & Stolte, A. (2014). Massive Star Formation. *Protostars and Planets VI*, 149–172. 5

Tapia, C., Lizano, S., Sierra, A., Carrasco-González, C. & Bayona-Bobadilla, E. (2019). Exploring the Grain Properties in the Disk of HL Tau with an Evolutionary Model. *ApJ*, **887**, 244. 79

Tazzari, M., Testi, L., Ercolano, B., Natta, A., Isella, A., Chandler, C.J., Pérez, L.M., Andrews, S., Wilner, D.J., Ricci, L., Henning, T., Linz, H., Kwon, W., Corder, S.A., Dullemond, C.P., Carpenter, J.M., Sargent, A.I., Mundy, L., Storm, S., Calvet, N., Greaves, J.A., Lazio, J. & Deller, A.T. (2016). Multiwavelength analysis for interferometric (sub-)mm observations of protoplanetary disks. Radial constraints on the dust properties and the disk structure. *A&A*, **588**, A53. 23

Teague, R., Guilloteau, S., Semenov, D., Henning, T., Dutrey, A., Piétu, V., Birnstiel, T., Chapillon, E., Hollenbach, D. & Gorti, U. (2016). Measuring turbulence in TW Hydrae with ALMA: methods and limitations. *A&A*, **592**, A49. 18

Teague, R., Semenov, D., Gorti, U., Guilloteau, S., Henning, T., Birnstiel, T., Dutrey, A., van Boekel, R. & Chapillon, E. (2017). A Surface Density Perturbation in the TW Hydrae Disk at 95 au Traced by Molecular Emission. *ApJ*, **835**, 228. 27

Teague, R., Bae, J., Bergin, E.A., Birnstiel, T. & Foreman-Mackey, D. (2018). A Kinematical Detection of Two Embedded Jupiter-mass Planets in HD 163296. *ApJ*, **860**, L12. 31, 54, 69, 70, 174

Terebey, S., Shu, F.H. & Cassen, P. (1984). The collapse of the cores of slowly rotating isothermal clouds. *ApJ*, **286**, 529–551. 3

Testi, L., Birnstiel, T., Ricci, L., Andrews, S., Blum, J., Carpenter, J., Dominik, C., Isella, A., Natta, A., Williams, J.P. & Wilner, D.J. (2014). Dust Evolution in Protoplanetary Disks. In H. Beuther, R.S. Klessen, C.P. Dullemond & T. Henning, eds., *Protostars and Planets VI*, 339. 7

Testi, L., Skemer, A., Henning, T., Bailey, V., Defrère, D., Hinz, P., Leisenring, J., Vaz, A., Esposito, S., Fontana, A., Marconi, A., Skrutskie, M. & Veillet, C. (2015). Hunting for Planets in the HL Tau Disk. *ApJ*, **812**, L38. 71

The, P.S., Felenbok, P., Cuypers, H. & Tjin-A-Djie, H.R.E. (1985). High resolution spectroscopic and photometric study of the possibility that HD 76534 and HD 163296 are Herbig Ae/Be-type stars. *A&A*, **149**, 429–436. 54

Thi, W.F., van Zadelhoff, G.J. & van Dishoeck, E.F. (2004). Organic molecules in protoplanetary disks around T Tauri and Herbig Ae stars. *A&A*, **425**, 955–972. 85

Thi, W.F., Ménard, F., Meeus, G., Martin-Zaïdi, C., Woitke, P., Tatulli, E., Benisty, M., Kamp, I., Pascucci, I., Pinte, C., Grady, C.A., Brittain, S., White, G.J., Howard, C.D., Sandell, G. & Eiroa, C. (2011). Detection of $CH^+$ emission from the disc around HD 100546. *A&A*, **530**, L2. 124

Tieftrunk, A., Pineau des Forets, G., Schilke, P. & Walmsley, C.M. (1994). SO and H2S in low density molecular clouds. *A&A*, **289**, 579–596. 14

Tilling, I., Woitke, P., Meeus, G., Mora, A., Montesinos, B., Riviere-Marichalar, P., Eiroa, C., Thi, W.F., Isella, A., Roberge, A., Martin-Zaidi, C., Kamp, I., Pinte, C., Sandell, G., Vacca, W.D., Ménard, F., Mendigutía, I., Duchêne, G., Dent, W.R.F., Aresu, G., Meijerink, R. & Spaans, M. (2012). Gas modelling in the disc of HD 163296. *A&A*, **538**, A20. 65

Toomre, A. (1964). On the gravitational stability of a disk of stars. *ApJ*, **139**, 1217–1238. 6, 69, 80

Tsukagoshi, T., Muto, T., Nomura, H., Kawabe, R., Kanagawa, K.D., Okuzumi, S., Ida, S., Walsh, C., Millar, T.J., Takahashi, S.Z., Hashimoto, J., Uyama, T. & Tamura, M. (2019). Discovery of An au-scale Excess in Millimeter Emission from the Protoplanetary Disk around TW Hya. *ApJ*, **878**, L8. 32

van Boekel, R., Waters, L.B.F.M., Dominik, C., Bouwman, J., de Koter, A., Dullemond, C.P. & Paresce, F. (2003). Grain growth in the inner regions of Herbig Ae/Be star disks. *A&A*, **400**, L21–L24. 15

van Boekel, R., Min, M., Waters, L.B.F.M., de Koter, A., Dominik, C., van den Ancker, M.E. & Bouwman, J. (2005). A 10 $\mu$m spectroscopic survey of Herbig Ae star disks: Grain growth and crystallization. *A&A*, **437**, 189–208. 15

van den Ancker, M.E., de Winter, D. & Tjin A Djie, H.R.E. (1998). HIPPARCOS photometry of Herbig Ae/Be stars. *A&A*, **330**, 145–154. 56, 86, 124

van der Marel, N., van Dishoeck, E.F., Bruderer, S., Birnstiel, T., Pinilla, P., Dullemond, C.P., van Kempen, T.A., Schmalzl, M.,

Brown, J.M., Herczeg, G.J., Mathews, G.S. & Geers, V. (2013). A Major Asymmetric Dust Trap in a Transition Disk. *Science*, **340**, 1199–1202. 25, 31, 145

van der Marel, N., van Dishoeck, E.F., Bruderer, S., Pérez, L. & Isella, A. (2015). Gas density drops inside dust cavities of transitional disks around young stars observed with ALMA. *A&A*, **579**, A106. 25

van der Marel, N., van Dishoeck, E.F., Bruderer, S., Andrews, S.M., Pontoppidan, K.M., Herczeg, G.J., van Kempen, T. & Miotello, A. (2016). Resolved gas cavities in transitional disks inferred from CO isotopologs with ALMA. *A&A*, **585**, A58. 25

van der Marel, N., Williams, J.P. & Bruderer, S. (2018). Rings and Gaps in Protoplanetary Disks: Planets or Snowlines? *ApJ*, **867**, L14. 120

van der Plas, G., van den Ancker, M.E., Acke, B., Carmona, A., Dominik, C., Fedele, D. & Waters, L.B.F.M. (2009). Evidence for CO depletion in the inner regions of gas-rich protoplanetary disks. *A&A*, **500**, 1137–1141. 86, 92

van der Plas, G., Casassus, S., Ménard, F., Perez, S., Thi, W.F., Pinte, C. & Christiaens, V. (2014). Spatially Resolved HCN J = 4-3 and CS J = 7-6 Emission from the Disk around HD 142527. *ApJ*, **792**, L25. 116

van der Plas, G., van den Ancker, M.E., Waters, L.B.F.M. & Dominik, C. (2015). The structure of disks around Herbig Ae/Be stars as traced by CO ro-vibrational emission. *A&A*, **574**, A75. 86

van der Plas, G., Wright, C.M., Ménard, F., Casassus, S., Canovas, H., Pinte, C., Maddison, S.T., Maaskant, K., Avenhaus, H., Cieza,

L., Perez, S. & Ubach, C. (2017). Cavity and other radial substructures in the disk around HD 97048. *A&A*, **597**, A32. 86, 87, 88, 90, 91, 119, 144, 176

van der Tak, F.F.S., Black, J.H., Schöier, F.L., Jansen, D.J. & van Dishoeck, E.F. (2007). A computer program for fast non-LTE analysis of interstellar line spectra. With diagnostic plots to interpret observed line intensity ratios. *A&A*, **468**, 627–635. 137

van Dishoeck, E.F. (2014). Astrochemistry of dust, ice and gas: introduction and overview. *Faraday Discussions*, **168**, 9. 43

van Dishoeck, E.F., Thi, W.F. & van Zadelhoff, G.J. (2003). Detection of $DCO^+$ in a circumstellar disk. *A&A*, **400**, L1–L4. 24

van Leeuwen, F. (2007). Validation of the new Hipparcos reduction. *A&A*, **474**, 653–664. 86

van 't Hoff, M.L.R., Walsh, C., Kama, M., Facchini, S. & van Dishoeck, E.F. (2017). Robustness of $N_2H^+$ as tracer of the CO snowline. *A&A*, **599**, A101. 28, 68

van 't Hoff, M.L.R., Persson, M.V., Harsono, D., Taquet, V., Jørgensen, J.K., Visser, R., Bergin, E.A. & van Dishoeck, E.F. (2018). Imaging the water snowline in a protostellar envelope with $H^{13}CO^+$. *A&A*, **613**, A29. 117

van Zadelhoff, G.J., van Dishoeck, E.F., Thi, W.F. & Blake, G.A. (2001). Submillimeter lines from circumstellar disks around pre-main sequence stars. *A&A*, **377**, 566–580. 85

Venuti, L., Bouvier, J., Flaccomio, E., Alencar, S.H.P., Irwin, J., Stauffer, J.R., Cody, A.M., Teixeira, P.S., Sousa, A.P., Micela,

G., Cuillandre, J.C. & Peres, G. (2014). Mapping accretion and its variability in the young open cluster NGC 2264: a study based on u-band photometry. *A&A*, **570**, A82. 70

Visser, R., van Dishoeck, E.F. & Black, J.H. (2009). The photodissociation and chemistry of CO isotopologues: applications to interstellar clouds and circumstellar disks. *A&A*, **503**, 323–343. 79, 96, 112

Visser, R., Bruderer, S., Cazzoletti, P., Facchini, S., Heays, A.N. & van Dishoeck, E.F. (2018). Nitrogen isotope fractionation in protoplanetary disks. *A&A*, **615**, A75. 25

Vlemmings, W.H.T., Lankhaar, B., Cazzoletti, P., Ceccobello, C., Dall'Olio, D., van Dishoeck, E.F., Facchini, S., Humphreys, E.M.L., Persson, M.V., Testi, L. & Williams, J.P. (2019). Stringent limits on the magnetic field strength in the disc of TW Hya. ALMA observations of CN polarisation. *A&A*, **624**, L7. 18

Wagner, K., Follette, K.B., Close, L.M., Apai, D., Gibbs, A., Kepler, M., Müller, A., Henning, T., Kasper, M., Wu, Y.L., Long, J., Males, J., Morzinski, K. & McClure, M. (2018). Magellan Adaptive Optics Imaging of PDS 70: Measuring the Mass Accretion Rate of a Young Giant Planet within a Gapped Disk. *ApJ*, **863**, L8. 32, 181

Wakelam, V., Herbst, E., Loison, J.C., Smith, I.W.M., Chandrasekaran, V., Pavone, B., Adams, N.G., Bacchus-Montabonel, M.C., Bergeat, A., Béroff, K., Bierbaum, V.M., Chabot, M., Dalgarno, A., van Dishoeck, E.F., Faure, A., Geppert, W.D., Gerlich, D., Galli, D., Hébrard, E., Hersant, F., Hickson, K.M., Honvault, P., Klippenstein, S.J., Le Picard, S., Nyman, G., Pernot, P.,

Schlemmer, S., Selsis, F., Sims, I.R., Talbi, D., Tennyson, J., Troe, J., Wester, R. & Wiesenfeld, L. (2012). A KInetic Database for Astrochemistry (KIDA). *ApJS*, **199**, 21. 42

Walsh, C., Millar, T.J. & Nomura, H. (2010). Chemical Processes in Protoplanetary Disks. *ApJ*, **722**, 1607–1623. 40, 60, 115

Walsh, C., Nomura, H., Millar, T.J. & Aikawa, Y. (2012). Chemical Processes in Protoplanetary Disks. II. On the Importance of Photochemistry and X-Ray Ionization. *ApJ*, **747**, 114. 40, 95

Walsh, C., Juhász, A., Pinilla, P., Harsono, D., Mathews, G.S., Dent, W.R.F., Hogerheijde, M.R., Birnstiel, T., Meeus, G., Nomura, H., Aikawa, Y., Millar, T.J. & Sandell, G. (2014a). ALMA Hints at the Presence of two Companions in the Disk around HD 100546. *ApJ*, **791**, L6. 15, 39, 124, 126, 127

Walsh, C., Millar, T.J., Nomura, H., Herbst, E., Widicus Weaver, S., Aikawa, Y., Laas, J.C. & Vasyunin, A.I. (2014b). Complex organic molecules in protoplanetary disks. *A&A*, **563**, A33. 44

Walsh, C., Nomura, H. & van Dishoeck, E. (2015). The molecular composition of the planet-forming regions of protoplanetary disks across the luminosity regime. *A&A*, **582**, A88. 16, 116, 156

Walsh, C., Juhász, A., Meeus, G., Dent, W.R.F., Maud, L.T., Aikawa, Y., Millar, T.J. & Nomura, H. (2016a). ALMA Reveals the Anatomy of the mm-sized Dust and Molecular Gas in the HD 97048 Disk. *ApJ*, **831**, 200. 86, 87, 88, 91, 92, 94, 104, 105, 119, 126, 143, 144, 176

Walsh, C., Loomis, R.A., Öberg, K.I., Kama, M., van 't Hoff, M.L.R., Millar, T.J., Aikawa, Y., Herbst, E., Widicus Weaver, S.L. & No-

MURA, H. (2016b). First Detection of Gas-phase Methanol in a Protoplanetary Disk. *ApJ*, **823**, L10. 180

WALSH, C., DALEY, C., FACCHINI, S. & JUHÁSZ, A. (2017). CO emission tracing a warp or radial flow within $\lesssim$100 au in the HD 100546 protoplanetary disk. *A&A*, **607**, A114. 31, 127, 143, 147

WATERS, L.B.F.M. & WAELKENS, C. (1998). Herbig Ae/Be Stars. *ARA&A*, **36**, 233–266. 5

WEIDENSCHILLING, S.J. (1977). Aerodynamics of solid bodies in the solar nebula. *MNRAS*, **180**, 57–70. 9

WICHITTANAKOM, C., OUDMAIJER, R.D., FAIRLAMB, J.R., MENDIGUTÍA, I., VIOQUE, M. & ABABAKR, K.M. (2020). The accretion rates and mechanisms of Herbig Ae/Be stars. *MNRAS*, 166. 54, 70, 86, 124

WILLIAMS, J.P. & BEST, W.M.J. (2014). A Parametric Modeling Approach to Measuring the Gas Masses of Circumstellar Disks. *ApJ*, **788**, 59. 13, 21, 65, 95, 179

WILLIAMS, J.P. & CIEZA, L.A. (2011). Protoplanetary Disks and Their Evolution. *ARA&A*, **49**, 67–117. 7, 8, 11

WILLIAMS, J.P. & MCPARTLAND, C. (2016). Measuring Protoplanetary Disk Gas Surface Density Profiles with ALMA. *ApJ*, **830**, 32. 65

WILNER, D.J. (2004). Imaging protoplanetary disks with a square kilometer array. *New A Rev.*, **48**, 1363–1375. 182

WILSON, T.L. (1999). Isotopes in the interstellar medium and circumstellar envelopes. *Reports on Progress in Physics*, **62**, 143–185. 58, 77, 93, 97

Woitke, P. (2015). Heating and cooling processes in disks. In *European Physical Journal Web of Conferences*, vol. 102 of *European Physical Journal Web of Conferences*, 00011. 12

Woitke, P., Kamp, I. & Thi, W.F. (2009a). Radiation thermo-chemical models of protoplanetary disks. I. Hydrostatic disk structure and inner rim. *A&A*, **501**, 383–406. 12

Woitke, P., Thi, W.F., Kamp, I. & Hogerheijde, M.R. (2009b). Hot and cool water in Herbig Ae protoplanetary disks. A challenge for Herschel. *A&A*, **501**, L5–L8. 117

Woitke, P., Min, M., Pinte, C., Thi, W.F., Kamp, I., Rab, C., Anthonioz, F., Antonellini, S., Baldovin-Saavedra, C., Carmona, A., Dominik, C., Dionatos, O., Greaves, J., Güdel, M., Ilee, J.D., Liebhart, A., Ménard, F., Rigon, L., Waters, L.B.F.M., Aresu, G., Meijerink, R. & Spaans, M. (2016). Consistent dust and gas models for protoplanetary disks. I. Disk shape, dust settling, opacities, and PAHs. *A&A*, **586**, A103. 94

Woitke, P., Kamp, I., Antonellini, S., Anthonioz, F., Baldovin-Saveedra, C., Carmona, A., Dionatos, O., Dominik, C., Greaves, J., Güdel, M., Ilee, J.D., Liebhardt, A., Menard, F., Min, M., Pinte, C., Rab, C., Rigon, L., Thi, W.F., Thureau, N. & Waters, L.B.F.M. (2019). Consistent Dust and Gas Models for Protoplanetary Disks. III. Models for Selected Objects from the FP7 DIANA Project. *PASP*, **131**, 064301. 65, 94, 156, 157

Wood, K., Kenyon, S.J., Whitney, B.A. & Bjorkman, J.E. (1996). Magnetic Accretion and Photopolarimetric Variability in T Tauri Stars. *ApJ*, **458**, L79. 4

Woods, P.M. & Willacy, K. (2009). Carbon Isotope Fractionation in Protoplanetary Disks. *ApJ*, **693**, 1360–1378. 25, 97, 100, 112, 113, 176

Wright, M., Plambeck, R., Hirota, T., Ginsburg, A., McGuire, B., Bally, J. & Goddi, C. (2020). Observations of the orion source i disk and outflow interface. *The Astrophysical Journal*, **889**, 155. 165

Wu, C.J., Hirano, N., Takakuwa, S., Yen, H.W. & Aso, Y. (2018). Physical and Chemical Conditions of the Protostellar Envelope and the Protoplanetary Disk in HL Tau. *ApJ*, **869**, 59. 72, 79, 80, 175

Yen, H.W., Koch, P.M., Liu, H.B., Puspitaningrum, E., Hirano, N., Lee, C.F. & Takakuwa, S. (2016a). Stacking Spectra in Protoplanetary Disks: Detecting Intensity Profiles from Hidden Molecular Lines in HD 163296. *ApJ*, **832**, 204. 56

Yen, H.W., Liu, H.B., Gu, P.G., Hirano, N., Lee, C.F., Puspitaningrum, E. & Takakuwa, S. (2016b). Gas Gaps in the Protoplanetary Disk around the Young Protostar HL Tau. *ApJ*, **820**, L25. 75

Yen, H.W., Gu, P.G., Hirano, N., Koch, P.M., Lee, C.F., Liu, H.B. & Takakuwa, S. (2019). HL Tau Disk in $HCO^+$ (32) and (10) with ALMA: Gas Density, Temperature, Gap, and One-arm Spiral. *ApJ*, **880**, 69. 76, 82

Youdin, A.N. & Goodman, J. (2005). Streaming Instabilities in Protoplanetary Disks. *ApJ*, **620**, 459–469. 9

Zhang, K., Blake, G.A. & Bergin, E.A. (2015). Evidence of Fast Pebble Growth Near Condensation Fronts in the HL Tau Protoplanetary Disk. *ApJ*, **806**, L7. 31, 71, 76

Zhang, K., Bergin, E.A., Blake, G.A., Cleeves, L.I., Hogerheijde, M., Salinas, V. & Schwarz, K.R. (2016). On the Commonality of 10-30 AU Sized Axisymmetric Dust Structures in Protoplanetary Disks. *ApJ*, **818**, L16. 92

Zhang, K., Bergin, E.A., Blake, G.A., Cleeves, L.I. & Schwarz, K.R. (2017). Mass inventory of the giant-planet formation zone in a solar nebula analogue. *Nature Astronomy*, **1**, 0130. 16, 21

Zhang, K., Bergin, E.A., Schwarz, K., Krijt, S. & Ciesla, F. (2019). Systematic Variations of CO Gas Abundance with Radius in Gas-rich Protoplanetary Disks. *ApJ*, **883**, 98. 26

Zhang, K., Bosman, A.D. & Bergin, E.A. (2020). Excess C/H in Protoplanetary Disk Gas from Icy Pebble Drift Across the CO Snowline. *ApJ*, **891**, L16. 67

Zhang, S., Zhu, Z., Huang, J., Guzmán, V.V., Andrews, S.M., Birnstiel, T., Dullemond, C.P., Carpenter, J.M., Isella, A., Pérez, L.M., Benisty, M., Wilner, D.J., Baruteau, C., Bai, X.N. & Ricci, L. (2018). The Disk Substructures at High Angular Resolution Project (DSHARP). VII. The Planet-Disk Interactions Interpretation. *ApJ*, **869**, L47. 25, 30

Zhu, Z., Nelson, R.P., Hartmann, L., Espaillat, C. & Calvet, N. (2011). Transitional and Pre-transitional Disks: Gap Opening by Multiple Planets? *ApJ*, **729**, 47. 29

Zhu, Z., Nelson, R.P., Dong, R., Espaillat, C. & Hartmann, L. (2012). Dust Filtration by Planet-induced Gap Edges: Implications for Transitional Disks. *ApJ*, **755**, 6. 119

Zhu, Z., Zhang, S., Jiang, Y.F., Kataoka, A., Birnstiel, T., Dullemond, C.P., Andrews, S.M., Huang, J., Pérez, L.M., Carpenter, J.M., Bai, X.N., Wilner, D.J. & Ricci, L. (2019). One Solution to the Mass Budget Problem for Planet Formation: Optically Thick Disks with Dust Scattering. *ApJ*, **877**, L18. 21, 83

Ziurys, L.M., Friberg, P. & Irvine, W.M. (1989). Interstellar SiO as a Tracer of High-Temperature Chemistry. *ApJ*, **343**, 201. 151

Zsom, A., Ormel, C.W., Güttler, C., Blum, J. & Dullemond, C.P. (2010). The outcome of protoplanetary dust growth: pebbles, boulders, or planetesimals? II. Introducing the bouncing barrier. *A&A*, **513**, A57. 7